

AN APPLICATION OF ADVANCED
OXIDATION PROCESS TO PHOTOPOLISH
PALM OIL MILL EFFLUENT OVER TiO_2 AND
 ZnO PHOTOCATALYSTS

NG KIM HOONG

UMP

DOCTOR OF PHILOSOPHY
(CHEMICAL ENGINEERING)

UNIVERSITI MALAYSIA PAHANG

UNIVERSITI MALAYSIA PAHANG

DECLARATION OF THESIS AND COPYRIGHT

Author's Full Name : NG KIM HOONG
Date of Birth : 05 APRIL 1990
Title : AN APPLICATION OF ADVANCED OXIDATION PROCESS
TO PHOTOPOLISH PALM OIL MILL EFFLUENT OVER TiO₂
AND ZnO PHOTOCATALYSTS
Academic Session : _____

I declare that this thesis is classified as:

- CONFIDENTIAL (Contains confidential information under the Official Secret Act 1997)*
- RESTRICTED (Contains restricted information as specified by the organization where research was done)*
- OPEN ACCESS I agree that my thesis to be published as online open access (Full Text)

I acknowledge that Universiti Malaysia Pahang reserves the following rights:

1. The Thesis is the Property of Universiti Malaysia Pahang
2. The Library of Universiti Malaysia Pahang has the right to make copies of the thesis for the purpose of research only.
3. The Library has the right to make copies of the thesis for academic exchange.

Certified by:

(Student's Signature)
NG KIM HOONG

900405085203
Date: 01/07/17

(Supervisor's Signature)
PM DR CHENG CHIN KUI

Name of Supervisor
Date: 01/07/17

NOTE : * If the thesis is CONFIDENTIAL or RESTRICTED, please attach a thesis declaration letter.

SUPERVISOR'S DECLARATION

We hereby declare that We have checked this thesis and in our opinion, this thesis is adequate in terms of scope and quality for the award of the degree of Doctor of Philosophy in Chemical Engineering

(Supervisor's Signature)

Full Name : Assoc. Prof. Dr. Cheng Chin Kui

Position : Associate Professor

Date : 01/07/17

(Co-supervisor's Signature)

Full Name : Assoc. Prof. Dr. Md. Maksudur Rahman Khan

Position : Associate Professor

Date : 01/07/17

STUDENT'S DECLARATION

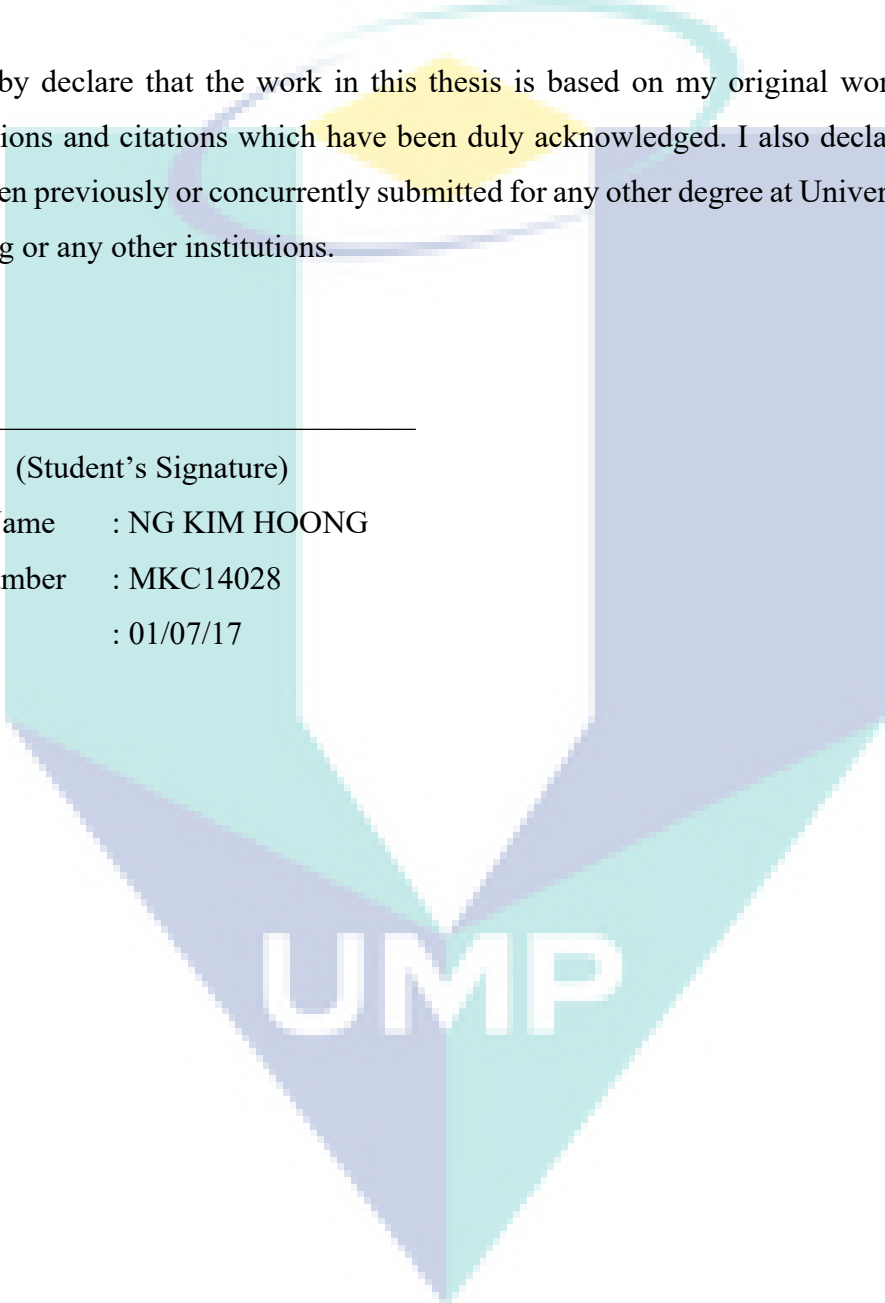
I hereby declare that the work in this thesis is based on my original work except for quotations and citations which have been duly acknowledged. I also declare that it has not been previously or concurrently submitted for any other degree at Universiti Malaysia Pahang or any other institutions.

(Student's Signature)

Full Name : NG KIM HOONG

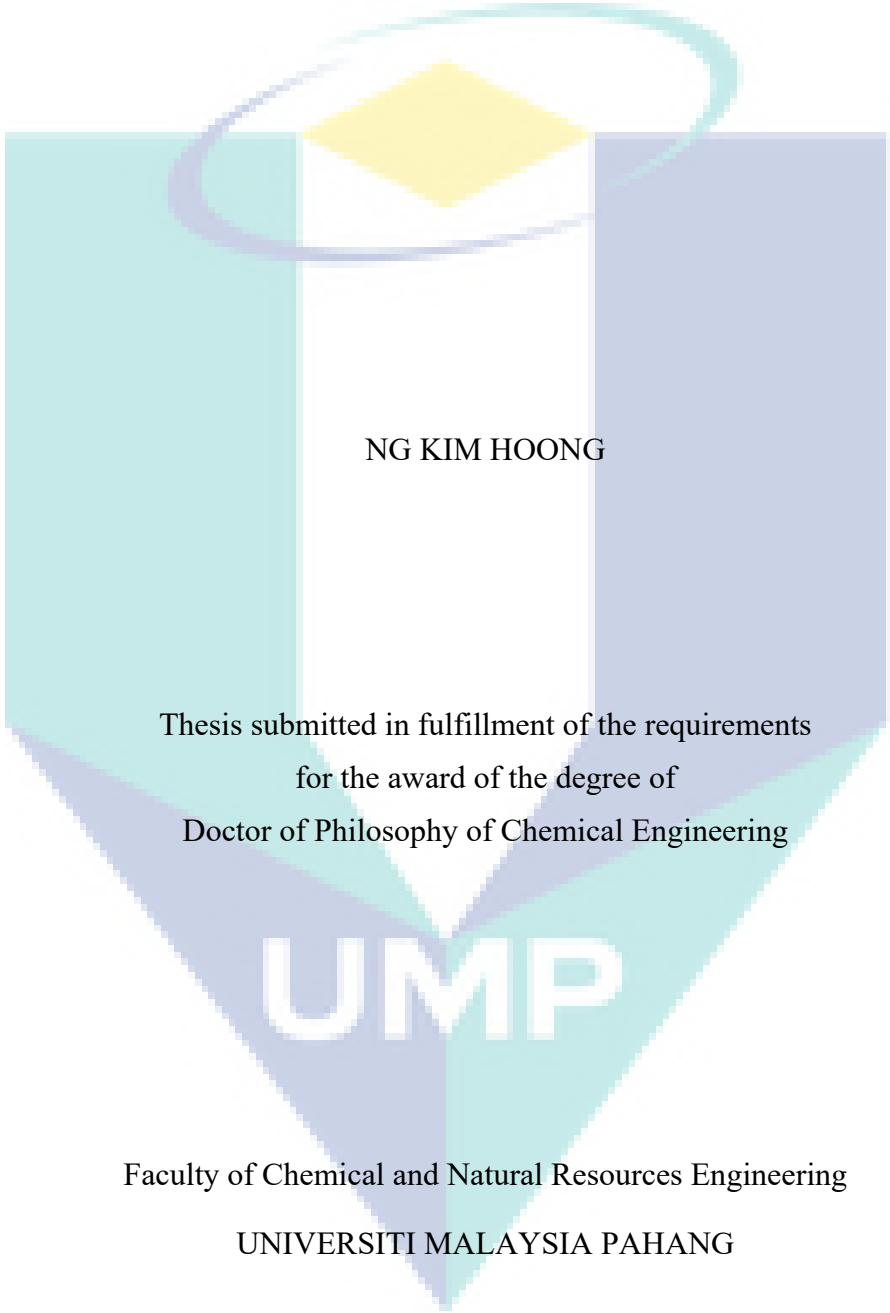
ID Number : MKC14028

Date : 01/07/17



UMP

AN APPLICATION OF ADVANCED OXIDATION PROCESS TO
PHOTOPOLISH PALM OIL MILL EFFLUENT OVER TiO_2 AND ZnO
PHOTOCATALYSTS



NG KIM HOONG

Thesis submitted in fulfillment of the requirements
for the award of the degree of
Doctor of Philosophy of Chemical Engineering

UMP

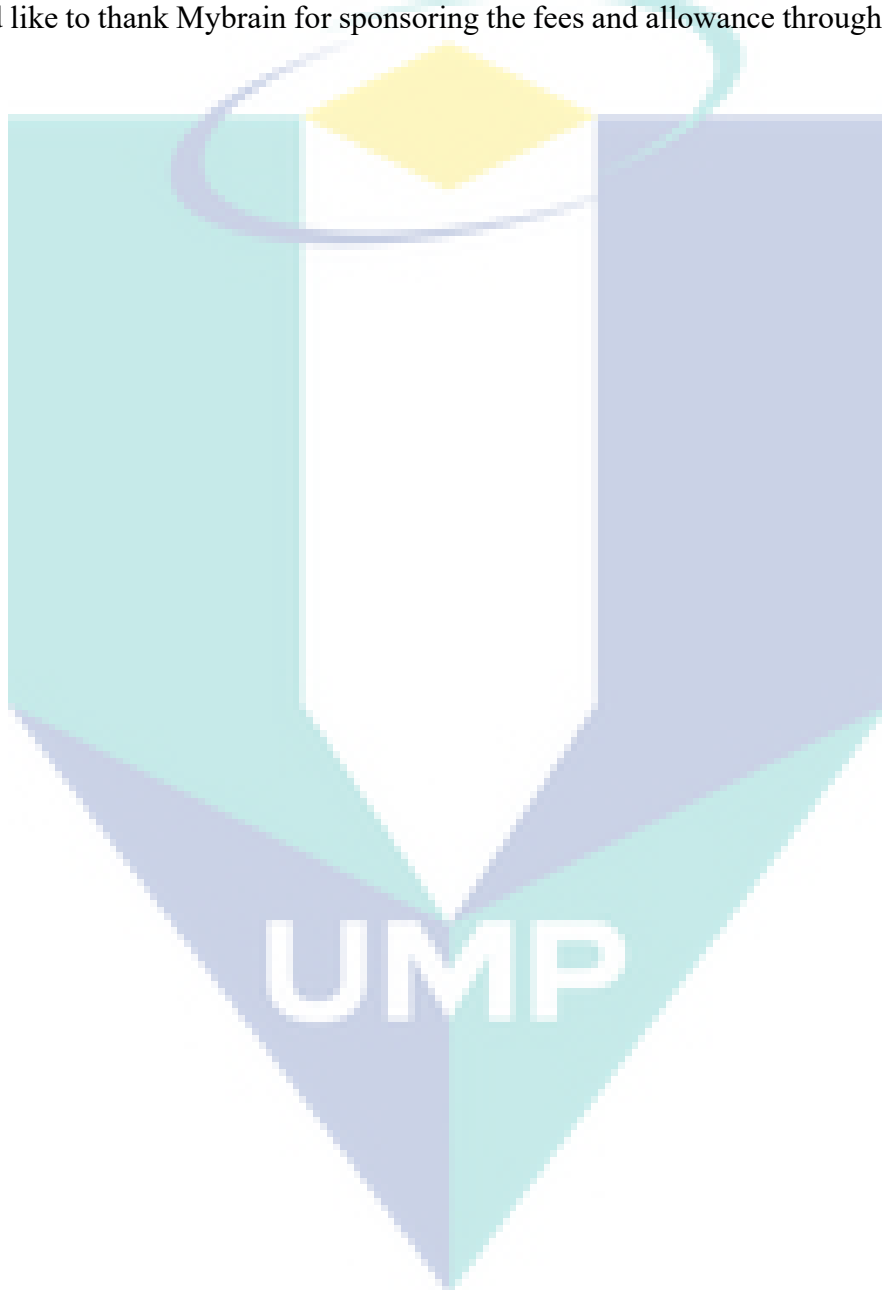
Faculty of Chemical and Natural Resources Engineering

UNIVERSITI MALAYSIA PAHANG

JULY 2017

ACKNOWLEDGEMENTS

I would like to express my sincere gratitude to my supervisor, Assoc. Prof. Dr. Cheng Chin Kui and myself in completing this thesis. Besides, I would also like to thank Malaysia Toray Science Fund (RDU 151501) for funding current project, Ministry of Higher Education Malaysia (MOHE) for ERGS (RDU120613), Universiti Malaysia Pahang for Doctoral Scholarship Scheme and PRGS (RDU150330). Last but not least, I would like to thank Mybrain for sponsoring the fees and allowance throughout the study.



ABSTRAK

Kereaktifan kedua-dua sistem UV/TiO₂ dan UV/ZnO di dalam rawatan kumbahan kilang minyak sawit (POME) telah dikaji dalam projek ini. XRD mendedahkan bahawa TiO₂ dan ZnO, dengan julat tenaga 3.15 dan 3.20 eV, adalah bebas daripada kekotoran. ZnO fotokatalis mempunyai struktur yang tidak teratur, saiz partikel yang lebih besar, tetapi keluasan kawasan permukaan BET yang lebih kecil (9.71 m²/g) berbanding dengan fotokatalis TiO₂ (11.34 m²/g). Proses degradasi POME telah dijalankan di dalam 500 mL fotoreaktor Pyrex pada suhu bilik dengan penyinaran 100 W lampu UV. Dengan muatan pemangkin 1.0 g/L dan 70 mL/min O₂, degradasi yang diperolehi oleh UV/ TiO₂ (52.0%) adalah lebih tinggi daripada UV/ZnO (50.0%) selepas 240 minit sinaran UV dan jurang prestasi penguraian antara kedua-dua sistem telah diperluaskan selepas 22 jam sinaran UV. Pada akhir eksperimen, degradasi yang dicapai adalah 80.35% dan 74.11% untuk UV/TiO₂ dan UV/ZnO. Walau bagaimanapun, bacaan akhir untuk COD, BOD dan O&G POME yang dicapai untuk UV /TiO₂ (33, 16, dan 10 ppm) dan UV/ZnO (44, 26, dan 20 ppm) telah berjaya diturunkan ke tahap yang selamat untuk dibuang. Dalam ujian kitaran, TiO₂ mempamerkan kestabilan yang lebih tinggi, kerana tiada penyahaktifan yang diperhatikan selepas tiga kitaran berturut-turut bagi tindak balas foto, berbanding dengan 24.0% penyahaktifan untuk sistem UV/ZnO. Ujian pemusnahan spesies reaktif mendedahkan bahawa spesies reaktif utama degradasi POME untuk kedua-dua sistem adalah berbeza. Radikal bebas OH• mengurai paling banyak organik dalam sistem UV/TiO₂ manakala sistem UV/ZnO menjana OH_{ads}• bagi kebanyakan degradasi organik. Keupayaan penjerapan organik di permukaan fotokatalisis ZnO membolehkan proses degradasi berlaku di permukaannya. Untuk TiO₂, degradasi organik hanya boleh berlaku dalam larutan pukal kerana afiniti TiO₂ terhadap pencemar organik adalah lemah. Ini turut disokong oleh analisis selepas tindakbalas yang dijalankan ke atas pemangkin kedua-dua sistem yang mengesahkan bahawa spesies karbon hanya dikesan pada permukaan ZnO. Rekaan 2³ faktorial penuh di dalam RSM mengesahkan bahawa kadar aliran O₂, muatan pemangkin dan kepekatan awal POME adalah faktor penting dalam kedua-dua sistem. Tambahan pula, ia juga mengesahkan kewujudan faktor interaktif dalam kedua-dua sistem. Selepas itu, ketiga-tiga faktor utama untuk kedua-dua sistem ini telah dioptimumkan dengan menggunakan CCD dalam RSM. Model kuadratik dengan nilai R² (> 0.9) yang tinggi dan analisis baki yang sangat baik telah diperolehi oleh kedua-dua sistem untuk mewakili degradasi. Syarat-syarat yang dioptimumkan telah dicadangkan dan eksperimen (diulang) telah dijalankan untuk kedua-dua sistem. Berdasarkan keputusan yang diperolehi, sistem UV/TiO₂ telah berjaya dioptimumkan kepada 54.33 dan 55.62% degradasi selepas 240 min sinaran UV dengan 1.04 g/L TiO₂, 66.0 mL/minit O₂ dan kepekatan awal POME 240 ppm. Selain itu, degradasi sistem UV/ZnO juga telah dioptimumkan kepada 55.25 dan 55.33%, dengan 60 mL/min O₂, 1.26 g/L ZnO dan 220 ppm POME, selepas 240 minit sinaran UV. Ralat antara degradasi anggaran dan eksperimen untuk sistem UV/TiO₂ dan sistem UV/ZnO adalah sangat rendah (4.41 dan 5.40%), mengesahkan keunggulan model-model ini.

ABSTRACT

The reactivity of both UV/TiO₂ and UV/ZnO systems in treating palm oil mill effluent (POME) were investigated in current study. XRD revealed that TiO₂ and ZnO, with the band gap energy of 3.15 and 3.20 eV respectively, were free from impurities. ZnO photocatalyst has irregular shape, bigger in particle size but lower BET specific surface area (9.71 m²/g) compared to the spherical TiO₂ photocatalysts (11.34 m²/g). The degradation process of POME was conducted in a 500 mL Pyrex photoreactor at room temperature with the irradiation of 100 W UV lamp. With 1.0 g/L of photocatalyst and 70 mL/min of O₂ bubbling, the degradation obtained by UV/TiO₂ system (52.0%) is slightly higher compared to UV/ZnO system (50.0%) in 240 min of UV irradiation and the performance gap between two systems was broaden after 22 h of UV irradiation. At the end of the experiments, the degradation achieved were 80.35% and 74.11% for UV/TiO₂ and UV/ZnO system, respectively. Nonetheless, the final COD, BOD and oil and grease (O&G) level of POME for UV/TiO₂ system (33, 16, and 10 ppm) and UV/ZnO system (44, 26, and 20 ppm) were successfully brought down to the safe level for discharging. In recyclability test, TiO₂ exhibits a higher stability, as no significant deactivation was observed after three consecutive cycle of photoreaction, compared to 24.0% of deactivation in UV/ZnO system. Scavenging test reveals that the main reactive species for POME degradation for both systems are different. OH[•] free radical decomposed most organics in UV/TiO₂ while UV/ZnO system generates OH_{ads}[•] for most of the organic degradation. The ability of organic-adsorption in ZnO photocatalyst allows the degradation process occurs on its surface. For TiO₂ photocatalyst, the organic degradation can only happen in bulk solution due to the poor affinity of TiO₂ towards organic pollutants. This is further supported by the post-reaction analysis conducted on spent photocatalysts both systems, confirming the carbonaceous species only detected on the surface of ZnO. 2³ full factorial design in Response Surface Methodology (RSM) was employed and confirmed that O₂ flowrate, photocatalyst loadings and initial concentration of POME are significant in both system. Furthermore, it also confirmed the existence of interactive factors in both systems. Subsequently, all three main factors for both systems were optimized by using Central Composite Design (CCD) in RSM. Quadratic models with high R² values (>0.9) and excellent residue analysis were developed for both systems to describe the degradation. The optimized conditions were suggested and experiments (duplicated) were conducted for both system. Based on the results obtained, the degradation of UV/TiO₂ system were successfully optimized to averaged degradation of 55.0% after 240 min of UV irradiation in the presence of 1.04 g/L of TiO₂, 66.0 mL/min of O₂ bubbling and initial POME concentration of 240 ppm. On the other hand, the degradations of UV/ZnO system were optimized to averaged degradation of 55.29%, with 60 mL/min of O₂ bubbling, 1.26 g/L of ZnO and 220 ppm of POME, after 240 min of UV irradiation. The errors between the estimated and experimental degradation recorded for UV/TiO₂ system and UV/ZnO system were very low (4.41 and 5.40%, respectively), hence confirming the adequacy of the models developed.

TABLE OF CONTENT

DECLARATION	
TITLE PAGE	
ACKNOWLEDGEMENTS	ii
ABSTRAK	iii
ABSTRACT	iii
TABLE OF CONTENT	v
LIST OF TABLES	x
LIST OF FIGURES	xii
LIST OF SYMBOLS	xvi
LIST OF ABBREVIATIONS	xvii
CHAPTER 1 INTRODUCTION	1
1.1 Background	1
1.2 Problem Statement	3
1.3 Objective	4
1.4 Scopes of Study	5
1.5 Rational and Significance	6
1.6 Outline of the Thesis	7
CHAPTER 2 LITERATURE REVIEW	8
2.1 Introduction	8
2.2 Palm Oil Mill Effluent (POME)	8
2.3 Laws and Legislations	9

2.4	Conventional POME Treatment	10
2.5	Tertiary Treatment for POME Polishing	12
2.6	Fundamentals and Concept of Advanced Oxidation Processes (AOPs)	16
2.7	Heterogeneous Photocatalysis	18
2.7.1	Basic Principles	18
2.7.2	Band Structure and Band Gap of Semiconductors	19
2.7.3	Charge Separation	21
2.7.4	Key Species in Organic Destruction	22
2.8	Past Works on Photodegradation of Organic Compounds	23
2.8.1	Photocatalysis with Different Photocatalysts	23
2.8.2	Past Research Works on TiO ₂ -based Photocatalysis	30
2.8.3	Past Research Works on ZnO-based Photocatalyst	35
2.9	Optimization Using Central Composite Design (CCD) in Response Surface Methodology (RSM)	37
2.10	Photocatalysts Characterization Techniques	41
2.10.1	X-Ray Diffraction (XRD)	41
2.10.2	N ₂ Physisorption Analysis	43
2.10.3	UV-Vis Diffuse Reflectance Spectroscopy	46
2.10.4	Field Emission Scanning Electron Microscopy (FESEM)	48
2.10.5	Fourier Transform Infrared Spectroscopy (FTIR)	49
2.10.6	Scanning Electron Microscopy with X-Ray Microanalysis (SEM-EDX)	49
2.11	Conclusion Remarks	50
CHAPTER 3 MATERIALS AND METHODS		52
3.1	Introduction	52
3.2	Overview of Methodology	52

3.3	Chemicals and Gases	53
3.4	POME Wastewater	54
3.4.1	POME Sampling and Preservation	54
3.4.2	Pre-reaction POME Characterization	54
3.4.3	Post-reaction POME analysis	58
3.5	Photocatalysts Preparation and Characterizations	59
3.5.1	Photocatalysts Preparation	59
3.5.2	Photocatalysts Characterization	60
3.5.3	Post-reaction Photocatalysts Analysis	61
3.6	Photocatalytic Degradation of POME	62
3.6.1	Photoreaction	62
3.6.2	Sample Analysis	63
3.7	Optimization of the Process	65
CHAPTER 4 PHOTOCATALYTIC TREATMENT OF POME WASTEWATER OVER UV/TIO₂ SYSTEM		67
4.1	Introduction	67
4.2	Characterization of POME Wastewater	68
4.3	Characterization of TiO ₂ Photocatalyst	70
4.4	Preliminary Works	74
4.4.1	Effects of Stirring Speed	74
4.4.2	Effects of O ₂ Flowrate	76
4.4.3	Control Reactions	78
4.5	Photocatalytic Degradation of POME	79
4.5.1	Effects of TiO ₂ Loadings	79
4.5.2	Langmuir-Hinshelwood (LH) Rate Law Modeling	81

4.5.3	Gaseous Products from the POME Degradation	85
4.5.4	Scavenging Study and Mechanisms of Degradation	88
4.5.5	Recyclability and Longevity Studies	90
4.6	Post-reaction Analysis for TiO ₂ Photocatalyst	95
4.7	Optimization of the Process	99
4.7.1	Significance Analysis of Main Factors	100
4.7.2	Optimization of the Factors	107
4.7.3	Optimization of the Process and Validation	116
4.8	Correlation between BOD and COD for UV/TiO ₂ System	118
4.9	Summary	119
CHAPTER 5 PHOTOCATALYTIC TREATMENT OF POME WASTEWATER OVER UV/ZNO SYSTEM		121
5.1	Introduction	121
5.2	Characterization of ZnO Photocatalyst	122
5.3	Photocatalytic Degradation of POME	124
5.3.1	Effects of ZnO Loadings	125
5.3.2	Langmuir-Hinshelwood (LH) Rate Law Modeling	128
5.3.3	Gaseous Products from the POME Degradation	130
5.3.4	Scavenging Study and Mechanisms of Degradation	133
5.3.5	Recyclability and Longevity Studies	137
5.4	Post-reaction Analysis for ZnO Photocatalyst	141
5.5	Optimization of the Process	146
5.5.1	Significance Analysis of Main Factors	146
5.5.2	Optimization of the Factors	153
5.6	Correlation between BOD and COD of POME Treated by UV/ZnO System	161

5.7	Summary	162
CHAPTER 6 MECHANISTICS AND PERFORMANCE COMPARISONS BETWEEN UV/TIO₂ AND UV/ZNO SYSTEMS		164
6.1	Introduction	164
6.2	Comparisons of Photocatalyst Properties	164
6.3	Response to Scavengers and Mechanisms of Degradation	166
6.4	Effects of Photocatalyst Loading Towards Both System	168
6.5	Recyclability and Longevity Studies	170
6.6	Summary	172
CHAPTER 7 CONCLUSION		174
7.1	Conclusion	174
7.2	Recommendations	178
REFERENCES		179
APPENDIX A List of publications		196

UMP

LIST OF TABLES

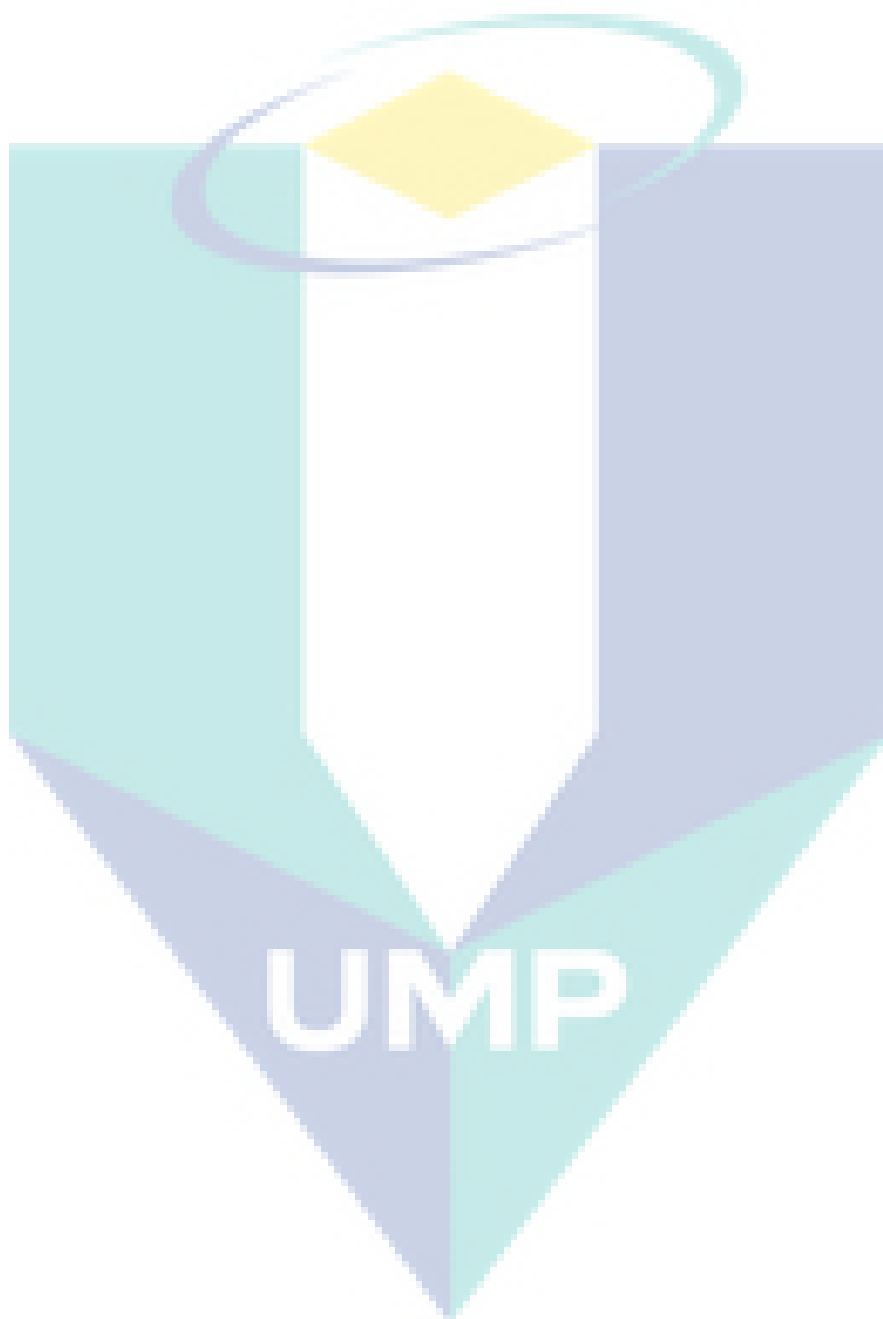
Table 2.1	Chatacteristic of POME	9
Table 2.2	POME discharge standards according to periods of discharge	10
Table 2.3	Summary of new proposed polishing technologies in POME tertiary treatment	15
Table 2.4	The summary of past researches on photocatalysis process	28
Table 2.5	Recent research works on decontaminat organic substrate over TiO ₂ photocatalyst	33
Table 2.6	Past research works using ZnO as the photocatalyst	37
Table 2.7	The examples of CCD optimization in analytical chemistry	40
Table 3.1	List of chemicals and gases	53
Table 3.2	Retention time A_{standard} and $X_{i,\text{standard}}$ for each speices	64
Table 4.1	Characteristics of ponding-treated POME	69
Table 4.2	k-values obtained from the photoreactions on POME with different TiO ₂ loadings	83
Table 4.3	Total gas products collected from photoreactions	88
Table 4.4	Comparisons of the parameters before and after photocatalytic treatment process	93
Table 4.5	The experimental conditions of photoreactions and the degradations obtained	101
Table 4.6	ANOVA analysis obtained from the response	104
Table 4.7	CCD for optimization of POME degradation	108
Table 4.7	ANOVA for response surface quadratic model	110
Table 4.9	The suggested experimental conditions and the actual experiment condition	118
Table 5.1	k-values obtained from the photodegradation of POME over different ZnO loadings	129
Table 5.2	Total gas products collected from photoreactions	132
Table 5.3	Comparisons of the parameters before and after photocatalytic treatment process	141
Table 5.4	Significance analysis of main factors	147
Table 5.5	Contribution of each factor towards degradation efficiency	150
Table 5.6	ANOVA analysis obtained from the response	150
Table 5.7	The design of experiment and degradation achieved for each run	154
Table 5.8	R-values of each model	155
Table 5.9	ANOVA for the quadratic model	156

Table 5.10 Results of experimental validation

161

Table 6.1 Characterization of TiO₂ and ZnO

165



LIST OF FIGURES

Figure 2.1	Illustration of photocatalysis mechanisms	19
Figure 2.2	Band structure of a semiconductor	20
Figure 2.3	Different crystalline structure of TiO ₂	21
Figure 2.4	Kinetics curves of conversion of phenol with Mn oxide as photocatalyst	24
Figure 2.5	The graph of removal (%) of organic substances versus photocatalyst concentration	24
Figure 2.6	Concentration of 2,4,6-TCP vs irradiation time under visible-light irradiation ($\lambda > 400$ nm) with the presence of LDH film catalysts with different thickness	25
Figure 2.7	Photoactivities of four metal oxides in deionized water at various concentration	26
Figure 2.8	Azobenzene formation in ethanol on Fe ₂ O ₃ at different aniline concentration under irradiation of UV-light and Solar(visible) light	27
Figure 2.9	Comparison of the decolorization efficiency of Procion red MX-5B by different %wt of Ag/TiO ₂	30
Figure 2.10	The graph of (C/C ₀) of congo red versus UV irradiation time with various catalyst composition	31
Figure 2.11	Crystalline structures for ZnO	35
Figure 2.12	The CCD for optimization process of two (left) and three (right) variables	39
Figure 2.13	A schematic diagram of XRD (A) Collimation (B) Sample (C) Slit (D) Exit Beam Monochromator (E) Detector (X) Source of X-Rays	43
Figure 2.14	The Jasco V-550 optical system schematic diagram	48
Figure 2.15	A Schematic diagram of FESEM	49
Figure 3.1	A Schematic diagram of FESEM	53
Figure 3.2	Set up for evaporation of n-hexane solvent	57
Figure 3.3	The schematic diagram of photoreaction set up	62
Figure 3.4	Gas chromatogram obtained for standard gas	65
Figure 4.1	FTIR spectrum of ponding-treated POME	70
Figure 4.2	XRD diffractogram of TiO ₂	71
Figure 4.3	FESEM images of TiO ₂ photocatalyst (a)10 kx (b) 35 kx (c) 55 kx (d) 100 kx	72
Figure 4.4	Isotherm of TiO ₂ obtained from N ₂ physisorption	73
Figure 4.5	Diffuse reflectance UV-Vis spectra of the TiO ₂	73

Figure 4.6	Plot of Kubelka-Munk function versus energy of light for TiO ₂	74
Figure 4.7	Degradation profile obtained for different stirring speed	75
Figure 4.8	Degradation of POME after 240 min of UV irradiation with different O ₂ flowrates. Reaction condition: 0.5 g/L TiO ₂ at room temperature	76
Figure 4.9	Degradation of adsorption study (with 0.5 g/L of TiO ₂) and photolysis study employing O ₂ flowrate of 70 mL/min	78
Figure 4.10	Transient COD level (ppm) and degradation (%) profiles for photoreactions at different TiO ₂ loadings	80
Figure 4.11	Influence of TiO ₂ loadings on the degradation rate	81
Figure 4.12	Illustration showing good adherence to 1 st order kinetics modelling	82
Figure 4.13	Comparison between predicted and actual $\ln(C_{A0}/C_A)$ values	84
Figure 4.14	Residual plot for POME degradation	84
Figure 4.15	pH and decolourization profiles for all the photoreactions	85
Figure 4.16	Gas products collected along the photoreaction with O ₂ flowrate of 70 ml/min and temperature maintained at room temperature. (a) CO ₂ (b) CH ₄	86
Figure 4.17	Results obtained from scavenging study employing 1.0 g/L of TiO ₂	88
Figure 4.18	The schematic diagram of POME photocatalytic degradation mechanism	90
Figure 4.19	Degradation of POME with recycled TiO ₂ over three consecutive runs	91
Figure 4.20	POME sample at t = 0 min (left) and t = 22 h (right)	92
Figure 4.21	COD Degradation profile of POME for longevity study	92
Figure 4.22	¹³ CMNR spectrums of POME, (a) 0 h (b) 2 h (c) 4 h (d) 22 h	94
Figure 4.23	FESEM images of used TiO ₂ photocatalysts from recyclability test (after 3 rd -cycle) under various magnifications (a) 10 kx (b) 30kx (c) 55kx (d) 100 kx	96
Figure 4.24	N ₂ physisorption isotherms of spent TiO ₂ photocatalyst	97
Figure 4.25	FTIR results of fresh and used TiO ₂ photocatalysts	97
Figure 4.26	EDX mapping of spent TiO ₂ photocatalyst (a: mixed; b: O atom; c: Ti atom)	98
Figure 4.27	EDX mapping of spent TiO ₂ photocatalyst (a: mixed; b: O atom; c: Ti atom)	99
Figure 4.28	Half-normal plot of the effects for degradation of POME waste	102
Figure 4.29	Pareto Charts of the main effects towards degradation	103
Figure 4.30	Plots of main factors and interaction effects towards the degradation (%)	106

Figure 4.31	The normal plot of the residuals	111
Figure 4.32	Predicted versus actual response	112
Figure 4.33	Residuals versus predicted response	112
Figure 4.34	Residuals versus experiment run	113
Figure 4.35	Effect of (a) O ₂ flowrate (b) TiO ₂ loading (c) initial concentration of POME towards degradation	114
Figure 4.36	Contour plots and the 3D surface response plots between (a) AB (250 ppm POME) (b) AC (1.10 g/L TiO ₂) (c) BC (70 mL/min O ₂)	116
Figure 4.37	The predicted 3D response surface with optimized conditions (239.53 ppm of POME)	117
Figure 4.38	Correlation of BOD and COD after phototreatment using UV/TiO ₂ system	119
Figure 5.1	XRD results of ZnO photocatalyst	122
Figure 5.2	FESEM images of ZnO photocatalyst employing magnifications of 10kx, top left; 30kx, top right and 50kx, bottom	123
Figure 5.3	N ₂ adsorption and desorption isotherms for fresh ZnO photocatalyst	124
Figure 5.37	(a) Diffuse reflectance UV-Vis spectra of the photo-catalysts. (b) Plot of Kubelka-Munk function versus light energy for ZnO	125
Figure 5.5	Results obtained from photoreaction at 70 ml/min of O ₂ employing different ZnO loadings	126
Figure 5.6	Illustration showing good adherence to the 1 st -order kinetics modeling	128
Figure 5.7	pH and decolourization profiles for all the photoreactions	129
Figure 5.8	Production rate for (a) CO ₂ (b) CH ₄	131
Figure 5.9	The relationship between gaseous products collected and photocatalytic degradation efficiency	133
Figure 5.10	Results obtained from scavenging study employing 1.0 g/L of ZnO	134
Figure 5.11	Mechanisms proposed for the photocatalytic degradation of organic pollutants in POME over ZnO photocatalyst under UV irradiation	137
Figure 5.12	Results obtained from recyclability test with reaction conditions of 1.0 g/L ZnO and 70 ml/min of O ₂ -bubbling rate	138
Figure 5.13	Results obtained from longevity test with reaction condition of 1.0 g/L of ZnO and 70 ml/min of O ₂ -bubbling	139
Figure 5.14	¹³ CNMR spectrums of POME (a) 0 h (b) 2 h (c) 4 h (d) 22 h	140
Figure 5.15	FESEM images of spent ZnO photocatalyst (a) 10kx (b) 30kx (c) 55kx (d) 100kx	142

Figure 5.16	N ₂ adsorption and desorption isotherms for recycled ZnO photocatalyst	143
Figure 5.17	FTIR spectra of fresh and recycled ZnO	144
Figure 5.18	EDX mapping for (a) combined (b) Carbon (c) Zn (d) Oxygen	145
Figure 5.19	EDX spectrum of used ZnO	145
Figure 5.20	Half-normal plot of the factors for degradation efficiency (A= O ₂ flowrate; B=ZnO loading; C=initial concentration of POME)	148
Figure 5.21	Pareto chart of the factors efficiency (A=O ₂ flowrate; B=ZnO loading; C=initial concentration of POME)	149
Figure 5.22	The effects of main factors and interactive factor	152
Figure 5.23	(a) Normal probability plot of residuals (b) Predicted vs actual response plot (c) Residuals vs predicted response plot (d) Residuals vs run number plot	157
Figure 5.24	The effects of (a) O ₂ flowrate (b) ZnO loading (c) initial concentration on the response	159
Figure 5.25	The interaction effects between (a) AB (b) AC (c) BC.	160
Figure 5.26	3D response surface for optimized condition	161
Figure 5.27	Correlation of BOD and COD after phototreatment using UV/ZnO system	162
Figure 6.1	Scavenging studies for TiO ₂ and ZnO (O ₂ -bubbling rate: 70 mL/min; photocatalyst loading: 1.0 g/L)	167
Figure 6.2	Effects of photocatalysts loading for both systems (initial concentration = 155-170 ppm; Oxygen bubbling = 70 mL/min)	168
Figure 6.3	Schematic diagram of organic pollutants degradation in TiO ₂ system	169
Figure 6.4	Recyclability study for both TiO ₂ and ZnO system	171
Figure 6.5	Longevity study for both TiO ₂ and ZnO system	172

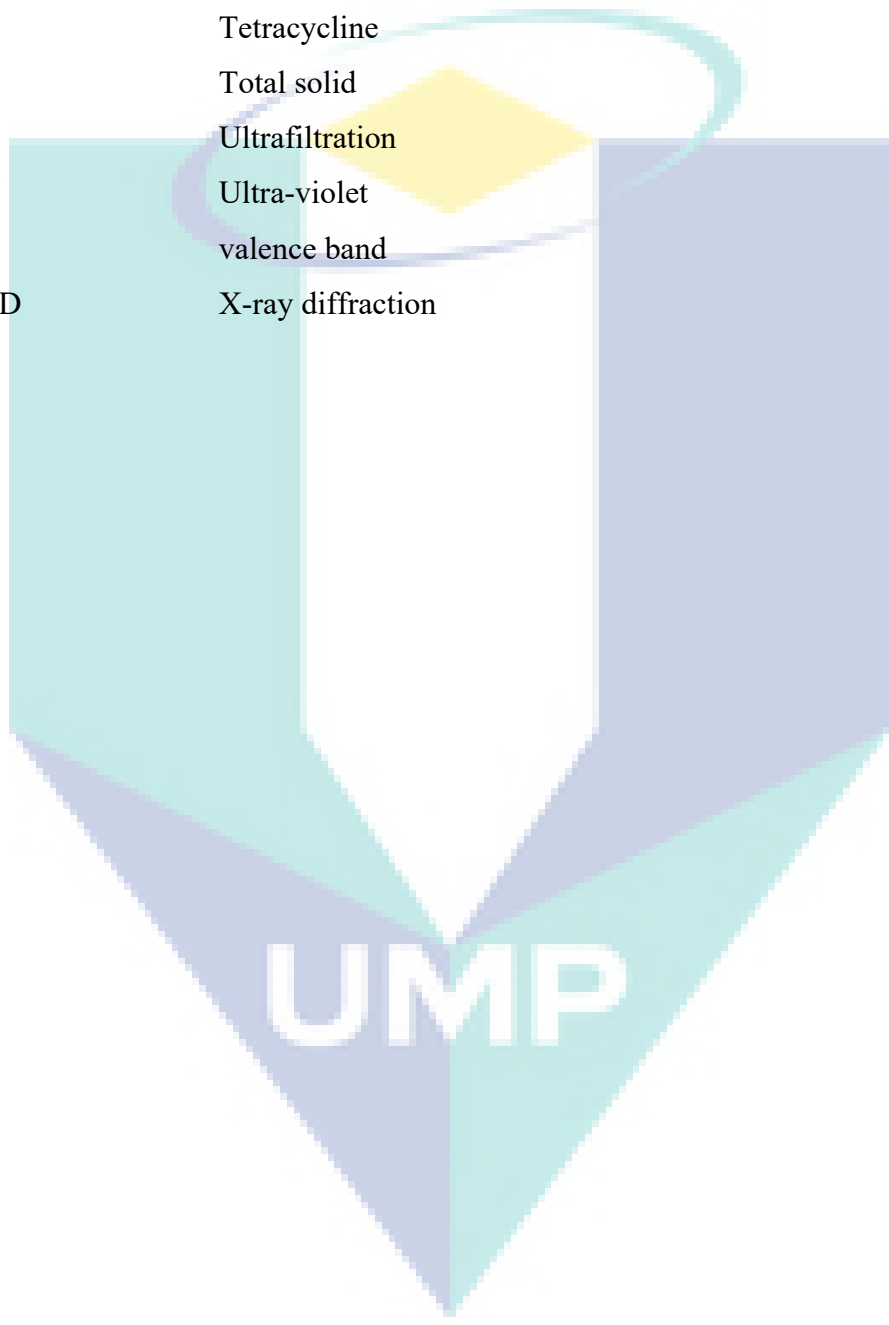
LIST OF SYMBOLS

θ	angle of incidence, Brag's angle
γ	the surface tension of N ₂ at its boiling point
λ	wavelength of X-ray beam (nm)
A	Absorbance
Ads _t	Absorption at time <i>t</i>
Ads _i	Absorption at time <i>θ</i>
β_d	true line width at half maximum intensity
β_{obs}	observed width at half maximum intensity
β_{inst}	instrumental line width by standard
β_d	angular width at half maximum intensity
C	a characteristic constant of the adsorbate
d	inter plane distance of crystal
D	crystalline size
D ₁ D ₂	DO values of POME
E _{bg}	band gap energy
<i>hν</i>	photon energy
k _{Sch}	Scherrer constant
n	order of reflection
P	decimal volumetric fraction of sample used
P	gas pressure
P _s	saturation pressure of the adsorbate gas
P _a	ambient pressure
P/P _o	relative pressure of N ₂
<i>r_k</i>	the Kelvin radius of the pore
R ₀ , R	apparent absorbance
R	gas constant
S _{BET}	BET specific surface area
t	thickness of the adsorbed layer
T	ambient temperature
V	volume of gas adsorbed
V _m	volume of gas adsorbed corresponding to monolayer coverage

LIST OF ABBREVIATIONS

AMP	Ampicillin
AMX	Amoxicillin
AOP	Advanced oxidation process
ASGSC	attached growth system where granular activated carbon was seeded with activated sludge
BET	Brunauer-Emmett-Teller
BOD	Biochemical oxygen demand
CB	Conduction band
CCD	Central composite design
CLX	Cloxacillin
COD	Chemical oxygen demand
CO _z	catalytic ozonation
CWPO	catalytic wet peroxide oxidation
DoE	Department of Environmental
DRS	diffuse reflectance spectroscopy
EDX	X-ray microanalysis
FESEM	Field Emission Scanning Microscopy Analysis
FTIR	Fourier transform infrared spectroscopy
HOMO	highest occupied molecular orbital
HRT	hydraulic retention time
LDH	layered double hydroxide
LED	Light emitting diodes
LUMO	lowest unoccupied molecular orbital
MBR	membrane bioreactor
MO	Methyl Orange
O&G	Oil and grease
OA	Oxolinic acid
OFAT	one variable at a time
POME	Palm oil mill effluent
R&D	Research and development
RSM	Response surface methodology

SAS	suspended activated sludge
SBR	sequencing batch reactor
SEM	Scanning electron microscopy
SKM	Schuster-Kubleka-Munk
SS	Suspended solid
TC	Tetracycline
TS	Total solid
UF	Ultrafiltration
UV	Ultra-violet
VB	valence band
XRD	X-ray diffraction



CHAPTER 1

INTRODUCTION

1.1 Background

Water pollution is the contamination of water bodies such as lakes, rivers, oceans, and groundwater caused by either human activities or industrial activities. With the increasing population worldwide, water preservation has become an increasingly thorny issue. Water in today's context, besides as means for supporting human daily life, large amount of water was also supplied to various industries as well as plantations; one of the best examples is the oil palm industry.

Malaysia is known as one of the major players in edible oils sector and is envied for its well-organized oleo-chemical industry. Indeed, oil palm plantation in Malaysia has occupied more than one-third of its total cultivated land (Rupani and Singh, 2010; Tamada et al., 2012). This culminates in strong income generation for agricultural sector through yielding more than 19.6 million tonnes of crude palm oil in 2014 (MPOB, 2014). However, the growth of this segment is accompanied by the massive industrial discharge from its mill. Regrettably, plethora of liquor waste commonly known as palm oil mill effluent (POME) is being produced incessantly during the oil extraction process. Past research report indicates that 0.5 – 0.75 tons of palm oil mills effluents (POME) is generated for every tonne of fresh fruit bunch processed (Yacob et al., 2006).

Significantly, raw POME is acidic (pH 4.5 – 5) and hot (353 – 363 K). Moreover, it presents in the form of thick brownish colloidal wastewater containing 95 – 96% of water, 4 – 5% of total solids including 2 – 4% of suspended solids, as well as 0.6-0.7% of oil and grease (Ahmad et al., 2005). Furthermore, it also contains organic matters such as lignin (4,700 ppm), phenolics (5,800 ppm), pectin (3,400 ppm) and amino acids (Ahmed et al., 2015; Sundram et al., 2003). Consequently, POME can inflict serious

environmental problem if discharged untreated owing to its high chemical oxygen demand (40,000 to 100,000 ppm) and biochemical oxygen demand (25,000 to 65,000 ppm) (Choorit and Wisarnwan, 2007; Wu et al., 2007; Zinatizadeh et al., 2006).

In order to mitigate pollution conundrum associated with POME, Malaysia's Department of Environmental (DoE) has since 1977, compelled the millers to reduce the POME's BOD value to 100 ppm threshold before discharge. This has been further revised down to 20 ppm recently, especially for R&D sector (MPOB, 2015). In a significant milestone, 20 ppm BOD discharge limit has been enforced in East Malaysia (MPOA, 2015). Besides the BOD value, COD reading is also another indicator of organic contents. According to Malaysia Sewage and Industrial Effluent Discharge Standard, the COD of the discharge wastewater must be kept below 50 ppm level to prevent pollution. Nonetheless, most of the millers in Malaysia fail to meet this stringent requirement due to the inefficiency of existing waste treatment system. In fact, more than 91% of the millers adopt open ponding system for POME treatment (MPOB, 2015). Unfortunately, this process has myriad of issues, i.e. requires long hydraulic retention time (HTR), massive land area for lagoon-creation, squalid environment and unable to cope with the updated discharge threshold (Wang et al., 2010), even after it was subjected to a series of anaerobic and aerobic treatments. To further treat the waste, millers have begun to test new "polishing" techniques, viz. chemical treatment (Aris et al., 2008), biological treatment (Chan et al., 2010; Zahrim et al., 2009) and membrane processes (Ahmad et al., 2003; Idris et al., 2010; Wu et al., 2007) to complement the existing treating system, in order to achieve better-controlled effluents. The efforts of all these researchers in POME waste treatments precisely portrait the severity of POME pollution towards the environment.

Significantly, there are voluminous publications on the subject of advanced oxidation process (AOP) for the destruction of organic compound. Photocatalysis process has been touted as a promising technology and hence widely investigated for application in treating aqueous organic contents (Cheng et al., 2016; Liu et al., 2016; Vilar et al., 2011). Thus, in the current study, photocatalysis technique was offered as a new polishing technology for POME after the bio-treated process. Concurrently, assessment of the gaseous products generated from the photodegradation of POME under the UV irradiation was also being carried out. The mechanisms of photocatalysis involve the

absorption of light-energy (from UV or visible light) by a photocatalyst, which consequently triggers the excitation of electrons across the energy gap into the conduction band. In the presence of oxygen and water, hydroxyl radical (OH^\bullet) would be generated, and eventually decompose organic compounds present in the POME.

UV/ TiO_2 -based photocatalyst system is one of the benchmark for advanced oxidation process due to its performance and versatility (Cao et al., 2006; Fujishima et al., 2000; Shahrezaei et al., 2012). TiO_2 is a semiconductor photocatalyst with low toxicity, high resistance towards corrosion and also readily-available. Furthermore, it is also an excellent photocatalyst material for environmental purification (Fujishima et al., 2000). Likewise, ZnO is also another type of semiconductor with equally extraordinary performance in the field of advanced oxidation process (AOP). ZnO is widely applied in various fields, such as electronics, gas sensors and biosensors, UV detectors, light-emitting diodes (LEDs), solar cells, photocatalysts and others, attributed to its unique electrical, optical and mechanical properties (Zhang et al., 2012). Due to its versatility, ZnO has been employed previously as a photocatalyst for degradation of environmental pollutants such as dye, pesticides and other organic pollutants under light irradiation (Achouri et al., 2016; Kuo et al., 2007; Xuewen Wang et al., 2016). The application of AOP using both TiO_2 and ZnO as the photocatalysts in the POME degradation represents another knowledge frontier that deserves a thorough investigation. Hence, in the current work, both TiO_2 and ZnO photocatalysts were thoroughly investigated, subsequently their performance was compared. In addition, to further maximizing the efficiency, both systems were subjected to the optimization process by employing central composite design model (CCD) in response surface methodology (RSM). CCD is a very common technique in the optimization process as it provides a powerful method to attain a breakthrough enhancement in the process efficiency.

1.2 Problem Statement

As aforementioned, Malaysia is one of the biggest palm oil producing country in the world. Hence, massive waste generation in the form of POME is unavoidable during the extraction of crude palm oil. The effluent contains high biochemical oxygen demand (BOD) liquid waste and chemical oxygen demand (COD) as reported by Ahmad et al. (2003), an indication of high organic load in the wastewater. The decomposition of organics by microorganisms in the rivers increases the consumption of dissolved oxygen,

causing oxygen depletion which is detrimental to aquatic lives. Hence, this waste needs to be treated before discharged into waterway as a direct release will destroy the aquatic life.

In Malaysia, the most common treatment employed is open ponding system. However, this system is very hard to control and the effluent does not really degrade to the discharge limits. In order to solve this problem, various treating methods were proposed as the tertiary polishing treatment to further degrade POME before discharging to the environment. Often, physical separation particularly membrane technology is proposed for polishing process (Ahmad et al., 2005; Ahmad et al., 2003; Wu et al., 2007). However, membrane fouling would be a critical issue, and would incur high treatment cost. Besides, biological treatments such as aerobic and anaerobic digestions are also commonly suggested for POME polishing (Chan et al., 2011, 2012; Ng et al., 2016; Yacob, Hassan, et al., 2006). Despite this, bio-pathway process will take up very long hydraulic retention time (HRT) to degrade the wastewater. There are also chemical degradation pathways, by using Solar-Fenton and Fenton processes, as suggested by Aris and co-workers (2015). However, addition of chemicals (H_2O_2) was necessary for the degradation to occur.

Therefore, for current study, photocatalysis pathway as a new polishing method was evaluated. Application of photocatalysis in POME treatment is very beneficial to the environment compared to the conventional treatment. It is a recognised green technology. To our best knowledge, the mechanisms of POME photocatalytic degradation have yet to be identified. Based on past research works, TiO_2 and ZnO were reported to be the best photocatalysts under UV irradiation, due to their versatility and efficiency. Furthermore, to enhance the photocatalytic treatment process, the optimization using CCD in RSM was carried out. This is also a subject of interest as the process optimization for photocatalytic degradation of POME has not been investigated prior to the current study.

1.3 Objective

There are four objectives for the current project:

- To evaluate the kinetics of UV/ TiO_2 and UV/ ZnO on POME degradation and to assess the gaseous products from photocatalytic degradation of POME.

- To investigate and develop the mechanistic steps of POME degradation for both systems
- To study the recyclability and longevity of both UV/TiO₂ and UV/ZnO systems.
- To conduct statistical evaluation and to determine the optimized conditions for POME degradation for both systems.

1.4 Scopes of Study

A few scopes were identified in current study in order to meet with the objectives above. To achieve first objective, the following works were completed:

- To determine the physicochemical properties, such as crystalline structure, surface morphology, surface area and light absorption properties of the photocatalysts (TiO₂ and ZnO for current study).
- To characterize fresh POME sample from settling pond and selected post-reaction POME sample uses various techniques, viz chemical oxygen demand (COD), biochemical oxygen demand (BOD), pH, total suspended solid (TSS), oil and grease analysis (O&G) and temperature reading.
- To conduct photo-treatment of POME using UV-responsive photocatalysts under irradiation of UV, varying oxygen flowrate (0 – 150 mL/min) and catalyst loadings (0.1 g/L – 2.0 g/L) for both UV/TiO₂ and UV/ZnO system.
- To analyse the gaseous products formed from the photodegradation process by using gas chromatography.

To fulfil second objective, the works conducted are as follows:

- To determine the key reactive species in POME degradation through by adding different scavengers in the photoreaction
- To propose the mechanisms of POME photocatalytic degradation for both systems.

- To conduct post reaction analysis for both spent photocatalysts and post-reaction POME samples.

The work scopes for third objective are:

- To lengthen the reaction time up to 22h.
- To conduct three consecutive cycles of photoreaction with same batch of recovered photocatalyst.

For fourth objective, the optimization process includes two major steps:

- To access the significance of the main factors using 2^3 full factorial design.
- To optimize the significant main factors by using central composite design (CCD) in response surface methodology (RSM).

Lastly, for the completion of the project, both systems were thoroughly compared from the perspectives of performances, stabilities, responses towards different scavengers and degradation mechanisms.

1.5 Rational and Significance

There are voluminous of POME generated every year due to the big success of palm oil industry in Malaysia. This POME is highly polluting if directly discharge into rivers without any treatment. Therefore, efficient POME treatment technology is desirable. With better treatment processes, the toxicity of the POME will be less harmful to environment or even diminished. Indirectly, this will help to prevent the environment being compromised, as well as maintaining the ecological balance.

This work helps in exploring the application potential of photocatalysis process in POME polishing treatment. By employing CCD technique, the optimized conditions for both TiO_2 and ZnO photocatalysts was determined, which greatly enhanced the effectiveness of photocatalysis for POME treatment. Moreover, the similar technique could also be employed not only in POME treatment but also prospectively for other organic industrial wastewater. This technology has potential to be commercialized for industrial application due to low cost and significantly low energy consumption.

1.6 Outline of the Thesis

Chapter 2 summarizes the characteristics of raw POME and the laws and regulation enforced in Malaysia to control the POME pollution. In addition, the newly proposed technologies in recent years for enhancing POME treatment were also reviewed in Chapter 2. Moreover, the fundamentals of photocatalysis as well as its effectiveness on degrading various organic compounds were also discussed in the same chapter.

Chapter 3 presents the materials and methods for this research. This encompasses pre-treatments and characterization of POME, as well as procedures to prepare and to characterize the photocatalysts. Besides, Chapter 3 also describes the steps of photoreaction as well as the sample analysis procedures. Moreover, the steps in optimizing the degradations described in the same chapter too.

Chapter 4 and Chapter 5 presents on the results obtained for both UV/TiO₂ system and UV/ZnO system, respectively, followed by detailed discussion of the results. The discussion includes pre-reaction and post reaction analyses for both photocatalysts and POME waste, parametric studies, mechanisms study, longevity test and process optimization.

Chapter 6 compares both systems thoroughly, in term of properties of photocatalyst, responses towards scavengers and performance of the photocatalysts. Detailed discussion was presented in the same chapter.

Finally, Chapter 7 highlights the main findings from this study, followed by some recommendations for future works.

CHAPTER 2

LITERATURE REVIEW

2.1 Introduction

Palm oil mill effluent (POME) is an organic wastewater generated from palm oil milling activities that will cause severe environmental pollution if is not handled properly. For a long time, a lot of researches have been carried out on the treatment of POME. Unfortunately, this results in the overlook of renewable energy generation from POME in commercial scale (Zafar, 2015).

Photocatalysis is a green pathway for POME treatment. Based on past research works, this method is also able to treat organic wastes effectively, particularly when TiO_2 and ZnO were employed as the photocatalysts. It is envisaged that through the photocatalysis process, POME is able to be treated down to the safety level before discharging. Concurrently, it will be a subject of interest to investigate the composition of gaseous products emanating from the photodegradation of POME, as it may offer potential as an alternative fuel that is renewable.

For this chapter, previous researches related to this topic is critically reviewed in particular research works that reported on the organic waste treatment through advanced oxidation process.

2.2 Palm Oil Mill Effluent (POME)

Palm oil mill effluent (POME) is a voluminous liquid waste produced during palm oil production. Past research report indicates that 0.5 – 0.75 tons of palm oil mills effluents (POME) is generated for every tonne of fresh fruit bunch processed (Yacob et al., 2006). The characteristics of POME depend on the quality of raw material and palm oil production processes in palm oil mills. The characteristics of POME is as summarized

in Table 2.1. Generally, POME is an acidic, thick colloidal slurry of water, oil and fine cellulosic fruit residues that comes in brownish colour. The BOD and COD of POME are very high, which range from 10250-43750 mg/L and 15000-100000 mg/L, respectively. In addition, fresh POME discharge is very hot too, typically in the range of 353-363 K. Moreover, suspended solids and dissolved solids are also common components of POME.

Table 2.1 Characteristic of POME

Parameter	Value (average)	Range
pH	4.2	3.4-5.2
Oil and grease	6000	130 - 18000
Biochemical oxygen demand (BOD)	25000	10250-43750
Chemical oxygen demand (COD)	51000	15000-100000
Total solids	40000	11500-79000
Suspended solid	18000	5000-54000
Ammoniacal Nitrogen	35	4-80
Temperature (K)	85	353-363

*All values are in mg/L except pH and temperature.
Source: <http://www.mpod.gov.my/2012>

POME is non-toxic, as no chemicals are added during extraction process. However, despite its biodegradability, POME can not be discharged without first being treated due to its acidic properties and high BOD value. High BOD value indicates high organics content whereby microbes in water will take in dissolved O₂ to digest organics matter. Consequently, the dissolved O₂ in the water will decrease and cause ecological-stress.

2.3 Laws and Legislations

POME has been identified as one of the major source of industrial pollutants in Malaysia. In order to counteract any negative impact from this source of pollutant, the Department of Environment (DOE) of Malaysia has implemented and enforced environmental regulations pertaining to the waste management practices of palm oil industry.

Specifically, the Environmental Quality Regulations enacted in the year of 1978 detailed out the thresholds for POME discharge. The required POME discharge standard

is summarized in Table 2.2. It can be seen that the BOD and COD are the key parameters in the standard. From an initial BOD level of 25000 ppm, it was required to reduce it to the level of 5000 ppm. This target is further revised to 100 ppm in the latest regulation which took effect since 1984. In recent years, DOE planned to revise the existing standard to a more stringent discharge limit for cleaner environment. There is an attempt to impose 20 ppm in BOD discharge limit for POME for palm oil mills that located in the environmentally-sensitive areas such as tourism areas in Sabah and Sarawak, as well as those closed to water intake points (Liew et al., 2015).

Likewise, in the earlier stage, the COD standard was capped at 10000 ppm and then progressively revised to lower concentration until the year of 1982. Since then, the COD standard was not enforced in the discharge standard. However, the Malaysia Sewage and Industrial Effluent Discharge Standard set the COD limit for industrial wastewater at 50 ppm level.

Table 2.2 POME discharge standards according to periods of discharge

Parameter	1/7/78 to 30/6/79	1/7/79 to 30/6/80	1/7/80 to 30/6/81	1/7/81 to 30/6/82	1/7/82 to 31/12/83	1/1/84 and thereafter
pH	5-9	5-9	5-9	5-9	5-9	5-9
BOD	5000	2000	1000	500	250	100
COD	10000	4000	2000	1000	-	-
Total Solid	4000	2500	2000	1500	-	-
Suspended solid	1200	800	600	400	400	400
Oil and Grease	150	100	75	50	50	50
Ammoniacal Nitrogen	25	15	15	10	150	100

*All units are in mg/L, except pH and temperature.

2.4 Conventional POME Treatment

In order to avoid POME pollution, it is mandatory to set up POME treatment system in every palm oil mill to strictly control the quality of the effluents discharge to the environment. The most common POME treatment adopted in Malaysia is open ponding system, implemented by 85% of the palm oil mills (Ma, 1999). Generally, ponding system consists of a series of waste stabilization ponds and multifunctional

oxidation ponds. The series of ponds in the ponding system are to prevent the mixing of the untreated POME with the treated one for better control on the residence time as well as the effluent quality. These ponds include cooling ponds, anaerobic ponds, facultative ponds, and aerobic ponds. As a pre-treatment, fresh POME will undergo filtration process to manually remove sand and oil before flows into series of man-made lagoons. Prior to feeding into anaerobic and aerobic ponds, POME will be cooled down to 308 K in cooling ponds. Subsequently, POME will undergo anaerobic digestion in deep ponds (usually 5 to 7 m). Anaerobic ponds are able to digest high amount of solids with low cost needed. According to Khalid and Mustafa (1992), about 4.8 kg/m³ of volatile solid can be digested in anaerobic ponds in a day. However, long hydraulic retention time of up to 20 days and large land area are needed for these ponds in order to achieve the satisfactory results (Yacob et al., 2006). Downstream to the anaerobic pond is facultative ponds which function to stabilise the effluent via combination of anaerobic and aerobic bacteria. Typically, facultative ponds are designed shallower, with depth up to 2.5 m only (Metcalf and Eddy Inc., 2003). Post facultative pond, POME is fed into aerobic ponds to undergo aerobic digestion. Aerobic ponds are usually constructed up to 1-1.5 m deep for better O₂ transfer rate into the entire column of POME wastewater. Sometimes, O₂ will be provided through mechanical aeration to speed up the aerobic digestion. Finally, the treated POME will flow through a settling pond before releasing to the environments. In due course of operation, solid sludge will accumulate at the bottom of the ponds where desludging is eventually required from time to time.

Basically, the advantages of open ponding system include low operating and maintenance cost, high process and operational simplicity, and are a feasible method for treating recalcitrant organic wastewater. However, it also comes with some disadvantages such as large land requirement, hard to control and long hydraulic retention time (up to months) to complete the treatment process. Unfortunately, more often than not, the POME discharge from the final pond (settling pond) has failed to meet the discharge standard due to highly dependence on the weather (Wang et al., 2010). Ahmad et al. (2005) also agreed that such treatment process with mainly biological treatment is insufficient in POME treatment due to high BOD load and low pH value, as well as the colloidal nature of suspended solids in the wastewater. At the same time, the ligneous structures within the organic complex in the POME waste tends to shield the organic from

enzymatic hydrolysis (Han and Anderson, 1975), eventually attributed to the insufficiency of biological treatment of POME.

Another common system applied in Malaysia is the conventional anaerobic-aerobic system that employed the open tank digestion and extended aeration (Chan et al., 2010). POME will undergo two-phases of anaerobic digestion in the open mild steel-made digesters for approximately 20 days of HRT. According to Yacob et al. (2006), these open tank digesters were capable to remove 81% of chemical oxygen demand (COD). Subsequently, the effluent from digestion tank was further treated in extended aeration ponds for about 10 days to bring down the COD and BOD value of the POME (Ugoji, 1997). Mechanical surface aerators were used to supply air to the treatment plant and supernatant was then discharged into a nearby watercourse (Ma, 1999; Chan et al., 2010). The disadvantages of the anaerobic-aerobic system are long HRT time for complete treatment of POME, and also the use of surface aerator will increase the cost of treatment despite high quality of effluent achieved.

2.5 Tertiary Treatment for POME Polishing

As mentioned in Section 2.3, effort is underway to impose BOD value of 20 ppm threshold in the near future. This poses a greater challenge as the existing treatment systems are highly dependent on biological treatment, which is inefficient in treating recalcitrant wastewater like POME (Wang et al., 2010; Han and Anderson, 1975). In addition, colour treatment of POME is also receiving attention as the final effluent appears dark brown. Hence, many innovative technologies have been proposed as tertiary treatment to further polish the final effluent.

Among the new technologies, membrane technology is frequently reported to demonstrate high efficiency in effluent treatment (Ahmad et al., 2005; Ahmad et al., 2003; Idris et al., 2010; Nor et al., 2015; Wu et al., 2007). Sulaiman and Chea (2004) reported that ultrafiltration (UF) with different molecular weight cut-off (MWCO) can effectively polish biological-treated POME with BOD and COD removal of 97% and 98%, respectively. At the same time, the turbidity of the effluent was also reduced up to 80% after treatment. Their finding was confirmed by (Idris et al., 2010). It was also suggested that pre-treatment of biologically-treated POME prior to UF membrane process was required, viz. chemical coagulation, followed by flocculation and then

adsorption. This can drastically improve the quality of effluent, especially colour removal. As a result, high quality permeate with more than 93% of COD removal and 99% of decolourization was obtained. Other examples of membrane processes as well as other processes on POME treatment are summarized in Table 2.3. All the studies have suggested that membrane technology is practical if sufficient pre-treatment to the POME is carried out. However, operation of membrane technology often comes with fouling issues and flux reduction phenomenon which will induce high treatment cost. Palm oil processing is a low cost activity. Hence, application of such high cost waste treatment process will not be appealing to the millers.

Besides membrane technology, biological treatment was also employed in the previous works as a tertiary treatment for POME. Zahrim et al. (2009) studied the effectiveness of suspended activated sludge (SAS) system on anaerobically-treated POME in a sequencing batch reactor (SBR). However, only 0-14% of colour removal and 27-39% of organic removal were observed. By applying attached growth system where granular activated carbon was seeded with activated sludge (ASGSC) in the similar SBR configuration, the performance was enhanced, with 28-41% of colour removal and 59-70% of organic removal. Similarly, Chan et al. (2010) have polished anaerobically-treated POME in SBR and significant COD, BOD and SS removal (95.96%, 97-98% and 98-99%, respectively) were accomplished due to high biomass acclimation during reactor start-up, high retention of mixed liquor volatile suspended solids and good settle-ability of activated flocs.

In addition, the integration of biological and physical treatment is also investigated for the application of POME tertiary treatment. For instance, Ahmad et al. (2009) combined the membrane technology and biological treatment into a hybrid membrane bioreactor (MBR) system for POME treatment. Raw POME was sequentially treated in a series of aerobic, anoxic and aerobic reactors followed by membrane separation in aerobic zone. High quality of final effluent was obtained. More than 94% of COD and 98% of SS were removed after the MBR treatment. However, the membrane system encountered systematic fouling issue in long term operation and permeability was not able to be restored to its nascent level even after the cleansing process. Besides, the use of MBR has also been reported by Sulong et al. (2007). After passing through anoxic and aerobic digestion with activated sludge process, UF membrane was use to permeate

the treated POME. After the treatment, more than 98% of COD, BOD and SS removal were achieved, producing high quality effluent.

Besides, chemical process was also employed in POME polishing. Combination of oxidation and purification processes able to produce high quality effluent, making them suitable for tertiary POME treatment. Jurgensen (2010) has evaluated the biological-chemical technology on algae- and aerobic-pond discharge POME, employing ozone oxidation as the pre-treatment prior to biodegradation in a submerged fixed bioreactor. Besides, the utilization of advanced oxidation process (AOP) has also been explored as POME tertiary treatment. This reaction pathway can produce highly reactive species hydroxyl radicals (OH^\bullet) to destruct and oxidize the organic molecules. Aris and co-workers (2008) generated this OH^\bullet by using Fenton and solar-Fenton processes to polish biologically- treated POME. The latter process exhibited rapid degradation of organic compounds in POME which subsequently lead to colour reduction in wastewater. 82.4% and 95.1% of COD and colour removal was achieved in solar-Fenton oxidation. In the absence of solar light, the removal efficiency for COD and colour was slightly reduced to 75.2% and 92.4%, respectively.

There are also numerous promising technologies, for instance, extended aeration in a fixed-packed activated sludge aeration tank (Muda et al., 2016), physicochemical treatment processes (Barr, 2010), biological-physicochemical treatment processes (Chong, 2010), and others that enhance the quality of final effluent before discharging. However, the sustainability, cost-effectiveness and consistency of POME tertiary treatment are the important criteria in the consideration of implementation. Often, new technologies that required chemical addition or replacement will induce high treatment cost, hence unfavourable by the millers.

Table 2.3 Summary of new proposed polishing technologies in POME tertiary treatment

Technology	Description	Removal efficiency	Reference
Membrane process	Hollow fibre polyethersulphone UF membrane was employed.	BOD 97%, COD 98%, turbidity 80%, Final COD: 24 ppm	(Sulaiman and Chea, 2004)
	Pre-treated with coagulation, flocculation, adsorption, followed by UF.	COD>93%, Colour>99%, Turbidity>99%	(Idris et al., 2010)
	Adsorption by activated carbon as pre-treatment prior to UF process.	Up to 90% removal of pollutant elements achieved.	(Azmi and Yunos, 2014)
	Final effluent from ponding system was collected and subjected to PES UF membrane.	80% to COD and TSS removal observed. However, did not achieve discharge limits.	(Said et al., 2015)
SBR	SBR with SAS, with 96h of SBR operation (Fill 5min, react 95h, settle 15min, decant 10min)	COD: 27-39%, Colour: 0-14%	(Zahrim et al., 2009)
	SBR with ASGAC with 96h of SBR operation (Fill 5min, react 95h, settle 15min, decant 10min)	COD: 59-70%, Colour: 28-41%	(Zahrim et al., 2009)
	22h SBR operation (fill, react 20h, settle 2h, decant).	BOD: 97-98%, COD: 95-96%, SS: 98-99%.	(Chan et al., 2010)

Table 2.3 Continue

Technology	Description	Removal efficiency	Reference
MBR	POME subjected to anaerobic digestion, followed by anoxic process and aerobic process with membrane submerged in the reactor.	COD: 94%, SS: 98%	(Ahmad et al., 2009)
	POME treated with anoxic and aerobic digestion using activated sludge process prior to UF process.	BOD: 99%, COD: 98%, SS: 99%	(Sulong et al., 2007)
Chemical degradation	Solar-Fenton process was employed.	COD: 95.1%, Colour: 82.4%	(Aris et al., 2008)
	Fenton process was employed.	COD: 92.4%, Colour: 75.2%	(Aris et al., 2008)

2.6 Fundamentals and Concept of Advanced Oxidation Processes (AOPs)

Chemical oxidation process is widely employed in organic waste water treatment due to its ability to degrade organic pollutants into less complex compounds, eventually completely mineralized it (Ribeiro et al., 2015). Generally, AOPs apply the concept of hydroxyl radical production which subsequently attacks the organics in the wastewater, yielding CO₂, H₂O and some other simple compounds (Hoigné, 1988). Hydroxyl radical is one of the strongest oxidants (Gligorovski et al., 2015) that could be produced by many pathways depending on different types of AOPs. Nonetheless, AOPs hold several exceptional advantages in the field of water treatment (Gilmour, 2012). Firstly, rather than removing or transferring the organic pollutants, AOPs are able to destroy them effectively in the aqueous phase itself through chemical reaction. Furthermore, AOPs is very versatile in the organic waste treatment due to the remarkable activity of OH[•] towards organics molecules. Moreover, some of the heavy metals can also be removed by precipitation into M(OH)_x, where M denotes for metal ion and X is the stoichiometry number. By comparing to other organics waste treating methods, critical secondary

wastes such as sludge are not generated during the oxidation process and thus, post-treatment or final disposal is not required. Finally, upon treatment, OH^\bullet will be reduced to H_2O , which does not introduce hazardous residue to the environment.

There are various pathways to generate OH^\bullet , depending on the type of process. These pathways can be divided into chemical, electro-chemical, sono-chemical and photo-chemical processes. Conventionally, AOPs can be classified into two categories, which are homogeneous and heterogeneous processes (Oliveira et al., 2014). Homogeneous process allows the oxidation process to occur in a single phase. This category is characterized by chemical changes depending on the interactions between the chemical reagents and target compounds only. Common examples of homogeneous processes are O_3 based processes which include O_3 in the system, wet peroxide oxidation that implementing H_2O_2 as oxidizing agent at room temperature, Fenton-based processes which introduce Fe-ions in the reaction, and also wet oxidation which operates at high temperature (470 to 600 K) and pressure (20 to 200 bar) to oxidize the substrates by using dissolved O_2 (Ribeiro et al., 2015).

In contrast, heterogeneous AOPs are those relying on the use of heterogeneous catalyst in the oxidation process. The efficiency of this category is highly dependent on the adsorption rate of reactants and desorption rate of products that occur on the active sides of the catalyst surface (Liu et al., 2012). According to Soon and Hameed (2011), the surface characteristics and pore structure of the catalyst highly contribute to the rate of reactants adsorbed and products desorbed, and thus the efficiency. According to Ribeiro et al. (2015), the most commonly employed heterogeneous AOPs are, (i) heterogeneous photocatalysis, where a semiconductor photocatalyst is mixed with substrates in aqueous solution and exposed under UV or visible light radiation, (ii) catalytic wet peroxide oxidation (CWPO) that uses heterogeneous catalysts at low temperature (323-353K), (iii) catalytic ozonation (CO_z) where the catalyst increases the mineralization rate and (iv) finally the catalytic wet oxidation where the added catalysts allow reactions to occur at comparatively lower temperature (400-520 K) and pressure (5-50 bar).

Among these categories of AOPs, heterogeneous photocatalysis is employed in the current study for the degradation of POME due to its high efficiency. Numerous works have reported on the effective degradation of organic substrates over

heterogeneous photocatalysts, particularly TiO₂-based photocatalysts (Borges et al., 2016; J. Li et al., 2016; Liao et al., 2004; Salaeh et al., 2016). According to Fujishima et al. (2000), TiO₂ is almost an ideal photocatalyst due to its cost-effective, chemical stability and its highly-oxidizing photo-generated holes.

2.7 Heterogeneous Photocatalysis

This sub-chapter highlights on the fundamental of photocatalysis process over the semiconductor materials.

2.7.1 Basic Principles

In 1972, Fujishima and Honda have discovered the photo-splitting of water into H₂ and O₂ via TiO₂ electrodes. Since then, photocatalysis process, especially heterogeneous photocatalysis over semiconductor is intensively researched for a wide range of applications, viz. disinfection of water and air, production of renewable fuels, mineralization of organic pollutants as well as organic synthesis, etc.

The illustration presented in Figure 2.1 explains the general principle of photocatalysis. In order to initiate photocatalytic reaction, a semiconductor of a given band gap energy (E_{bg}) must be exposed to a light source (UV or visible light) with equal or greater energy than its E_{bg} . Upon exposure, the excitation of electron from the valence band to the conduction band is accomplished through the absorption of photons. As the results of photo-excitation, electron-hole pairs will be generated and this is a prerequisite step in all semiconductor-mediated photocatalytic processes. These photo-generated electron-hole pairs will be scavenged by a suitable scavenger to prevent the recombination process. The photo-induced electrons will be transferred to the adsorbed electron-acceptor species (A) and at the same time, the holes generated will be filled by electron transferred from electron-donor species (D). Along the electron transfer process, electron-acceptor (O₂ in aerated solution) will be reduced into other compound while the electron donor will undergo oxidation process, which subsequently leads to a series of redox reactions. However, the rate of charge transfer for electrons and holes depends on the respective positions of band edges for conduction and valence bands, as well as the redox potential levels of the electron-acceptor/donor species. For successful electron-transfer process, the potential of electron acceptor has to be located below or in other words, more positive than the conduction band of the semiconductor, while the potential

for electron donor species should be more negative than the valence band of the semiconductor. According to Gratzel (1989), the potential for valence band and conduction band ranged +1.0 to +3.5V and +0.5 to -1.5 V (vs NHE), respectively, depending on types of semiconductor and pH values.

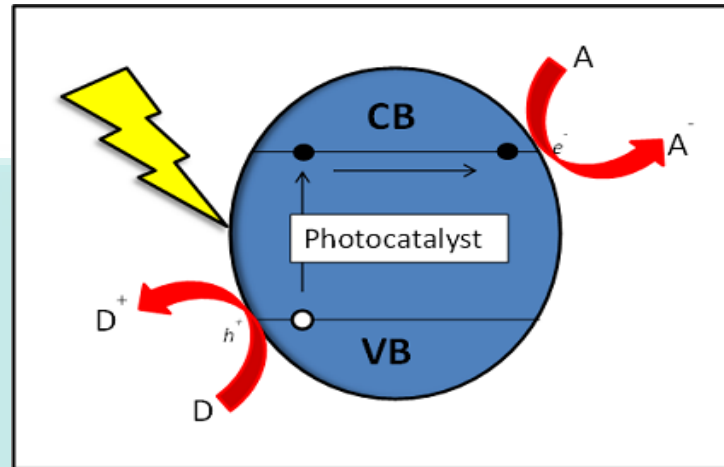


Figure 2.1 Illustration of photocatalysis mechanisms

Source: Fujishima and Honda (1972)

With these configurations, most of the organics degradation reaction could be accomplished. Hence, this process is widely employed in organics destruction process as the process gradually break down the organic pollutants with no residue, i.e. sludge, which would require further treatments (Puzyn and Mostrag-Szlichtyng, 2012; Lima et al., 2015; Shahrezaei et al., 2012)). Besides, after the photocatalysis process, the semiconductor photocatalyst is highly stable towards biological and chemical corrosions, results in considerable saving in treatment cost. With modifications, for instance, metal doping (Murakami et al., 2008, 2010; Zhu et al., 2006), non-metal doping (Chen and Dawson, 2015; Cheng et al., 2012; Gorska et al., 2009) and dye sensitization (Wu et al., 1999; Xu and Langford, 2001; Cho et al., 2001), the activity for high E_{bg} photocatalyst can be effectively extended to visible light region, making sun harvesting becomes possible for photocatalysis process. This may further reduce the treatment cost.

2.7.2 Band Structure and Band Gap of Semiconductors

As mentioned earlier, the prerequisite step of photocatalysis is the absorption of photon by the photocatalyst, in which the photon irradiated must possess energy that is equal or higher than the E_{bg} . Figure 2.2 shows the band structure for a semiconductor material. According to the energy band theory, large number of atoms that interact in

solids will result in closely-spaced energy levels that form bands. The highest occupied molecular orbital (HOMO), usually partially filled or fully-filled, that possess highest electron energy is called valence band (VB). The next higher, unfilled energy band is called conduction band (CB), which is also the lowest unoccupied molecular orbital (LUMO) (Ibach and Luth, 2010; Rajh et al., 2003). Band gap energy (E_{bg}) of a particular semiconductor is defined as the difference between the valence band and conduction band energy.

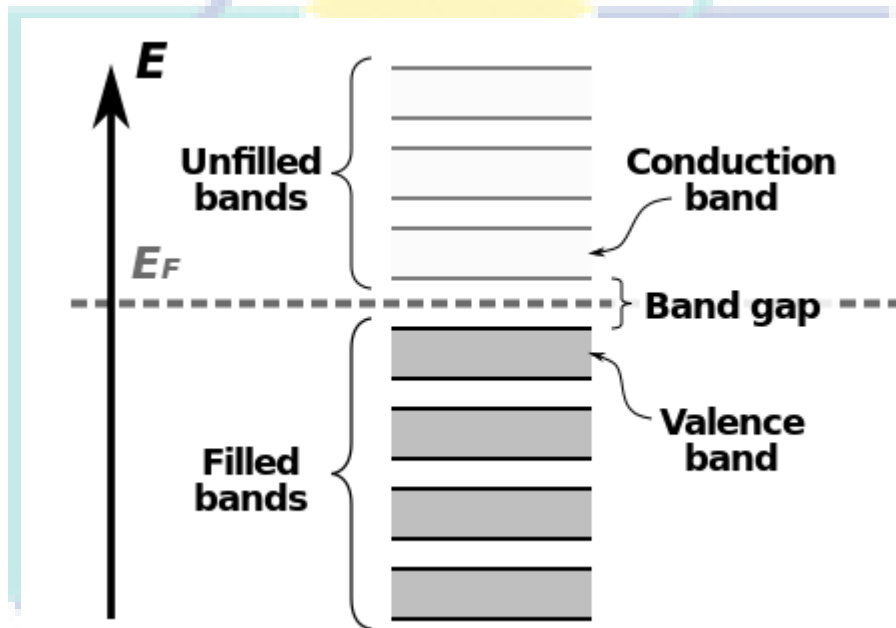


Figure 2.2 Band structure of a semiconductor

Source: Ibach and Luth (2010)

The band structure, and hence the band gap energy of a semiconductor, is highly dependent on the crystal structure and chemical composition. A good example to explain this phenomenon would be the benchmark photocatalyst, TiO_2 . TiO_2 exists in three different crystalline structures, viz. rutile, anatase and brookite. The compositions of these crystals are basically the same. However, different crystalline structure of them leading to the difference in band structures and hence the band gap energy. The detailed crystal structures of TiO_2 are presented in Figure 2.3. Both rutile and anatase crystallizes in a tetragonal crystal system, but with space group of $P4_2/mnm$ and $I4_1/amd$ (Rasmussen, 2003), respectively. In contrast, brookite has a shape of orthorhombic with space group $Pbca$ (Djerdj and Tonejc, 2006). Since the band structure is a measure of the chemical bonding, it differs significantly for these different arrangements. Consequently, the band gap for rutile, anatase and brookite TiO_2 are 3.03, 3.23 and 3.14 eV, respectively

(Goodenough et al., 1984; Paola et al., 2013). The difference in band gap energy would be more obvious when the chemical composition is altered.

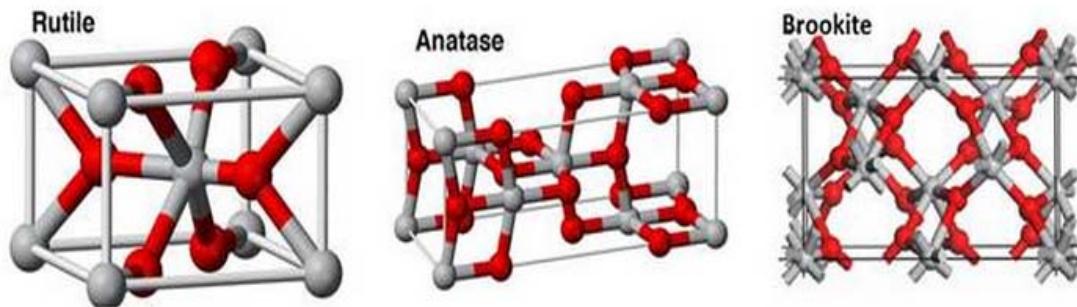


Figure 2.3 Different crystalline structure of TiO₂

Source: Goodenough et al. (1984)

2.7.3 Charge Separation

Due to photo-excitation, electron-hole pairs will be produced which subsequently partake in redox reactions. Hence, charge separation of this electron and hole is very important for good photocatalytic performance. After excitation, the energy captured in the system will either be lost through the desired reactive way, or through the recombination of the photo-generated electrons and holes. For better photocatalytic effect, the latter must be prevented.

In general, the combination of the electron and hole is an attribute of crystal defects in the photocatalyst. Poor crystallinity and large amount of impurities that present in photocatalyst function as charge-trapping area; ultimately it promotes the recombination of electron and hole, causing low photocatalytic performance (Kudo and Miseki, 2009). Hence, to ensure excellent photocatalytic activity, minimal crystal defect is desirable via production of smaller crystal size (Morris, 2007). Significantly, this has boosted interest in the area of nanoparticles. Moreover, nanoparticle photocatalysts also provide larger surface area, higher degree of crystallinity and shorter charge diffusion path to the particle surface.

Another characteristic that affects the charge separation is the crystal structure of the photocatalysts. It is reported that photocatalysts consist of layered-structures crystal, performed excellently in photocatalytic reaction due to efficiently separated electrons and holes (Domen et al., 1993; Huang et al., 2014). A possible explanation is that the nature

of the different layers of the compound can be closely related to the CB and VB, respectively, which effectively separated the charges within the crystal and resulted in low tendency of charges recombination.

2.7.4 Key Species in Organic Destruction

Generally, the most important reactive species in organic degradation is hydroxyl radical (OH^\bullet). The OH^\bullet generated is well-known as a highly reactive and responsible for organic compounds degradation (Lazar and Daoud, 2013).

Based on the concept of photocatalytic degradation, upon photo-excitation, a negatively charged electron and positively charged hole are generated. The formation of highly reactive OH^\bullet will be initiated from this electron-hole pair. The generated hole (h^+) will then attack H_2O , producing a pair of hydroxyl (OH^\bullet) and proton (H^+). At the same time, the generated electron will be accepted by O_2 to form super-oxide anions, O_2^- . O_2 molecule is commonly known as the electron acceptor, as it is readily available in the air and the organic liquid, as well as the high affinity behaviour (-0.13 eV) that can be easily adsorbed onto the surface of semiconductor photocatalyst (Coronado et al., 2013). Subsequently, the O_2^- ion will react with H^+ to form hydrogen peroxide. Hydrogen peroxide (H_2O_2) formed will further dissociate into OH^\bullet free radical upon exposure to the UV irradiation (Dong et al., 2015; Lightcap et al., 2010; Makarova et al., 2000; Williams et al., 2008).

However, besides the OH^\bullet degradation path, there are reports on the non-oxygen radicals degradation pathway. Methyl radical was frequently reported as the important reactive species in photo-decomposition of adsorbed acetone (Henderson, 2005; Henderson, 2008). Recently, Shen and Henderson (2011) also reported on the ejection of methyl radicals into ice over-layers (water or methanol) react to form variety of products including CH_4 and C_2H_6 . Besides, organic radicals had also been reported in past research works, suggesting the secondary reaction of these radicals may play important mechanistic roles in photocatalytic reactions on high surface area photocatalysts (White and Henderson, 2005).

In addition, direct involvement of holes in photo-oxidation of organic compounds has also been investigated. For instance, (Minero et al., 2000) discovered that the initial step for photo-oxidation of phenol is h^+ -mediated, followed by photo-mineralization by

the OH^\bullet . Besides, Yu & Chuang (2007) reported that both photo-generated h^+ and OH^\bullet are viable oxidizers for ethanol and h^+ become the key reactive species at high ethanol coverage on the photocatalyst's surface.

2.8 Past Works on Photodegradation of Organic Compounds

Some of the important past research works on the decomposition of organic compound by using photocatalysis are critically discussed in the current section.

2.8.1 Photocatalysis with Different Photocatalysts

A wide range of semiconductors can be used for photocatalysis process, such as TiO_2 , CdS , SnO_2 , WO_3 , SiO_2 , ZrO_2 , ZnO , Nb_2O_3 , Fe_2O_3 , SrTiO_3 , CeO_2 , Sb_2O_4 , V_2O_5 , etc.

According to (Zhang et al., 2011), manganese oxide (MnO) is very effective in decomposing organic substrate. It is a class of active oxides widespread in the environment (Nesbitt and Banerjee, 1998). MnO has been extensively studied as an adsorbent, oxidant, in catalysis and as a material for rechargeable battery due to its special physiochemical properties, severe defects and non-stoichiometric in the structure (Suib, 2008), concurred by (Liu et al., 2011). The property of MnO has attracted increasing attention due to its semiconducting electronic structure. (Zhang et al., 2011) found that, MnO is very efficient in decomposing phenol when exposed to UV light as 92% of phenol was decomposed over 12 h of UV irradiation (Figure 2.4).

On the other hand, (Liao et al., 2004) claimed that TiO_2 was a better photocatalyst since it has many advantages to other materials, such as possesses high activity, lower prices and property of tolerating chemical and photo corrosions. Upon incorporation with sulphuric acid, the degradation ratio of methyl has attained 71.9%. However, (Fenoll et al., 2012) disagreed that TiO_2 was a good photocatalyst when it came to decomposition of simazine, prometryn, terbutryn, atrazine, terbuthylazine, propachlor, s-metolachlor and alachlor. Figure 2.5 shows the comparison on the efficiency of ZnO and TiO_2 as photocatalyst on decomposition of various organic substances. The ZnO performed better in decomposition of the particular organic substances.

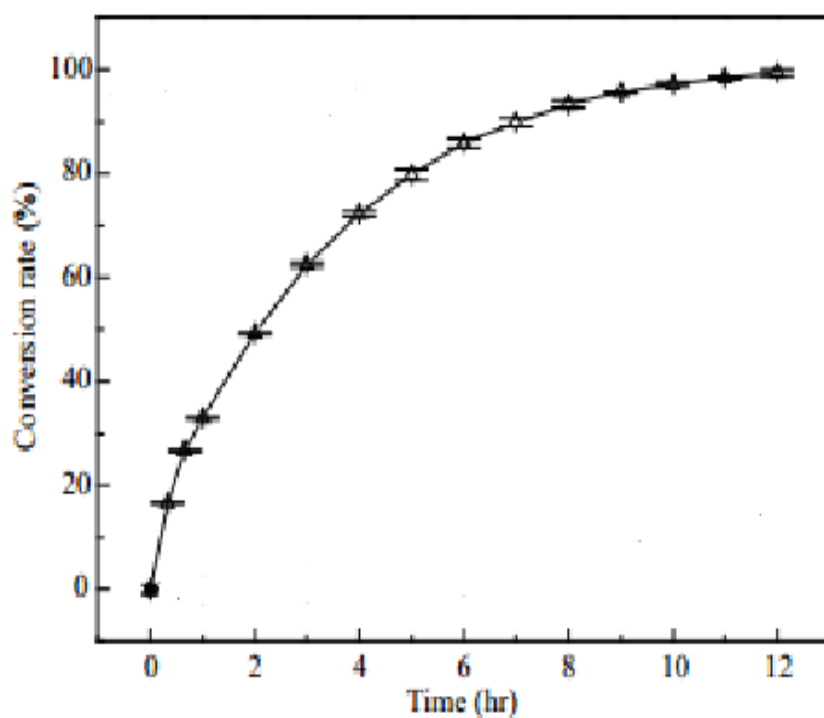


Figure 2.4 Kinetics curves of conversion of phenol with Mn oxide as photocatalyst

Source: Zhang et al. (2011)

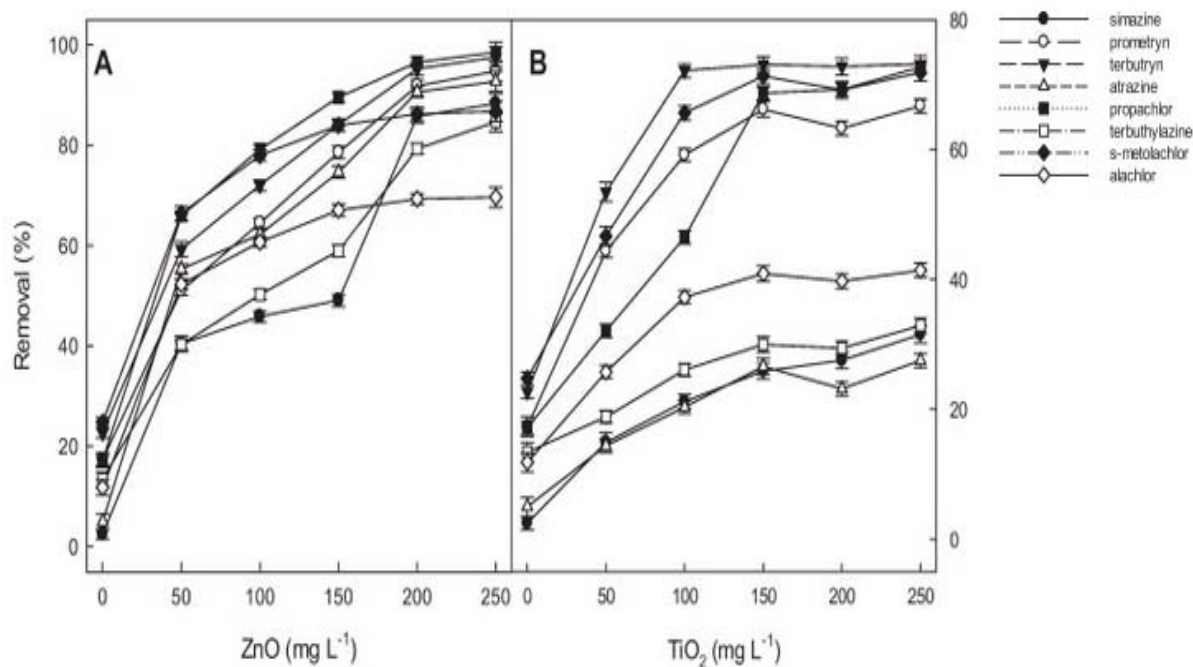


Figure 2.5 The graph of removal (%) of organic substances versus photocatalyst concentration

Source: Fenoll et al. (2012)

Besides, Yu et al. (2005) reported that ZnO was a good photocatalyst. High purity nano-ZnO was employed as a photocatalyst to remove 4-nitrochlorobenzene from the product and the results showed that the removal rate of 4-nitrochlorobenzene can reach a high 98% when the illumination time was 100 min. It increased with the prolonging of illumination time.

Another research conducted by Tian et al. presented the potential in Cu–Cr layered double hydroxide (LDH) films to become the photocatalyst. According to Tian et al. (2012), LDH can be used as photocatalysts for the degradation of organic pollutants under visible-light irradiation. Referring Figure 2.6, over 90% of 2,4,6-trichlorophenol (2,4,6-TCP) was decomposed by the 16.5 μm LDH films after 200 min of visible light irradiation.

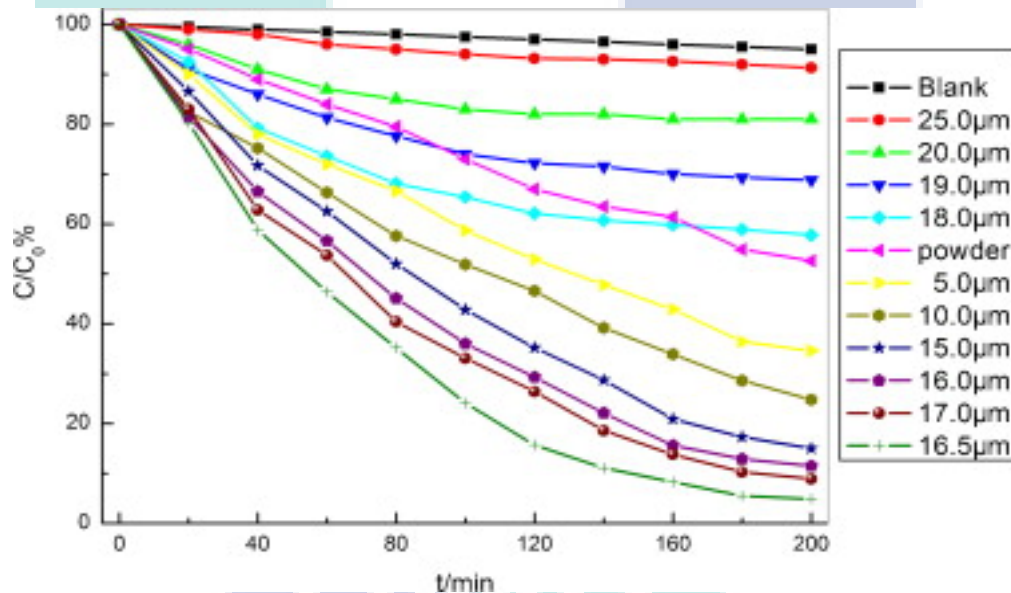


Figure 2.6 Concentration of 2,4,6-TCP vs irradiation time under visible-light irradiation ($\lambda > 400 \text{ nm}$) with the presence of LDH film catalysts with different thickness

Source: Tian et al. (2004)

Similarly, CeO₂ nanoparticle also exhibits good performance in photocatalytic activities (Qian et al., 2012). This can be proven from the degradation of methylene blue under solar energy irradiation. The photocatalytic activity of the CeO₂ was evaluated by photodegradation efficiency of methylene blue in aqueous solution under daylight irradiation and the results showed that almost all of the methylene blue decomposed after 100 min of light exposure (Qian et al., 2012). Similar results were obtained from Hernández-Alonso et al. (2004) when CeO₂ was used as the photocatalyst to degrade

toluene under the irradiation of UV-light. Unlike TiO₂, CeO₂ did not deactivate during the photocatalytic removal of toluene and other aromatic compounds.

A comparison of photo-activity of CeO₂, γ -Fe₂O₃, TiO₂ and ZnO was reported by (Bennett and Keller, 2011) and the results are presented in Figure 2.7. The probe molecule employed for this research was coumarin. Coumarin is a colorless crystalline organic chemical compound in the benzopyrone chemical class. The photo-activity of four nanoscale metal oxides was investigated, at various dilution levels of deionized water. Generally, TiO₂ was the better photocatalyst in deionized water with the highest reaction kinetics, which was $5.0 \times 10^{-5} \text{ s}^{-1}$ with catalyst loading of 10 mg/L. It is also the most effective photocatalyst for degradation of coumarin.

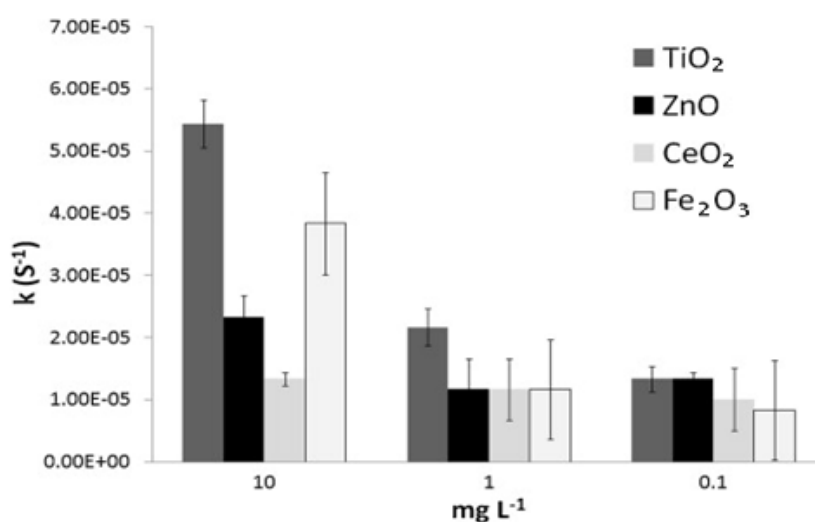


Figure 2.7 Photoactivities of four metal oxides in deionized water at various concentration

Source: Bennett and Keller (2011)

The Fe₂O₃ material exhibited sustainable catalytic activity when photocatalyzed the oxidation of aniline in ethanol to azobenzene (Karunakaran and Senthilvelan, 2006). Karunakaran and Senthilvelan (2006) claimed that Fe₂O₃ was able to be activated by both solar light and UV-light. An experiment was conducted to find out the effectiveness of UV-light and solar light on the formation rate of azobenzene with different initial concentrations of aniline in ethanol. The catalyst weight used in the experiment was 1.0 g. The results are shown in the Figure 2.8. To sum up, both UV-light and solar light are able to activate the photo-oxidation process, however, Fe₂O₃ is more sensitive to UV-light as more azobenzene formed under UV irradiation.

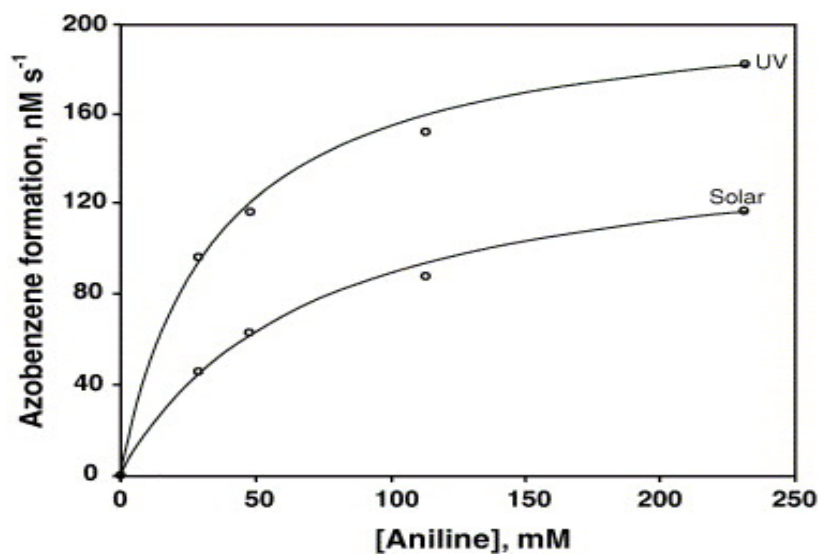


Figure 2.8 Azobenzene formation in ethanol on Fe_2O_3 at different aniline concentration under irradiation of UV-light and Solar(visible) light

Source: Karunakaran and Senthilvelan (2006)

There are still numerous reports of past photocatalysis works in the open literature employing different photocatalysts, of which the significant and relevant ones are summarized in Table 2.4. To conclude, heterogenous photocatalysis is an effective technique for degrading organic compounds. However, different photocatalysts will show different reactivity with different substrates due to the nature of both of them. Besides, the activator (UV/visible light) also plays a very important role in the photocatalysis, for instance material with wide band gap can only be activated by UV light. Hence, the selection of photocatalyst material and activator is vital to be sure of the effectiveness of organic degradation.

Table 2.4 The summary of past researches on photocatalysis process

Photocatalyst	Activator	Substrate	Results	Reference
Manganese oxides	UV-light	Phenol	92% of the substrate decomposed.	(Zhang et al., 2011)
TiO ₂	UV-light	methyl orange	71.9% of methyl orange degraded.	(Liao et al., 2004)
Cu–Cr layered double hydroxide (LDH)	Visible light	2,4,6-Trichlorophenol	Less than 10% of 2,4,6-Trichlorophenol present after 200 minutes	(Tian et al., 2012)
TiO ₂	UV-light	Simazine, prometryn, terbutryn, atrazine, terbuthylazine, propachlor, s-metolachlor and alachlor	Effectively degrades certain organic compounds. Detailed results are presented in Figure 2.5.	(Fenoll et al., 2012)
ZnO	UV-light	Simazine, prometryn, terbutryn, atrazine, terbuthylazine, propachlor, s-metolachlor and alachlor	All these organic compounds degraded effectively. Refer to Figure 2.5.	(Fenoll et al., 2012)
ZnO	UV-light	4-nitrochlorobenzene	98% of 4-nitrochlorobenzene removed over 100 minutes	(Yu et al., 2005)
CeO ₂	UV-light	Methylene blue	Almost 100% methylene blue is converted over 100 minutes.	(Qian et al., 2012)
CeO ₂	UV-light	Toluene	Deactivation of catalyst doesn't occurs.	(Hernández-Alonso et al., 2004)

Table 2.4 *Continue*

Photocatalyst	Activator	Substrate	Results	Reference
Meso-30 Fe ₂ O ₃ /TiO ₂	wt% Visible light	4-chlorophenol	All the 4-chlorophenol decomposed after 180 minutes of the experiment started.	(Palanisamy et al., 2013)
Fe ₂ O ₃ -TiO ₂ /ACF	Visible light	Methyl orange	(C/Co) ratio of methyl orange dropped to 0.32 after exposing under sun for 4 hours.	(Zhang and Lei, 2008)
Fe ₂ O ₃ and ZrO ₂ /Al ₂ O ₃ (9.1, 31.5, 54.1 wt% respectively)	UV-light	Phenol	93% phenol removed after 120 minutes.	(Liu et al., 2012)
Fe ₂ O ₃ /SnO ₂	Visible light	Acid blue 62	98.0% acid blue 62 can be degraded in 60 min under illumination of the visible light	(Xia et al., 2008)
Pd-MoO ₃ /SiO ₂	UV-light	Ethane	The selectivity of ethanal as high as 63.5% compared to 0% without the presence of catalyst.	(Wang et al., 2007)
CeO ₂ , γ-Fe ₂ O ₃ , TiO ₂ and ZnO	UV-light	Coumarin	TiO ₂ shows the best photocatalytic effect. With 10 mg/L, reaction constant of 5.0×10 ⁻⁵ s ⁻¹ was recorded.	(Bennett and Keller, 2011)
Fe ₂ O ₃	UV-light/Visible light	Aniline	Fe ₂ O ₃ is more sensitive to UV-light. More aniline converted under irradiation of UV-light.	(Karunakaran and Senthilvelan, 2006)

2.8.2 Past Research Works on TiO₂-based Photocatalysis

Since POME treatment is to remove the organic content, the discussion in the current section focuses on the removal of organic compound by using TiO₂-based photocatalysts. The vast arrays of organic compounds that are susceptible to the oxidative degradation from TiO₂ comprises of families of dyes, phenolic compounds, toxin and more. The photo-generated charges from TiO₂ possess high oxidative force that able to decompose most of the organic compounds.

Lin and Lee (2010) discovered that TiO₂ photocatalyst can effectively decolourize Procion red MX-5B under UV light irradiation after a modification with Ag. As can be seen in Figure 2.9, the most effective catalyst was 50%wt Ag/TiO₂ with more than 80% removal efficiency after 120 min of UV irradiation.

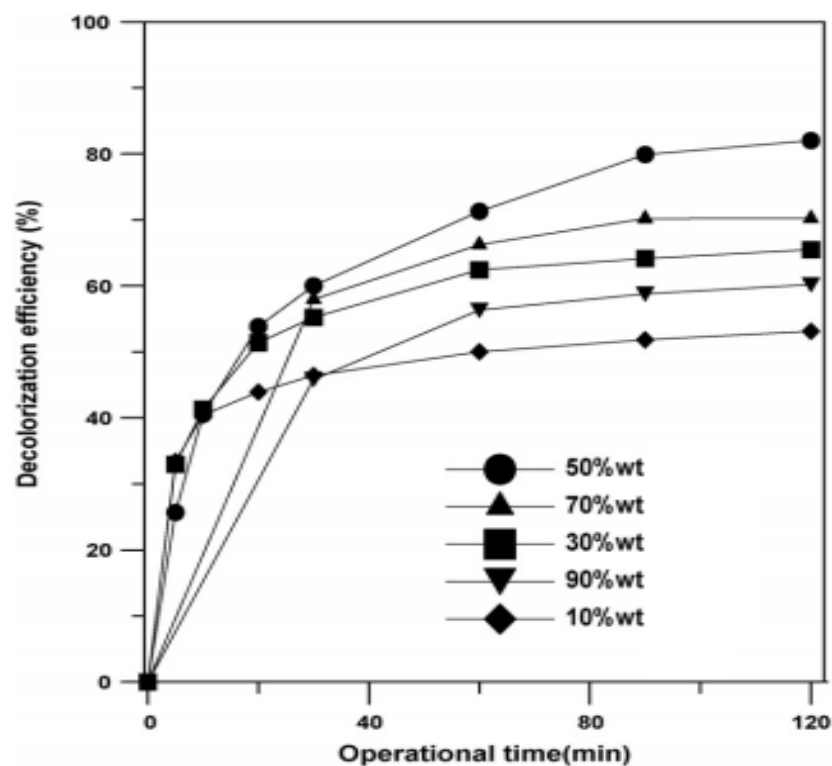


Figure 2.9 Comparison of the decolorization efficiency of Procion red MX-5B by different %wt of Ag/TiO₂

Source: Lin and Lee (2010)

On the other hand, Farbod and Kajbafvala (2013) reported on the TiO₂ photocatalytic decolourization of congo red. No obvious decolourization was observed in the absence of photocatalyst. However, in the presence of TiO₂, more than 90% of

decolourization was observed after 210 min under UV irradiation, and the rate of decolourization could even boost up with the inclusion of gadolinium (Gd). With 1.8wt% Gd/TiO₂, almost 100% of congo red decomposed after 120 min of UV radiation. The results obtained are illustrated in Figure 2.10.

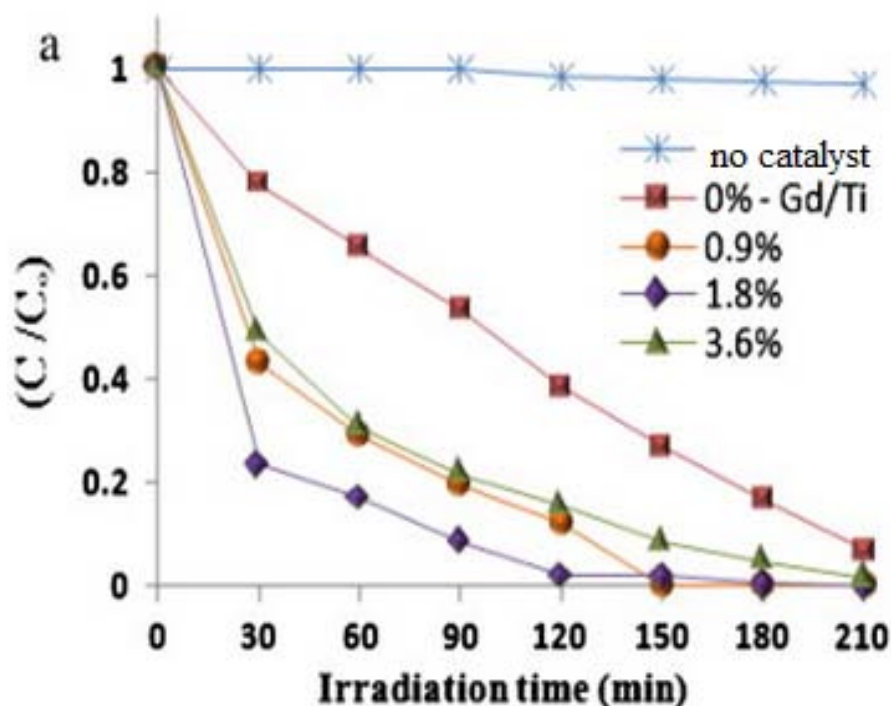


Figure 2.10 The graph of (C/C_0) of congo red versus UV irradiation time with various catalyst composition

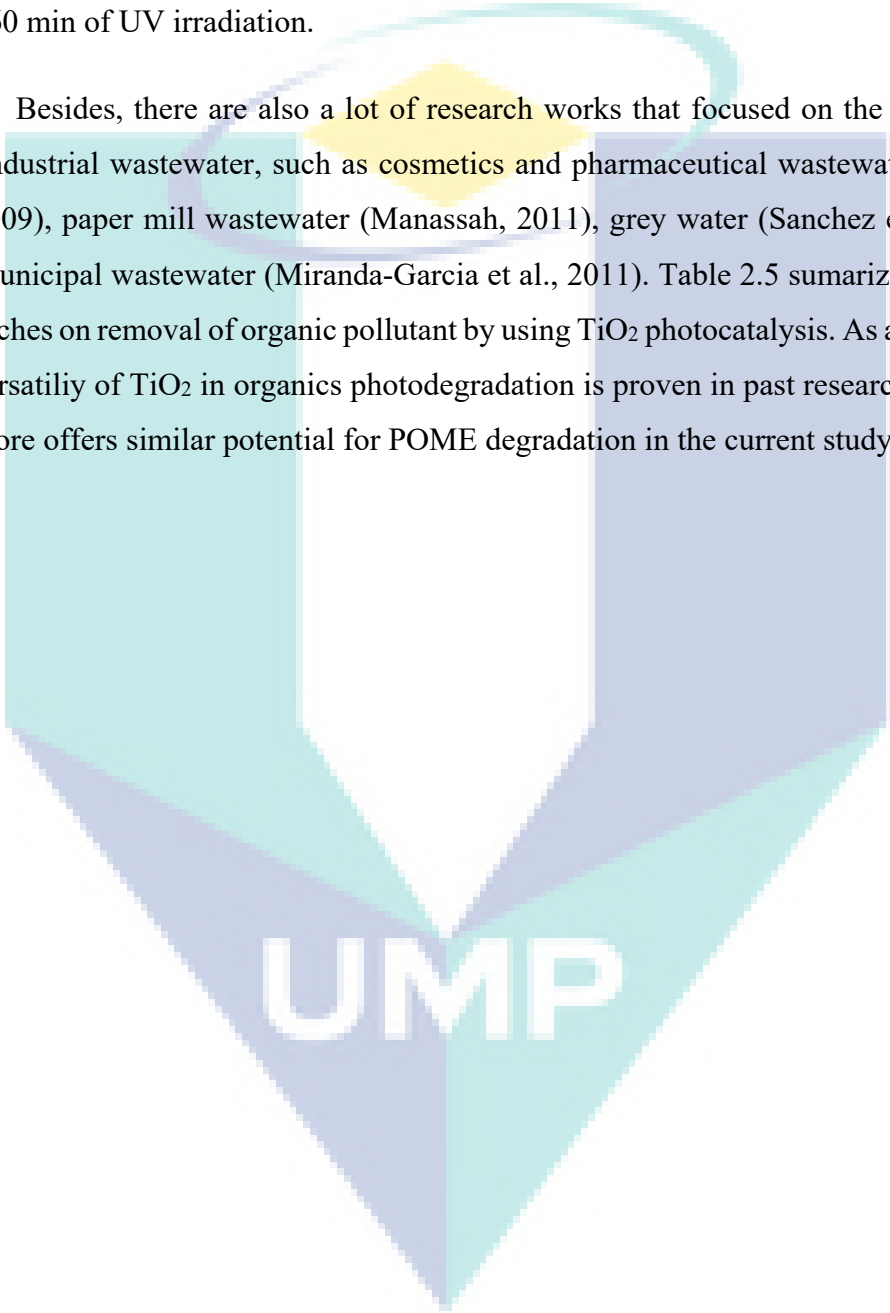
Source: Farbod and Kajbafvala (2013)

In the research conducted by Chen et al. (2007), 0.5 wt% Pt was used to modify the TiO₂ catalyst for decomposing the *o*-cresol. The decomposition rate of *o*-cresol under visible light irradiation from a fluorescent lamp was enhanced considerably (Chen et al., 2007) due to the formation of Schottky barrier between Pt and TiO₂, therefore preventing the recombination of electric holes and electrons. Ultimately, over 80% of *o*-cresol was degraded after 400 min of photo-reaction.

Besides, Giraldo et al. (2010) confirmed on the effectiveness of TiO₂ photocatalysis on drugs. Oxolinic acid (OA) is one of the quinolone antibiotics commonly used in veterinary medicine or aquaculture as a prophylactic. However, high concentrations of OA have been found in the aquatic environment (Rigos et al., 2004), which have led to the adverse environmental effects. Giraldo and co-workers (2010)

conducted photodegradation of OA over TiO₂ suspension under UV irradiation and found that, under optimal conditions (1.0 g/L and pH 7.5), 60% of removal was achieved after 30 min of photoreaction. Besides, An et al. (2011) also applied TiO₂ on medical wastewater treatment by degrading antiviral drug, lamivudine. Similarly, 1.0 g/L TiO₂ was found to be the optimum catalyst loading with more than 90% degradation achieved after 60 min of UV irradiation.

Besides, there are also a lot of research works that focused on the treatment of real industrial wastewater, such as cosmetics and pharmaceutical wastewater (Rizzo et al., 2009), paper mill wastewater (Manassah, 2011), grey water (Sanchez et al., 2010), and municipal wastewater (Miranda-Garcia et al., 2011). Table 2.5 summarizes the recent researches on removal of organic pollutant by using TiO₂ photocatalysis. As a conclusion, the versatility of TiO₂ in organics photodegradation is proven in past research works and therefore offers similar potential for POME degradation in the current study.



UMP

Table 2.5 Recent research works on decontaminat organic substrate over TiO₂ photocatalyst

Contaminant	Photocatalytic system	Ref.
<u>Dyes</u>		
Reactive violet 5	UV/Anatase powder (Sigma Aldrich)	(Chung and Chen, 2009)
Blue 9, Red 51 and Yellow 23	Solar/TiO ₂ (Degussa P25)	(Dias and Azevedo, 2009)
Methylene blue	UV/TiO ₂ (Merck) on volcanic ash	(Esparza et al., 2010)
Rhodamine B	UV/TiO ₂ bilayer	(Zhuang et al., 2010)
<u>Pesticides and herbicides</u>		
Organophosphate and Phosphonoglycine	UV/TiO ₂ immobilized on silica gel	(Echavia et al., 2009)
Azimsulfuron	UV/TiO ₂ coated on glass rings	(Stathatos et al., 2008)
Swep residues	Simulated sunlight/TiO ₂ (Degussa P25)	(Fabbri et al., 2009)
<u>Pharmaceuticals and cosmetics</u>		
Benzylparaben	Electrocoagulation and UV/TiO ₂ /H ₂ O ₂	(Boroski et al., 2009)
	UV/TiO ₂ (Aeroxide P25)	(Rizzo et al., 2009)
	TiO ₂ /Fe ₃ O ₄ and TiO ₂ /SiO ₂ /Fe ₃ O ₄	(Alvarez et al., 2010)
	UV/TiO ₂ (Degussa P25)	(Lin et al., 2011)
<u>Drugs</u>		
Lamivudine	UV/TiO ₂ (Degussa P25)	(An et al., 2011)
Oxytetracycline	UV/TiO ₂ (Degussa P25)	(Pereira et al., 2011)

Table 2.5 *Continue*

Contaminant	Photocatalytic system	Ref.
<u>Drugs</u>		
Oxolinic acid	UV/TiO ₂ (Degussa P25)	(Giraldo et al., 2010)
Atenolol and propranolol	UV/Commercial TiO ₂ s	(Hapeshi et al., 2010)
Ciprofloxacin, ofloxacin, norfloxacin and enrofloxacin	UV/TiO ₂ (Degussa P25)	(An et al., 2010)
<u>Others</u>		
<i>N,N</i> -diethyl- <i>m</i> -toluamide	UV/TiO ₂ (Degussa P25)	(Adams and Impellitteri, 2009)
β-naphthol	UV/TiO ₂ -SiO ₂	(Qourzal et al., 2009)
15 emerging contaminants	Solar UV/TiO ₂ coated on glass spheres	(Miranda-Garcia et al., 2010)
Grey water	UV/TiO ₂ (Aeroxide P25)	(Sanchez et al., 2010)
Microcystins (Cyanotoxin)	UV/TiO ₂ film	(Antoniou et al., 2008)
	UV/Doped TiO ₂	
	UV/ Nitrogen doped TiO ₂	(Triantis et al., 2012)
Lipid vesicles and <i>E. coli</i> cells	UV/TiO ₂ (Degussa P25)	(Dalrymple et al., 2011)
Bacterial colony	UV/TiO ₂ on titanium beads	(Li et al., 2011)
	UV/TiO ₂ -coated bio-film	
Paper mill wastewater	Solar/TiO ₂	(Manassah, 2011)
Endocrine disrupting compounds	UV/TiO ₂ (Degussa P25)	(W. Zhang et al., 2012)
Municipal waste water	Solar/sol-gel TiO ₂ and Degussa P25	(Miranda-Garcia et al., 2011)
Contaminated soil	Plasma/TiO ₂ ((Degussa P25)	(Wang et al., 2011)

2.8.3 Past Research Works on ZnO-based Photocatalyst

Besides TiO₂, ZnO is another semiconductor that is commonly used in heterogeneous photocatalysis. Similar to TiO₂, the band gap of ZnO is comparatively wide (~3.3 eV), hence only functional under UV irradiation (Lu et al., 2008). ZnO is widely applied in various fields, such as electronics, gas sensors and biosensors, UV detectors, light-emitting diodes (LEDs), solar cells, photocatalysts and others due to its unique electrical, optical and mechanical properties (Zhang et al., 2012). Furthermore, it is also biocompatible, biodegradable and bio-safe for both medical and environmental application (Zhou et al., 2006). There are two forms of crystalline structures for ZnO, *viz* cubic zinc blende and hexagonal wurtzite, as in Figure 2.11. However, under ambient conditions, ZnO exhibits in latter structure form due to higher stability. Due to its versatility, ZnO has been employed as a photocatalyst for degradation of environmental pollutants such as dye, pesticides and other organic pollutants under appropriate light irradiation (Di Mauro et al., 2016; Pan et al., 2016; Wang et al., 2016).

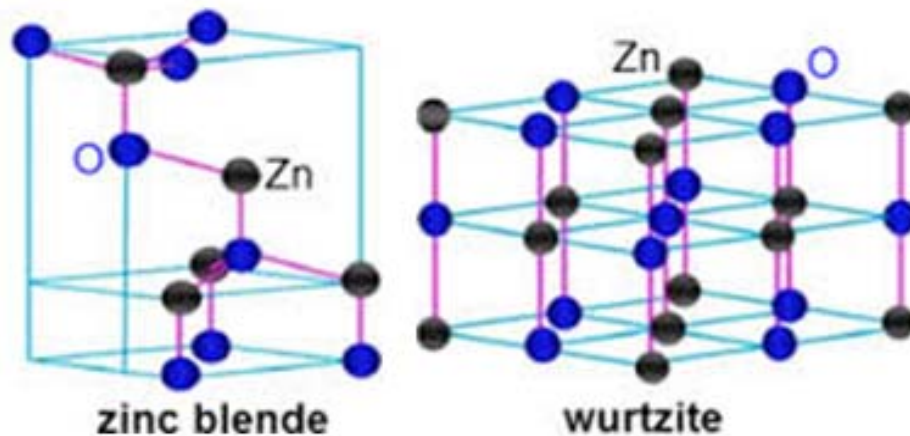


Figure 2.11 Crystalline structures for ZnO

Source: Lu et al. (2008)

Many research groups reported on the use of ZnO to photo-degrade various organic pollutants under UV light irradiation. (Baruah et al., 2008) reported on the deposition of ZnO on woven polyethylene fibres for photocatalytic degradation of methylene blue. The results revealed that the photocatalytic effect was enhanced by 300% compared to bare polyethylene fibres. In addition, Kuo et al. (2007) reported that ultra-

long ZnO nanowires on silicon, synthesized by vapour transport process, is very reactive towards the degradation of rhodamine B and 4-chlorophenol. Only a slight decrease in the photodecomposition rate was observed after 10 cycles of photoreaction.

In addition, the photocatalytic effect of ZnO nanowires was tested over dichlorobenzene and methyl orange in water (Zhang et al., 2012). The experiments were conducted under white light (60 W/m² in visible light and 2 W/m² in UV) or UV (30 W/m²) irradiations. Results showed that the dichlorobenzene was fully decomposed within 2 h for both white light and UV light in the presence of ZnO photocatalyst. The rate of decomposition was even enhanced by doping ZnO photocatalyst with Iron (Fe). With the ZnO/Fe photocatalyst, complete decomposition of dichlorobenzene was observed within 1 h for both light sources. In contrast, ZnO seems to be less effective towards decomposition of methyl orange under white light irradiation. After 4 h of photoreaction, the degradation observed was around 16% and further increased to 34% by using ZnO/Fe photocatalyst. However, under UV irradiations, full decomposition was observed after 4 h in the presence of ZnO photocatalyst. With the enhancement of Fe, the reaction time for full decomposition was further reduced to 2 h.

Doping with transition metal ions is a good strategy to extend the absorbance of ZnO to the visible light region. It was found that the 3wt% Cr-modified ZnO photocatalyst has successfully decolorized methyl orange under visible light irradiation (Wu et al., 2011). Besides, Jia et al. (2009) also discovered that with 2% of La metal doping, the band gap energy of ZnO photocatalyst was reduced and able to decompose Rhodamine B under visible light irradiation. Moreover, Li et al. (2011) have investigated the structural, electronic and optical properties of Ag-modified ZnO photocatalyst using first-principles calculations based on DFT (density functional theory). The results proved that the photocatalyst possessed significant activity under the visible light. In addition to doping, Jung and Yong, (2011) also reported on the fabrication of CuO-ZnO nanowires on stainless steel mesh for effective photocatalytic applications.

More past works using ZnO photocatalyst are summarized in Table 2.6. All these past reports confirmed on the versatility of ZnO as a photocatalyst. With appropriate modifications, it can degrade most of the organics under suitable activator. Therefore, it is chosen in the current study for POME degradation due to its reported versatility potential.

Table 2.6 Past research works using ZnO as the photocatalyst

Contaminant	Photocatalytic system	Ref.
<u>Dye</u>		
Methylene blue	UV/deposited ZnO on woven polyethylene fibres	(Baruah et al., 2008)
	Solar light/C-modified ZnO	(Haibo et al., 2013)
Methyl orange	Visible light/Cr-modified ZnO	(Wu et al., 2011)
Rhodamine B		(Jia et al., 2009)
Methyl Orange (MO)	UV/ZnO nanoneedle	(Tripathy et al., 2014)
Rhodamine 6G	UV/N-modified ZnO	(Wu et al., 2014)
<u>Pesticides & Herbicides</u>		
Dimethoate	UV/ZnO	(Evgenidou et al., 2005)
Metamitron	UV/ZnO	(Mijin et al., 2009)
<u>Fungicides & Insecticides</u>		
2-phenylphenol (OPP)	UV/ZnO	(Khodja et al., 2001)
Diazinon	UV/ZnO	(Daneshvar et al., 2007)
Dichlorvos	UV/ZnO	(Evgenidou et al., 2005)
Imidacloprid	UV/ZnO	(Papp, 2014)
<u>Pharmaceuticals</u>		
Amoxicillin (AMX), Ampicillin (AMP), Cloxacillin (CLX)	UV/ZnO	(Elmolla and Chaudhuri, 2010)
Tetracycline (TC)	UV/ZnO	(Palominos et al., 2009)
<u>Phenolics</u>		
4-chlorophenol (4CP)	UV/ZnO	(Gaya et al., 2009)
Phenylhydrazine	UV/ZnO	(Nezamzadeh-Ejhih and Khodabakhshi-Chermahini, 2014)

2.9 Optimization Using Central Composite Design (CCD) in Response Surface Methodology (RSM)

Optimization refers to maximizing the benefit from the process by improving its performance. In analytical chemistry, it is commonly defined as discovering conditions at which to apply a procedure that produces the best possible response (Araujo and

Brereton, 1996). Traditionally, the optimization of a process is conducted by studying the effect of one variable at a time (OFAT). However, this is impracticable and does not really consider the interaction between the variables (Mohajeri et al., 2010). Consequently, the complete effects of the variables on the response are not fully understood. Besides, this traditional optimization process may also lead to increase in the number of experiments, causing waste of time and waste of resources. Hence, experimental statistical design was treated as one of the efficient way to obtain accurate and statistically significant models of the process with minimal number of experiment. During optimization process, the interactions among the variables are also considered for more accurate optimization conditions in multivariable analyses.

Among the multivariate techniques, response surface methodology (RSM) is considered as one of the most commonly employed technique. RSM is a collection of mathematical and statistical techniques based on the fit of a polynomial equation to the experimental data, which must describe the behaviour of a data set with the objective of making statistical previsions. Before applying the RSM, the experimental design must be chosen to define the conditions of the experiments based on the independent variables. A favourite model in RSM is the central composite design (CCD), which is efficient and flexible in providing adequate data on the effects of variables and overall experiment error even with a fewer number of experiments (Montgomery, 2008). CCD is a useful technique that considers direct effects, pairwise interactions and curvilinear variable effects, eventually giving accurate results as the outcome (Mohajeri et al., 2010) .

CCD was first proposed by Box and Wilson (1951), which consists of (1) a full factorial or fractional factorial design; (2) an additional design, often a star design in which experimental points are a away from the centre; and (3) the central point. The CCD for optimization of two and three variables is illustrated in Figure 2.12.

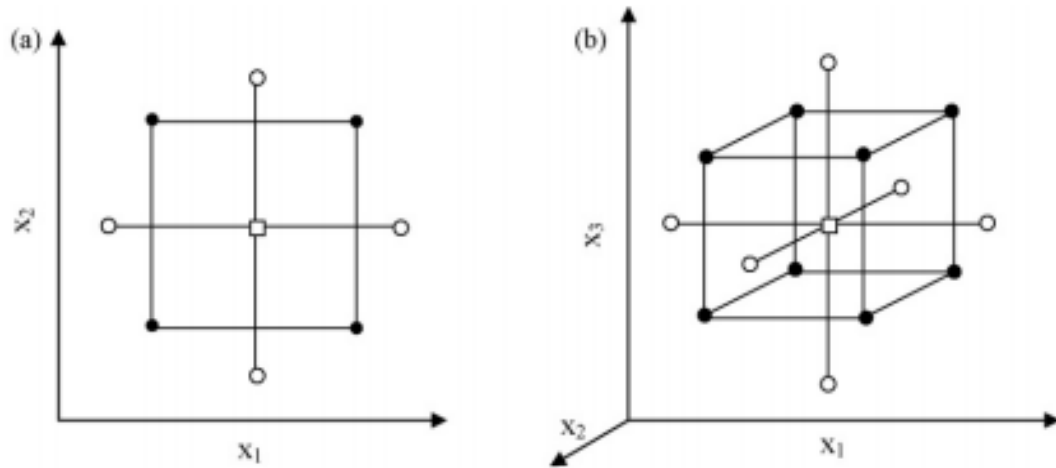


Figure 2.12 The CCD for optimization process of two (left) and three (right) variables

Source: Box and Wilson (1951)

Generally, a full uniformly routable CCD requires an experiment number according to $N = k^2 + 2k + c_p$, in which k is the number of factors and c_p is the replicate number of the central point. All the factors are studied in five levels, namely $-a$, -1 , 0 , $+1$, and $+a$, while a can be defined by $a = 2^{(k-p)/4}$. Based on calculation, a for two, three and four variables are 1.41, 1.68 and 2.00, respectively.

As aforementioned, CCD is one of the favourite models in RSM. There are numerous previous works that have applied this technique in optimizing their process. Table 2.7 summarizes some of the important prior works on CCD optimization in analytical chemistry.

UMP

Table 2.7 The examples of CCD optimization in analytical chemistry

Analytes	Samples	Analytical technique	Objective	Reference
Chlorobenzenes	Environmental water	HPLC	Developing a headspace single-drop micro-extraction procedure using room temperature ionic liquid for determination of trace amounts of these substances.	(Vidal et al., 2007)
Human immunoglobulin G	Artificial mixture of proteins	Affinity HPLC	Optimizing the purification of these proteins from a mixture.	(Rosa et al., 2007)
Organochlorine pesticides and polychlorinated biphenyls	Human serum	GC	Developing a procedure for the determination of these substances using headspace solid-phase micro-extraction	(Lopez et al., 2007)
Tetracycline, chlortetracycline, oxytetracycline and doxycycline	Pharmaceuticals	Capillary zone electrophoresis	Investigating the influence of the electrolyte composition, pH and concentration, as well as temperature and applied voltage in the separation of the analytes	(Mamani et al., 2006)
Hydroxymethylfurfural	Honey	Amperometry	Development of microbiosensors built by photolithographic techniques and based on a Pt microelectrode chip	(Lomillo et al., 2006)
Polybrominated diphenyl ethers, polybrominated biphenyls and polychlorinated naphthalenes	Sediment samples	GC-MS	Optimization of the experimental conditions for a method involving microwave-assisted extraction and large-volume injection	(Yusà et al., 2006)
As, Cd, Cu, Fe, Mg, Pb and Zn	Mussel tissues	ICP OES	Evaluation of different variables affecting the enzymatic hydrolysis of samples by five enzymes	(Peña-Farfal et al., 2004)

2.10 Photocatalysts Characterization Techniques

This section describes the fundamentals of techniques that employed in photocatalysts characterization.

2.10.1 X-Ray Diffraction (XRD)

X-ray diffraction (XRD) is a non-destructive analytical technique which is widely used for the identification of structure, crystalline phases, and also sizes of crystallites of natural or synthetic materials. The sample used for this analysis may be powders, solids, films or ribbons and the amount needed is a few milligrams. Nonetheless, greater accuracy is achieved if sample used is up to few grams (Smyth and Martin, 2000). XRD patterns or also known as “fingerprint” varied based on the internal structure of the material and hence the characteristics can be identified.

From this technique, the sample mean crystallite size in the range 3 to 50 nm can be estimated. When crystallite size is smaller than 3 nm, the diffraction lines of X-ray pattern would be diffused or absent. However, if crystallite size is larger than 50 nm, the change in the line shape would not be apparent (Cullity, 1957).

In XRD analysis, the sample is ground to powder for the purpose of revealing all possible orientations of the crystal structure to the X-ray beam. When X-ray beam with wavelength, λ is incident on the crystalline structure, diffraction occurs due to interference caused by the nature of the material. The angle at which constructive interference occurred was measured and subsequently the inter-planar distances or “d-spacings” between the crystal lattice was identified from Bragg equation (Cullity, 1957). The interplanar spacings depend solely on the dimension of the crystal’s unit cell, on the other hand, the intensities of the diffracted rays function as the placement of the atoms in the unit cell (Klug and Alexander, 1956). Bragg formula is given by Equation 2.1.

$$n\lambda = 2d \sin \theta \quad (2.1)$$

where n is the order of reflection (integer), λ is wavelength of X-ray beam (nm), d is inter plane distance of crystal (d-spacing) and θ is angle of incidence (degree).

By assuming the diffraction line shapes are Gaussian, the squares of the contributing width factors are additive. The line width due to particle size broadening can be defined as Equation 2.2.

$$\beta_d^2 = \beta_{\text{obs}}^2 + \beta_{\text{inst}}^2 \quad (2.2)$$

where β_d is true line width at half maximum intensity (degree), β_{obs} is observed width at half maximum intensity (degree) and β_{inst} is instrumental line width by standard (degree). β_{inst} is obtained from a calibration process using a standard of high quality with a crystalline size greater than 1000 Å. From the results, the mean crystallite size is later calculated by Scherrer equation, Equation 2.3.

$$D = \frac{k_{\text{sch}} \lambda}{\beta_d \times \cos \theta} \quad (2.3)$$

where D is the crystalline size (nm), λ is wavelength of X-ray (nm), β_d is angular width at half maximum intensity (radian), θ is the Bragg's angle degree and k_{sch} is Scherrer constant and equals to 0.93 (Warren, 1969).

The schematic of X-ray Diffusion is presented in Figure 2.13. The specimen was initially ground to fine powder (<100 µm). It was then placed on a glass specimen holder and pressed using a glass slide. Scanning of sample was then performed starting from 20 to 90° at a speed of 1° min⁻¹. Peaks obtained from the analysis were evaluated using The International Centre for Diffraction Data (ICDD) database search match interpretation method to determine the type of phases present.

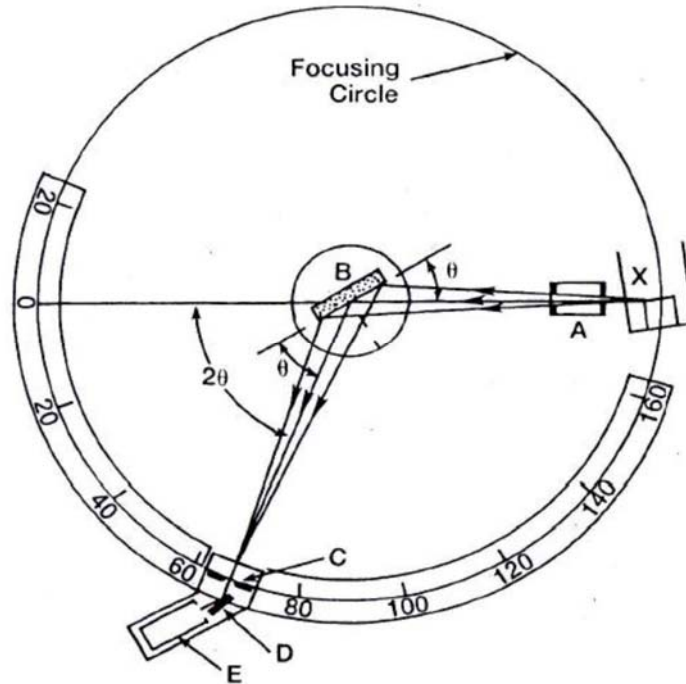


Figure 2.13 A schematic diagram of XRD (A) Collimation (B) Sample (C) Slit (D) Exit Beam Monochromator (E) Detector (X) Source of X-Rays

Source: Cullity (1978)

2.10.2 N₂ Physisorption Analysis

The most widely used procedure for the determination of the specific surface area of solid materials is the Brunauer-Emmett-Teller (BET) method, which is an extension of the Langmuir's pioneer work for monomolecular adsorption. BET equation is derived for multilayer adsorption and based on the relationship between the volume of gas physically adsorbed and the total area of adsorbent, given by:

$$\frac{P}{V(P_s - P)} = \frac{1}{cV_m} + \frac{(c - 1)P}{cV_m P_s} \quad (2.4)$$

where P = gas pressure

P_s = saturation pressure of the adsorbate gas

V = volume of gas adsorbed

V_m = volume of gas adsorbed corresponding to monolayer coverage

c = a characteristic constant of the adsorbate

A plot of $P/V(P_s - P)$ against P/P_s provides a linear plot from which V_m and c may be calculated via the slope and intercept, respectively. The volume V_m , can then be converted to the number of molecules adsorbed if the cross-sectional area of the adsorbent gas molecule is known. The most commonly used adsorbate is N_2 , which has cross-sectional area of 16.2 \AA^2 . Therefore, the adsorption of N_2 is carried out at the N_2 boiling point of about 77 K.

Porosity of powder and other porous materials may be characterized by N_2 adsorption study. Two common techniques for describing porosity are the determination of total pore volume and pore size distribution. For the evaluation of the porosity of most solid materials, N_2 at 77 K is the most suitable adsorbate (the material in the adsorbed state). The forces involved in physisorption are the same as those responsible for the condensation of vapour, which include the London dispersion forces and the short-range intermolecular repulsion.

An understanding of porosity of a solid material can be obtained by the construction of an adsorption isotherm by measuring the quantity of adsorbate on the surface over a wide range of relative pressures at constant temperature. The adsorption isotherm is obtained point-by-point on the equipment by admitting successive known volumes of N_2 to the adsorbent (solid surface) and measuring the equilibrium pressure. Similarly, desorption isotherm can be obtained by measuring the quantities of gas removed from the sample as the relative pressure is lowered.

The total pore volume is derived from the amount of vapour adsorbed at a relative pressure close to unity, by assuming that the pores are then filled with liquid N_2 . If the solid material contains no macropores (pore width $> 50 \text{ nm}$), the isotherm will remain nearly horizontal over a range of P/P_0 near the unity and the pore volume is well defined.

Nevertheless, the isotherm rises rapidly near P/P_0 close to unity for macropores, and in this case it may exhibit an essentially vertical rise. Thus, the limiting adsorption may be identified with the total pore volume. The volume of nitrogen adsorbed (V_{ads}) can be converted to the volume of N_2 (V_{liq}) contained in the pores using the following equation:

$$V_{liq} = \frac{P_a V_{ads} V_m}{RT} \quad (2.5)$$

where P_a and T are ambient pressure and temperature, and V_m is the molar volume of the N_2 ($34.7 \text{ cm}^3 \cdot \text{mol}^{-1}$) respectively.

Since pores which would not be filled below a P/P_o of unity have a negligible contribution to the total pore volume, the average pore size can be estimated from the pore volume. The distribution of pore volume with respect to pore size is known as a pore size distribution. It is generally accepted that the desorption isotherm is more appropriate than the adsorption isotherm for evaluating the pore size distribution of a solid material. The desorption branch of the isotherm exhibits a lower relative pressure (P/P_o) resulting in a lower free energy state, and therefore the desorption isotherm is closer to the true thermodynamic stability. Mesopore size calculation was computed assuming cylindrical pore geometry using the Kelvin equation (Gregg and Sing, 1982):

$$r_k = \frac{-2\gamma V_m}{RT \ln\left(\frac{P}{P_o}\right)} \quad (2.6)$$

where γ = the surface tension of N_2 at its boiling point ($8.85 \text{ ergs} \cdot \text{cm}^2$ at 77 K)

V_m = the molar volume of liquid N_2 ($34.7 \text{ cm}^3 \cdot \text{mol}^{-1}$)

R = gas constant ($8.314 \text{ E}7 \text{ ergs} \cdot \text{K}^{-1} \cdot \text{mol}^{-1}$)

T = N_2 boiling point (77 K)

P/P_o = relative pressure of N_2

r_k = the Kelvin radius of the pore

Using the appropriate constants for N_2 , above equation reduces to:

$$r_k \left(\text{\AA} \right) = \frac{4.15}{\lg\left(\frac{P}{P_o}\right)} \quad (2.7)$$

The Kelvin radius is the radius of the pore in which condensation happens at P/P_o .

However, r_k does not represent the actual pore radius because some adsorption has taken

place prior to condensation on the walls of the pore. In addition, during desorption, an adsorbed layer remains on the walls when evaporation occurs. Therefore, the actual pore radius (r_p) is given by:

$$r_p = r_k + t \quad (2.8)$$

where t is the thickness of the adsorbed layer. The t -value can be estimated by following equation:

$$t(\text{\AA}) = \left[\frac{13.99}{\log\left(\frac{P}{P_0}\right) + 0.034} \right]^{1/2} \quad (2.9)$$

Surfer Acquisition software offers the pore size distribution using the methods proposed by Barrett, Joyner and Halenda (BJH) and by Dollimore and Heal (DH). However, the BJH method is the most widely used for the computation of the pore size distribution. The BJH procedures are based on the emptying of the pores by a step-wise reduction of P/P_0 , and the derived pore size distribution is normally expressed in the graphical form $(\delta V_p / \delta r_p)$ versus r_p or d_p .

Furthermore the specific surface area of TiO_2 can be estimated using the following equation:

$$S_{BET} = \frac{v_m \times N \times s}{V \times g} \quad (2.10)$$

where v_m is the volume of gas adsorbed corresponding to monolayer coverage, N is the Avogadro's constant, s denotes for cross-sectional area of N_2 , V represents molar volume of N_2 and lastly g is the mass of photocatalyst used in analysis.

2.10.3 UV-Vis Diffuse Reflectance Spectroscopy

Band-gap energy, E_{bg} , values will be obtained from the UV-vis diffuse reflectance measurement. The instrument measures the absorption spectrum of a sample at wavelengths in the range 190 to 900 nm. The light source used are deuterium lamp for

wavelength 190 – 350 nm (UV region) and halogen (WI) lamp for 340 –2500 nm (VIS/NIR region).

The light from the light source is converged and enters the monochromator (Figure 2.14). It is dispersed by the grating in the monochromator and the light passing through the exit slit is monochromated. Then this light is split into two light paths by a sector mirror, one incident on the sample to be measured and the other on the reference sample. The light that has passed through the sample and reference is incident on the photomultiplier tube or Pbs photoconductive cell, and subsequently converted into an electrical signal. This signal will then be synchronously rectified before is converted and processed as digital data or a spectrum.

The Schuster-Kubelka-Munk (SKM) model is widely accepted for quantitative measurement of the absorption spectrum of a solid sample from diffuse reflectance measurements. The apparent absorbance can be expressed by R and R_0 , the total reflectances of the sample and reference, respectively, collected by an integrating sphere (the detector of a double beam spectrometer) as:

$$A = \log\left(\frac{R_0}{R}\right) \quad (2.11)$$

In diffuse reflectance measurements, the light remitted by the sample and the reference is collected by an integration sphere coated with a white standard showing a high diffuse reflectance. This white standard can be MgO or BaSO₄ or PTFE (polytetrafluoroethylene) and is normally used as a reference sample. In order to determine the band gap energy, the original coordinates of the spectra (reflectance vs. wavelength) were transformed to Kubelka–Munk function (K) vs. photon energy ($h\nu$). The final plot of $(ah\nu)^{1/2}$ as a function of $h\nu$ is in accordance with the theoretical equation 2.12:

$$ah\nu = \text{const}(h\nu - E_{bg})^2 \quad (2.12)$$

whereby “ a ” is an absorption coefficient of the photocatalyst and E_{bg} is the band gap energy. The Kubelka–Munk function (K) calculated from the reflectance spectra is pre-determined to be directly proportional to the absorption coefficient (α). The current work employed method based on the fitting of the experimental dependences by Boltzmann symmetrical function using non-linear regression.

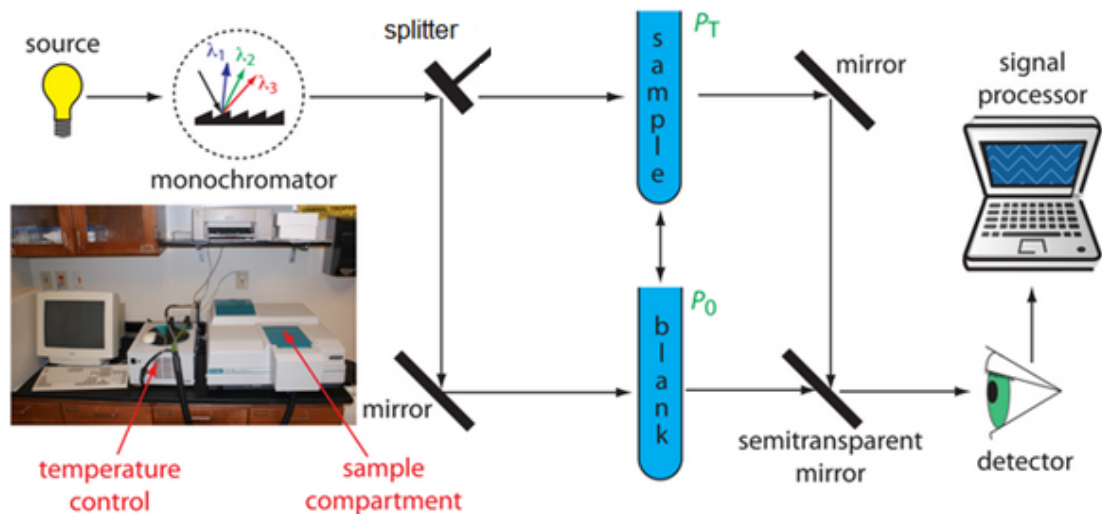


Figure 2.14 The Jasco V-550 optical system schematic diagram

2.10.4 Field Emission Scanning Electron Microscopy (FESEM)

Field Emission Scanning Microscopy Analysis (FESEM) as shown in Figure 2.15 is a non-destructive analysis technique that reveals information such as sample morphology or texture, sample topography, sample compositions, crystalline structure and orientation of materials which contribute to the structure of the sample from electron-sample interactions by directing a beam of high energy electrons to produce a variety of electrons emitted from surface of the sample. A detector caught the secondary electrons and an image of the coked sample surface was constructed by comparing the intensity of these secondary electrons to the scanning primary electron beam. Finally the image was displayed on a monitor. Commonly, data can be collected from a selected area of the surface of the specimen and a 3-dimensional image was obtained. During the acceleration of electrons in FESEM, the electrons carried a significant amount of kinetics energy generated by electrons- sample interactions which consequently dissipated as signal. This signal included secondary electrons which produced the FESEM images (morphology and topography of samples), backscattered electrons (BSE) and diffracted backscattered electrons (Michler, 2004). The dissimilarities of the image are due to difference in electron collection efficiency that depends on the angle of emission, atomic number of elements and surface relief.

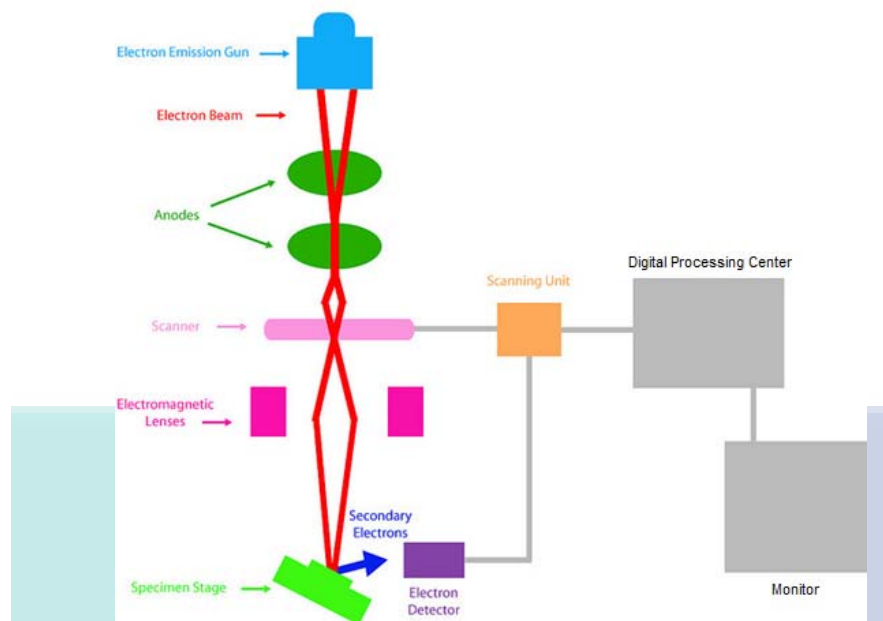


Figure 2.15 A Schematic diagram of FESEM

Source: Materials and Metallurgical Engineering Department, New Mexico Tech

2.10.5 Fourier Transform Infrared Spectroscopy (FTIR)

Fourier transform infrared spectroscopy (FTIR) is a technique used to identify the functional groups of the species by obtaining an infrared spectrum of adsorption, emission, photoconductivity or Raman scattering of a solid, liquid or gas. It is an in-situ method and one of the mostly used spectroscopic tools for catalyst chemical fingerprinting. As the IR radiation passes through a sample, different species will have different responses towards the exposure. As a result, some of the IR radiation will be absorbed, while some will not. Hence, it produces a wave-like pattern named as an interferogram. Subsequently, Fourier transformation takes place to transform the interferogram obtained into a spectrum. The spectrum can be expressed in two forms, *viz* absorbance or transmittance against frequency, and it corresponds to the molecular vibrations between the chemical bonds, creating an infrared correlation between chemical structure and infrared absorption.

2.10.6 Scanning Electron Microscopy with X-Ray Microanalysis (SEM-EDX)

The basic fundamentals of SEM-EDX presented in the current section were adapted from the website of the University of Buffalo in New York (n.d.). SEM is a technique that uses an electron beam to scan a sample's surface, subsequently displaying the surface morphology of the sample through the analyser. During the analysis, the electrons are released and

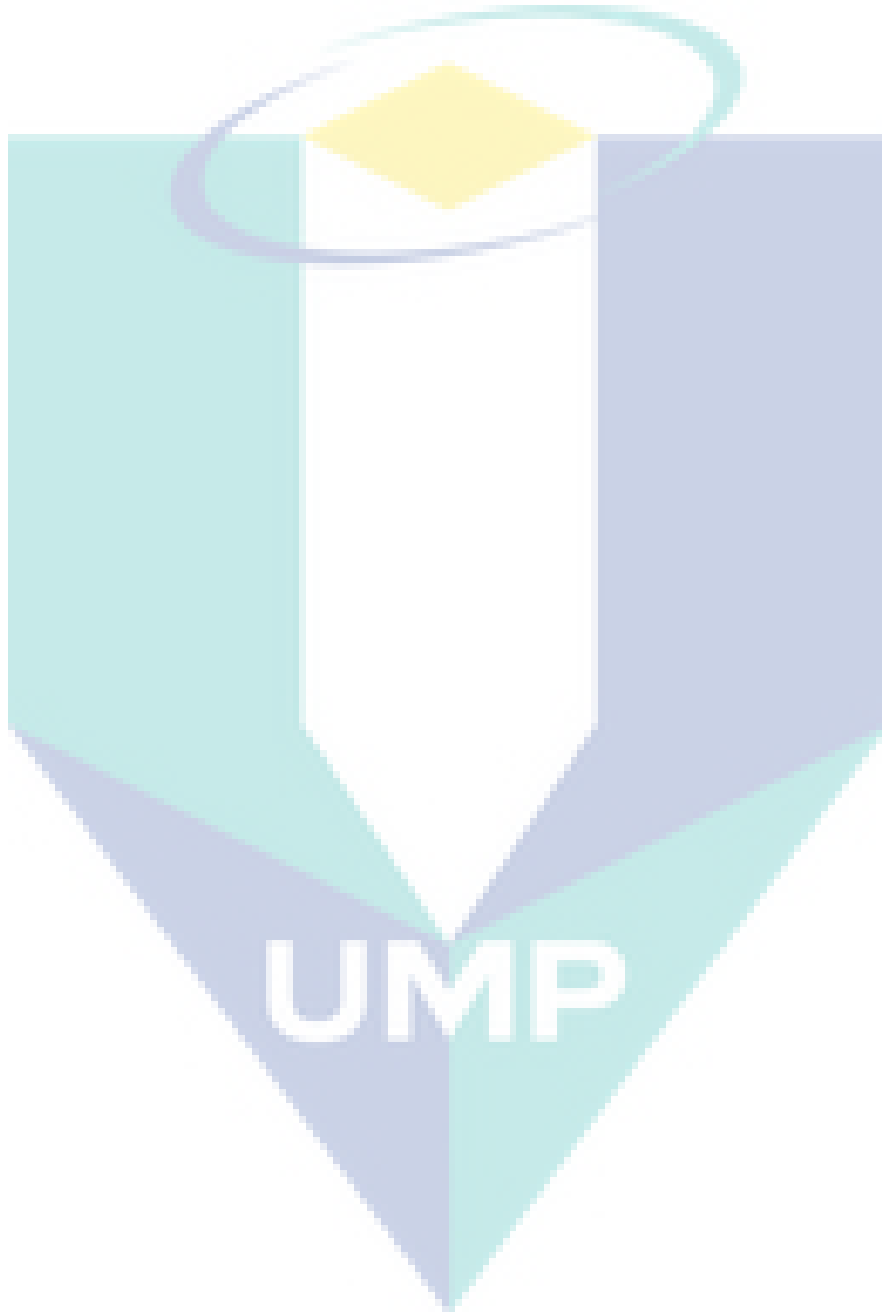
allowed to collide the sample. The electrons interact with atoms in the sample, generating a variety of signals that contains the information about the sample's surface topography. These detected signals will produce an image that corresponds to the surface of the sample. There are three type of signals provide the greatest information in SEM analysis, namely secondary electrons, backscattered electrons and X-rays. Often, secondary electrons were selected in the analysis, as the signal generated able to produce a high resolution image from the small diameter of primary electron beam.

To further strength the analysis, SEM was often combined with EDX for elementary analysis. During analysis, primary electron beam was allowed to strike on the sample surface. These electrons will interact with the atoms in the samples, inducing the shell transitions phenomenon that results in the emission of an X-ray. This emitted X-ray has an energy level that symptomized to its parent element. Hence, detection and measurement of the energy permits elemental analysis. EDX provides quantitative and qualitative information on elemental composition of the sample, with a sampling depth of 1-2 microns. An EDS mapping can be generated, showing the elemental distribution in a sample surface.

2.11 Conclusion Remarks

As a conclusion, POME waste contains of high amount of organics judging from the high COD and BOD level. The conventional treatment employed in Malaysia is open ponding system, which required long HTR and large land area. Besides, more often than not, the POME discharge from the final pond (settling pond) fails to meet the discharge standard in Malaysia. In order to avoid POME pollution, Malaysia's Department of Environmental has made it a mandatory for palm oil millers to reduce the POME's BOD standard to 100 ppm threshold, and further revised down to 20 ppm recently in some places. It would be a great challenge for millers to accomplish this standard due to ineffectiveness of ponding system in treating low concentration POME. Significantly, there were a lot of new technologies proposed, which seem to be promising way to further purifying POME. However, these technologies are neither cheap nor easy to control. In current study, heterogeneous photocatalysis over a semiconductor photocatalyst is proposed as the new technology for tertiary POME treatment. Past reseaches had proven on the effectiveness of photocatalysis on degrading the organic compounds. Particularly, TiO_2 and ZnO seem to be the potential photocatalysts for current study due to high

efficiency in degrading various organic compounds. Besides, it is also found that renewable energy is able to be produced as a side products from the photodegradation of organic compounds. With the assistance of CCD, the optimized conditions can be determined, which can further increase the efficiency of photocatalysis towards POME treatment. Hence, heterogeneous photocatalysis is very potential in POME treatment.



CHAPTER 3

MATERIALS AND METHODS

3.1 Introduction

In this chapter, details on the preparations and characterization of both POME waste and photocatalysts is presented. The characterization techniques for POME waste characterizations include chemical oxygen demand (COD), biochemical oxygen demand (BOD), total suspended solid (TSS), pH, oil and grease analysis (O&G), Fourier transform infrared spectroscopy (FTIR), and Carbon-13 nuclear magnetic resonance ($^{13}\text{CNMR}$). For photocatalysts, the characterization techniques include X-ray diffraction (XRD), field emission scanning electron microscopy (FESEM), N_2 physisorption analysis and UV-Vis diffuse reflectance spectroscopy (DRS). The operational procedures of the characterization techniques are also included in this chapter. For post reaction analysis, some selected photocatalysts were analysed by using field emission scanning electron microscopy (FESEM), N_2 physisorption analysis, Fourier transform infrared spectroscopy (FTIR) and scanning electron microscopy with X-ray microanalysis (SEM-EDX). In addition, all the post reaction POME samples were subjected to COD and pH analysis, and some of the selected post reaction POME samples were characterized using COD, BOD, O&G and $^{13}\text{CNMR}$. In addition, the decolourization efficiency of the selected POME samples were also determined

3.2 Overview of Methodology

The flowchart in Figure 3.1 is the flow of the work for entire phototreatment of POME.

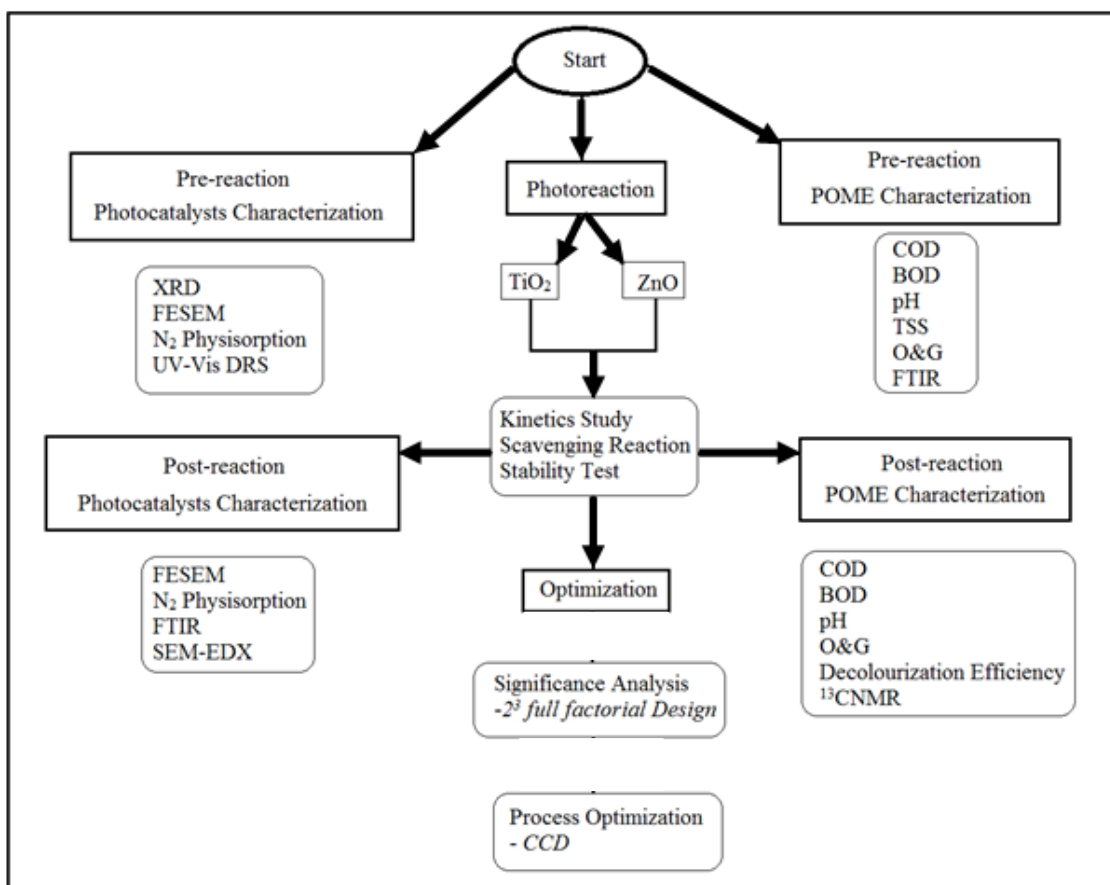


Figure 3.1 A Schematic diagram of FESEM

3.3 Chemicals and Gases

The chemicals and gases needed in this study are listed in the Table 3.1. Other than the distilled water, all the chemicals listed in Table 3.1 were sourced from Sigma-Aldrich while the gases were from Linde. The distilled water was available from laboratory of Universiti Malaysia Pahang (UMP).

Table 3.1 List of chemicals and gases

Chemical	Purity	Application
TiO ₂ , ZnO	100%	Photocatalysts
Air	> 99.99%	N ₂ physisorption analysis, GC
He	> 99.99%	N ₂ physisorption analysis, GC
O ₂	>99.99%	Photoreaction
N ₂	>99.99%	Photoreaction
High range COD reagent	-	Results analysis

3.4 POME Wastewater

This section presented about the sampling process and preservation of POME waste, followed by the methods to characterize it.

3.4.1 POME Sampling and Preservation

The final effluent from an open pond that belongs to a local palm oil mill based in Jalan Tun Razak, Kuantan, Malaysia, was collected as a substrate for the current investigation in the afternoon. The temperature of the effluent was measured on-the-spot, using thermometer and recorded. During sampling process, POME was stored in a black, air-tight container to avoid light exposure. Besides, the container was filled up to the brim to avoid reaeration. Immediately, the POME sample was filtered to remove any suspended solids and stored at 277 K for preservation, until use, by using refrigerator.

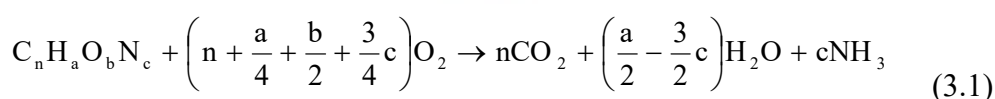
3.4.2 Pre-reaction POME Characterization

The following 7 technique were employed to characterize POME, viz chemical oxygen demand (COD), biochemical oxygen demand (BOD), total suspended solid (TSS), pH, oil and grease analysis (O&G) and Fourier transform infrared spectroscopy (FTIR).

3.4.2.1 Chemical Oxygen Demand (COD)

Chemical oxygen demand (COD) is used as a measure of oxygen requirement of a sample that is susceptible to oxidation by strong chemical oxidant (Clair et al., 2003). It is a standard method used to measure the amount of organic compounds in wastewater.

The basis for the COD test is to fully oxidize all organic compounds to carbon dioxide with a strong oxidizing agent under acidic conditions. The amount of oxygen required oxidizing an organic compound to CO₂, NH₃, and H₂O is given by Equation (3.1).



For the current study, the model of COD reactor used was a *Hach DRB-200 COD* Reactor. Before the COD test, the withdrawn POME samples would undergo centrifugal

separation to separate the catalyst from the sample. In addition, an oxidation vial was also prepared. Oxidation vial is a light-sensitive liquid and must be closed in box if it is unused.

2.0 ml of the prepared POME sample was pipetted into the oxidation vial. Concurrently, a blank vial was prepared by pipetting clean water into the vial. The purpose of blank vial was as the datum. These vials were inverted several times before and post-mixing to ensure the bottom sediment transformed into suspension; hence the well mixing. The vials with sample would become very hot upon mixing due to the oxidation. The mixture in the vials was in brownish yellow colour. If COD concentration has far exceeded the stated range of 0-1500 ppm, the resulting mixture would show a green colour formation. Consequently, false readings would be obtained. The vial was placed in the DRB200 reactor followed by heating to 423 K and maintained at the stipulated temperature for 2 h. Subsequently, the vial was gently transferred into a rack for convective cooling to room temperature. During the transfer, any shaking of the vial was avoided as the resuspension of sediment in the vial would disturb the COD reading. After cooling, the exterior wall of the vials was thoroughly cleaned and the samples were ready to be analysed.

The blank vial is placed into the cell holder and 'zero' button was pressed after the lid was closed. This is the baseline for the following sample analysis. After zeroing process, blank vial was removed and sample vial was placed into the cell holder. For sample analysis, 'start' button was pressed for COD reading of the sample. The instrument reads the barcode and reads the sample. All the readings were in mg/L COD and the measurement of same sample was repeated thrice to ensure accuracy.

3.4.2.2 Biochemical Oxygen Demand (BOD)

Biochemical oxygen demand (BOD) is a measure of amount of dissolved oxygen consumed by aerobic biological organisms in the wastewater to break down organic compounds over a specific time and temperature. Often, the BOD value is expressed as mg of dissolved O₂ consumed per litre of sample for 5 days of incubation at 293 K. It is another common indicator for organic wastewater. Similar with COD, BOD can be used to measure the amount of organics present in the wastewater judging from the oxygen consumed. However, it is more specific as only biologically active organic matter was

considered in the measurement, while COD measures compounds that can be chemically oxidized.

For BOD measurement, dilution water was prepared by mixing 1 mL of phosphate buffer, magnesium sulphate ($MgSO_4$), calcium chloride ($CaCl_2$), ferric chloride ($FeCl_3$) solution and diluted to 1000 mL by distilled water. Then, 10 mL of POME sample was diluted with 300 mL by using dilution water. The pH of diluted POME was adjusted to the range of 6.5 to 7.5 before transferring into an incubation bottle. The dissolved oxygen (DO) concentration for POME sample was analysed using a dissolved oxygen meter before sealing the incubation bottle. Finally, the incubation bottle was placed in a BOD incubator (temperature = 298 K) for five days before the final DO value was taken. BOD level can be calculated according to the Equation 3.2.

$$BOD \text{ (ppm)} = (D_1 - D_2) / P \quad (3.2)$$

where D_1 and D_2 are the initial and final DO values of POME sample, and P denotes for the decimal volumetric fraction of sample used.

3.4.2.3 pH Value

The pH value of POME was measured using pH indicator strips, sourced from Merck

3.4.2.4 Total Suspended Solid (TSS)

Total suspended solid (TSS) is another common water quality parameter to assess the quality of treated wastewater. It measures the turbidity of wastewater. Suspended solids are classified as important pollutants as pathogens might be carried on the surface of the particles.

For the current study, the TSS of POME was determined using vacuum filtration through a 47 mm nylon membrane with a pore size of 0.45 μm . Before filtering through the membrane, POME sample was shaken in the original container to re-suspend the sediments. Subsequently, 100 mL of POME sample was filtered through the membrane, which has been washed and dried to a constant weight. Finally the membrane was dried again at 323 K until a constant weight obtained. The weight difference of the membrane was determined and TSS was expressed in mg/L.

3.4.2.5 Oil and Grease Analysis (O&G)

Oil and grease analysis is a measurement of oil content in the water body. One of the most common used methods for oil and grease analysis is hexane extractable gravimetric method (HEM). The fundamental of this technique is to extract the oil content in the wastewater by using hexane, followed by evaporation of hexane at low temperature, leaving the extracted oil as residue. Figure 3.2 illustrates the set up for solvent evaporation after oil extraction.

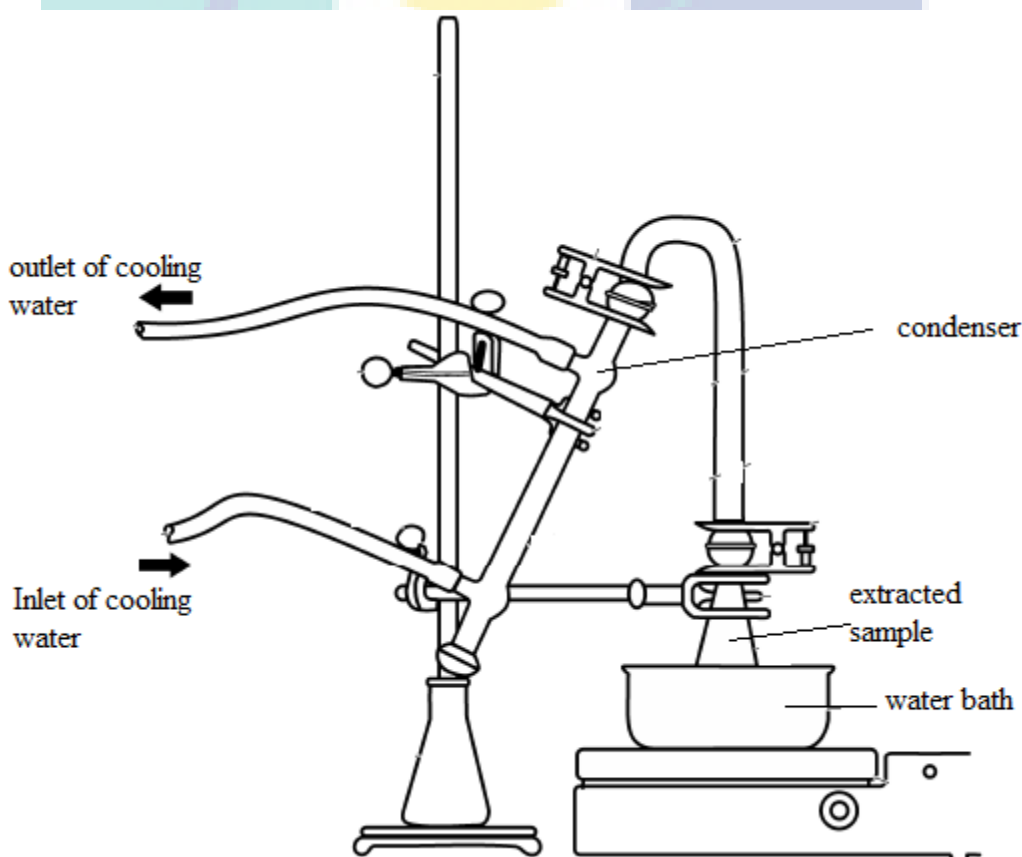


Figure 3.2 Set up for evaporation of n-hexane solvent

For current study, mixture of 350 mL of POME waste and 20 mL of n-hexane was shaken vigorously in a funnel for the extraction of the oil content in POME waste. Prior to extraction process, the pH value of POME was adjusted to 2 or lesser for hydrolysis of oils and grease and prevent the interference from sodium sulphate which was used in later step. Next, the funnel was clamped vertically for 10 min to allow the separation of the water layer and solvent layer and subsequently remove water layer by draining into a volumetric flask. Multiple extractions (3 times) were conducted on the water layer to ensure complete extraction of oil content. After extraction process, the

solvent layer drained into a pre-weighed boiling flask through a funnel that contains filter paper and 10 g of anhydrous sodium sulphate (NaSO₄). The purpose of NaSO₄ is to absorb the water content in the solvent layer. Contamination of NaSO₄ must be avoided by re-filtering the solvent through a filter paper. Subsequently, the evaporation of n-hexane was conducted at 343 K. The process is completed when the hexane is completely removed. The boiling flask is now weighed again and the weight difference before and after was recorded. Usually, the oil and grease content was expressed in mg/L of HEM.

3.4.2.6 Fourier Transform Infrared Spectroscopy (FTIR)

10.0 ml of filtered POME was also air-dried, to preserve the original components, until the formation of dry crystal. Subsequently, the POME crystal was subjected to Fourier Transform Infrared (FTIR) using ATR mode on Perkin Elmer Spectrum 100 (U.S.) instrument for the determination of its functional groups. The range of wavenumber employed was from 4000 to 1000 cm⁻¹ with 32 scans at a resolution of 4 cm⁻¹.

3.4.3 Post-reaction POME analysis

After reaction, the selected POME samples were subjected to post reaction analysis to further support the discussion. The analysis for post-reaction POME samples include COD, BOD, O&G, pH, decolourization efficiency and Carbon-13 nuclear magnetic resonance (¹³CNMR)

3.4.3.1 Chemical Oxygen Demand (COD)

The operational procedure and parameters were fully described in Section 3.4.2.1.

3.4.3.2 Biochemical Oxygen Demand (BOD)

Post-reaction BOD of samples was analysed with the steps presented in Section 3.4.2.2

3.4.3.3 pH Value

The pH value of POME was measured using pH indicator strips, sourced from Merck

3.4.3.4 Oil and Grease (O&G)

The O&G level of POME was determined by the method described in Section 3.4.2.5.

3.4.3.5 Decolourization Efficiency

The light adsorption of the POME sample was determined by using UV-Vis Absorption Spectroscopy. 3.0 mL of POME sample was pipetted into a quartz cuvette that subsequently placed in the cuvette socket of Hitachi U-1800 spectrophotometer machine. The adsorption peak at 254 nm for each sample was recorded and the decolourization efficiency was computed using Equation 3.3, whereby “Abs” represents the absorption peak of the sample at a wavelength of 254 nm, while t and i denote for time t and initial value.

$$\text{Decolourization (\%)} = \left(1 - \frac{\text{Abs}_t}{\text{Abs}_i}\right) \times 100\% \quad (3.3)$$

3.4.3.6 Carbon-13 Nuclear Magnetic Resonance (¹³CNMR)

¹³CNMR analysis of post-reaction POME sample was conducted by using Bruker Av II-400 cm⁻¹ spectrometer to determine the type of carbon presented in the sample. The chemical shifts were stated in term of ppm and the detected peaks were identified with the assistance of Bruker Topspin Software 2016.

3.5 Photocatalysts Preparation and Characterizations

Current section is presenting on the photocatalysts preparation and the techniques to characterize them.

3.5.1 Photocatalysts Preparation

TiO₂ powder and ZnO powder were directly procured from Sigma-Aldrich and undergo calcination process of 473 K for 3 h to remove the volatiles and impurities on the surface.

3.5.2 Photocatalysts Characterization

Photocatalysts were characterized by using X-ray Diffraction (XRD), Field Emission Scanning Electron Microscopy (FESEM), N₂ physisorption and UV-Vis Diffuse Reflectance Spectroscopy (DRS) as pre-reaction characterization. After photoreaction, the selected spent photocatalysts were subjected to field emission scanning electron microscopy (FESEM), N₂ physisorption analysis, Fourier transform infrared spectroscopy (FTIR) and scanning electron microscopy with X-ray microanalysis (SEM-EDX).

3.5.2.1 X-Ray Diffraction (XRD)

XRD analysis was conducted at room temperature using Rigaku MiniFlex II at Bragg angle of $2\theta = 3 - 80^\circ$, with the scan step of 0.02° . The analysis was conducted at 30kV and 15mA using Cu-K α emission and a nicker filter. At the same time, the mean crystal size would be determined by using Equation 2.3.

3.5.2.2 Field Emission Scanning Electron Microscopy (FESEM)

Surface morphology of photocatalysts were observed by using FESEM provided by JEOL JSM-5410LV machine from Japan. The samples were sputtered by spray/dip-coated (Pt) to see the morphology of photocatalysts. The images of 10k, 35k, 55k and 100k of magnification power were taken for TiO₂ photocatalyst, while 10k, 30k and 50k of magnified images were taken for ZnO photocatalyst.

3.5.2.3 N₂ Physisorption Analysis

The adsorption and desorption isotherms of each photocatalysts were obtained by using equipment Micromeritics ASAP 2020. Prior to the analysis, the samples were degassed for 24 h in 473 K under vacuum to ensure the absence of the impurities. The surface area of the monolayer coverage was determined by using BET method (Equation 2.10).

3.5.2.4 UV-Vis Diffuse Reflectance Spectroscopy (DRS)

The adsorption properties of TiO₂ and ZnO were determined by using Shimadzu UV 2600 UV-Vis spectrophotometer with the wavelength ranged from 200 – 900 nm.

Furthermore, the band gap energy of the photocatalyst can also be determined by plotting Tauc's plot according to Equation 2.12. The band gap energy can be obtained by extending the gradient of the graph to x-axis.

3.5.3 Post-reaction Photocatalysts Analysis

The selected spent photocatalysts were subjected to field emission scanning electron microscopy (FESEM), N₂ physisorption analysis, Fourier transform infrared spectroscopy (FTIR) and scanning electron microscopy with X-ray microanalysis (SEM-EDX).

3.5.3.1 Field Emission Scanning Electron Microscopy (FESEM)

FESEM images of spent photocatalysts were captured by using the same method employed for pre-reaction analysis. Details of the method were presented in Section 3.5.2.2.

3.5.3.2 N₂ Physisorption Analysis

Similar with pre-reaction analysis, the isotherms were obtained by using Micromeritics ASAP 2020 machine. However, the degassing temperature was maintained at room temperature to preserve the deposited species on the surface of photocatalysts. The duration of degassing process is 24 h.

3.5.3.3 Fourier Transform Infrared Spectroscopy (FTIR)

For current study, FTIR analysis for selected photocatalysts was carried out using Perkin Elmer Spectrum 100 (U.S.) by using ATR method to investigate the functional groups observed on photocatalyst's surface. The range of wavenumber used for analysis in current project is 4000 to 1000 cm⁻¹ with 32 scans at the resolution of 4 cm⁻¹. Spent catalyst was filtered by using vacuum filtration and gently draped with smooth clean tissue to dry it, followed by analysis using ATR-FTIR. By using ATR, the spent catalyst was readily scanned without having the need to pre-treat it.

3.5.3.4 Scanning Electron Microscopy with X-Ray Microanalysis (SEM-EDX)

Elemental analysis and distribution of spent photocatalyst was observed by using SEM-EDX conducted by Hitachi TM3030Plus machine. The accelerating voltage employed during the analysis was 20 kV.

3.6 Photocatalytic Degradation of POME

The steps of photoreaction and the results analysis are presented in current section.

3.6.1 Photoreaction

The setup for the photoreactor is illustrated in Figure 3.3. The photocatalytic degradation of POME under the UV light was carried out in an air-tight photoreactor system. The whole photoreactor system was meticulously-covered with aluminum foil to minimize energy loss, and stored under dark environment to prevent external stray light from interfering with the experiment. A 500 mL Pyrex quartz reactor was used for the photoreaction of POME. A few set of preliminary works with photocatalyst loading of 0.5g/L were conducted for 240min of UV irradiation to determine the suitable O₂ flowrate and stirring speed. The results obtained were carry forward to subsequent experiments.

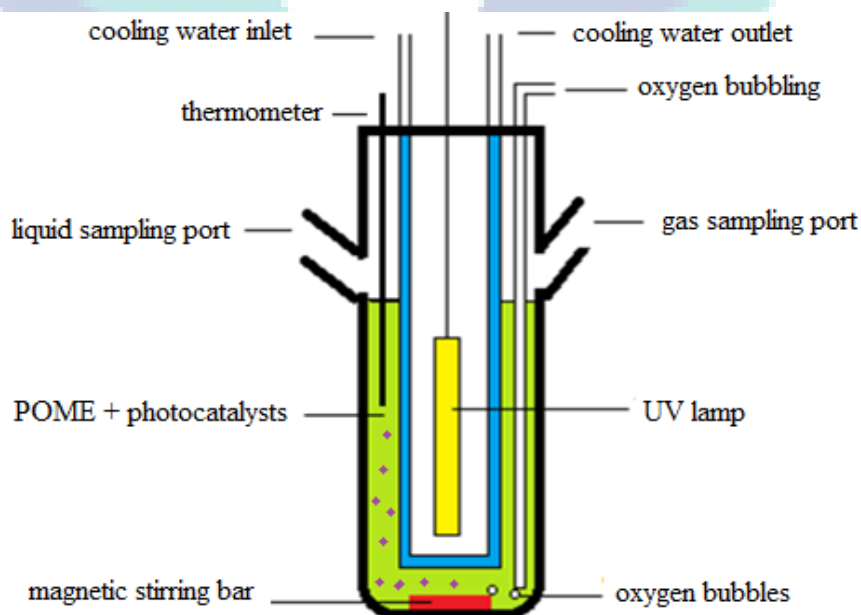


Figure 3.3 The schematic diagram of photoreaction set up

Prior to photoreaction, POME sample and photoreactor were autoclaved at 333 K by using equipment provided by Hitachi to eliminate the mesophiles inside the sample. During the reaction, 450 mL of pre-treated POME was mixed with pre-determined photocatalyst loading, and stirred vigorously (r.p.m carried forward from preliminary work) for 30 min. At the same time, zero-grade O₂ gas (flowrate carried forward from preliminary work) was metered into the reactor to provide O₂ blanket and to establish equilibrium point of dissolved O₂ in the POME wastewater. The cooling water compartment that jackets the UV light source was continuously circulated with water to remove dissipated heat from the UV lamp. This would ensure that the reaction slurry was always maintained at the room temperature. The temperature of the reaction is monitored digitally. Subsequently, a 100 watt low pressure mercury UV lamp (intensity peaked at 365nm), with an intensity averaging 11.0 W/m², measured by using photometer, was switched on, to initiate the photoreaction. For sampling purpose, 3 ml of aliquot was withdrawn from the reactor at every 60 min interval for COD, decolourization and pH measurement using Hach DRB-200 COD instrument, Hitachi U-1800 spectrophotometer and pH indicator strips, respectively. After the experiment, the BOD and O&G values of the final POME sample were determined for the comparisons purpose. At the same time, during the reaction, the gas sample was collected every 30 min intervals for first 2 h and every 60 min intervals for the subsequent hours by using sampling bags. These collected gas samples were then eluted by gas chromatography (GC).

Recyclability, scavenging and longevity study followed the similar outline of the photoreaction, with some modifications made. For recyclability study, the same photocatalyst was recovered by using filtering process and subjected to 3 consecutive photoreactions, while for scavenging study, different scavengers, viz Na₂CO₃, NaI and N₂ gas, would be added into the photoreactor prior to the reaction. Lastly, for longevity study, the reaction time would be extended to 22h from 4h in the normal photoreaction.

3.6.2 Sample Analysis

The parameters for liquid analysis for current study are COD, BOD, pH, decolourization efficiency and O&G. The procedures these parameters were pre-described in Section 3.3.

On the other hand, gas products collected by aluminium foil sample bags were analysed by using gas chromatography (GC). GC is a technique that measures the content of various components in a sample based on differences in partitioning behavior in the column. The sample injected into the equipment was carried by a moving gas stream through a column packed with a finely divided solid that might be coated with film of liquid. It is one of the most important tools in the analytical chemistry industry for species detection in the gas mixture due to high simplicity, sensitivity, and effectiveness.

For current study, the GC instrument provided by Agilent company (model: GC-Agilent 6890 N series) was used for gaseous product analysis. This GC equipment comes with two packed bed columns, viz. Supelco Molecular Sieve 13x (10 ft × 1/8 in OD × 2mm ID, 60/80 mesh, SS) and Agilent HayeSep DB (30 ft × 1/8 in OD × 2 mm ID, 100/120 mesh, SS). The carrier gas used was He gas with the flow rate of 20 ml/min. Oven and detector were operated at 393 and 423 K, respectively. Before analysis, 25 µL of sample was pushed into the sample loop from the sampling bag and press ‘start’ button on the control panel of GC equipment to initiate the analysis. Full separation of the gas components will take 20 min and the results in chromatogram with peaks indicate the gas species with different intensity providing information on the quantitative information. Figure 3.4 depicts the typical chromatogram obtained from the standard gas for calibration process. This standard gas contains of 10% of H₂, 0.1% of CH₄, CO₂ and CO. The content of gas samples can be determined by using Equation 3.4, where X_i denotes for the composition of i species in the gas sample, A_{sample} and A_{standard} denote for area of the peak for sample and standard gas respectively and $X_{i,\text{standard}}$ represents the concentration of i species in standard gas. The retention time, A_{standard} and $X_{i,\text{standard}}$ for each species were summarized in Table 3.2.

$$X_i = (A_{\text{sample}} / A_{\text{standard}}) * X_{i,\text{standard}} \quad (3.4)$$

Table 3.2 Retention time A_{standard} and $X_{i,\text{standard}}$ for each speices

Gas component	Retention time (min)	$X_{i,\text{standard}}$ (%)	A_{standard}
H ₂	5.42	10	18.13
CH ₄	7.2	0.1	66.29
CO ₂	10	0.1	138.64
CO	12.3	0.1	98.58

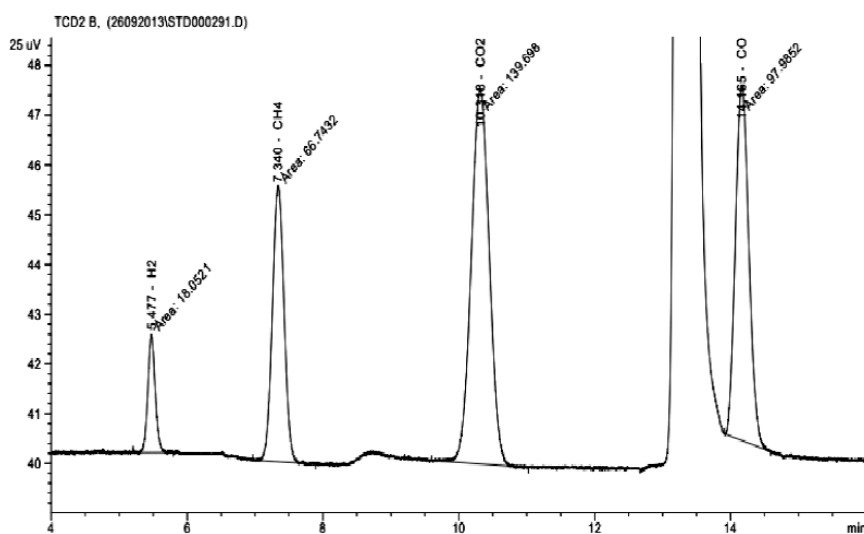


Figure 3.4 Gas chromatogram obtained for standard gas

3.7 Optimization of the Process

The optimization in current study was separated into two parts, significance analysis of factors and optimization of factors, and conducted by using Response Surface Methodology (RSM) in Design Expert 6.0.7. The potential factors in current study are O₂ flowrate, photocatalyst loadings and initial concentration of POME. Both UV/TiO₂ and UV/ZnO systems were subjected to optimization process to further enhance the degradation achieved. Prior to optimization process, the factors mentioned undergo screening process by using 2-level factorial to determine the significance of each factor. The ranges employed for O₂ flowrate, photocatalyst loadings and initial concentration of POME in the screening process are 0 – 150 mL/min, 0 - 1.5 g/L and 100 – 400 ppm, respectively, which adopted from preliminary results (O₂ flowrate and photocatalyst loading) and the original condition for ponding-treated POME waste. Subsequently, the significant factors were optimized by using central composite design model. The ranges for O₂ flowrate and photocatalyst loadings were adopted from the mechanistic study conducted (Section 4.5 for TiO₂ system; Section 5.3 for ZnO system), while the concentration of POME retained as above (100 – 400 ppm).

CHAPTER 4

PHOTOCATALYTIC TREATMENT OF POME WASTEWATER OVER UV/TiO₂ SYSTEM

4.1 Introduction

Briefly, the outline of this chapter is as follows:

- Section 4.2 presents the POME characterization. POME waste was measured for the pH, COD, BOD, suspended solid, O&G and temperature using various techniques. In addition, FTIR was also employed to obtain the functional groups of organic compounds present in POME waste.
- Section 4.3 is about characterizing the physicochemical properties of the TiO₂ photocatalysts via several well-established techniques, viz. X-ray diffraction (XRD), N₂ physisorption analysis, UV-Vis diffuse reflectance spectroscopy (DRS) and field emission scanning electron microscopy (FESEM).
- Sections 4.4 and 4.5 present the results obtained from the photocatalytic degradation of POME over UV/TiO₂ system. This encompasses the parametric study, kinetics and mechanistic determinations, as well as recyclability and longevity test. From the experimental works, the correlations between the photocatalytic activity and the physicochemical properties were determined and the degradation mechanism was also proposed based on the results obtained.
- Section 4.6 presents the post reaction analysis for used TiO₂ photocatalyst and also post-reaction POME waste. Used TiO₂ photocatalyst from recyclability test was collected and studied using FESEM imaging, N₂-physisorption, FTIR and EDX mapping to further support the discussion. At the same time, some

selected post-reaction POME samples were characterized by BOD, COD, O&G and ^{13}C MNR.

- Section 4.7 discusses on the process optimization of the system. Prior to optimization, the potential factors, i.e., O_2 flowrate, TiO_2 loading and initial concentration of POME waste were subjected to significance study using a 2^3 -full factorial design. Subsequently, the significant factors were subjected to the process optimization using CCD in RSM.

The last section, Section 4.8 correlates between BOD and COD of POME waste after the photocatalytic degradation process over UV/ TiO_2 system.

4.2 Characterization of POME Wastewater

In order to characterize POME waste from the last pond (settling pond) to determine whether it meets the standard discharge limit, POME samplings from the same pond were carried out and analysed, subsequently compared with the POME discharge standard required by *Department of Environment (DoE)*, as well as Malaysia Sewage and Industrial Effluent Discharge Standard (only COD). The results obtained are tabulated in Table 4.1. In Table 4.1, the pH, suspended solid and temperature of the collected POME effluent are well controlled within the required standard. However, there are some parameters of the effluent that fail to fulfill the requirements. In particular, both the BOD and COD readings, at the range of 111.6 – 250 ppm and 170 – 400 ppm, respectively, have exceeded the standard (100 and 50 ppm, respectively). Besides, the oil and grease (O&G) content in the effluent was also higher than standard, further indicating the inefficiency of open ponding system, which is consistent with past research (Wang et al., 2010). Significantly, the inconsistency observed in these parameters also indicated the difficulties in controlling the existing ponding system.

Table 4.1 Characteristics of ponding-treated POME

Parameter*	POME Discharge standard (DoE)	POME sample
pH	5-9	7.5
BOD	100 ppm; 20 ppm in Sabah and Sarawak	111.6 – 250 ppm
COD**	50 ppm	170 – 400 ppm
Total Suspended solid (TSS)	400 ppm	288 – 336 ppm
Oil and Grease (O&G)	50 ppm	101 – 163 ppm
Temperature (°C)	45	30

Furthermore, POME was also air-dried under room temperature to preserve the raw POME until it turned into powder. This POME powder was subsequently subjected to FTIR scanning and the resulting spectrum is shown in Figure 4.1. Referring to Figure 4.1, broad and weak peak observed at the range of 3800 to 2400 cm^{-1} is symptomatic of O-H stretching from the moisture content in the powder. In addition, nitrogenous organic compounds, nitriles group ($\text{C}\equiv\text{N}$) and aliphatic amines group ($\text{C}-\text{N}$) are also found in the POME sample, judging from the small absorption peak observed at 2250 cm^{-1} and 1050 cm^{-1} (Federal University of Minas Gerais, 2013; Central Connecticut State University, 2001). The characteristic peak from stretching of carbonyl group ($\text{C}=\text{O}$) that appears at 1650 cm^{-1} is an indicative of the carbonyl group's presence in POME (WebSpectra, 2000). However, the peak as can be seen in the figure is slightly overlapped by the peak of O-H bending peak observed at 1419 cm^{-1} (Central Connecticut State University, 2001). During anaerobic digestion in open ponding system, organic compounds tend to be fermented to volatile fatty acids comprised of mainly acetic, propionic and butyric acids in the acidogenic phase (Mumtaz et al., 2008). Hence, the sharp peak observed at 1419 cm^{-1} could be possibly attributed to the presence of these carboxylic acids.

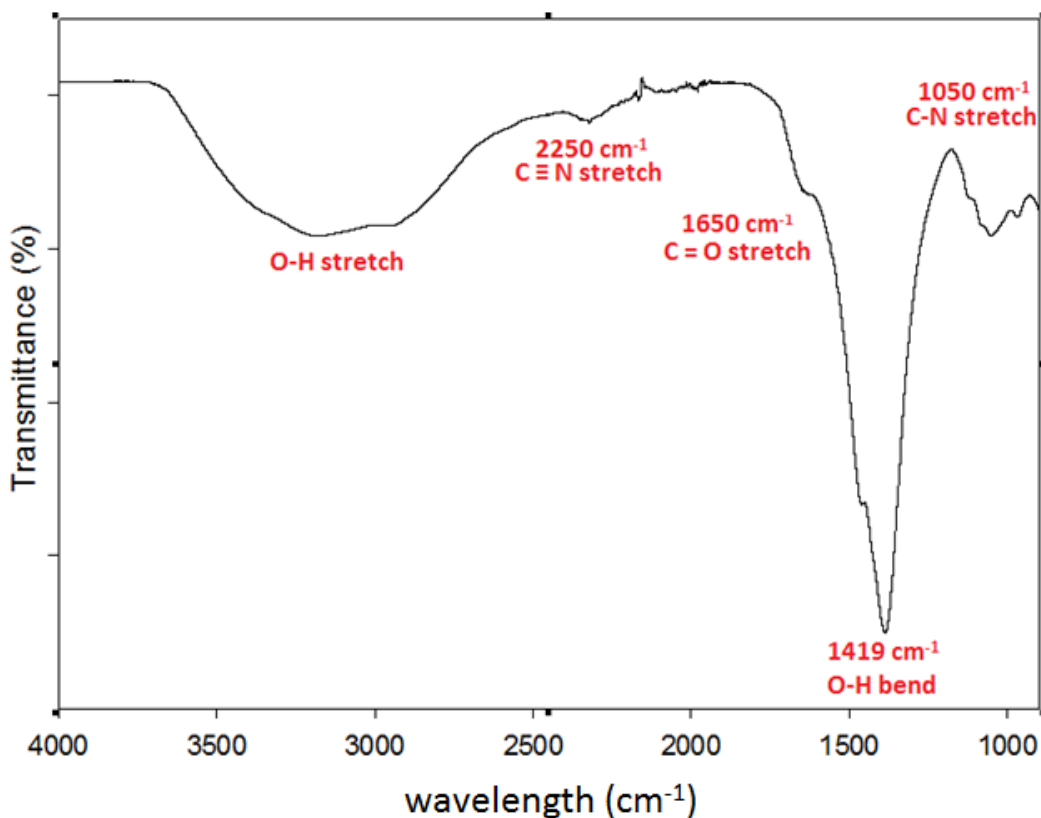


Figure 4.1 FTIR spectrum of ponding-treated POME

4.3 Characterization of TiO₂ Photocatalyst

Commercial TiO₂ which was procured from Sigma-Aldrich was subjected to the XRD measurement without any pre-treatment and the diffractogram obtained is presented in Figure 4.2. Based on Figure 4.2, the peaks recorded at 2θ readings of 25.5°, 37.2°, 38.0°, 38.8°, 48.2°, 54.0°, 55.0°, 62.0°, 70.0° and 76.0° have indicated that anatase was indeed the predominant crystalline phase. All the peaks were sharp which was indicative of good crystallinity of the solid sample. Poor crystallinity in the photocatalyst will promote the recombination of electron and hole, causing low photocatalytic performance as defects of crystal in solid will act as a trapping and recombination centre (Kudo and Miseki, 2009). Hence, high crystallinity observed in the photocatalyst of current study was actually favouring the photocatalytic degradation process. The highest peak was observed at 2θ reading of 25.5°, with crystal phase of (1,0,1). Based on this highest peak, the crystallite size was estimated as 45.7 nm.

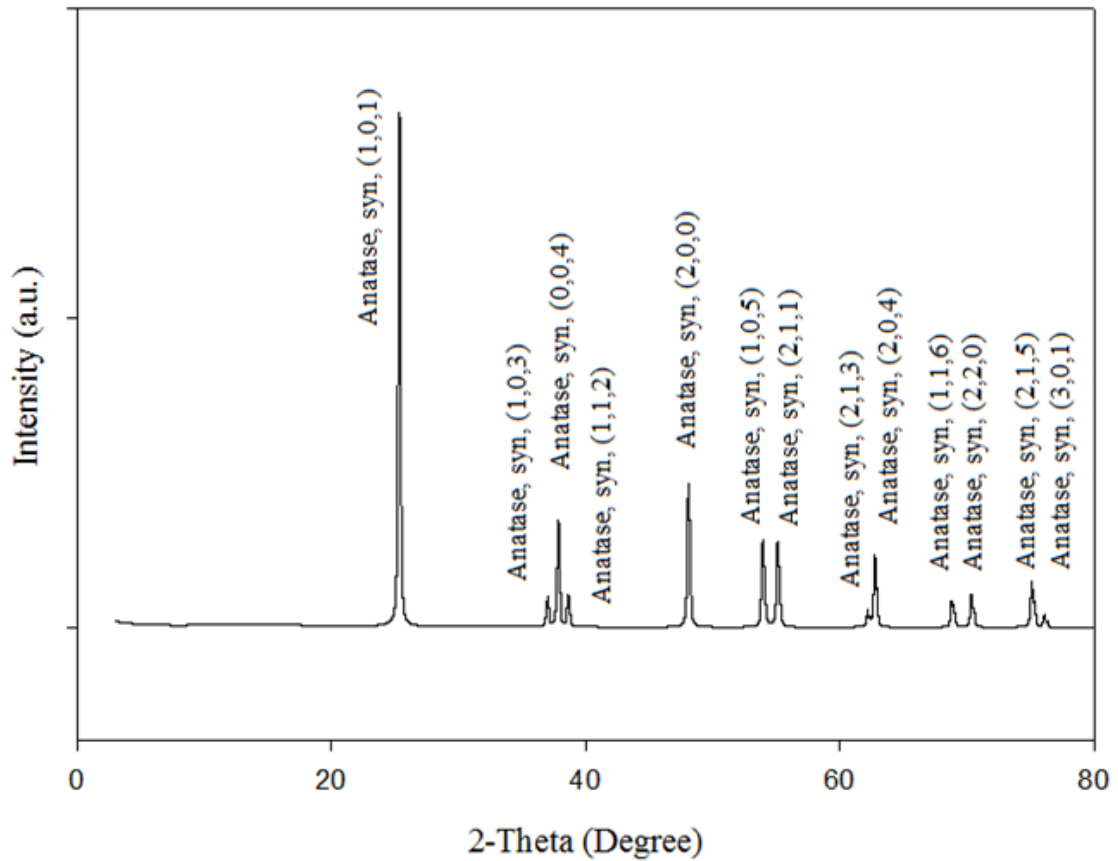


Figure 4.2 XRD diffractogram of TiO₂

On the other hand, the surface morphology of TiO₂ was observed via different magnification powers. Image of spherical particles of TiO₂ with smooth surface was observed through the FESEM images presented in Figure 4.3. The non-uniformity of the particle sizes was observed too, judging by the different particle sizes estimated. Besides, the particle size estimated was ranging from 70 – 100 nm.

In addition, Figure 4.4 shows the isotherm of TiO₂ obtained from N₂ physisorption. This obtained isotherm can be classified as a type-V isotherm according to the IUPAC identification system, which indicates the mesoporous structure material (2-50 nm). Indeed, the estimation using *Barrett-Joyner-Halenda (BJH)* equation gave an average TiO₂ pore diameter of 22.0 nm. Besides, the N₂ physisorption also reveals that the virgin TiO₂ has a considerably low BET specific surface area (11.34 m²/g) by employing Equation 2.10.

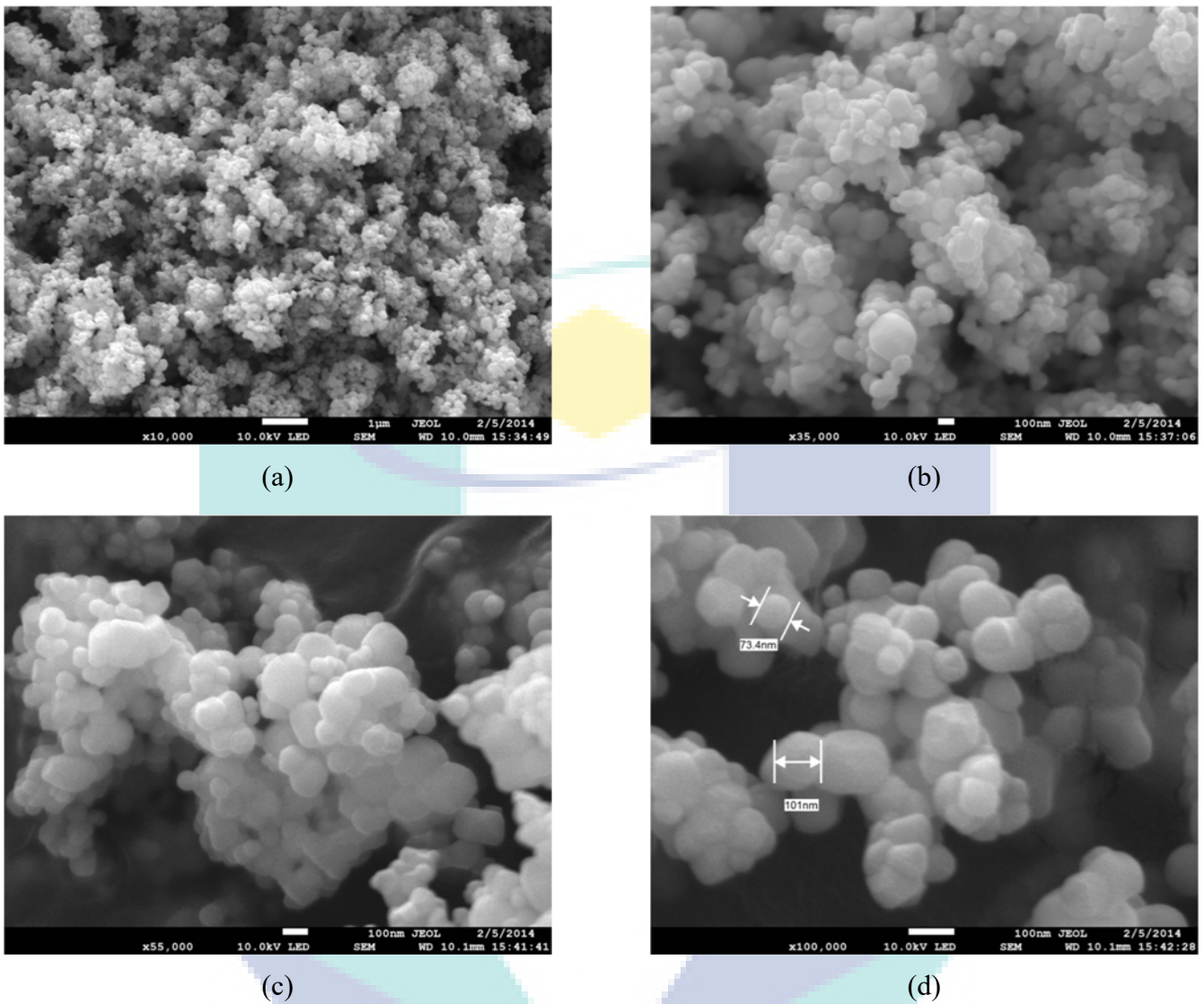


Figure 4.3 FESEM images of TiO₂ photocatalyst (a) 10 kx (b) 35 kx (c) 55 kx (d) 100 kx

For the optical property characterization, Figure 4.5 shows the diffuse reflective UV-vis spectrum of TiO₂. The results obtained demonstrated excellent light energy spectrum absorption at $\lambda < 350$ nm (UV region), whilst in the visible light region, the absorption value has plummeted. This observation reaffirms the UV-photosorption ability of TiO₂ material. Subsequently, the band gap energy of TiO₂ photocatalyst was estimated by plotting $(ah\nu)^{1/2}$ versus band gap energy $(h\nu)$ (Figure 4.6) using Kubelka-Munk functions (cf. Equation 2.12). As shown in Figure 4.6 (red dotted line), the band gap energy of TiO₂ was 3.15 eV, which is in accordance with the findings of past works (3.15 ~ 3.27 eV) (Valencia et al., 2010).

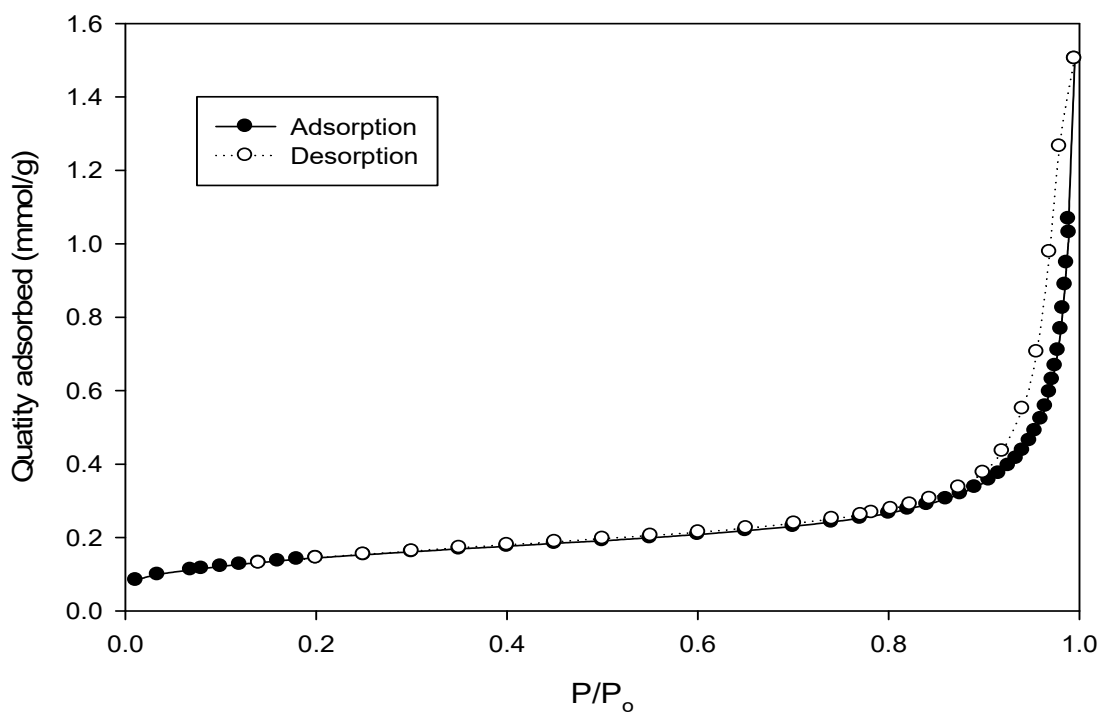


Figure 4.4 Isotherm of TiO₂ obtained from N₂ physisorption

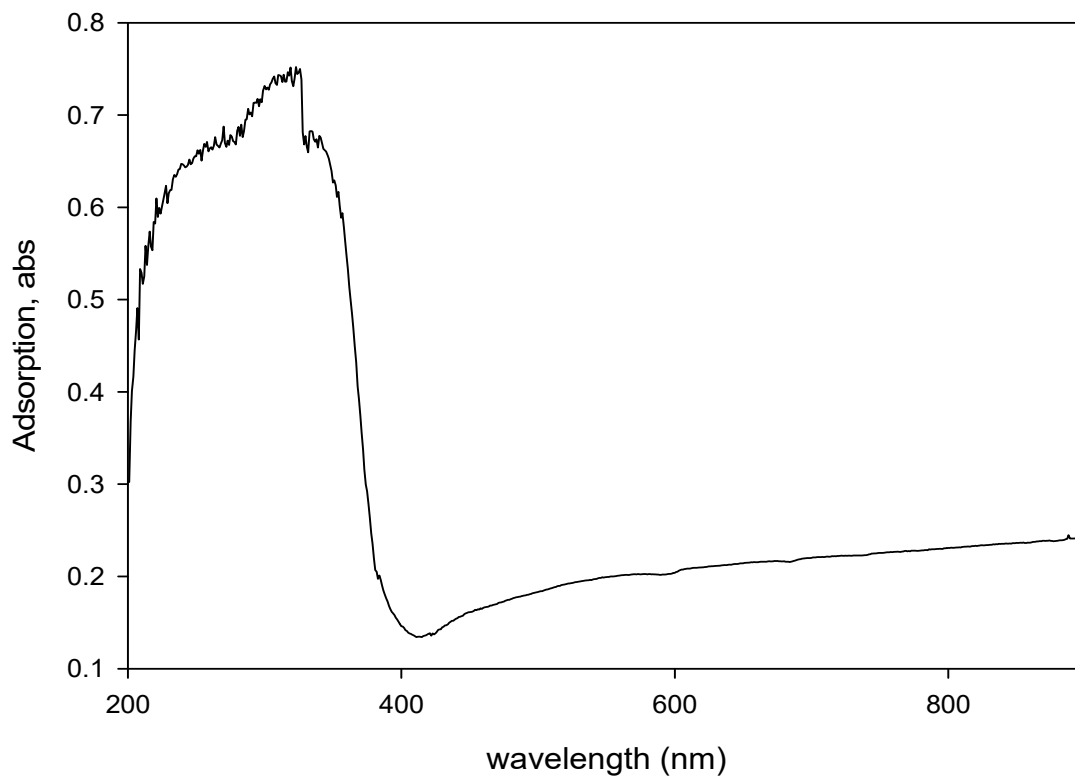


Figure 4.5 Diffuse reflectance UV-Vis spectra of the TiO₂

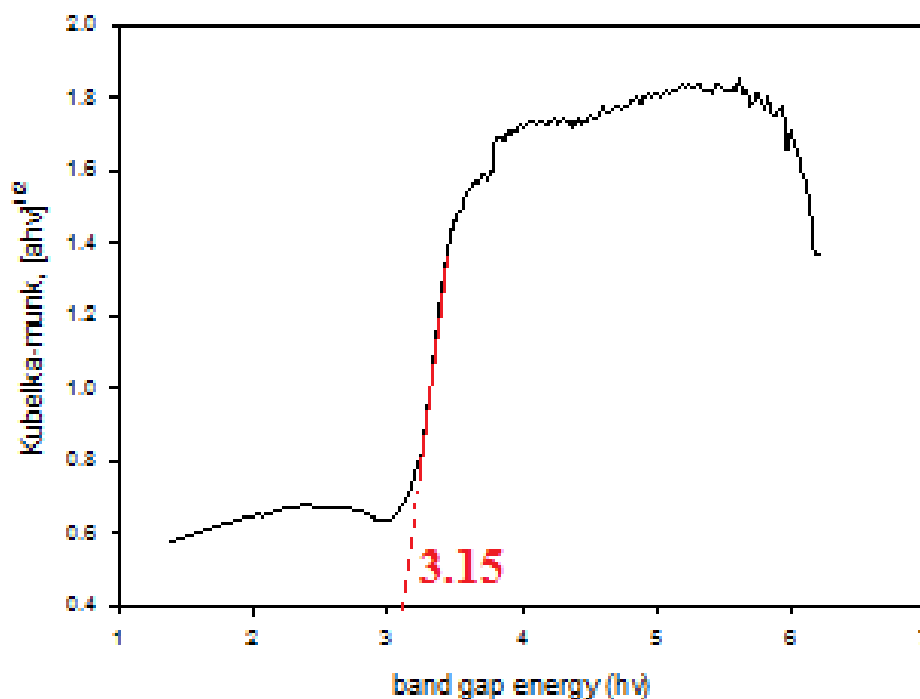


Figure 4.6 Plot of Kubelka-Munk function versus energy of light for TiO₂

Lastly, the density of TiO₂ photocatalyst was also determined by using gas pycnometer instrument. Based on the results, the average density obtained for TiO₂ photocatalyst was 4.1075 g/cm³ after three measurements.

4.4 Preliminary Works

A few sets of preliminary experiments were conducted to determine the suitable stirring speed and O₂ bubbling rate for the upcoming experiments. At the same time, blank runs were also conducted to serve as the background study.

4.4.1 Effects of Stirring Speed

The minimum COD level of POME sample is 170 ppm (cf. Table 4.1) Hence, for the current section, the COD level of POME was well-controlled within the similar range (155 to 170 ppm), through dilution. The effects of stirring speed were determined by conducting a few set of photoreactions with 0.5 g/L of TiO₂ and 60 mL/min of O₂ bubbling, but at different stirring speed. Figure 4.7 shows the results obtained after 240 min of UV irradiation.

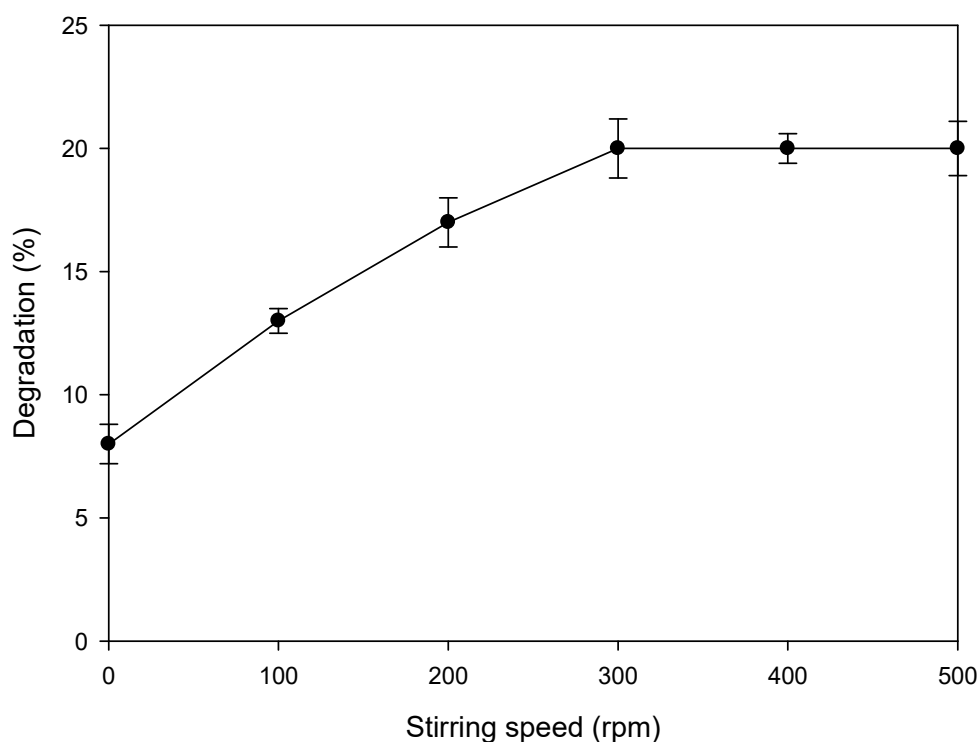


Figure 4.7 Degradation profile obtained for different stirring speed

The degradation profile presented in Figure 4.7 exhibited an increasing trend with the stirring speed. In the absence of stirring, the degradation obtained was around 8.0% and increased to around 20.0 % with stirring speed of 300 rpm. Increasing the stirring speed will increase the chances of collisions between the substrates and reactive species. Furthermore, the external mass transfer limitation can also be avoided with high stirring speed, which further increase the degradation achieved. At this point (300 rpm), the external mass transfer limitation was overcome, judging from the constant degradation achieved after 300 rpm.

On the other hand, the smooth surfaces of photocatalysts (proven by FESEM) with hardly visible pore will reduce the effects of internal mass transfer limitation. In addition, the low viscosity of the POME solution is further diminishing the negative effects, making it insignificant during the degradation process. Hence, for subsequent experiments, the stirring speed was fixed at 400 rpm to ensure the degradation of POME was indeed kinetic region and free of mass transfer limitation.

4.4.2 Effects of O₂ Flowrate

A series of photoreactions were conducted employing 0.5 g/L of TiO₂ at room temperature, but at different O₂ flowrates. Figure 4.8 shows the degradation achieved at $t = 240$ min for different sets of photoreactions.

For the case of 0 ml/min O₂ flowrate, N₂ gas was initially purged into the photoreactor for 30 min followed by metering at 30 ml/min to provide N₂-blanket. It can be observed that only 4% of degradation was achieved after 240 min of UV irradiation. Significantly, an increasing trend was observed from 0 ml/min O₂ flowrate (N₂-blanket) to the highest degradation (circa 23.0%) at O₂ flowrate of 70 ml/min. Beyond that, the degradation efficiency actually decreased with the O₂ flowrate, i.e. at 150 ml/min, the degradation was noticeably lower at 16.0%.

The following outlined mechanisms describe the generation of hydroxyl radicals which can shed some light into the degradation trend (cf. Figure 4.8).

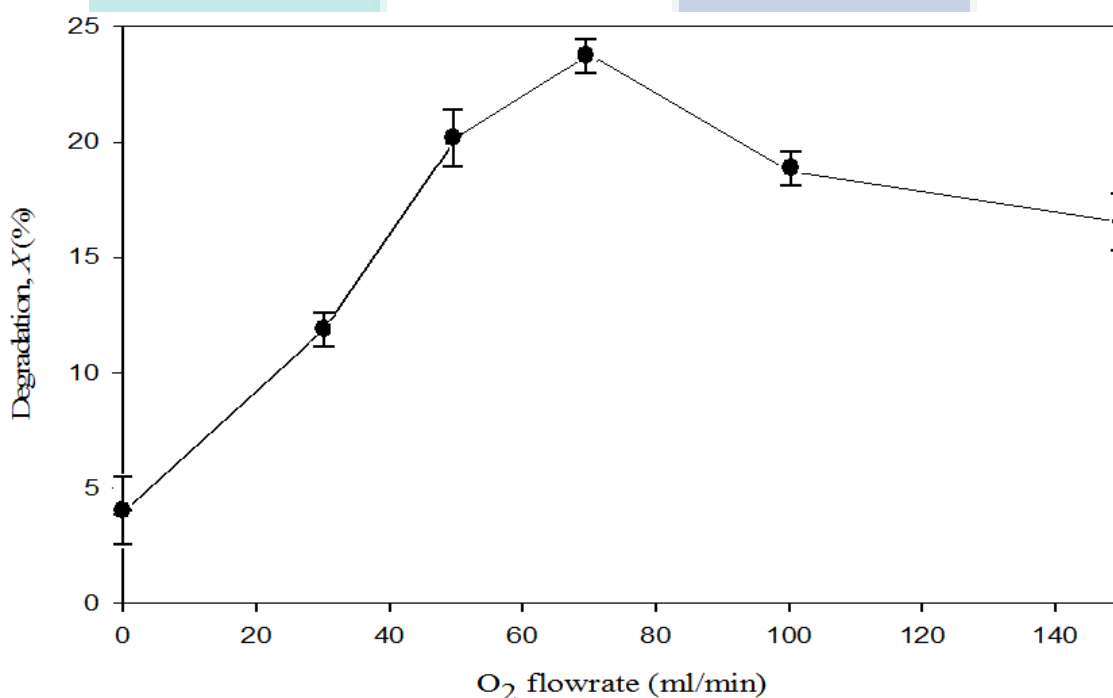
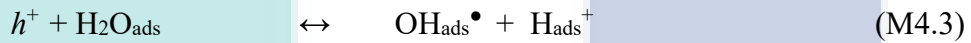
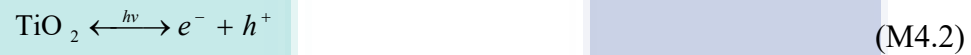


Figure 4.8 Degradation of POME after 240 min of UV irradiation with different O₂ flowrates. Reaction condition: 0.5 g/L TiO₂ at room temperature

Based on the concept of photocatalytic degradation, the H₂O and O₂ molecules have to be adsorbed on the surface of TiO₂ (M4.1). Upon photo-excitement, a negatively charged electron(e⁻) and positively charged hole(h⁺) are generated (cf. (M4.2)). The

generated hole (h^+) would attack on adsorbed H_2O , producing a pair of hydroxyl radical (OH_{ads}^\bullet) and proton (H^+) (refers to (M4.3)). The hydroxyl radicals are highly reactive and responsible for organic compounds degradation (Lazar and Daoud, 2013). This OH_{ads}^\bullet was then desorbed from the TiO_2 surface as a free hydroxyl radical (M4.4). On the other hand, the generated electron was accepted by adsorbed O_2 to form super-oxide anions, $O_{2,ads}^-$ (M4.4). Subsequently, the $O_{2,ads}^-$ ion would react with H_{ads}^+ (from (M4.5)) through (M4.6) and (M4.7). Hydrogen peroxide (H_2O_2) formed would further dissociate into OH_{ads}^\bullet (M4.8) upon exposure to the UV irradiation. These OH^\bullet radical generation steps are consistent with past researches (Dong et al., 2015; Lightcap et al., 2010; Makarova et al., 2000; Williams et al., 2008).



As aforementioned, when O_2 was practically absent as in the case of N_2 -blanket, a meagre POME degradation was recorded (cf. Figure 4.8) whilst in contrast, a significant increment in degradation was recorded when O_2 was metered into the system. Therefore, it can be surmised that the rate of hydroxyl radical generation via steps (M4.4) – (M4.7) was significantly faster than the steps (M4.3). Moreover, unlike N_2 , O_2 is an electron-acceptor that would hold the electron generated upon excitement of TiO_2 photocatalyst, preventing recombination of holes(h^+) and electrons(e^-); eventually this would have enhance the photo-degradability of POME. This likely explained the increase in degradation trend when O_2 flowrate was varied from 0 to 70 ml/min. However, beyond 70 ml/min, formation of large bubbles in the POME liquor may have induced boundary

layer effects. Due to this physical limitation, photocatalytic degradation of POME was affected. Therefore, the best O₂ flowrate for POME degradation in the current work was 70 ml/min and hence was employed thereafter for further POME degradation studies.

4.4.3 Control Reactions

In order to be certain that the POME degradation in the current work was primarily due to photocatalytic effect, two control reactions (adsorption study and photolysis) were conducted. For the adsorption study, the experiment was conducted with 0.5 g/L of TiO₂ and 70 mL/min of O₂ flowrate under dark environment, while for photolysis, the run was conducted in the absence of TiO₂ photocatalyst but 70 mL/min of O₂ under UV light irradiation. The results obtained depicted in the Figure 4.9.

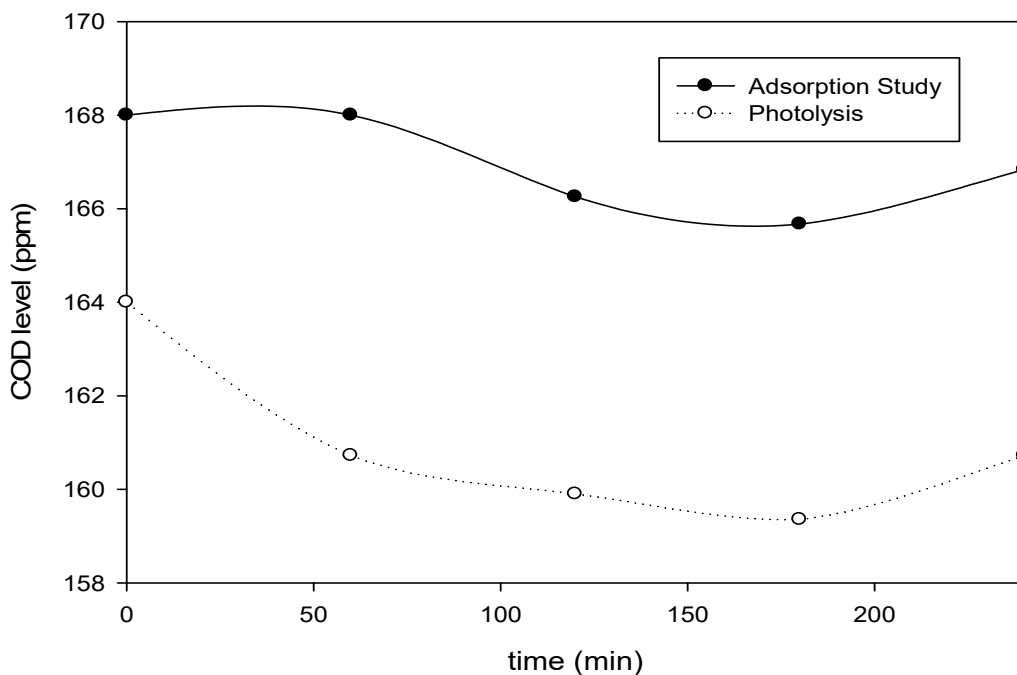


Figure 4.9 Degradation of adsorption study (with 0.5 g/L of TiO₂) and photolysis study employing O₂ flowrate of 70 mL/min

The results obtained shows that the COD level and eventually the degradation for this set were nearly invariant with time. This suggests that the adsorption process was practically negligible for the current type of photocatalyst. Significantly, this can be ascribed to the poor affinity of the TiO₂ photocatalyst towards organics compounds (Dong et al., 2015). Moreover, the considerably low BET specific surface area (11.34 m²

g^{-1}) as proven by N_2 physisorption has further limited the adsorption of organics onto the photocatalyst's surface.

For the photolysis experiment, after 240 min of UV irradiation, no significant degradation to the COD values ($< 2.0\%$) was observed. Significantly, GC analysis of the collected gas samples for both blank runs did not show any traces of biogas (mixture of CO_2 and CH_4). This only serves to confirm that neither adsorption nor photolysis processes occurred at significant rates to simultaneously degrade POME and yield any gas compounds.

4.5 Photocatalytic Degradation of POME

The photocatalytic degradation process of POME over TiO_2 was thoroughly discussed in the current section.

4.5.1 Effects of TiO_2 Loadings

Photoreaction runs were conducted with 70 ml/min of oxygen flowrate and presence of UV-light (100 W) but at different TiO_2 loading to determine the effects of varying TiO_2 photocatalyst loading, and also to identify the best TiO_2 loading. The results obtained are shown in Figure 4.10.

Significantly, in terms of degradation, compared to photolysis ($< 2.0\%$ degradation; presented in Figure 4.9), an obvious increment in COD degradation was recorded when TiO_2 was present. The results obtained demonstrated that more than 15.0% of organics in POME was degraded after 240 min of UV irradiation when 0.1 g/L of TiO_2 was employed. Furthermore, the highest POME degradation, 52.0%, was achieved by photoreaction over TiO_2 loading of 1.0 g/L. Generally, higher TiO_2 loading indicates higher organics degradation rate. Thus, an increasing trend of COD degradation rate was obtained from 0.1 to 1.0 g/L. However, beyond 1.0 g/L, the degradation efficiency reduced. This may be ascribed to the increase in TiO_2 loading that would have increased the solution opacity. Eventually, this has induced shielding effects that diminished the penetration of the light into the solution slurry. Hence, the photocatalytic degradation rate reduced to 48% and 41.18% for 1.5 g/L and 2.0 g/L of TiO_2 , respectively. Significantly, this confirmed that 1.0 g/L loading of TiO_2 was the best.

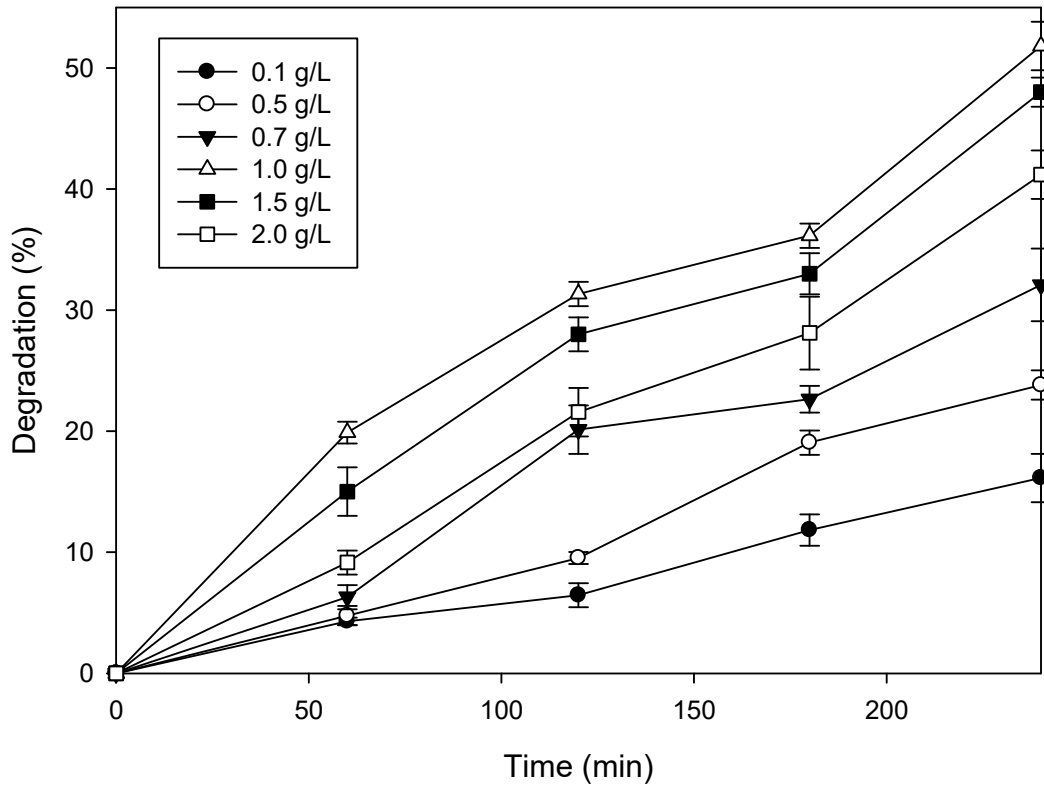


Figure 4.10 Transient COD level (ppm) and degradation (%) profiles for photoreactions at different TiO₂ loadings

By employing the method of initial rates (Fogler, 1999) to obtain the initial POME degradation rate $(-r_{COD}^o)$ via finite differentiation of transient COD profiles, Figure 4.11 was further plotted to show the effects of initial TiO₂ loading on $(-r_{COD}^o)$. It can be seen that the POME degradation rate peaked at TiO₂ loading of 1.0 g/L. Thereafter, the negative effects arising from TiO₂ particle shielding has largely overtaken the beneficial catalytic effects. The data in Figure 4.11 may be presented by the following empirical formula which fitted well with the experimental data ($R^2 = 0.97$).

$$-r_{COD} = \frac{k_{cat} W_{cat}^{2.6}}{S^{4.6} + W_{cat}^{4.6}} \quad (4.1)$$

where W_{cat} is TiO₂ loading (g/L), k_{cat} is the pseudo-rate constant for TiO₂ loading (1.0 ppm g²/ min L²), and S is the parameter for volumetric light shielding effect (1.052 g/L) with a correlation coefficient of 0.97.

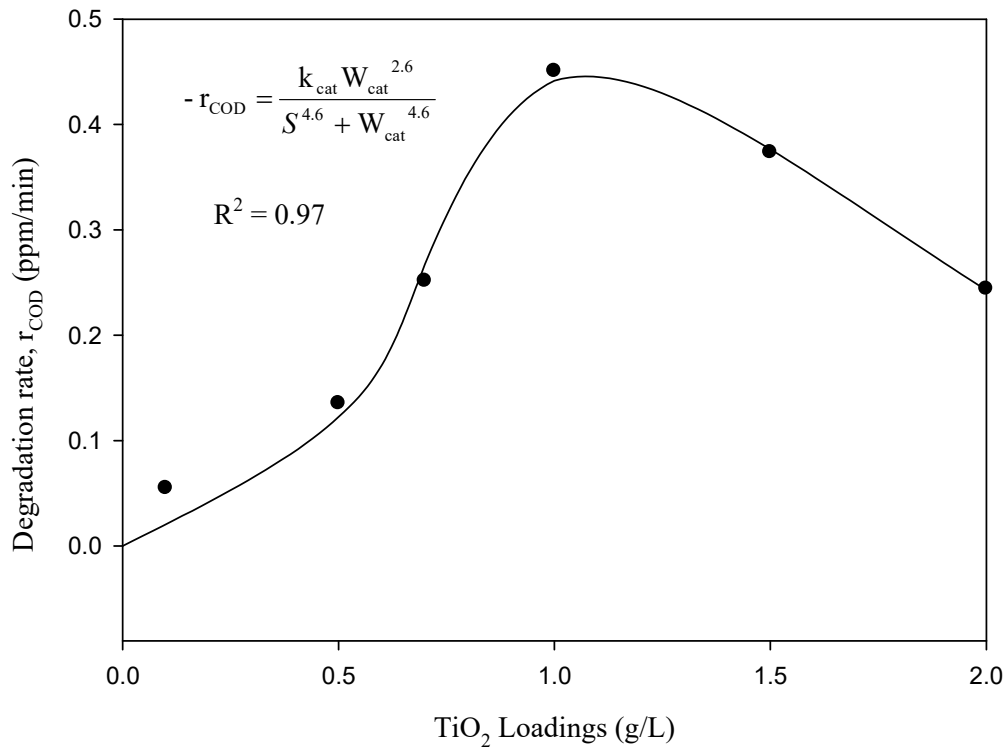


Figure 4.11 Influence of TiO₂ loadings on the degradation rate

4.5.2 Langmuir-Hinshelwood (LH) Rate Law Modeling

Next, Langmuir-Hinshelwood (LH) rate law model was employed to model the kinetics data (cf. Figure 4.10). For irreversible and surface limited reaction that occurs on single site, the reaction rate can be described by:

$$-r_{\text{COD}} = -\frac{dC_A}{dt} = \frac{kC_A}{1 + K_A C_A} \quad (4.2)$$

where $-r_{\text{COD}}$ = COD degradation rate (ppm min⁻¹).

The concentration of oxygen remained constant throughout the experiments as O₂ was continuously supplied to the reacting system. Due to the low concentration of organics in the sample, the denominator can further simplified into 1 ($1 \gg K_A C_A$). Ultimately, this was a reaction system that displayed first-order reaction kinetics.

$$-\frac{dC_A}{dt} = kC_A \quad (4.3)$$

By integrating both sides of Equation 4.3, the following expression was obtained:

$$\ln \frac{C_{AO}}{C_A} = kt \quad (4.4)$$

where C_{AO} = initial COD level of the sample (ppm)

C_A = COD level of the sample at time t (ppm)

k = apparent specific reaction rate (min^{-1})

t = time (min)

Figure 4.12 shows the resulting modelling exercise by employing Equation 4.4 derived above. In lieu of excellent linearity, it can be concluded that the decomposition of organics in POME indeed adhered to 1st order reaction.

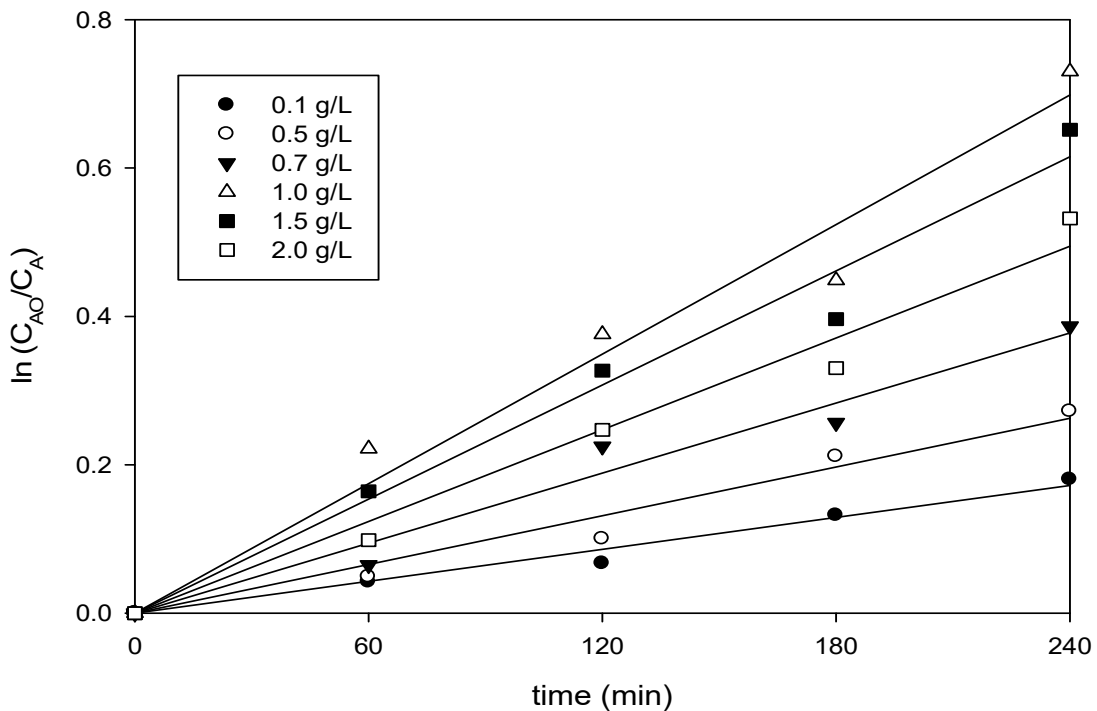


Figure 4.12 Illustration showing good adherence to 1st order kinetics modelling

In addition, the k -values can be obtained by determining the slope of each graph in Figure 4.12. The k -values of the photoreactions are summarized in Table 4.2. As can be seen in Table 4.2, k values that were sorted according to the highest to lowest ranking

were $2.90 \times 10^{-3} \text{ min}^{-1}$ (1.0 g/L TiO_2 loading) $>$ $(2.60 \times 10^{-3} \text{ min}^{-1})$ (1.5 g/L loading) $>$ $2.10 \times 10^{-3} \text{ min}^{-1}$ (2.0 g/L loading) $>$ $1.60 \times 10^{-3} \text{ min}^{-1}$ (0.7 g/L loading) $>$ $1.10 \times 10^{-3} \text{ min}^{-1}$ (0.5 g/L loading) $>$ 0.1 g/L ($0.70 \times 10^{-3} \text{ min}^{-1}$). Interestingly, this trend is also consistent with the profiles in Figures 4.8 and 4.9.

Table 4.2 k -values obtained from the photoreactions on POME with different TiO_2 loadings

TiO₂ loading (g/L)	(k) × 10³ (min)⁻¹	R²
0.1	0.7	0.98
0.5	1.1	0.97
0.7	1.6	0.97
1	2.9	0.97
1.5	2.6	0.98
2	2.1	0.98

Statistical analysis was subsequently carried out to justify the adequacy of the model developed. Figure 4.13 shows the parity plot that suggests a good agreement with R^2 value of 0.98 between the predicted and actual $\ln(C_{AO}/C_A)$ values. Furthermore, the residual data plotted in Figure 4.14 indicates no obvious pattern (random pattern) was observed, indicating that the developed model was statistically sound (Montgomery, 1997).

On the other hand, the decolourization rate and the pH value of the sample were also monitored throughout the experiment and the results obtained are depicted in Figure 4.15. By observing into Figure 4.15, POME sample did not decolourize in the absence of UV irradiation (adsorption study). However, in photolysis process, about 50% of decolourization achieved after 240 min of UV irradiation. In the presence of TiO_2 photocatalyst, the decolourization rate was enhanced to more than 90% for all sets of experiments, despite 0.1 g/L of TiO_2 exhibited a lower decolourization rate at the initial stage. This shows that photocatalysis is very effective in decomposing the refractory components in POME waste. In opposite trend to the decolourization trend, pH value of all the samples remained unchanged at 7.5 throughout the experiments.

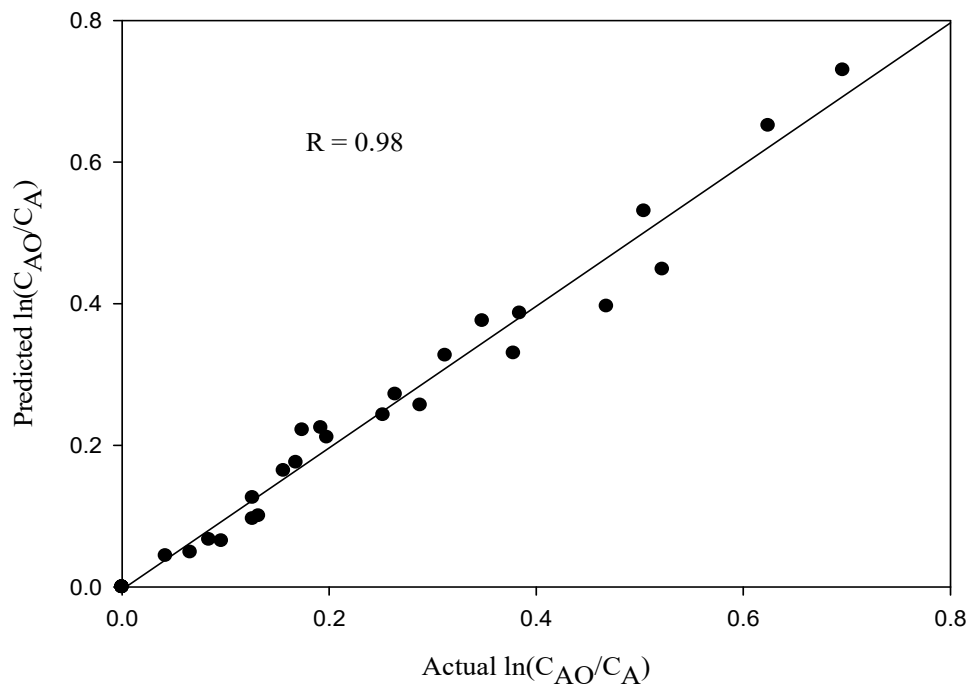


Figure 4.13 Comparison between predicted and actual $\ln(C_{AO}/C_A)$ values

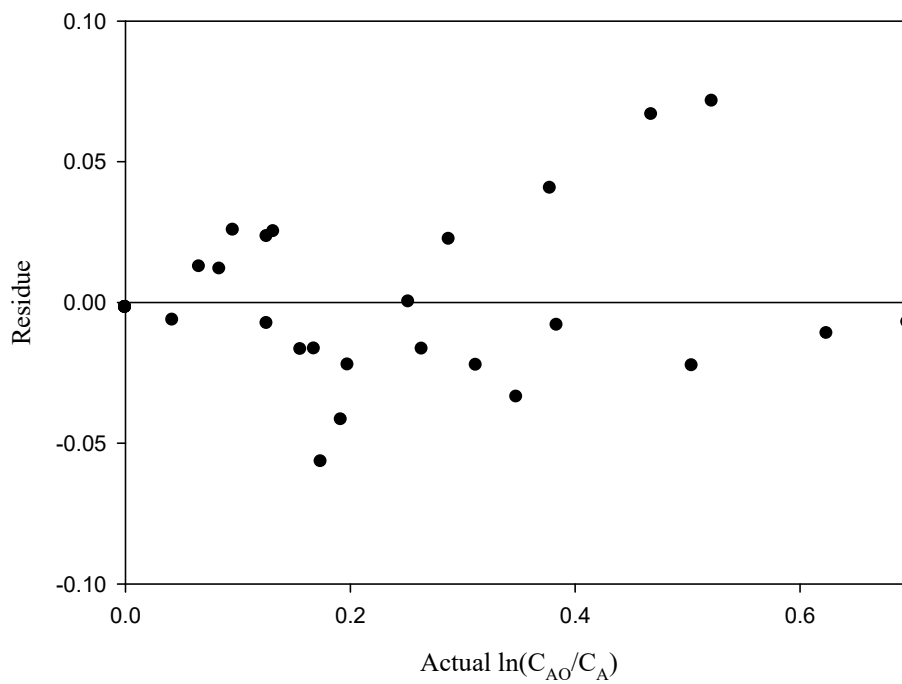


Figure 4.14 Residual plot for POME degradation

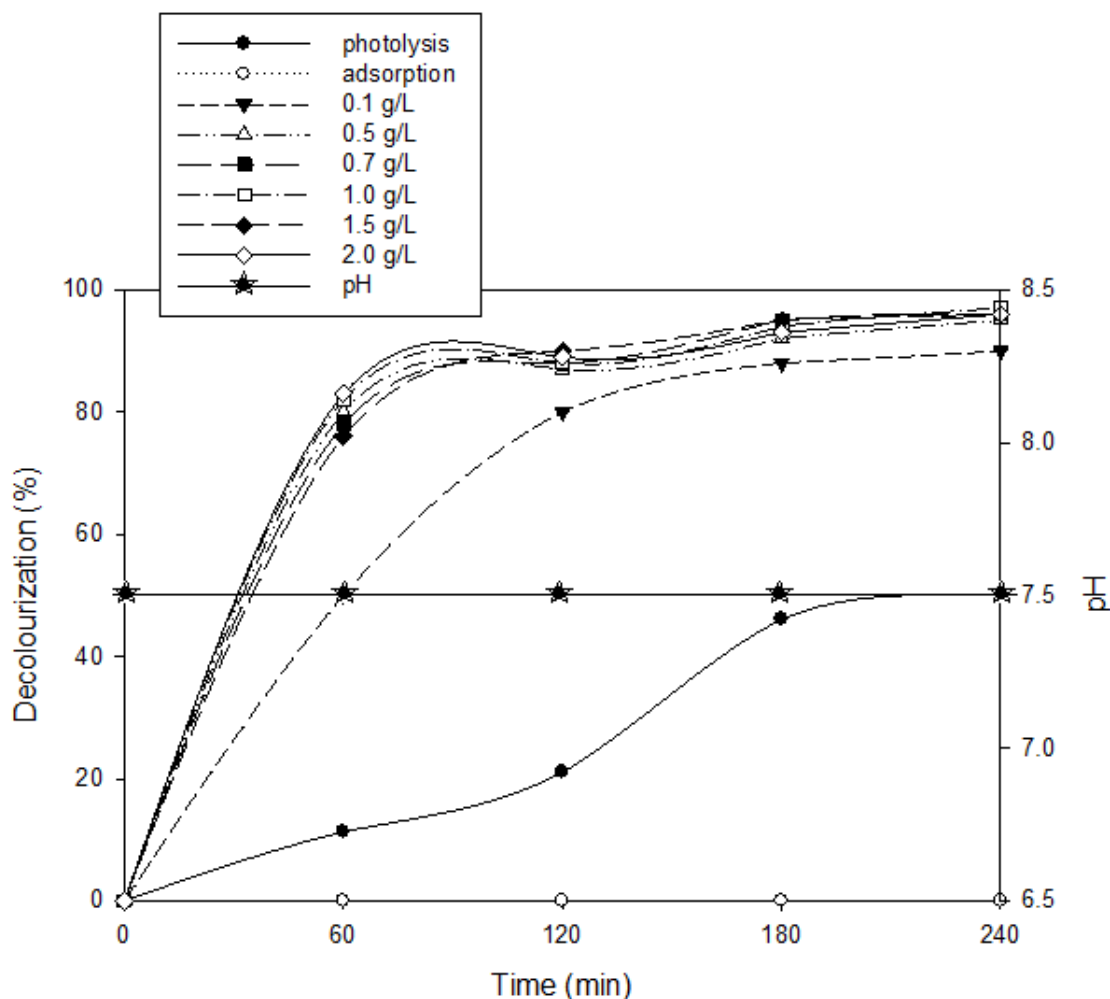
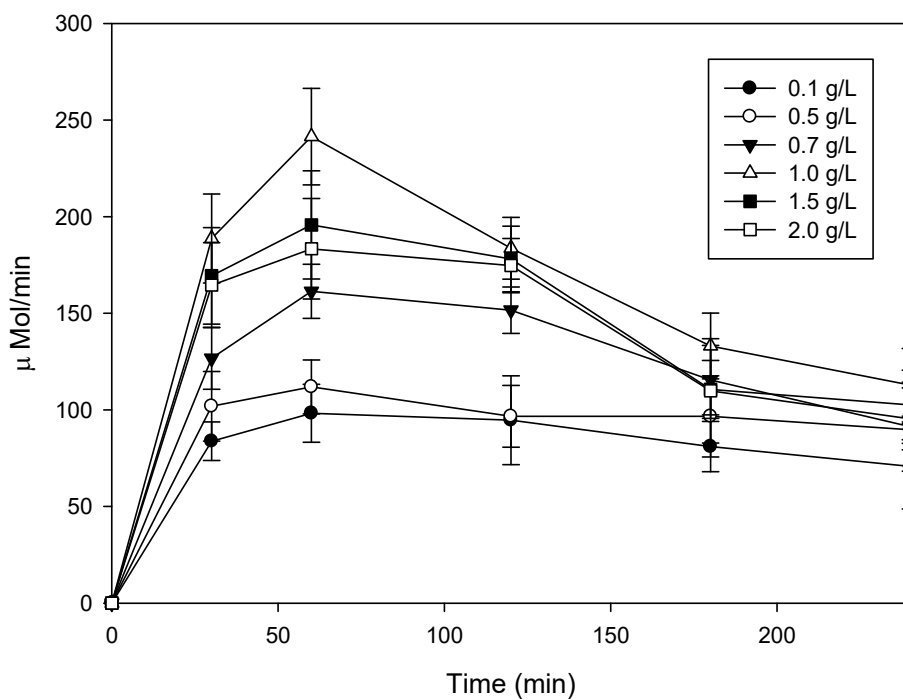


Figure 4.15 pH and decolourization profiles for all the photoreactions

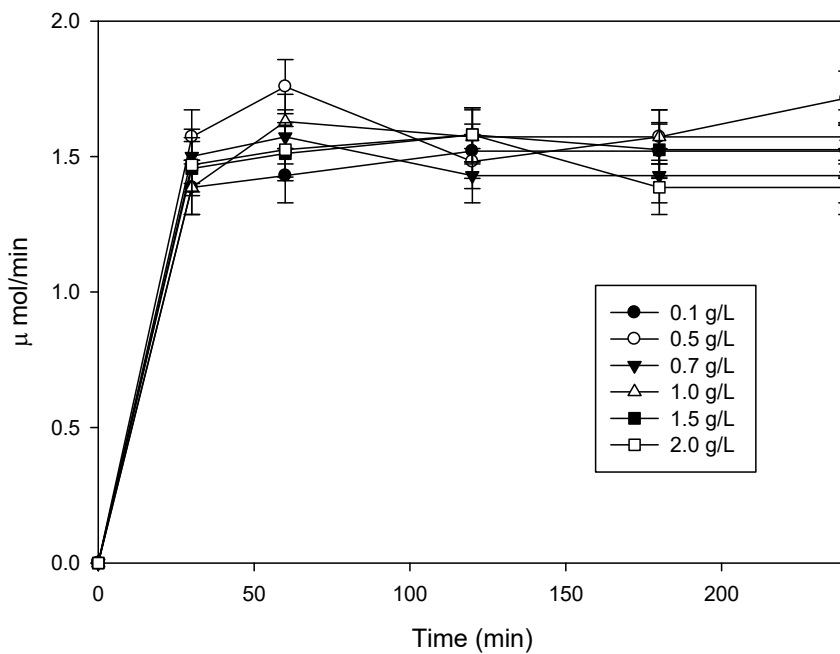
4.5.3 Gaseous Products from the POME Degradation

In terms of the assessment of gaseous products that was collected during the POME irradiation by UV-light, Figure 4.16 shows the transient profiles of gas products that were produced directly from the photocatalytic degradation of POME.

Significantly, two types of gaseous products were formed, viz. CO_2 and CH_4 . From Figure 4.16a, a general trend of CO_2 production can be observed for all sets of experiments, in which the production rate increased at the initial stage of photoreaction and peaked at 60 min. Thereafter, the production rate decreased. The decrease in CO_2 production could be due to the exhausting of organics in the POME sample. This can be confirmed by the recyclability study which is presented in Section 4.5.5.



(a)



(b)

Figure 4.16 Gas products collected along the photoreaction with O₂ flowrate of 70 ml/min and temperature maintained at room temperature. (a) CO₂ (b) CH₄

Interestingly, CH₄ was also produced and its production rate (cf. Figure 4.16b) was comparatively stable over the entire irradiation period. The detection of both CO₂ and CH₄ indicated a continuous carbon loss from the liquid POME (albeit may not be in its entirety) as gaseous products, symptomatic of photodegradation process. From Figure 4.16, CO₂ seems to be the major product from the POME photocatalytic degradation. Based on Manickam et al. (2014), with continuous supply of O₂ to the system, the organics in POME have higher tendency to be degraded into CO₂ compared to the other species. This is unsurprising considering that CO₂ ($\Delta G_f^\circ = -394.39$ kJ/mol) is thermodynamically very stable species (Dean, 1990), and therefore very easy to form. For CH₄ species (a component in natural gas), the possible reason for its formation is, upon UV irradiation, the organics in the POME would have decompose into smaller intermediate species and CH₄.

In addition, the total gas produced for all set of experiments were further calculated and tabulated in Table 4.3. Based on Table 4.3, photoreaction with 1.0 g/L TiO₂ produced the highest amount of gas products (CO₂ + CH₄), followed by 1.5 g/L, 2.0 g/L, 0.7 g/L, 0.5 g/L and 0.1 g/L, consistent with the COD degradation results (cf. Figure 4.10). Moreover, photoreaction over 1.0 g/L of TiO₂ yielded the most CO₂ (38913 μ mol) due to the highest degradation rate of organics. In terms of CH₄, the production of photoreaction with 0.5 g/L TiO₂ (361 μ mol) was slightly higher compared to others under similar experimental conditions. On the other hand, the purity of CH₄ in gas products showed a contradicting trend with the increasing TiO₂ loading. Lower TiO₂ loadings (0.1 and 0.5 g/L; 1.7% and 1.6%) produced gas product with higher composition of CH₄ compared to the higher TiO₂ loadings. These could be reasonably deduced as lower TiO₂ loadings would degrade lesser organics, and eventually lower CO₂ formation rate; hence higher CH₄ composition in the gas product. For TiO₂ loadings higher than 0.7 g/L, the CH₄ composition in gas products was almost similar, ranging from 0.9 to 1.1%.

Table 4.3 Total gas products collected from photoreactions

TiO ₂ loadings (g/L)	Gas accumulated over 240 min of photoreaction (μmol)		CH ₄ composition (%)
	CO ₂	CH ₄	
0.1	19599	334	1.7
0.5	22384	361	1.6
0.7	29823	330	1.1
1	38913	351	0.9
1.5	34291	344	1
2	33124	332	1

4.5.4 Scavenging Study and Mechanisms of Degradation

In order to identify the actual reactive species responsible on organic degradation, the role of electrons(e⁻), holes(h⁺) and hydroxyl(OH[•]) radicals were scavenged in a series of controlled experiments. The results obtained are shown in Figure 4.17.

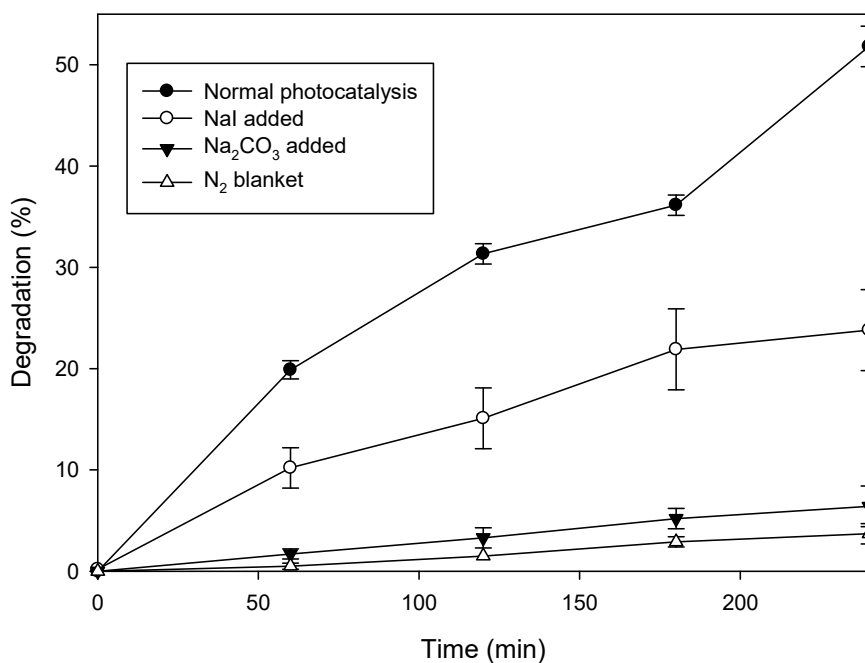


Figure 4.17 Results obtained from scavenging study employing 1.0 g/L of TiO₂

Oxygen is a well-known electron acceptor. In order to determine the role of electron in current study, O₂-bubbling was replaced with N₂-bubbling to eliminate the possibility of electron consumption. As can be observed in Figure 4.17, the photocatalytic degradation of organic in POME was drastically suppressed, plummeting from 51.8% to a meagre 3.6%, after 240 min of UV irradiation. Under anoxic condition, the photo-generated electrons were not consumed by the inert N₂, which subsequently led to recombination of the photo-generated charges; hence, a reduction in photocatalytic degradation efficiency. Thus, electron is not the major reactive species in current process.

Similarly, in subsequent experiment, 1.0 g/L of TiO₂ photocatalyst was added into POME sample, but bubbled with 70 mL/min of O₂. At the same time, 1 mL of 1.35 M of Na₂CO₃ was added into the POME substrate before initiation of experiment. The result obtained is also plotted in Figure 4.17. Coincidentally, the degradation efficiency was also significantly reduced to 6.6%. The inhibition of degradation observed in this set of experiment could be attributed to the consumption of the free hydroxyl radical, OH[•]_{free}, subsequently forming a highly selective carbonate radical, CO₃^{•-}, which was less active towards organics destruction (Equation M4.8)). This finding was also agreed by the past research (Tarr, 2003). Hence, the OH[•]_{free} was confirmed as the major reactive species in the current system.



Subsequently, another set of photoreaction was conducted, with an addition of NaI (1 mL, 1.35 M). In POME substrate, I⁻ ions (electron donor) would be released and occupied the photogenerated positive holes (h⁺) (Ji, 2013) that was responsible hydroxyl radical production through water-pathway (M4.3), as described in Equation (M4.9). Based on the results, the system has lost part of the reactivity, with only 24.1% of degradation achieved after 240 min of UV irradiation. This confirmed that OH[•]_{free} produced from water-pathway significantly contributed to the total degradation. Based on calculation, OH[•]_{free} produced from water-pathway through h⁺ contributed about 53.4% to the total degradation, making it the biggest contributor in the process, while the remaining was contributed by the OH[•]_{free} from oxygen pathway (M4.4-M4.7), photolysis and the synergic effects of all factors.



Summarizing from the results obtained from POME degradation, gaseous product formations and scavenging study, the mechanisms of POME decomposition during photocatalysis is proposed in Figure 4.18.

In the first step, OH^\bullet radicals would be generated through (M4.1) to (M4.7). Subsequently, the OH^\bullet radicals would desorb from the surface of TiO_2 photocatalyst (M4.10) and directly attack the organics (denoted by $\text{C}_a\text{H}_b\text{O}_c$ in M4.11) in POME sample and degraded them into intermediate species, CH_4 , H_2O and CO_2 .



The oxygen-rich environment in the system inducing high oxidation possibility and eventually the organics have higher tendency to be degraded into CO_2 and H_2O compared to CH_4 . Thus, the CH_4 composition should be comparatively low as proven experimentally from the current work.

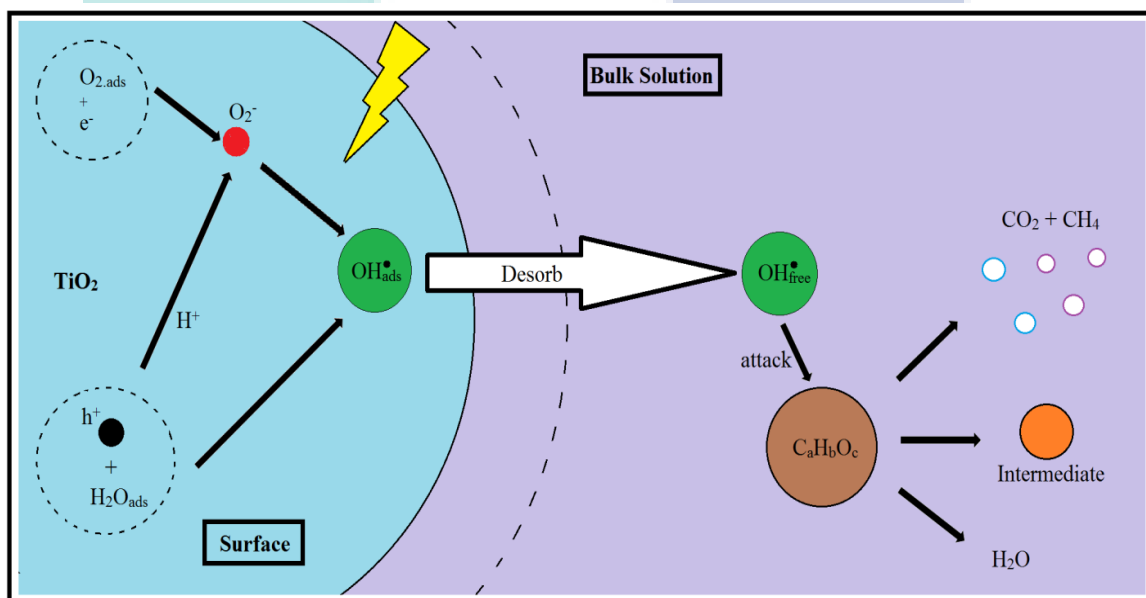


Figure 4.18 The schematic diagram of POME photocatalytic degradation mechanism

4.5.5 Recyclability and Longevity Studies

The stability of TiO_2 was studied from the view-point of practical application. A successful recyclable photocatalyst is very important for photo-degradation process of wastewater. Based on previous findings, the best condition for POME degradation was

70 ml/min of O₂ flowrate and 1.0 g/L of TiO₂. The recyclability of TiO₂ was performed for three consecutive runs. Recovery of TiO₂ in between the runs was achieved by filtering process. Results obtained are presented in Figure 4.19. For the 1st-cycle, more than 52.0% degradation was achieved after 240 min of UV irradiation while for 2nd and 3rd cycles, the degradation dropped slightly to 48.0% and 49.0%, respectively, possibly due to the error of the experiments. No significant deactivation of TiO₂ was observed, which confirmed the excellent recyclability of TiO₂ in POME degradation.

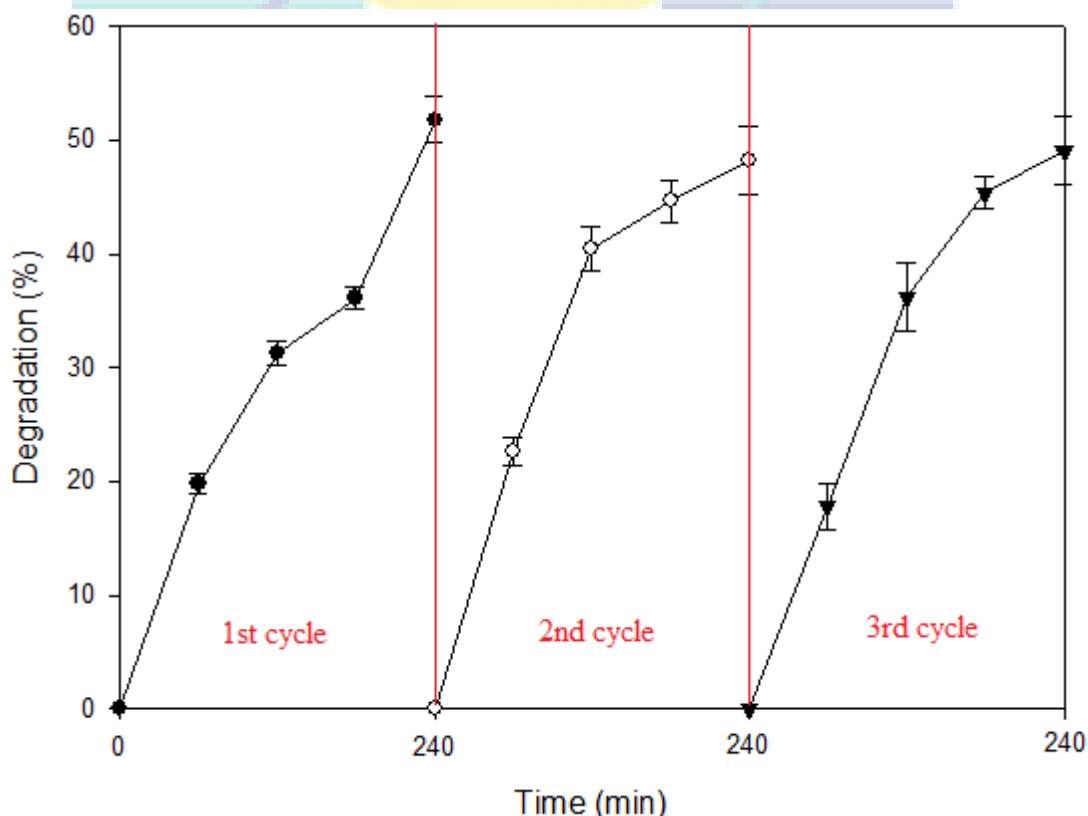


Figure 4.19 Degradation of POME with recycled TiO₂ over three consecutive runs

In addition, the longevity test of 22 h was also conducted. The comparison of POME sample before and after photoreaction is presented in Figure 4.20. Based on the results obtained in Figure 4.20, POME sample was fully decolourized after 22 h of UV irradiation. As shown in Figure 4.21, high degradation rate was observed during the first 4 h of the reaction. Thereafter, the exhaustion of the organics in the POME progressively slowed down the reaction. Based on the results, after 22 h, about 80.35% of COD reduction were achieved, with 33 ppm as the final COD level of POME (initial = 168 ppm), which is now under the required standard (50 ppm). For gaseous product

formations, once again, only the CO₂ and CH₄ were detected, with the total cumulative amounts of 77150 μmol and 1070 μmol, respectively, after 24 h of UV irradiation.



Figure 4.20 POME sample at t = 0 min (left) and t = 22 h (right)

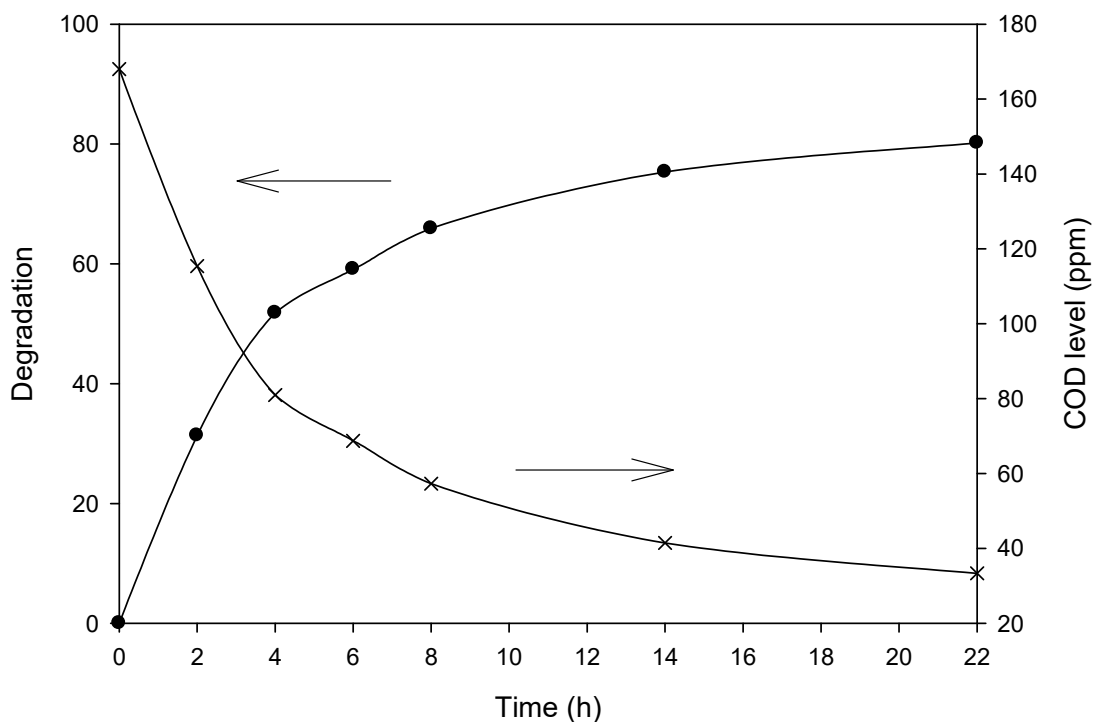


Figure 4.21 COD Degradation profile of POME for longevity study

As mentioned in Chapter 1, the main focus of current project is to further degrade POME to the discharge threshold set by DoE. The POME sample from longevity could

effectively estimate the required reaction time for future implementation works. Hence, some selected POME samples (0, 2nd, 4th, and 22nd hour) from longevity test were collected and subjected to ¹³CMNR analysis for carbon elucidation. The ¹³CMNR spectrums obtained are presented in Figure 4.22. Initially, only one peak was resonating at low frequency region (approximately d 160 ppm) as observed in Figure 4.22a, which corresponds to the carbonyl carbon. Referring to Figure 4.1 in Section 4.2, traces of carboxylic acids were detected in air-dried POME through FTIR analysis. Therefore, the peak that was detected in current section agreed and hence confirmed the findings of FTIR in Section 4.2. After 2 h of UV irradiation (Figure 4.22b), three new peaks were detected at d 129.73 ppm (=CH group), d 27.58 ppm (R₃C-, R₂CH or RCH₂ group) and d 10.03 ppm (CH₃- group), in addition to the original peak at around d 160 ppm. These additional peaks could be due to the intermediate products formed from the decomposition of the big organic molecules during the photocatalytic degradation process. This is aligned and hence confirmed the mechanisms proposed in Section 4.5.4. After 4 h of UV irradiation, the minor peaks disappeared, possibly due to the low concentration of the intermediate products after the total mineralization process. Hence, for both Figures 4.22c and 4.22d, only one peak was detected at around 160 ppm.

Previously, in Table 4.1, the BOD, COD and O&G values of the POME sample were above the discharge threshold. Hence, the POME sample from longevity test (at 22nd h) was collected and subjected to these analyses and the results obtained are tabulated in Table 4.4.

Table 4.4 Comparisons of the parameters before and after photocatalytic treatment process

Parameter	Before reaction (ppm)	After reaction (ppm)	Required level (ppm)	Degradation (%)
COD	168	33	50	80.35
BOD	112	16	20	85.66
Oil and Grease (O&G)	101	10	50	90.09

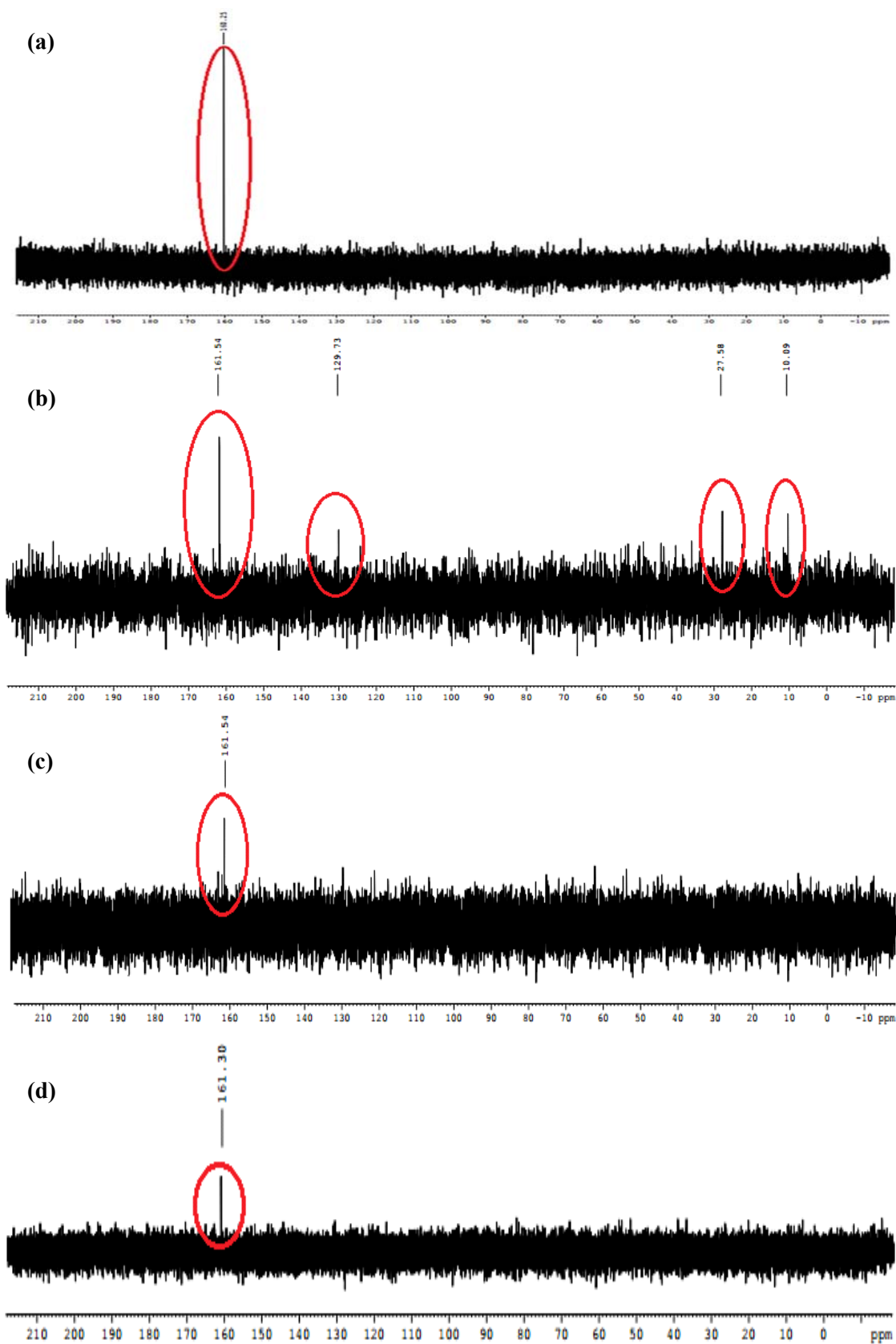


Figure 4.22 ^{13}C -MNMR spectrums of POME, (a) 0 h (b) 2 h (c) 4 h (d) 22 h

It can be seen that a total of 85.66%, 80.35% and 90.09% of BOD, COD and O&G removals were achieved after 22 h of photocatalytic treatment with 1.0 g/L of TiO₂ and 70 mL/min of O₂ bubbling. The final BOD, COD and O&G level of POME were 16, 33 and 10 ppm, respectively, which was below the discharge threshold.

4.6 Post-reaction Analysis for TiO₂ Photocatalyst

For photocatalyst, TiO₂ from recyclability test was selected for the post reaction analysis, as the photocatalyst from this condition has been extensively used, viz. for three consecutive cycles. Used TiO₂ photocatalyst was filtered, washed multiple times with DI water and ethanol in order to remove the physisorbed organics on the photocatalyst's surface. The photocatalyst was then dried at 323 K for 60 min and subjected to post reaction analyses.

Figure 4.23 shows the images of used TiO₂ photocatalyst from the recyclability test taken using FESEM technique under various magnifications. Apparently, no changes were observed even after three consecutive cycles of photocatalytic degradation process, suggesting the high resistance and durability of the TiO₂ photocatalyst in current process. By comparing to the FESEM images depicting fresh TiO₂ (Figure 4.3), it can be observed that the TiO₂ spheres have retained their smooth texture and are free from impurities, suggesting absence of organic adsorption during the degradation process.

Furthermore, the N₂ physisorption isotherms (cf. Figure 4.24) of the same batch of used TiO₂ photocatalyst shows that the photocatalytic degradation process did not alter the textural properties of TiO₂ photocatalyst. A type-V isotherm, according to the IUPAC identification, was obtained. This has confirmed that the post-reaction TiO₂ photocatalyst was still a mesoporous material. The BET specific surface area and BJH diameter were 11.53 m²/g and 23.2 nm, respectively. These values were invariant from its fresh counterpart (11.34 m²/g and 22.0 nm). The results also were consistent with the FESEM images as aforementioned.

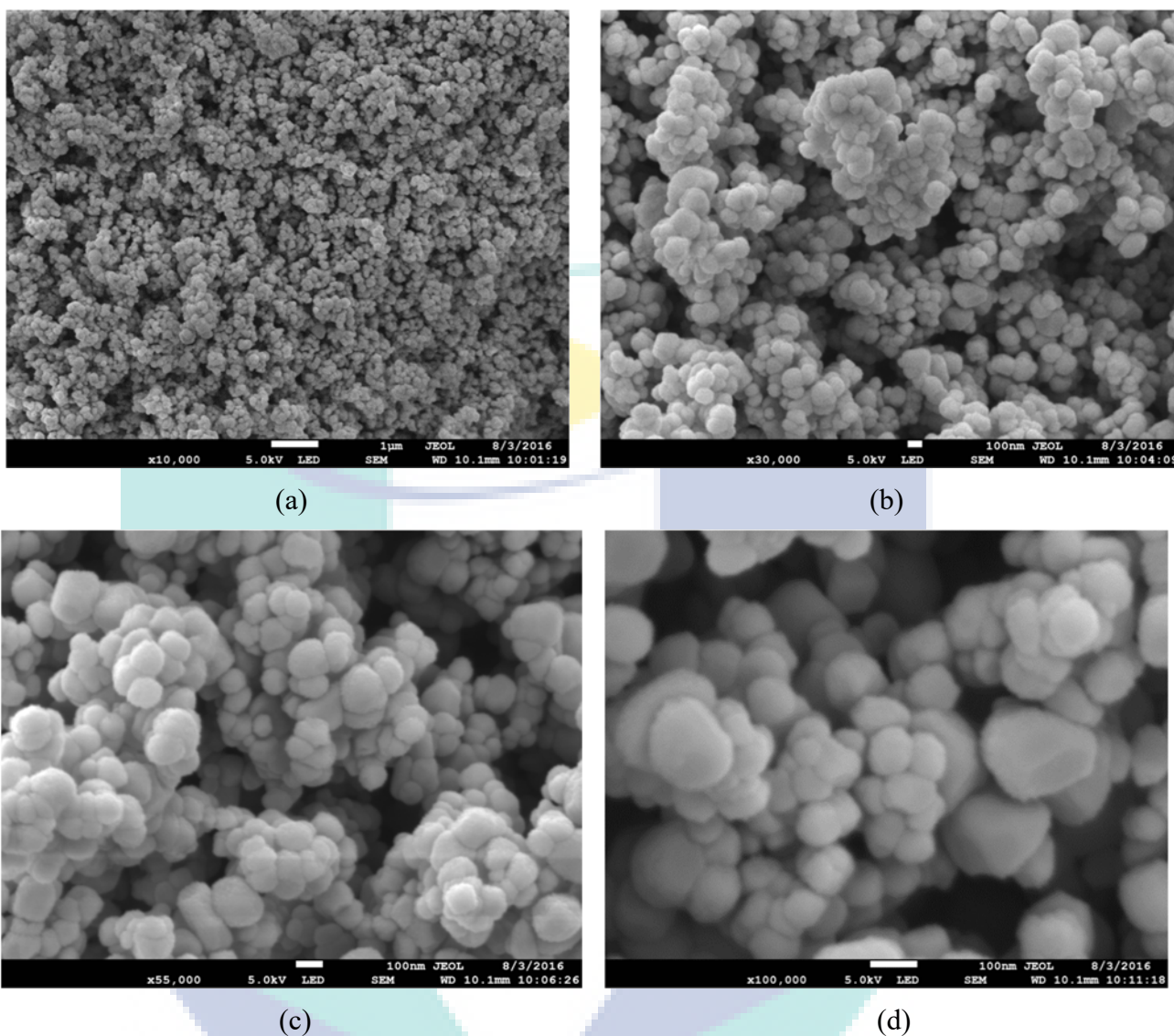


Figure 4.23 FESEM images of used TiO₂ photocatalysts from recyclability test (after 3rd-cycle) under various magnifications (a) 10 kx (b) 30kx (c) 55kx (d) 100 kx

Figure 4.25 shows the FTIR results for both fresh and used TiO₂ photocatalysts. OH and Ti-O bonds were detected at wavenumber of 3400 and 1650 cm⁻¹, respectively, for both fresh and recycled TiO₂. Apparently, no other functional groups were detected on the surface of used TiO₂. Besides, this also confirmed the results of adsorption study discussed earlier in Section 4.4.2, where adsorption of organic species on the TiO₂ surface was practically negligible. Furthermore, the results obtained from both FESEM images and N₂ physisorption also consistent with the FTIR analysis in Figure 4.25, in which no impurities were detected on the spent TiO₂ photocatalysts.

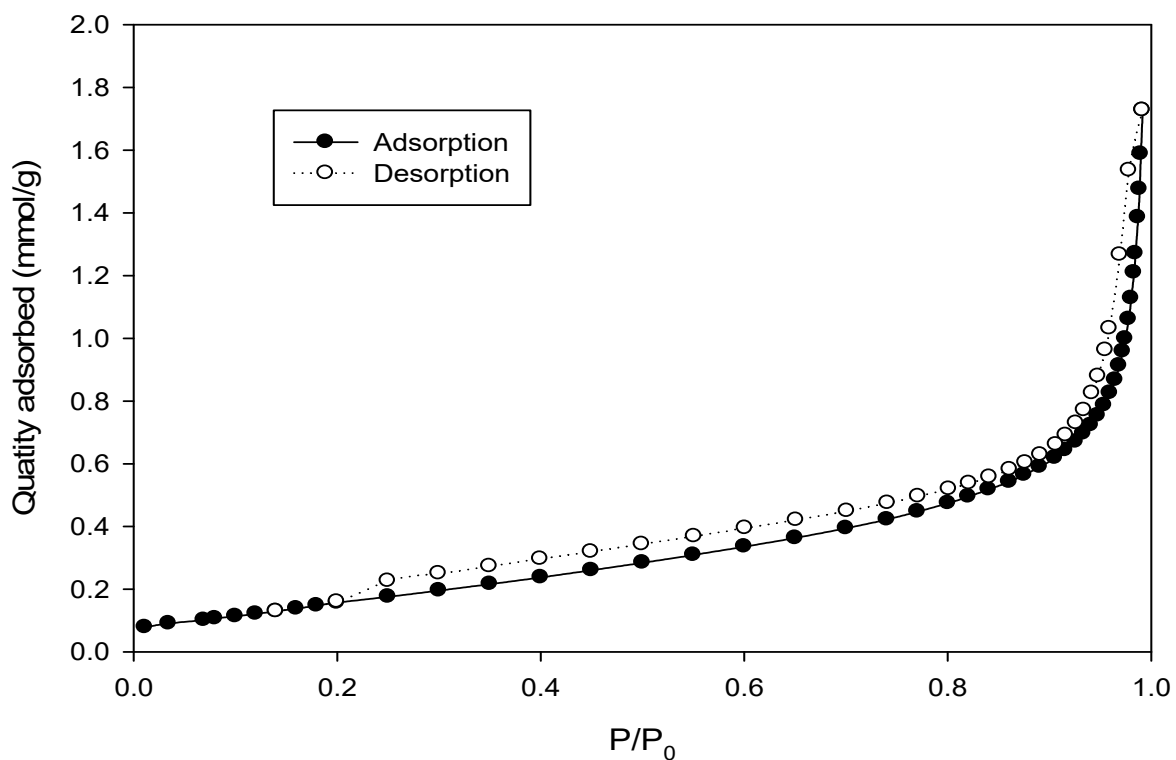


Figure 4.24 N₂ physisorption isotherms of spent TiO₂ photocatalyst

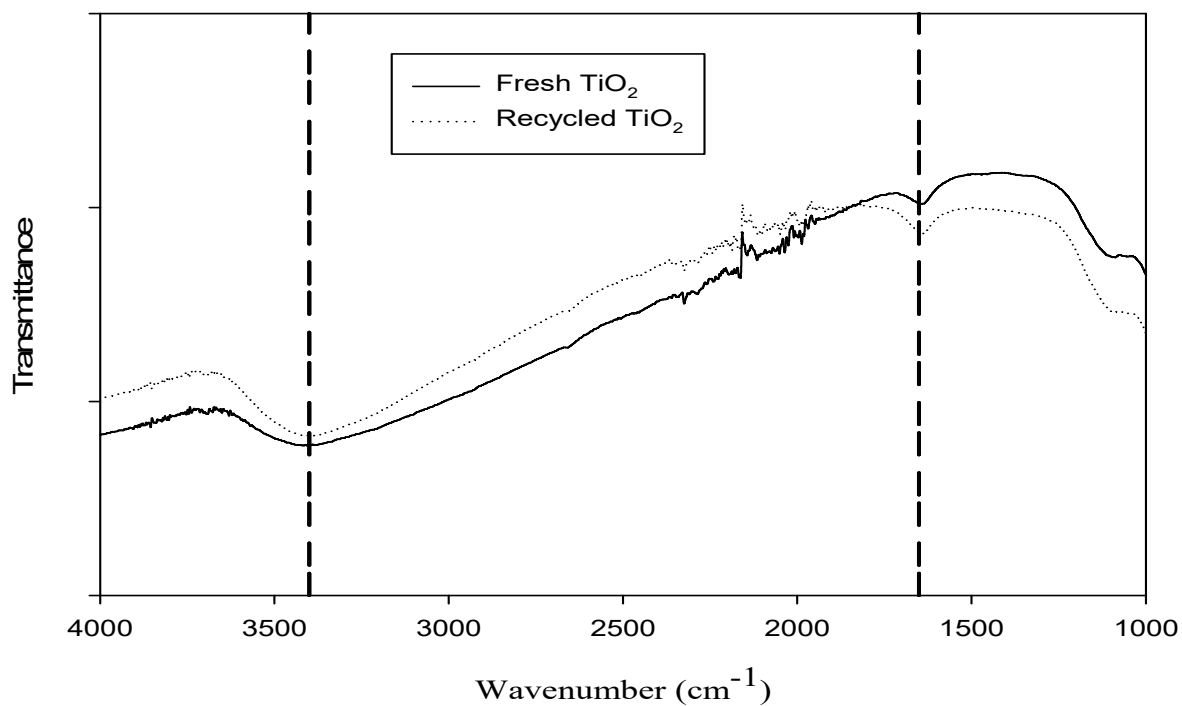


Figure 4.25 FTIR results of fresh and used TiO₂ photocatalysts

Finally, same batch of spent TiO₂ photocatalyst was introduced to EDX mapping for carbonaceous species detection to totally eliminate the possibility of organic adsorption during the process. Based on EDX analysis spectrum presented in Figure 4.26, the peaks observed at 452 eV and 4508 eV were identified as Ti L α peak and Ti K α peak, while peak located at 525 eV corresponds to O K α peak, hence confirming the presence of Ti and O elements only in the sample, with elemental composition of 63.5wt% and 36.5wt%, respectively. The molar ratio of Ti:O detect was 1:1.7 (36.78% for Ti; 63.23% for O), which approximated the theoretical ratio (1:2). This proved that the TiO₂ photocatalyst was very stable even after three consecutive of recyclability reaction. The EDX mappings obtained are also presented in Figure 4.27, where Ti atoms are illustrated in blue colour while O atom in green colour. The good dispersion of these atoms could be one of the important factors in enhancing the efficiency the whole system.

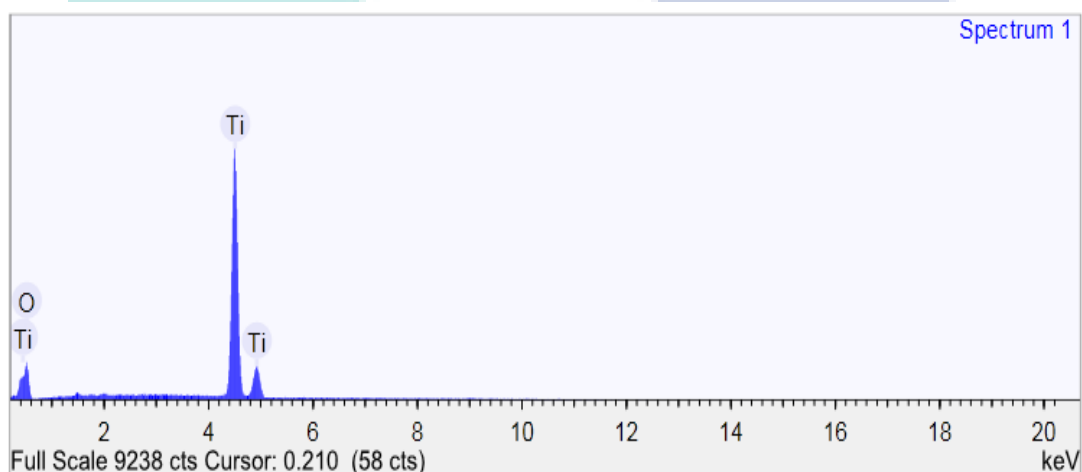


Figure 4.26 EDX mapping of spent TiO₂ photocatalyst (a: mixed; b: O atom; c: Ti atom)

Significantly, all the post reaction analyses results confirmed that TiO₂ surface remained clean, thus validate the adsorption results obtained in Section 4.4.2, where no COD reduction was observed. At the same time, these results also confirmed the mechanisms proposed in Section 4.5.4, in which the OH[•] formed would directly attack the organics without the need to adsorb on the photocatalyst's surface during the POME degradation process. These findings are also consistent with the past research conducted by Dong et al. (2015), in their review paper, that the absence of organic compounds adsorption on the TiO₂ surface was due to the poor affinity towards organic pollutants. For the same reason, TiO₂ photocatalysts exhibited almost deactivation-free in the

recyclability test, as the active sites for OH^\bullet production were always free from blockage. As summary, TiO_2 photocatalyst possessed strong reactivity and high stability towards POME photocatalytic degradation.

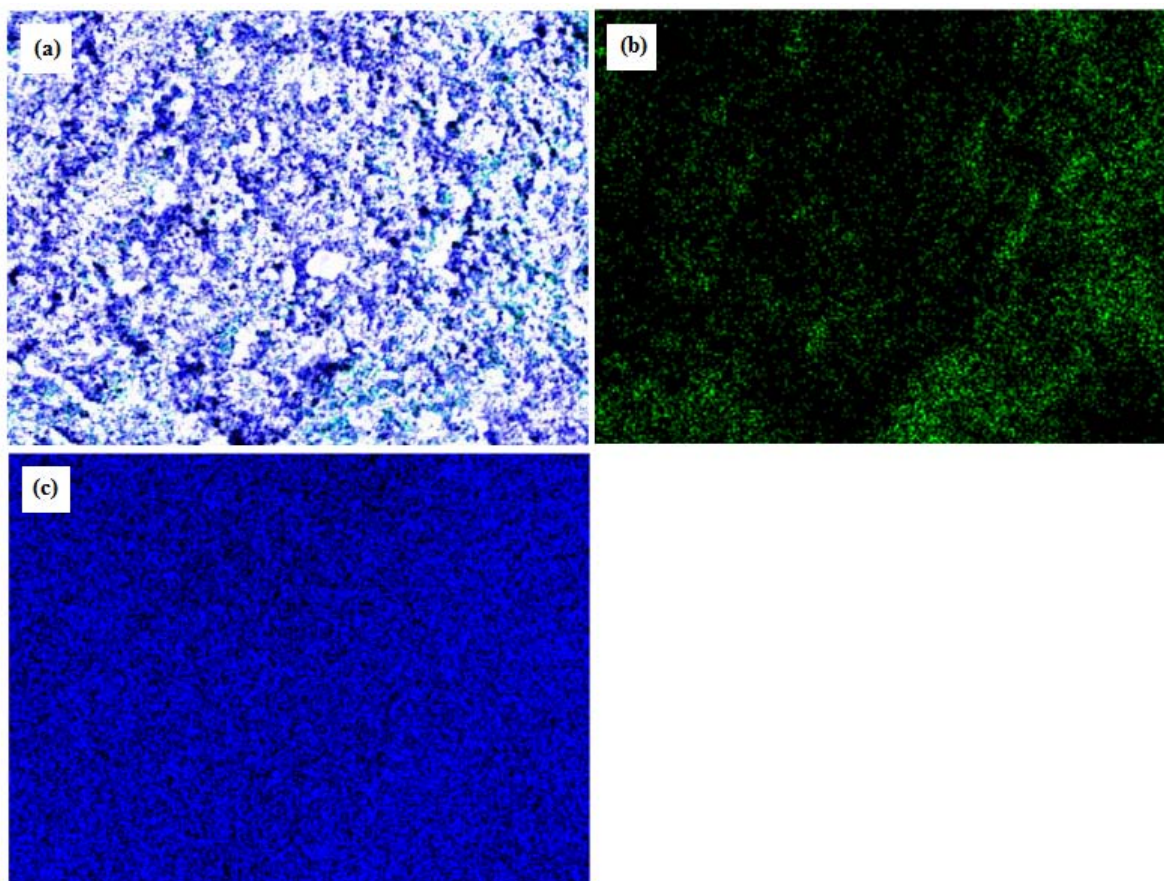


Figure 4.27 EDX mapping of spent TiO_2 photocatalyst (a: mixed; b: O atom; c: Ti atom)

4.7 Optimization of the Process

In the current section, the process efficiency was enhanced through the optimization process using CCD in RSM. Based on past works (Ahmadi et al., 2005; Khataee et al., 2010; Aljuboury et al., 2015; Berkani et al., 2015; Vaez et al., 2012), apart from the factors (oxygen flowrate and TiO_2 loading) investigated earlier, initial concentration of the substrate (POME, in current study) was also another important factor in the optimization process. Hence, all three factors were considered during the optimization process. Initially, all the factors were subjected to significance test, while at the same time, observing the interaction effects between the factors by using a 2^3 -level full factorial design. Subsequently, the significant factors were brought forward to CCD optimization stage.

4.7.1 Significance Analysis of Main Factors

The discussions on the significance test and interaction effects of the factors are presented in the ensuing sections.

4.7.1.1 Design of Experiments: Two-level Full Factorial Design

Prior to the optimization process, the potential factors were subjected to a significance analysis by using a 2^3 full factorial design to identify the degree of effects from the factors to the response. For O_2 flowrate and TiO_2 loadings, the ranges were adapted from Section 4.4.1 and 4.5.1 in current study, which are 0-150 mL/min and 0-1.5 g/L, respectively. According to Table 4.1, the highest COD level of the POME was 400 ppm, which was fixed as the upper range. The lower range of the initial concentration was substantially brought down to 100 ppm, which is the discharge threshold of POME waste, to investigate the effects of initial concentration. Also, wider range will result in higher patency of the responses (degradation efficiency in current study) between lower boundary and upper boundary. The factors were coded as -1 (low level) and +1 (high level), which denote for the lowest and highest range of the factors, respectively. All the experiments were triplicated, with a total number of 24 experimental runs for a statistical adequacy. The experiments were conducted in the recommended sequence to avoid lurking variables. Table 4.5 summarizes the responses obtained (degradation (%)). Based on Table 4.5, the degradations achieved ranged 1.24 to 18.98%. Compared to the results obtained in previous sections (4.4.1 and 4.5.1), the curvatures (peak points) must be lying somewhere in between the upper and lower boundary values.

Table 4.5 The experimental conditions of photoreactions and the degradations obtained

Run	O ₂ flowrate (mL/min)	TiO ₂ loading (g/L)	Initial Concentration POME (ppm)	Degradation of (%)
1	150	1.5	400	17.65
2	150	0	400	17.36
3	0	0	100	1.88
4	0	1.5	400	7.94
5	150	0	100	7.66
6	150	1.5	100	10.78
7	0	0	100	1.235
8	0	0	400	4.35
9	0	1.5	100	3.456
10	150	0	400	13.66
11	0	1.5	400	8.64
12	150	1.5	400	16.53
13	0	1.5	100	4.68
14	150	1.5	400	18.98
15	0	1.5	400	8.93
16	0	0	100	2.35
17	0	1.5	100	6.03
18	150	0	400	15.22
19	0	0	400	3.66
20	0	0	400	6.28
21	150	0	100	12.33
22	150	0	100	8.53
23	150	1.5	100	8.93
24	150	1.5	100	11.96

4.7.1.2 Statistical Analysis

The half-normal plot of cumulative probability versus standardized effect is illustrated in Figure 4.28. It is to be noted that the all the main effects (*A*, *B*, *C*) and *AC* are located at the right of the normal plot, suggesting that these four effects are more likely significant from the statistical perspective. This finding is consistent with the results presented in Pareto Chart (Figure 4.29).

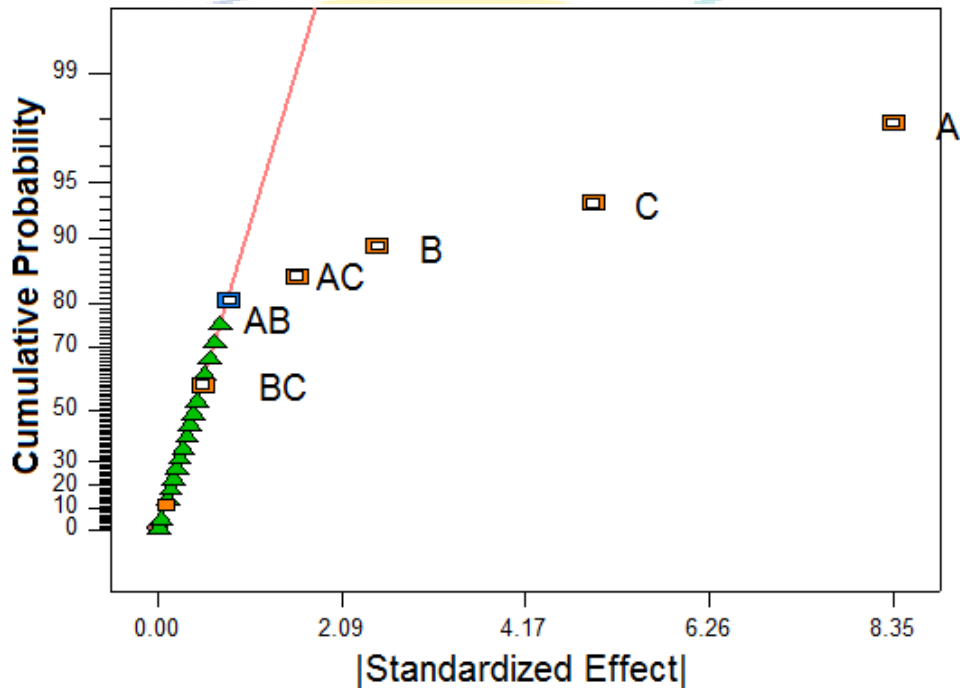


Figure 4.28 Half-normal plot of the effects for degradation of POME waste

The main effects of the factors studied are also presented in the Pareto charts illustrated in Figure 4.29. Figure 4.29 confirmed that all main and interactive factors exhibited positive effects (orange colour) towards the degradation achieved, asides from the factor AB. The Pareto chart is presented in term of t-values with two threshold limits (t-value and Bonferroni Limits). For current study, t-value limit was set to be the benchmarks for the significance test. Obviously, four factors (*A*, *B*, *C*, and *AC*) have exceeded the t-limit threshold, reflecting the statistical significance in this study, which further confirmed the previous discussion. Moreover, by judging from the height of the bars, main factors (*A*, *B* and *C*) have greater effects on the response, degradation (%), compared to the interactions effects. The effect list in the software (not shown) revealed that the O₂ flowrate (*A*) contributes the highest effects (63.5%) to the degradation (%),

follows by the initial concentration of POME (*C*, 22.32%), TiO₂ loading (*B*, 5.69%), and finally interaction effect of *AC* (2.29%).

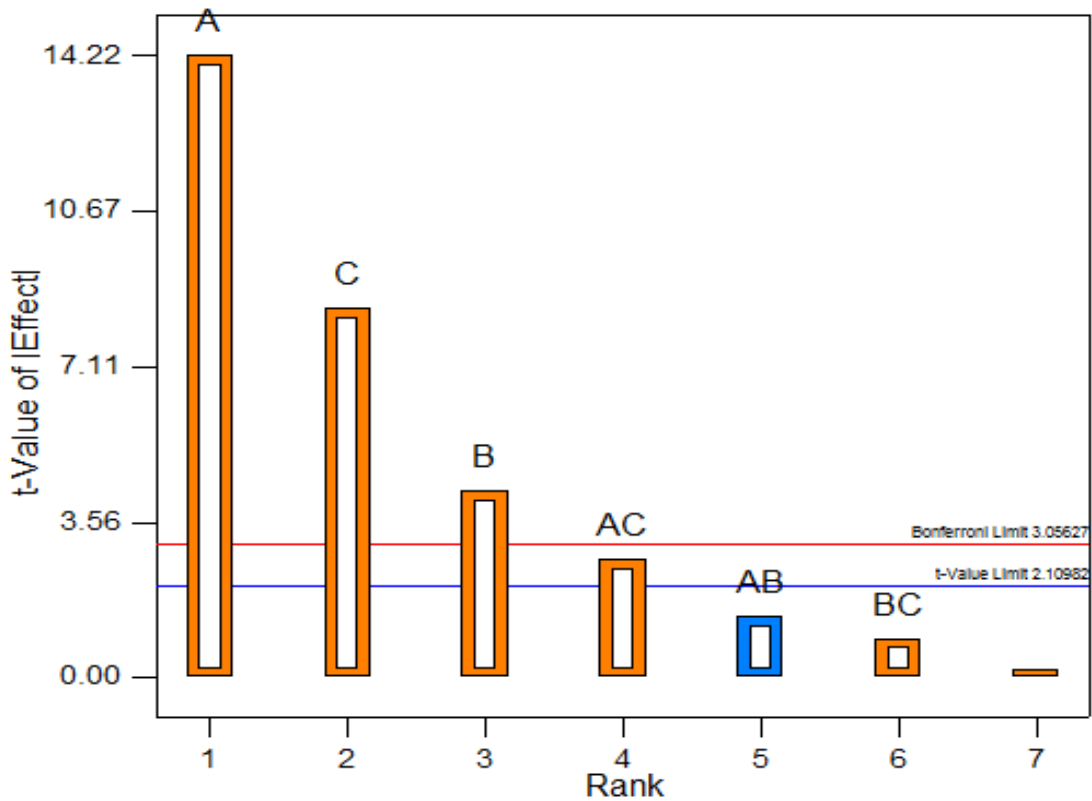


Figure 4.29 Pareto Charts of the main effects towards degradation

Furthermore, Table 4.6 summarizes the ANOVA analysis obtained from the response study. Referring Table 4.6, the low p-value (<0.0001) indicates that the model employed was significant. On the other hand, the obtained p-value for all the main factors (O₂ flowrate, TiO₂ loading and initial concentration of POME) were lesser than 0.05, suggesting high significance of these factors in affecting the output of the study (degradation). Other than the main effect, the interaction effects between two factors were also investigated. By referring to the p-values obtained, only the interaction effect of O₂ and initial concentration (*AC*) is significant due to low p-value (0.015). As a summary, the significance analysis revealed that all three main factors (*A*, *B* and *C*) were statistically-significant.

Table 4.6 ANOVA analysis obtained from the response

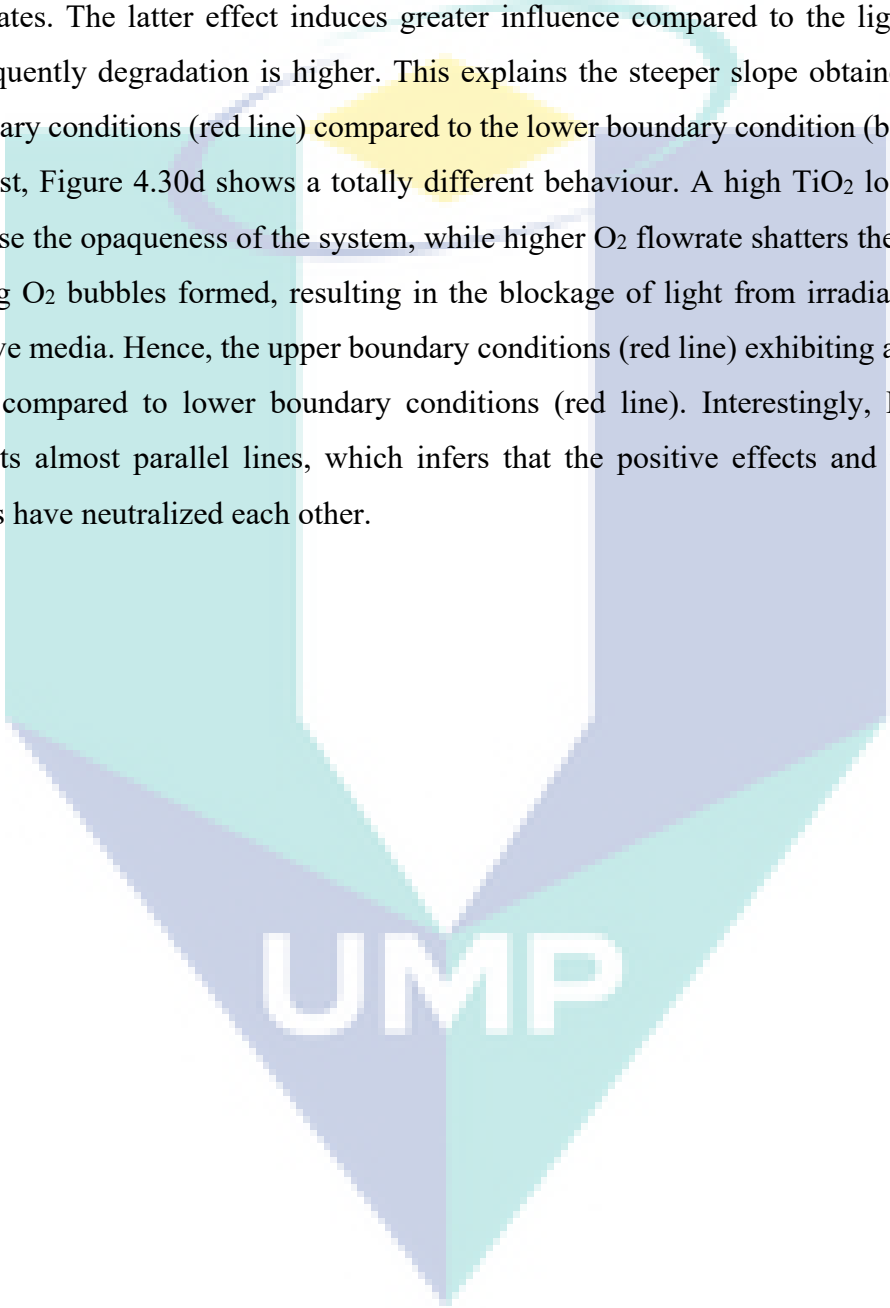
Source	Degree		Mean square	F-value	p-value
	Sum of square	of freedom			
Model	623.179	6	103.863	50.2697	< 0.0001
A-O ₂ flowrate	417.993	1	417.993	202.308	< 0.0001
B-TiO ₂ loading	37.4775	1	37.4775	18.1391	0.0005
C-Initial concentration of POME	146.911	1	146.911	71.1048	< 0.0001
AB	4.04343	1	4.04343	1.95701	0.1798
AC	15.1067	1	15.1067	7.31161	0.015

4.7.1.3 Main Factors and Interactive Factors Effects

Figure 4.30 shows the plots of main effects (4.30a-4.30c) and interaction effects (4.30d-4.30f) towards the degradation (%). The slope of the plot indicates the relative strength for the effect of the factors. By comparing Figure 4.30a-4.30c, O₂ flowrate profile exhibits the steepest slope, followed by initial concentration of POME (4.30c) and TiO₂ loading (4.30b). As explained earlier, in the absence of O₂, high recombination rate of photo-induced charges occurs; hence the low degradation (1.24%). When O₂ was supplied into the system, the O₂ molecules would consume the photo-generated electrons to form hydroxyl radical, drastically enhanced the degradation (%). From Figures 4.30b and 4.30c, higher TiO₂ loading and higher POME concentration increase the POME degradation. However, the increase in these two factors also would simultaneously induce a light shattering effect, therefore capping the degradation performance. Consequently, less-steep slopes were observed.

Figures 4.30d-4.30f show the resulting interaction plots. Interestingly, the “unparallel” characteristics of the profiles imply an existence of factors’ interaction. Generally, the degradation (%) achieved is net effects arising from the competition between the light shattering effects in the system (viz. bubble from the O₂, TiO₂ particle and the presence of refractory compounds in the POME) and the frequency of collision

between the substrate and the reactive species ($\bullet\text{OH}$, based on the results above). Referring to Figure 4.30e, the increase in POME waste concentration and O_2 flowrate would increase the light shattering effects, arising from the O_2 bubble formation and the presence of refractory compounds in the POME. At the same time, the decomposition of the organics in the system would also increase due to the increment in the density of the substrates. The latter effect induces greater influence compared to the light shattered, subsequently degradation is higher. This explains the steeper slope obtained for upper boundary conditions (red line) compared to the lower boundary condition (black line). In contrast, Figure 4.30d shows a totally different behaviour. A high TiO_2 loading would increase the opaqueness of the system, while higher O_2 flowrate shatters the light due to the big O_2 bubbles formed, resulting in the blockage of light from irradiating into the reactive media. Hence, the upper boundary conditions (red line) exhibiting a less steeper slope compared to lower boundary conditions (red line). Interestingly, Figure 4.30f exhibits almost parallel lines, which infers that the positive effects and the negative effects have neutralized each other.

The logo for UIMP (Universiti Malaysia Perlis) is a large, downward-pointing arrow shape. It is composed of four triangular sections meeting at a central point. The top-left and bottom-right sections are light blue, while the top-right and bottom-left sections are a slightly darker shade of blue. The letters 'UIMP' are written in a bold, white, sans-serif font across the center of the arrow.

UIMP

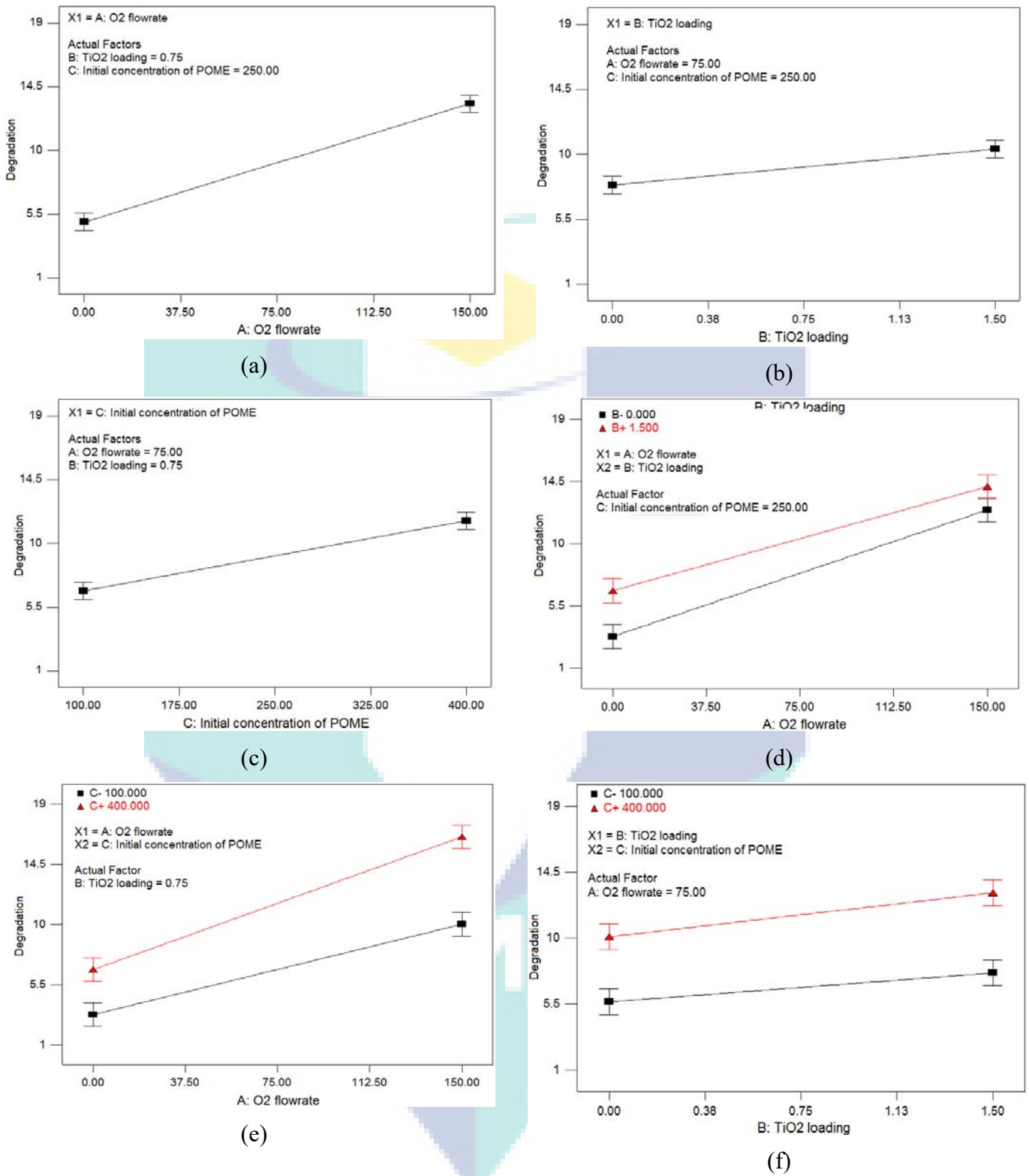


Figure 4.30 Plots of main factors and interaction effects towards the degradation (%)

4.7.2 Optimization of the Factors

The optimization process for phototreatment of POME using UV/TiO₂ system is presented in the current section, with an outcome of the optimum values of the factors, as well as the validation of the predicted response (degradation, %).

4.7.2.1 Optimization Range and Design of the Experiments

In Sections 4.4.1 and 4.5.1, the optimum range for O₂ flowrate and TiO₂ loading was found to be in the range of 40 – 100 mL/min and 0.7 – 1.5 g/L, respectively. Therefore, these values were employed as the $-\alpha$ and $+\alpha$ in the optimization process, and the α in current study is 2.0. For initial concentration of POME, the optimization range remains unchanged, with 100 ppm and 400 ppm as the $-\alpha$ and $+\alpha$, respectively. As aforementioned, CCD was employed for the optimization process. The design of experiments, as well as the degradation (%) achieved are presented in Table 4.7. The factorial points and the axial points were duplicated while the center point was repeated 6 times, with a total of 34 set of experiments generated. The experiments were conducted in the recommended order in order to avoid errors. By observing into Table 4.7, the degradation (%) achieved ranged 27.33 – 53.66%. The highest degradation was achieved in the center point of the design, which is the experiment with 70 mL/min, 1.10 g/L of TiO₂ and 250 ppm of POME. The degradation achieved were from 50.63 – 53.66%.

Table 4.7 CCD for optimization of POME degradation

Run	O ₂ flowrate (mL/min)	TiO ₂ loading (g/L)	Initial concentration (ppm)	Degradation (%)
1	85	1.3	175	38.36
2	55	1.3	325	34.35
3	85	0.9	325	34.49
4	85	1.3	325	34.95
5	85	0.9	175	39.69
6	55	0.9	175	46.77
7	100	1.1	250	37.27
8	85	0.9	325	36.98
9	100	1.1	250	35.35
10	55	0.9	175	48.02
11	70	1.1	250	52.65
12	55	1.3	325	31.23
13	70	1.1	100	28.63
14	85	1.3	325	36.95
15	55	1.3	175	45.15
16	70	1.1	250	51.55
17	70	1.5	250	41.66
18	85	1.3	175	37.63
19	55	1.3	175	43.61
20	85	0.9	175	40.65
21	70	1.1	250	50.63
22	70	0.7	250	41.77
23	70	1.5	250	40.25
24	70	1.1	100	29.35
25	70	1.1	400	28.25
26	70	1.1	250	51.67
27	55	0.9	325	42.66
28	40	1.1	250	39.35
29	55	0.9	325	43.64
30	70	1.1	250	53.66
31	70	0.7	250	43.54
32	70	1.1	400	27.33
33	70	1.1	250	53.66
34	40	1.1	250	37.66

4.7.2.2 Model Fitting, ANOVA and Residual Analysis

Various models (linear, two factorial, quadratic and cubic) were employed for the fitting test. Based on the fitting results, quadratic model seems to offer the best compliance due to the high R^2 and adjusted- R^2 values (0.92 and 0.90, respectively) compared to the linear (0.098, 0.0076) and also two factorial models (0.13, -0.063). Hence, quadratic model was adjudged the best and was employed for the optimization process. Second-order polynomial model was used to express the degradation of POME (%) as a function of the O_2 flowrate (A, mL/min), TiO_2 loading (B, g/L) and initial concentration of POME (C, ppm). The generated equations are as in Equations 4.5 and 4.6, in terms of coded and actual levels, respectively.

Degradation (%) =

$$52.21 - 1.39A - 1.17B - 1.54C + 1.43AB + 1.17AC - 0.62BC - 3.74A^2 - 2.64B^2 - 5.99C^2 \quad (4.5)$$

Degradation (%) =

$$-113.946 + 1.449A + 116.198B + 0.485C + 0.476AB + 1.039 \times 10^{-3} AC - 0.0413BC - 0.0166A^2 - 65.920B^2 - 1.065 \times 10^{-3} C^2 \quad (4.6)$$

The ANOVA analysis of current section was performed to estimate the coefficient of the model, at the same time validate the significance of each parameter and indicate the interaction strength of the main factors. The results are summarized in Table 4.8. As predicted, the p-value obtained was very low (<0.0001), which confirmed that the quadratic model employed was adequate to describe the optimization process. Based on Ingvarsson et al. (2013), the R values for a good fitted model should be higher than 0.80. The high R^2 , adjusted R^2 and predicted R^2 (0.93, 0.90 and 0.84) obtained have vindicated the picked model due to the adequacy of the applied regression model. In addition, high adequacy precision (20.532) was obtained, revealing high signal to noise ratio and hence confirms adequate signal.

Table 4.8 ANOVA for response surface quadratic model

Source	Degree		Mean Square	F value	p-value Prob > F
	Sum of Squares	Freedom			
Model	1719.85	9	191.094	32.3763	< 0.0001
A-O ₂ flowrate	61.9106	1	61.9106	10.4892	0.0035
B-TiO ₂ loading	43.875	1	43.875	7.43355	0.0118
C-Initial concentration of POME	76.3539	1	76.3539	12.9363	0.0014
AB	32.5756	1	32.5756	5.51913	0.0274
AC	21.879	1	21.879	3.70686	0.0661
BC	6.13801	1	6.13801	1.03994	0.318
A ²	540.726	1	540.726	91.6128	< 0.0001
B ²	269.325	1	269.325	45.6305	< 0.0001
C ²	1390.13	1	1390.13	235.524	< 0.0001

Similarly, the main factors and interaction effects with low p-value (<0.05 for 95% confidence level) would be the significant term. Based on calculated p-values, with exception to AC (0.0661) and BC (0.3180), all the factors are significant due to low p-values. Hence, Equations 4.7 and 4.8 can be further simplified into Equations 4.9 and 4.10.

Degradation (%) =

$$52.21 - 1.39A - 1.17B - 1.54C + 1.43AB - 3.74A^2 - 2.64B^2 - 5.99C^2 \quad (4.7)$$

Degradation (%) =

$$-113.946 + 1.449A + 116.198B + 0.485C + 0.476AB - 0.0166A^2 - 65.920B^2 - 1.065 \times 10^{-3}C^2 \quad (4.8)$$

On the other hand, the investigation of the residual was conducted to validate the adequacy of the model. The normal plot of the residuals is presented in Figure 4.31. Referring to Figure 4.31, the data points are close and evenly distributed along the normal line, which indicates that the data were sampled from a normal distribution.

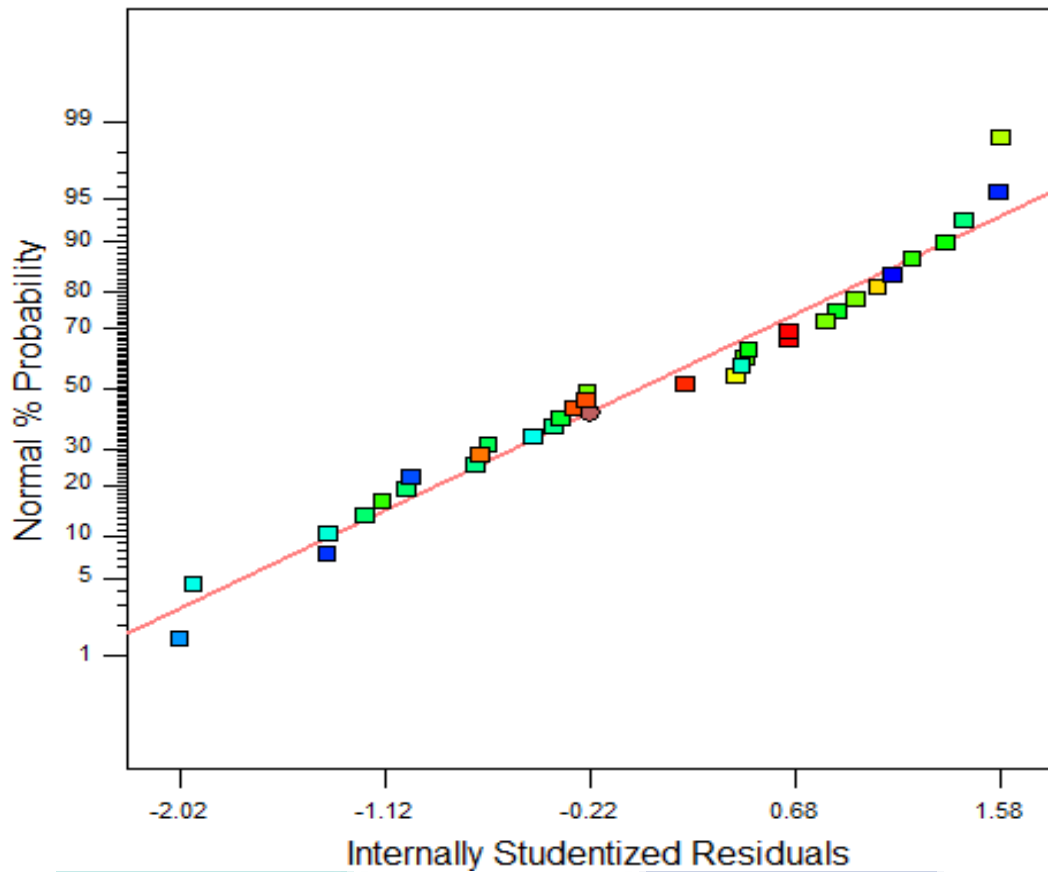


Figure 4.31 The normal plot of the residuals

Furthermore, the parity plots of predicted versus actual response and residuals versus predicted response are also demonstrated in Figure 4.32. From Figure 4.32, it can be observed that the data points are linearly distributed around the 45° line, indicating a well-fitted model, which is also reflected from the high R^2 -value (0.9356) as discussed earlier. In addition, the residuals data in Figure 4.33 are randomly distributed in both sides of the zero line which indicate that the model employed is sufficient to describe the response of the process. Moreover, the statistical results also suggest that the conducted experiments were free from the independence violation. The residual plot was also obtained and shown in Figure 4.34. Once again, the data points were randomly scattered and exhibit no specific trends, further confirming the adequacy of the model and the system; hence the reliability of the data.

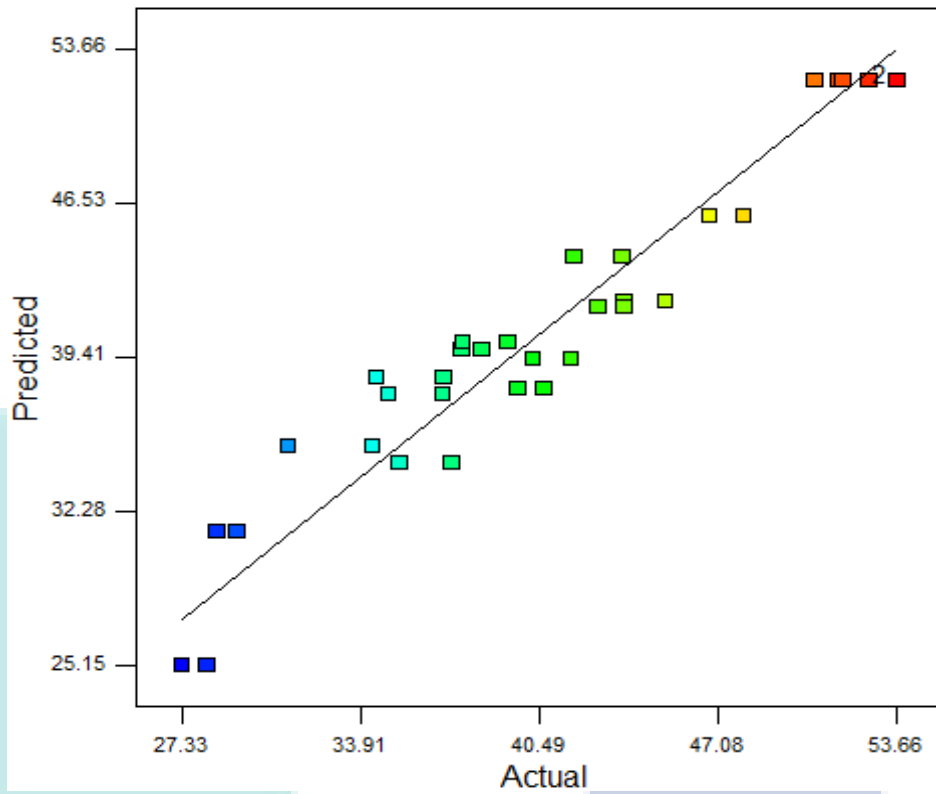


Figure 4.32 Predicted versus actual response

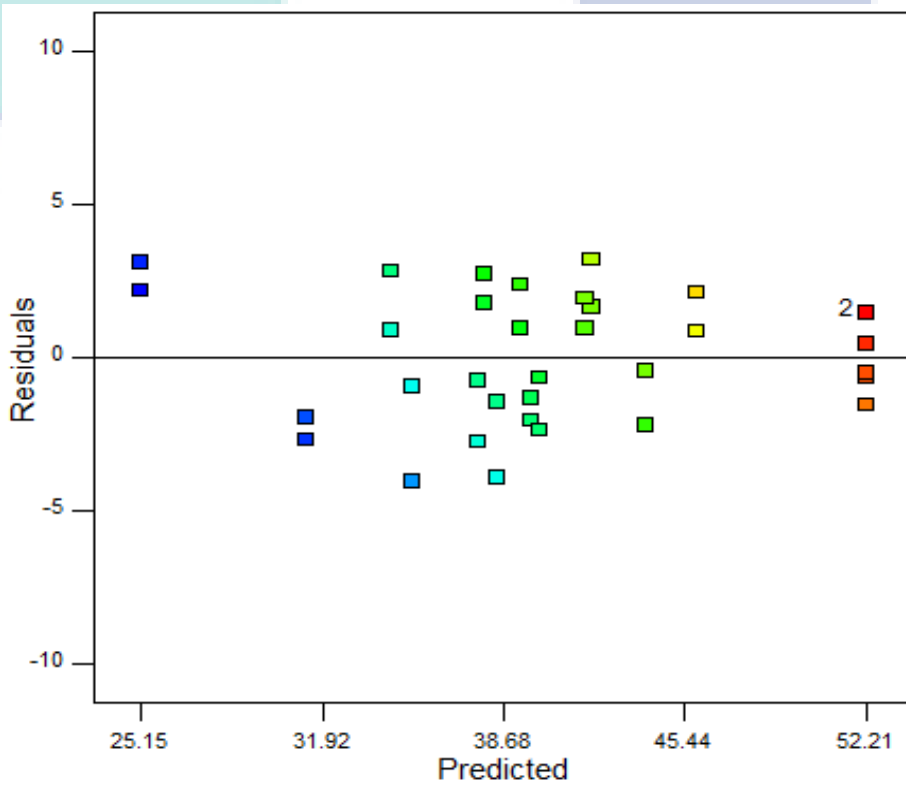


Figure 4.33 Residuals versus predicted response

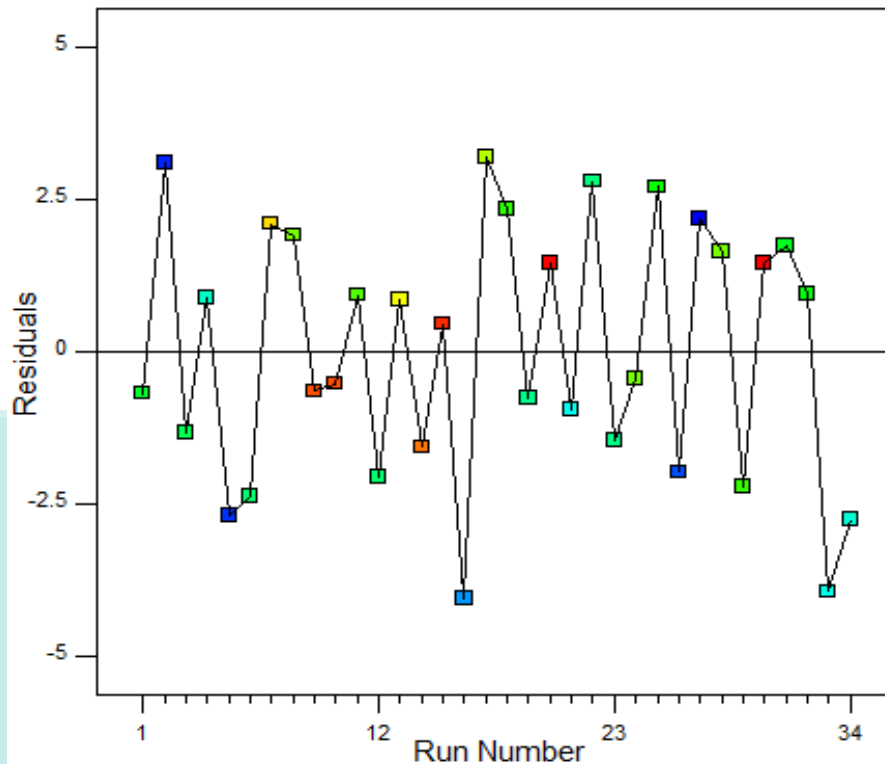


Figure 4.34 Residuals versus experiment run

4.7.2.3 Main Factors and Interaction Effects

Figure 4.35 shows the effects of O₂ flowrate, TiO₂ loading and initial concentration on the degradation. Referring to Figure 4.35a, the degradation achieved with 55 ml/min of O₂ flowrate (1.1 g/L of TiO₂ and 250 ppm of POME) was around 50% and slightly increased to an optimum point of 52% at ± 70 ml/min O₂ flowrate. Thereafter, the degradation exhibits a decreasing trend and eventually attaining only 48% of degradation with 85 ml of O₂ flowrate. Interestingly, all three factors exhibited a similar trend, in which an optimum was obtained. According to Figures 4.34b and 4.34c, the optimum points observed for TiO₂ loading and initial concentration of POME were ± 1.05 g/L and ± 250 ppm, respectively, with degradations of $\pm 52\%$ and $\pm 53\%$, respectively. By comparing all three figures, the lines in Figure 4.35a and 4.34b are comparatively straighter. The curve of the line was symptomizing the strength of the particular factor on the response. Compared to the two factors mentioned, the initial concentration of POME seems to have stronger negative effects on the degradation at higher concentration (> 250 ppm) as a curvier response line was obtained.

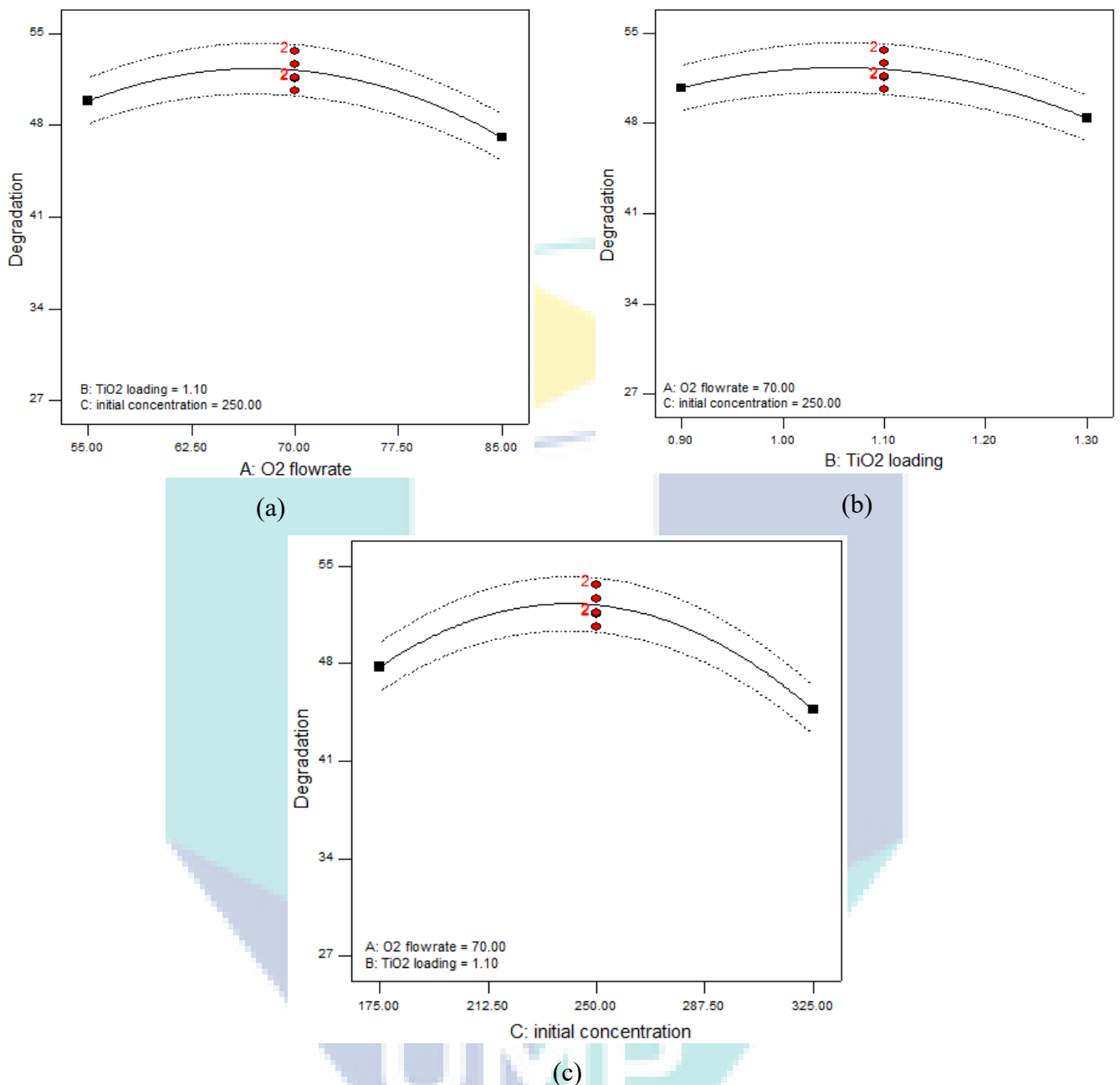


Figure 4.35 Effect of (a) O₂ flowrate (b) TiO₂ loading (c) initial concentration of POME towards degradation

In addition, the interaction effects of the factors are presented in Figure 4.36. Figure 4.36a reveals that the degradation indeed is a function of the O₂ flowrate (A) and TiO₂ loading and the 3D surface plot exhibits a smooth curvature, indicating the existence of an optimum point. The 3D surface and the contour lines beneath the 3D surface suggest that the optimum region lies somewhere between 1.0 – 1.1 g/L of TiO₂ and 65.0 – 75.0 ml/min of O₂ flowrate, with 250 ppm of POME initial concentration. Beyond this region, both factors combined to induce negative effects that suppress the degradation. Once

again, this can be attributed to the boundary layer effects and the light scattering effects induced by high O₂ flowrate and TiO₂ loading as discussed earlier. By comparing Figure 4.36a with the experimental results obtained (cf. Table 4.7), with 85.0 ml/min of O₂ and 1.30 g/L of TiO₂, the degradation achieved were comparatively low (38.36, 34.95, 36.95 and 37.63 % in Experiment 1, 4, 15 and 18), further confirming the adequacy of the model.

Figures 4.35b and 4.35c depict the interaction effects between O₂ flowrate and initial concentration of POME (AC) and TiO₂ loading and initial concentration of POME (BC), respectively. Coincidentally, these two 3D plots show a similar pattern to Figure 4.36a. The edges of the plots exhibit lower degradation achieved (green and yellow region) that correctly matched with the experimental results presented in Table 4.7. In addition, these results are also consistent with the discussions earlier, in which, any of the main factors exceed the optimum region would induce negative effect to the system. By referring to the 3D response surfaces in Figures 4.35b and 4.35c, both edges at the 'initial concentration of POME' bend downwards, showing lower degradation compared to the middle region. Section 4.5.2 reveals that the substrate in the POME is degraded according to 1st order reaction. Hence, increasing the concentration of POME will boost up the reaction rate. However, the colour of the POME will also increase at the same time, limiting the admission of the UV light, subsequently losing the driving force. Moreover, the increasing of O₂ flowrate (as in Figure 4.35b) or TiO₂ loading (Figure 4.35c) after the optimum region will also induced negative to the system as discussed earlier. Therefore, decreasing trends were observed in both 3D response surface plots. Nonetheless, the optimum regions were still successfully identified in both plots: 220 to 270 ppm of POME waste and 60 – 75 ml/min of O₂ flowrate with 1.10 g/L of TiO₂ and 220 to 270 ppm of POME waste and 0.9 – 1.2 g/L of TiO₂ with 70 ml/min of O₂ flowrate from Figure 4.36.

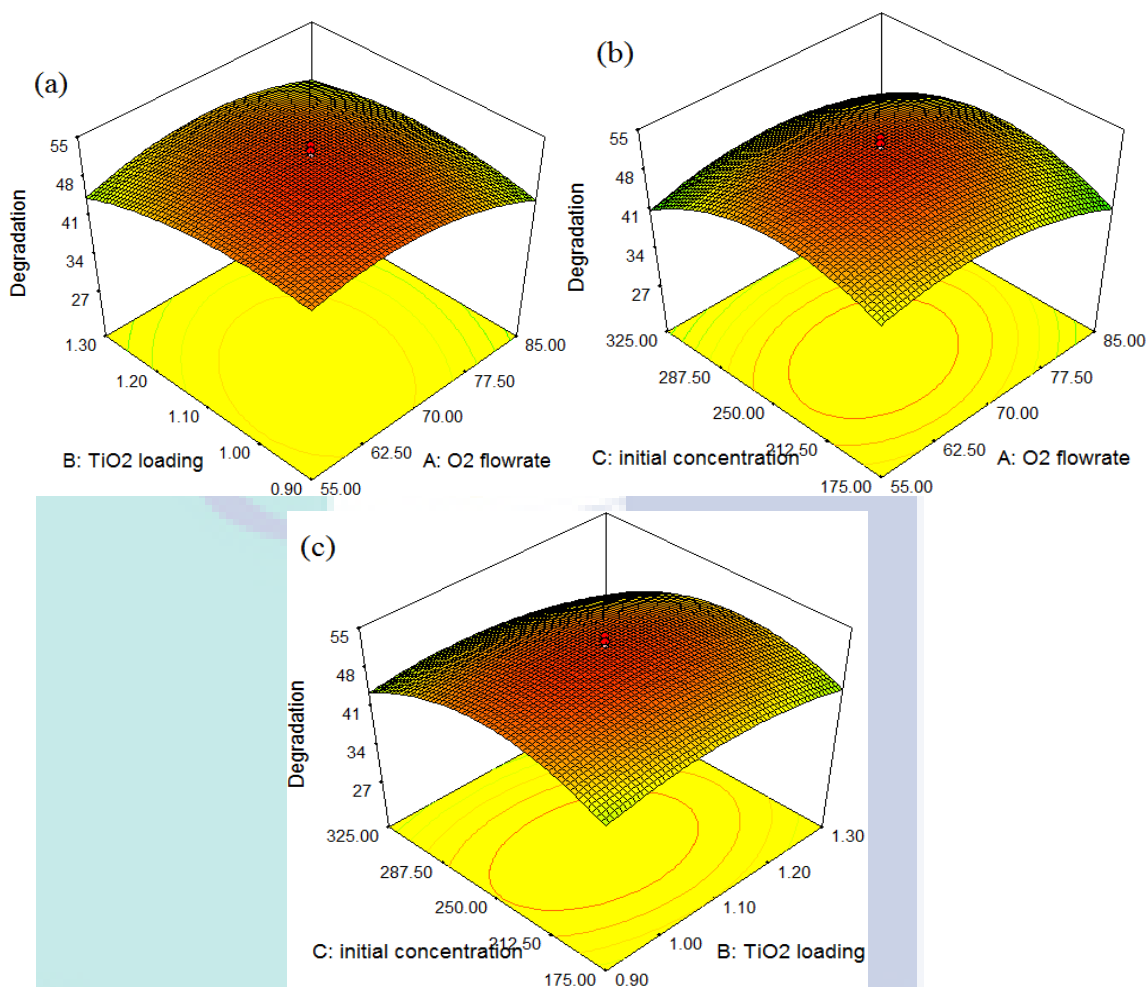


Figure 4.36 Contour plots and the 3D surface response plots between (a) AB (250 ppm POME) (b) AC (1.10 g/L TiO₂) (c) BC (70 mL/min O₂)

4.7.3 Optimization of the Process and Validation

Summarizing from the findings in previous sections, a 3D response surface was generated by using Equation 4.8 and is illustrated in Figure 4.37. At the same time, the optimized conditions for the degradation process was also generated by the system and presented in Table 4.9, together with the predicted response (52.66%). However, due to the limitations of the equipment, the suggested parameters were slightly round off to 66 ml/min of O₂ flowrate, 1.04 g/L of TiO₂ and 240 ppm of POME waste. The predicted response of the actual experiment was computed by using Equation 4.8 and the result obtained is shown in Table 6 (52.65 %). The validation experiment was duplicated and the results obtained were 54.33% and 55.62% after 240 min of UV irradiation. The error analysis for COD was conducted by employing Equation 4.9,

$$\text{Error}(\%) = \left| \frac{(R_1 + R_2)/2 - (R_p)}{R_p} \right| \times 100\% \quad (4.9)$$

where R1 and R2 are the results obtained from the validation experiment and R_p denoted for the predicted result computed by using Equation 4.8, which is 52.65% as aforementioned. Based on the error analysis, there is only 4.41% difference between the predicted and actual response, proving the model employed in current study is adequate to describe the degradation process. At the same time, the optimization of current process was also accomplished.

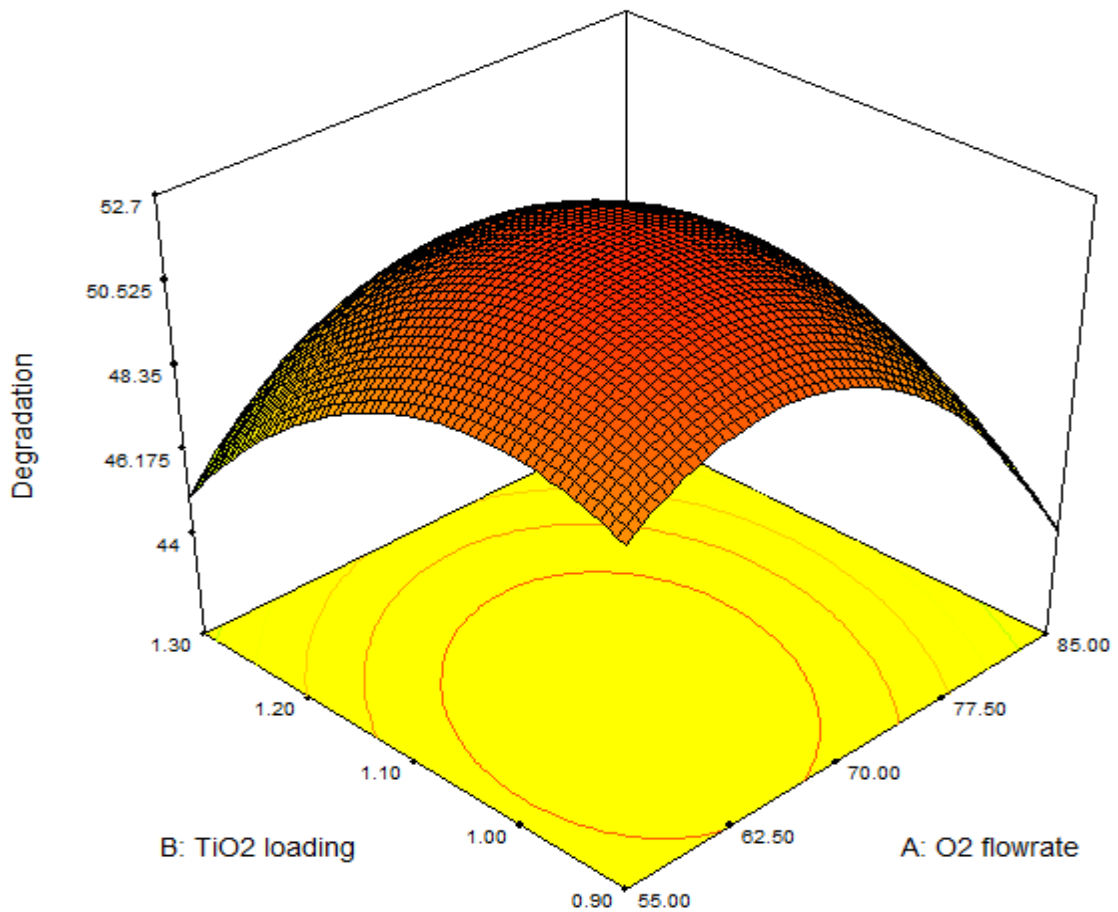


Figure 4.37 The predicted 3D respond surface with optimized conditions (239.53 ppm of POME)

Table 4.9 The suggested experimental conditions and the actual experiment condition

Parameters	Suggested conditions	Actual experiment
O ₂ flowrate (ml/min)	66.09	66
TiO ₂ loading (g/L)	1.04	1.04
Initial concentration of POME (ppm)	239.53	240
Predicted Degradation (%)	52.66	52.65
Actual Degradation (%)	-	54.33 and 55.62
Averaged Degradation (%)	-	55.0
Error (%)	-	4.41

4.8 Correlation between BOD and COD for UV/TiO₂ System

All COD and BOD data that were measured are plotted together in Figure 4.38. By definition, COD level is an indicator of all the organics in the POME waste while BOD level only indicates the amount of organics that could be consumed by the microorganisms. Figure 4.38 shows the correlation between BOD and COD after the photocatalytic treatment process in UV/TiO₂ system. It can be seen that the data points are randomly scattered within the boundaries of $y = 0.4x$ to $y=0.6x$. As discussed earlier, the main reactive species for POME degradation is OH[•]_{free}, which is well-known for its unselective behavior in organic destruction. Hence, the decomposition of organic matters in POME waste was completely random. The removal of organics that respond to BOD analysis could be varied due to the same reason and this explains the scattered data points presented in Figure 4.38. Nonetheless, the BOD level for all the data points are still well-bounded within the $y=0.4x$ and $y=0.6x$ lines, suggesting that the BOD level of the sample would be 40%-60% of COD level after the photocatalytic treatment in a UV/TiO₂ system.

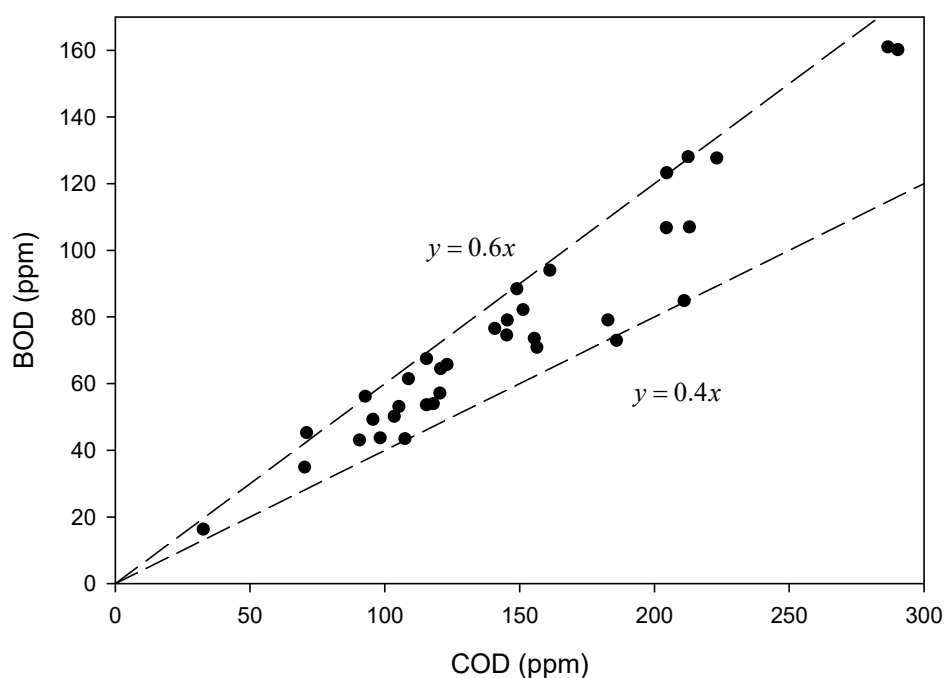


Figure 4.38 Correlation of BOD and COD after phototreatment using UV/TiO₂ system

4.9 Summary

Based on the results obtained, the best TiO₂ loading for POME degradation in mechanistic study was 1.0 g/L whereby 52.0% of organic removal was achieved after 240 min of UV irradiation. Significantly, CO₂ was the major gaseous component and the photoreaction with 1.0 g/L of TiO₂ released the highest amount of CO₂ (38913 μmol), whilst photoreaction with 0.5 g/L TiO₂ produced the highest amount of CH₄ (361 μmol). Our results also demonstrated that the OH[•] radicals' generation was primarily from O₂ and not from H₂O that was readily present in the POME. Moreover, we proposed herein reaction pathways that involved firstly the OH[•] radicals generation, followed by direct attack on the organics into smaller organic intermediates, CH₄ and also CO₂. In addition, recyclability and longevity studies were also conducted. Based on the recyclability study, no significant deactivation of TiO₂ was observed after three consecutive POME degradation runs. The degradation achieved were 52.0%, 48.0% and 49.0%, respectively. FTIR analysis of the post-reaction TiO₂ suggested an absence of organics adsorption on the TiO₂ surface. Therefore, we infer that instead of organic compounds adsorbed onto the TiO₂ surface, the organic compounds were directly attacked by the OH[•] radicals and decomposed into gaseous products. Moreover, after 22 hours of UV irradiation, 80.35%

of POME degradation was achieved and the COD level of POME dropped from 168 ppm to 33 ppm, which was lower than the permitted discharge limits (50 ppm). Moreover, the recorded BOD and O&G level for the same POME sample were 16 ppm and 10 ppm, which is also lower than the discharge threshold.

On the other hand, 2^3 full factorial design confirmed that O_2 flowrate, TiO_2 loading and initial concentration of POME waste were significance in influencing the final POME degradation. Moreover, statistical analysis also revealed interactions between the main factors, with the O_2 flowrate (A) contributes the highest effects to the degradation (63.5%), follows by the initial concentration of POME (C, 22.32%), TiO_2 loading (B, 5.69%), and finally the interaction effect of AC (2.29%). From the optimization study, a quadratic model was found to offer the best correlation judging from a high R^2 -value (0.92), fitting test as well as the residual analysis. Based on the ANOVA analysis, all the terms, including main factors and interaction effects, are significant to the degradation, except the interactions between O_2 flowrate and initial concentration of POME (AC), as well as TiO_2 loading and initial concentration of POME (BC). Software suggests that the optimized conditions would be 66.09 mL/min of O_2 flowrate, 1.04 g/L of TiO_2 and initial POME concentration of 239.53 ppm, with a predicted degradation of 52.66%. However, due to limitation of the equipment, validation experiments were conducted at 66.0 mL/min of O_2 flowrate, 1.04 g/L of TiO_2 and 240 ppm of initial POME concentration. The degradations achieved were successfully optimized to (duplicate) 54.33 and 55.62%, respectively, with only 4.41% error compared to the prediction generated by the model equation (52.65%).

CHAPTER 5

PHOTOCATALYTIC TREATMENT OF POME WASTEWATER OVER UV/ZnO SYSTEM

5.1 Introduction

In brief, the outline of this chapter is as follows:

- Section 5.2 presents the characterization of ZnO photocatalyst through XRD, FESEM imaging, N₂-physisorption, and UV-Vis DRS, followed by the detailed discussion.
- The photocatalytic degradation of POME in UV/ZnO system, including the effects of ZnO loading, modelling development, mechanism study and the stability of ZnO photocatalyst were thoroughly investigated and discussed in Section 5.3.
- Section 5.4 is about the post reaction analyses of both selected used ZnO photocatalyst and POME sample. FESEM imaging, N₂-physisorption, FTIR and EDX mapping were employed for used ZnO photocatalyst while the POME sample was analysed by using BOD method, COD method, O&G determination and ¹³CMNR.
- Process optimization was conducted and presented in Section 5.5. The significance of the factors was statistically-assessed using a 2³ full factorial design as in Section 5.5.1. Subsequently, the system was optimized using CCD in RSM and discussed in Section 5.5.2.
- Finally, the correlation between BOD and COD of POME treated by UV/ZnO system was determined and presented in Section 5.6.

5.2 Characterization of ZnO Photocatalyst

Figure 5.1 shows the XRD spectrum obtained for ZnO photocatalyst. Apparently, only ZnO crystalline phase was present. Besides, the sharp peaks obtained indicate the high crystallinity in the ZnO photocatalyst, which favours the degradation process. The sharpest peak observed in Figure 5.1 is at 36.34° and by employing Equation 2.3, the crystal size was estimated to be 62.3 nm.

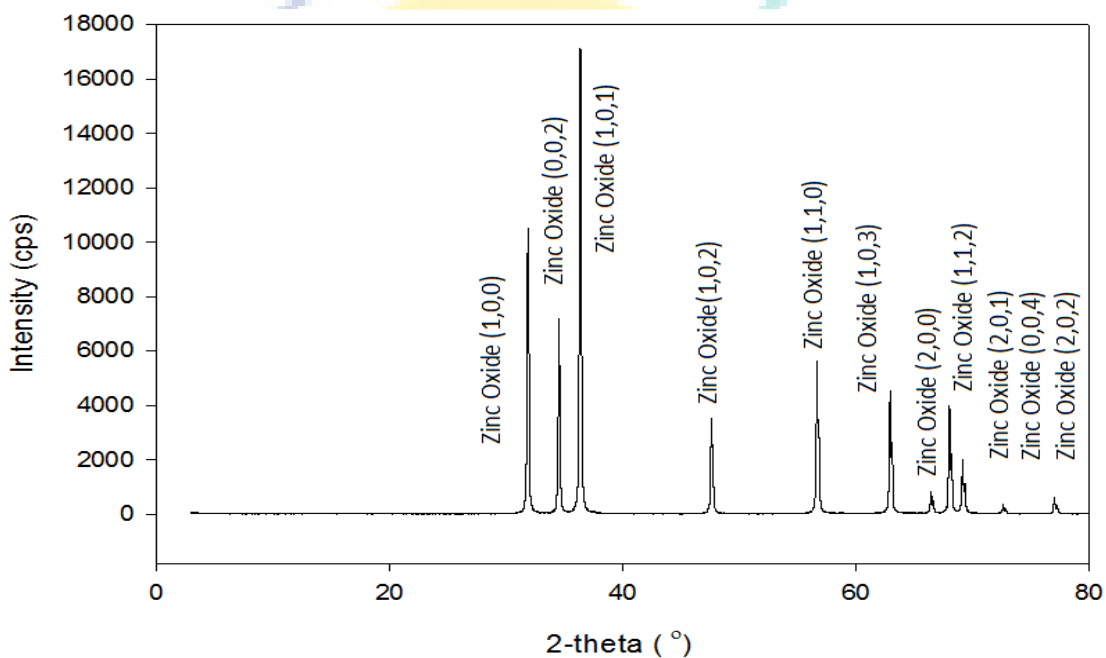


Figure 5.1 XRD results of ZnO photocatalyst

Figure 5.2 shows the FESEM images of fresh ZnO photocatalyst employed in the current study, captured at different magnifications. Figure 5.2a shows that the ZnO photocatalyst has irregular shape, which is believed due to the sintering of the ZnO photocatalyst particles during the calcination procedure. Under higher magnification (30kx and 50kx, Figure 5.2), significant variation in terms of both diameter and length is noticeable. Indeed, the diameter of the ZnO nanorods ranged from 160 to 480 nm while the length ranged from 200 to 820 nm. In addition, the smooth surface of ZnO photocatalyst particles (cf. Figure 5.2) proves the presence of micropores.

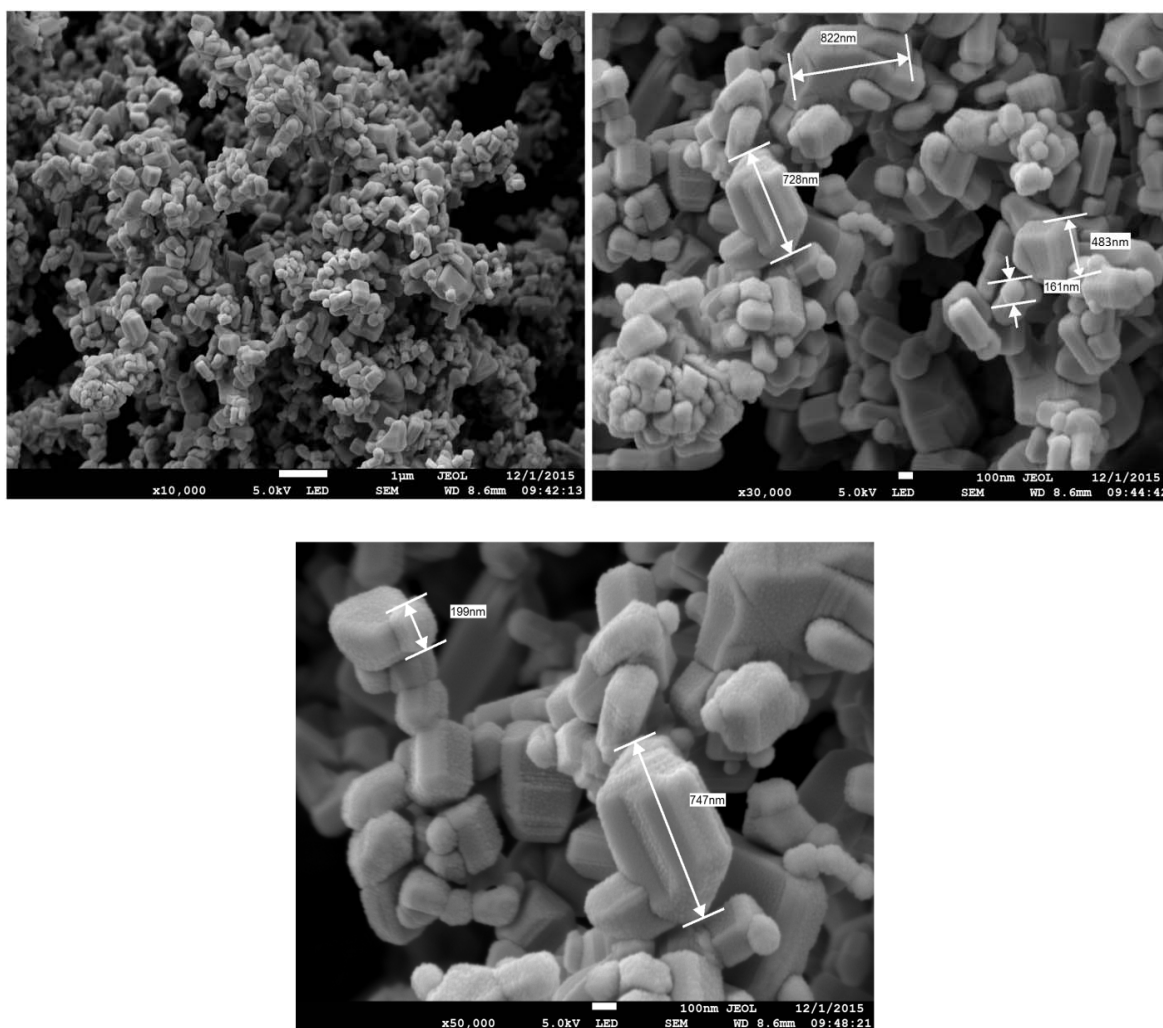


Figure 5.2 FESEM images of ZnO photocatalyst employing magnifications of 10kx, top left; 30kx, top right and 50kx, bottom

The adsorption-desorption isotherm for ZnO photocatalyst is as in Figure 5.3. As can be observed in Figure 5.3, both the adsorption and desorption isotherms have overlapped, indicating weak interaction between the N_2 and ZnO. According to IUPAC identification system, the isotherms obtained can be classified as type-III isotherm, characteristic of weak adsorbate-adsorbent interactions. By employing Barrett-Joyner-Halenda (BJH) model, the average pore diameter for ZnO photocatalyst was 6.47 nm, which fall in the mesoporous range (2-50 nm). In addition, the N_2 physisorption also reveals that the BET specific surface area of ZnO photocatalyst was $9.71 \text{ m}^2\text{g}^{-1}$.

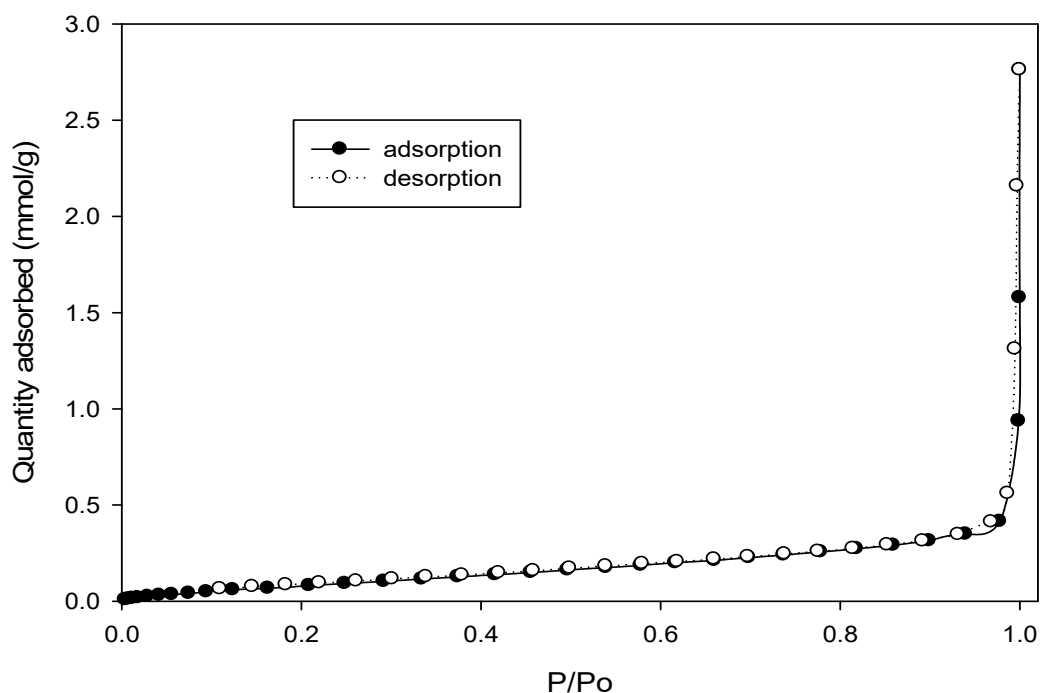


Figure 5.3 N_2 adsorption and desorption isotherms for fresh ZnO photocatalyst

Figure 5.4a shows the light adsorption properties of ZnO photocatalyst. Obviously, ZnO exhibits strong adsorption in the UV-region ($\lambda < 390$ nm), while in the visible light region ($\lambda > 390$ nm), the adsorption profile plummets. This confirms that ZnO is strongly asserted as a UV-responsive photocatalyst. Subsequently, band gap energy of ZnO photocatalyst was determined by transforming the adsorption data into the Tauc plot by using Kubelka-Munk functions (cf. Figure 5.4b). Based on the red-dotted line in Figure 5.4b, the band gap energy of the ZnO was estimated at 3.2 eV.

5.3 Photocatalytic Degradation of POME

The degradation of POME was conducted in the presence of ZnO photocatalysts and UV light. The related discussion is presented in current section.

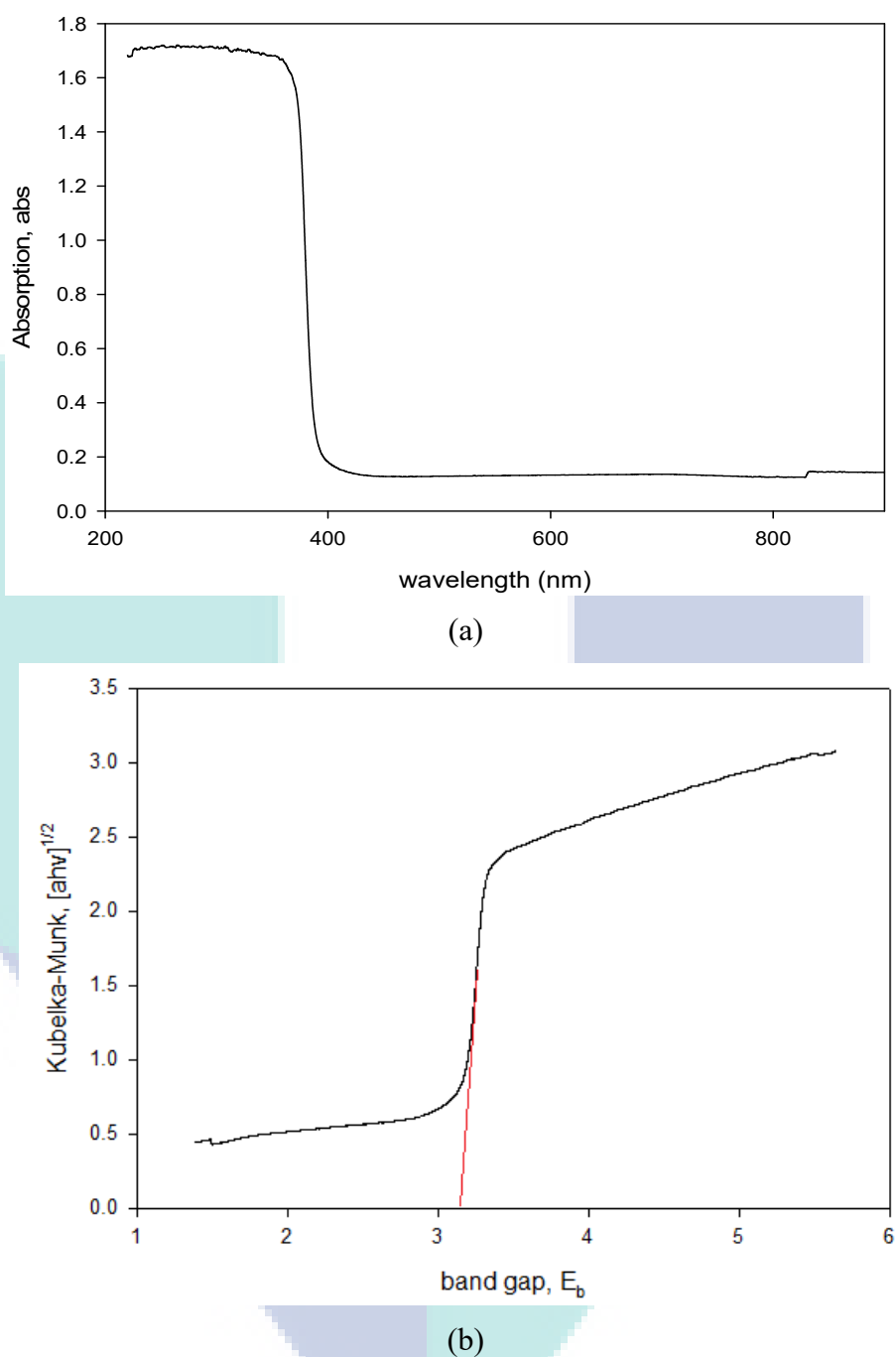


Figure 5.4 (a) Diffuse reflectance UV-Vis spectra of the photo-catalysts. (b) Plot of Kubelka-Munk function versus light energy for ZnO

5.3.1 Effects of ZnO Loadings

Based on our previous chapter, the best O₂ bubbling rate was 70 ml/min. Hence, for current study, all photoreaction runs were conducted employing the similar O₂-bubbling rate. Figure 5.5 shows the results obtained for the adsorption study, as well as photoreactions over different ZnO loadings, from 0 – 2.0 g/L.

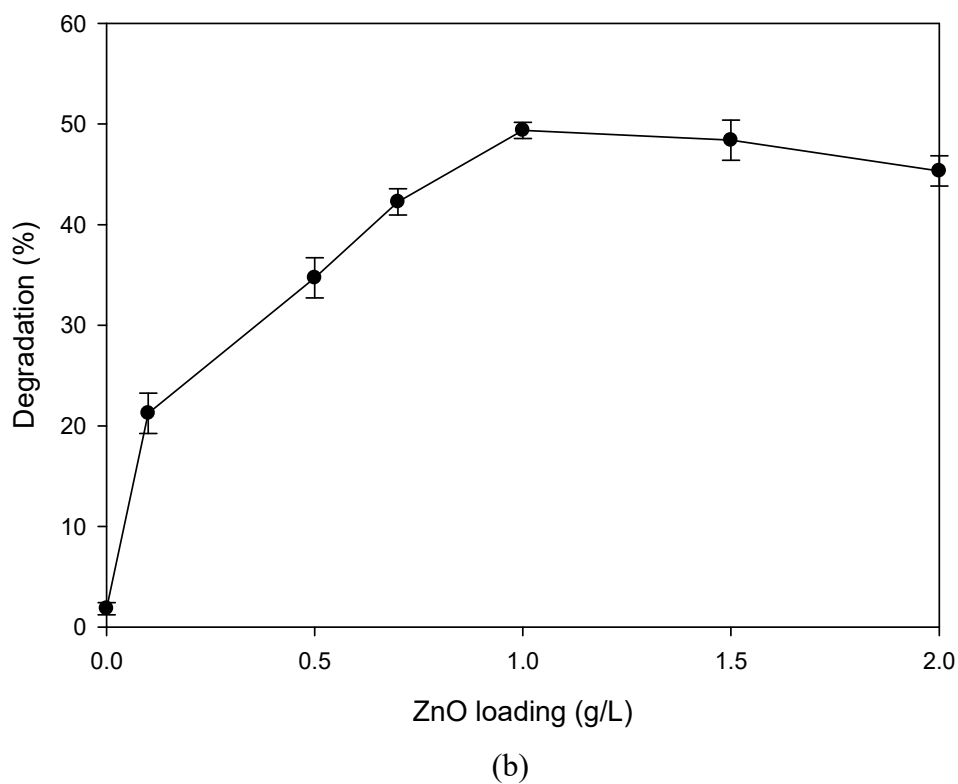
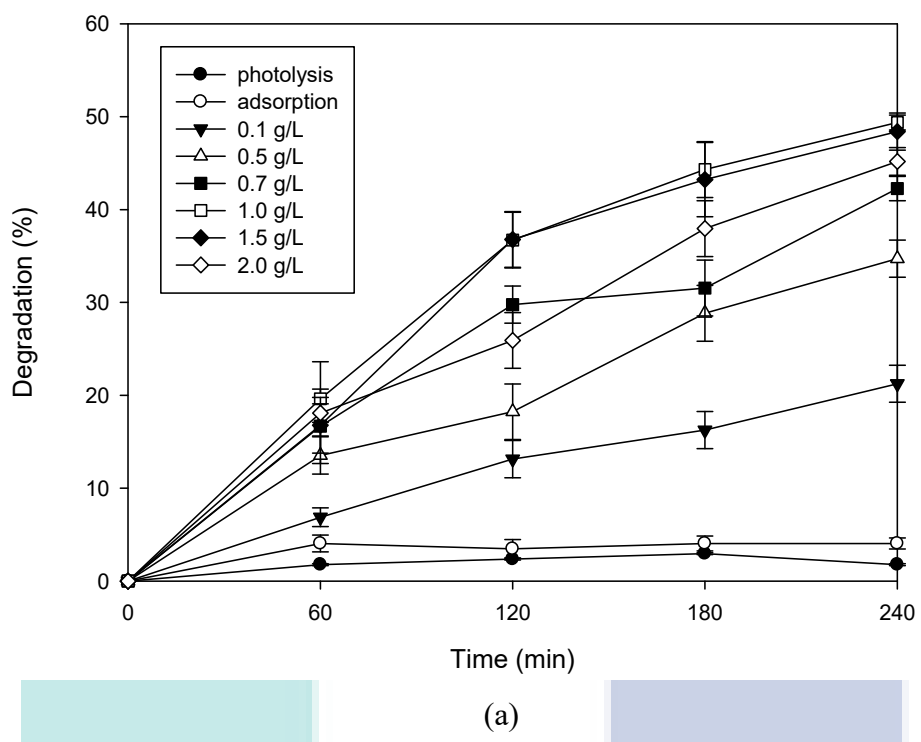


Figure 5.5 Results obtained from photoreaction at 70 ml/min of O₂ employing different ZnO loadings

Figure 5.5a shows that the photocatalytic degradation profiles for both adsorption study and photolysis are nearly invariant with time. For adsorption study, 0.5 g/L of ZnO was added into the POME waste and stirred vigorously. After 60 mins, about 4% of COD reduction was recorded, which can be ascribed to the adsorption of the organic pollutants onto the surface of ZnO. Thereafter, the COD profile remains almost constant until the 240th min, indicating that the saturation of organic adsorption can be achieved in considerably short period (< 60 min). The adsorption of organic pollutants was very limited (< 4.0% after 240 min of stirring) presumably due to the low BET specific surface area (9.71 m²/g) and also due to the adsorptive competition with H₂O and O₂ molecules. For photolysis, the photoreaction was conducted under UV-irradiation and 70 ml/min of O₂-bubbling rate in the absence of ZnO photocatalyst. Similar with previous chapter, after 240 min of UV irradiation, less than 2.0% of photocatalytic degradation was achieved, demonstrating high resistance of the recalcitrant organic pollutants in POME waste towards UV irradiation. Moreover, the gaseous products for both adsorption study and photolysis were collected and eluted by GC. Unsurprisingly, no carbon-based species can be detected in the gaseous samples presumably due to the insufficient quantity. Significantly, in the presence of both ZnO photocatalyst and UV-irradiation, substantial COD reductions were recorded.

The results obtained for 0.1 – 2.0 g/L of ZnO loadings are shown in Figure 5.5a. In Figure 5.5a, smooth photocatalytic degradation profiles are obtained for all sets of photoreactions. This proves that the ZnO photocatalyst was highly reactive under UV irradiation, attributed to its large band gap value (3.2 eV), as aforementioned in the UV-Vis DRS results. In addition, the photocatalytic degradation efficiency values at 240th min for all sets of photoreaction runs were computed using Equation (1) and shown in Figure 5.5b. At a zero ZnO loading (photolysis), low photocatalytic degradation efficiency (< 2.0%) was obtained. In the presence of 0.1 g/L of ZnO, the degradation efficiency was drastically enhanced to more than 20%. Furthermore, the degradation efficiency increased with the ZnO loading until an optimum point at a catalyst loading of 1.0 g/L, with around 50% of degradation efficiency achieved. The increment in catalyst loading has increased the surface area responsible for the organics photocatalytic degradation; hence the efficiency. However, beyond 1.0 g/L loading, no enhancement in degradation was observed. Most likely, the light-scattering effect due to the excessive presence of ZnO particles has overwhelmed the effects of increase in surface area.

Consequently, for 2.0 g/L of ZnO photocatalyst, 45.33 % of degradation was achieved, slightly lower than the 1.0 g/L loading (50%).

5.3.2 Langmuir-Hinshelwood (LH) Rate Law Modeling

The kinetics data for the reaction was modelled to the Langmuir-Hinshelwood (LH) rate law equation. Similar with previous chapter, photodegradation of POME over UV/ZnO system was also an irreversible and surface limited reaction that occurred on single site. Hence, Equations 4.2 – 4.4 were employed for the modeling practice.

Figure 5.6, which compiles the modelling exercise, shows excellent model-adherence with R^2 -value of at least 0.95. This confirms that the decomposition of organics in POME followed 1st order reaction kinetics. The reaction constant, k , determined from the linear slopes, is summarized in Table 5.1. It can be seen that the highest k -value was $3.118 \times 10^{-3} \text{ min}^{-1}$ for 1.0 g/L of ZnO loading $> 3.025 \times 10^{-3} \text{ min}^{-1}$ (1.5g/L) $> 2.575 \times 10^{-3} \text{ min}^{-1}$ (2.0 g/L) $> 2.346 \times 10^{-3} \text{ min}^{-1}$ (0.7 g/L) $> 1.18 \times 10^{-3} \text{ min}^{-1}$ (0.5 g/L) $> 1.022 \times 10^{-3} \text{ min}^{-1}$ (0.1 g/L).

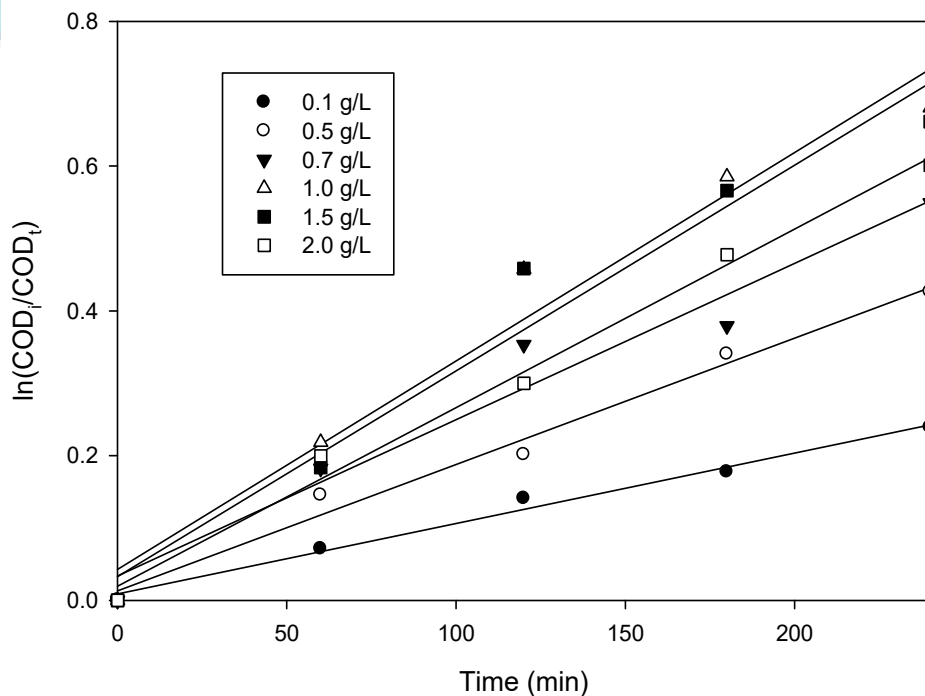


Figure 5.6 Illustration showing good adherence to the 1st-order kinetics modeling

Table 5.1 k -values obtained from the photodegradation of POME over different ZnO loadings

ZnO loading (g/L)	$(k) \times 10^3 \text{ (min)}^{-1}$	R^2
0.1	1.022	0.99
0.5	1.818	0.98
0.7	2.346	0.95
1	3.118	0.96
1.5	3.025	0.96
2	2.575	0.99

In addition to the degradation, the pH and decolourization of the POME sample were also monitored the readings are presented in Figure 5.7.

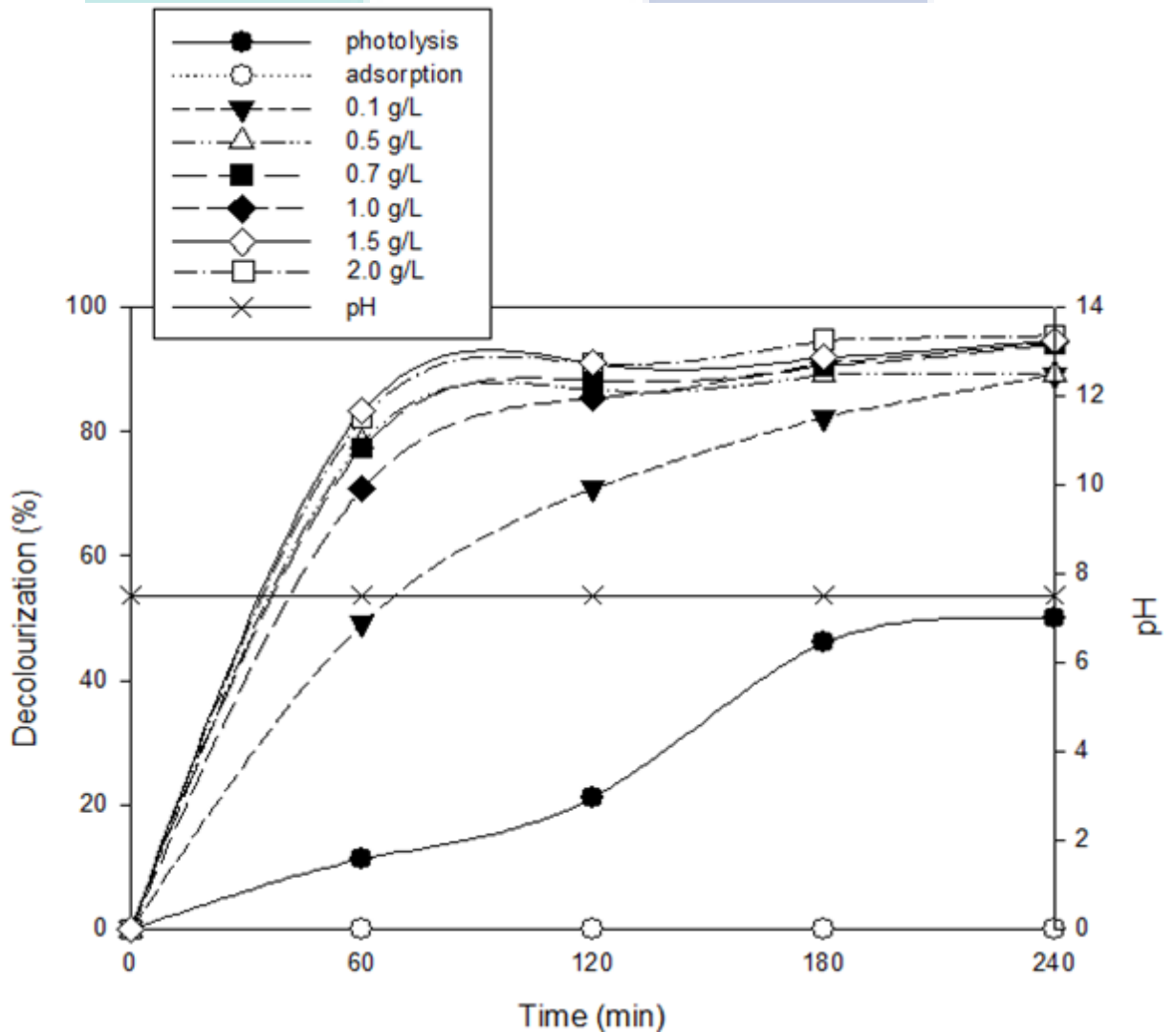


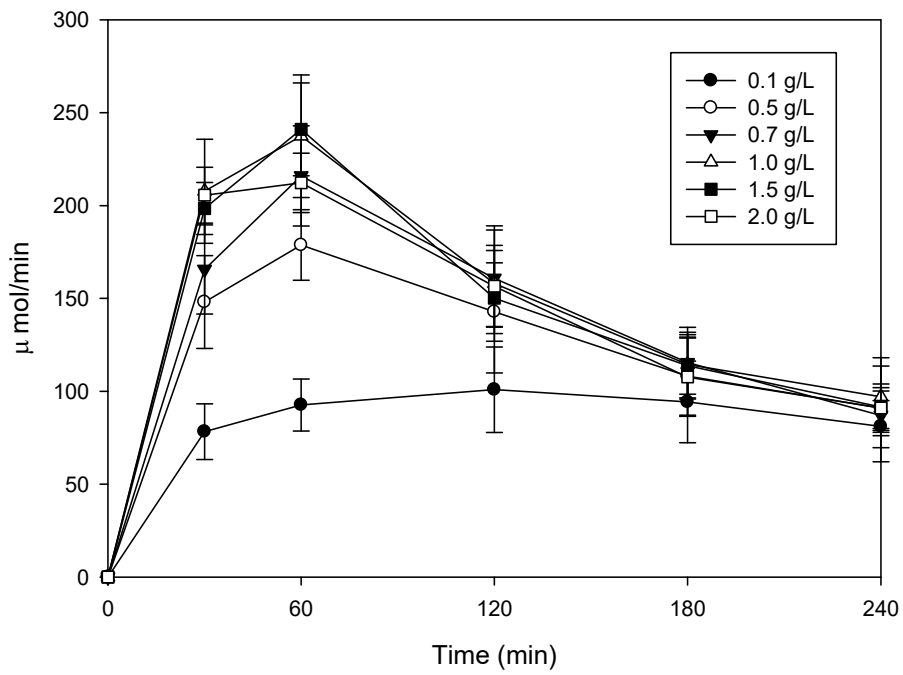
Figure 5.7 pH and decolourization profiles for all the photoreactions

The initial pH value of POME for all sets of photoreaction was 7.5. The transient pH value was also, always maintained at its nascent value. Therefore, it can be inferred that the initial concentration of substrate in POME sample was low and the photocatalytic degradation process did not affect the pH value. In addition, the POME decolourization profiles were also plotted and illustrated in Figure 5.7. POME sample from the adsorption study showed zero decolourization, as no reaction has occurred in the absence of UV irradiation. For photolysis process, about 45% of decolourization was obtained. In the presence of ZnO photocatalyst, decolourization was further exacerbated with higher catalyst loadings. Nonetheless, at 240th min, the decolourization achieved for all the photocatalytic reactions have attained 90 – 95% indicative of near complete destruction of refractory-organic compounds in the sample.

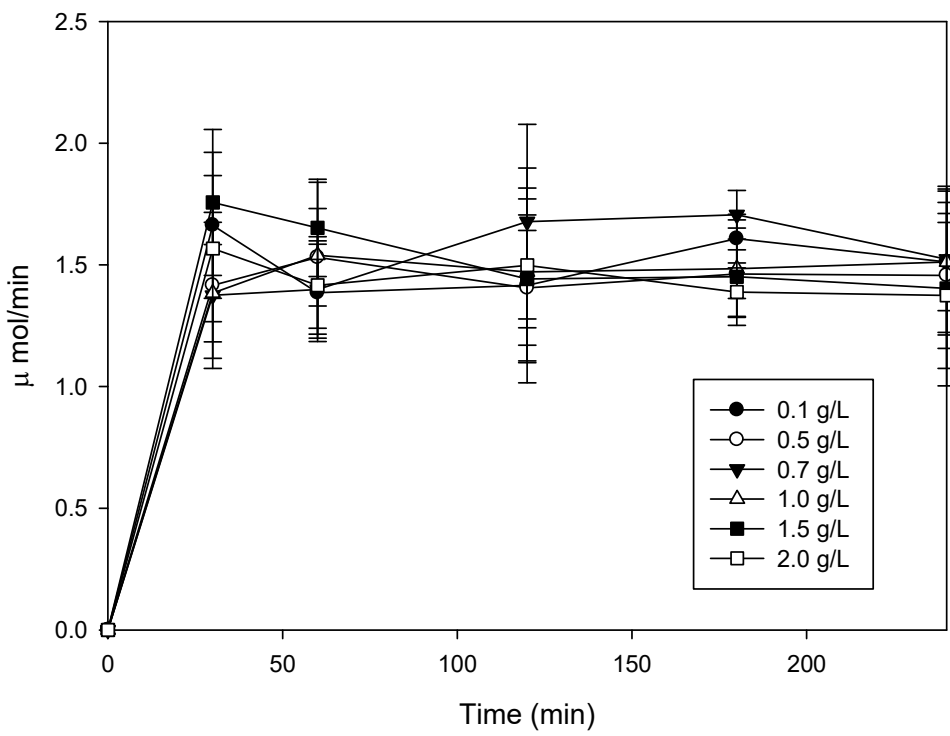
5.3.3 Gaseous Products from the POME Degradation

Besides, the gaseous products collected were eluted by using GC and the results are plotted in Figure 5.8. Based on the results, there were two product species detected in the sample, namely CO₂ and CH₄. Referring to Figure 5.8a, similar with the previous chapter, a general trend was observed in CO₂ production rate, in which the production rate increased at the initial stage of the photoreaction and achieved maximum point at around 60 mins. After that, the production rate decreased, mainly due to the exhaustion of organic substrates in the POME waste. However, compared to CO₂ production, CH₄ shows a comparatively stable production trend over the entire 240 min of photoreaction (refers to Figure 5.8b). The detection of carbon species as gaseous products showed that the carbonaceous species from the liquid POME has been converted into gas species. Indeed, this serves to confirm that a photocatalytic degradation process has taken place.

In addition, the total gas produced through the entire photoreaction process for each experiment was calculated and tabulated in Table 5.2. By referring to Table 5.2, CO₂ seems to be the major product from the photocatalytic degradation process due to the continuous flow of O₂ into the system. As aforementioned, this is unsurprising considering that CO₂ is a very stable species. Consequently, it is very easy to form especially when the photocatalytic degradation process occurs under oxygen-rich environment like in the current work. This finding was supported by Manickam et al. (2014) and consistent with previous chapter.



(a)



(b)

Figure 5.8 Production rate for (a) CO₂ (b) CH₄

Similarly, during photocatalytic degradation process, the organic pollutant in POME has been degraded into smaller fragments before fully mineralized, and CH₄ was one of the products formed during the decomposition. Hence, trace of CH₄ was detected in the gaseous product. For CO₂, the highest CO₂ amount produced after 240 min of UV irradiation was 36,172 μmol, achieved by employing 1.0 g/L of ZnO, whilst the lowest CO₂ production observed was by 0.1 g/L, which accounts for only 20,662 μmol (cf. Table 5.2). In terms of CH₄, the production after 240 min was very similar for all the experiments, ranged from 325 to 353 μmol, without any obvious trend. As mentioned earlier, the loss of carbonaceous species from the system indicates the occurrence of photocatalytic degradation process. Therefore, the total amount of collected gas shall correlate with the photocatalytic degradation efficiency. In Figure 5.9, the relationship between the product gas and the degradation efficiency is illustrated. Interestingly, the total gas produced exhibits similar trend with the degradation efficiency (cf. Figure 5.9). This posits that the gaseous products were directly originating from the organic degradation contained in the POME waste.

Table 5.2 Total gas products collected from photoreactions

ZnO loadings (g/L)	Gas accumulated over 240 min of photoreaction (μmol)	
	CO ₂	CH ₄
0.1	20662	339
0.5	30275	327
0.7	33873	353
1.0	36172	333
1.5	35383	342
2.0	34296	325

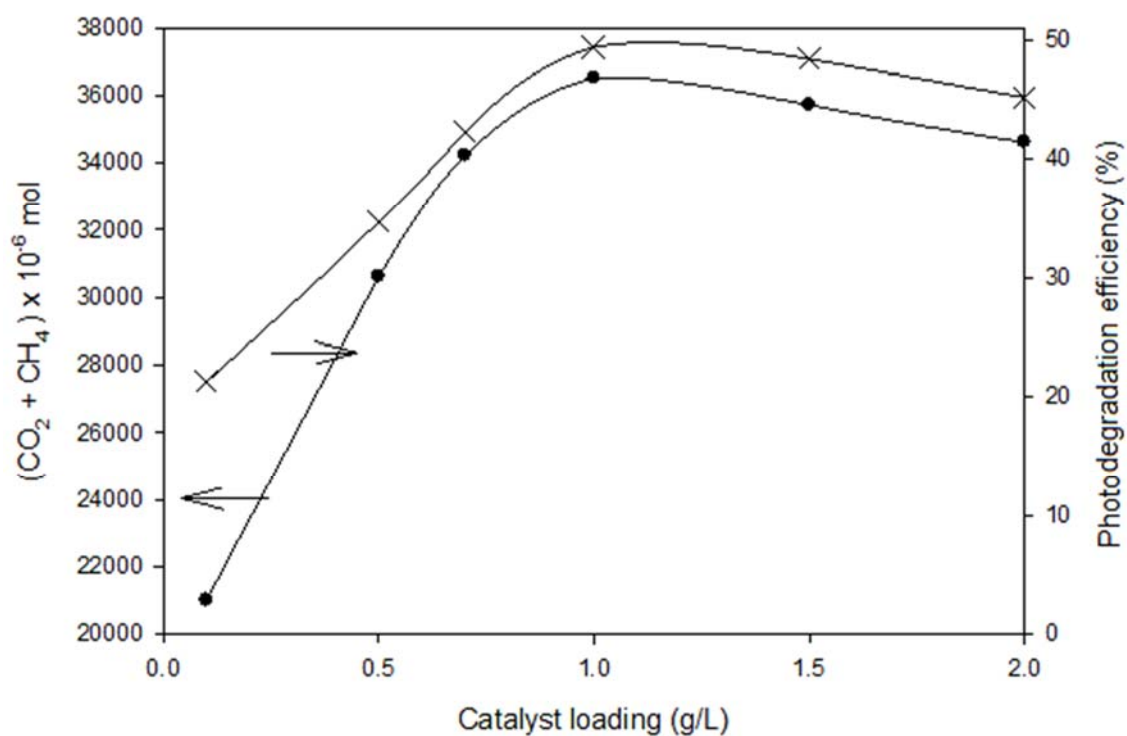


Figure 5.9 The relationship between gaseous products collected and photocatalytic degradation efficiency

5.3.4 Scavenging Study and Mechanisms of Degradation

The scavenging study was conducted with the same scavengers described in previous chapter. The role of reactive species, i.e. electrons(e^-), holes(h^+) and hydroxyl(OH^\bullet) radicals were determined by using a series of controlled experiments with different additives. Figure 5.10 displays the results obtained from the scavenging study. As aforementioned, O_2 is a well-known electron acceptor that suppresses the recombination of electrons and holes. Hence for electron-scavenged experiment, O_2 -bubbling was replaced with N_2 -bubbling to eliminate the possibility of electron consumption. In Figure 5.10, the degradation efficiency achieved for this set of experiment was significantly prohibited, dropping almost 50.0% to 1.0 % after 240 min of UV irradiation. Without O_2 molecules, the electron acceptor, in the slurry solution, the recombination rate of the photo-generated charges was very fast that the degradation was almost completely disabled.

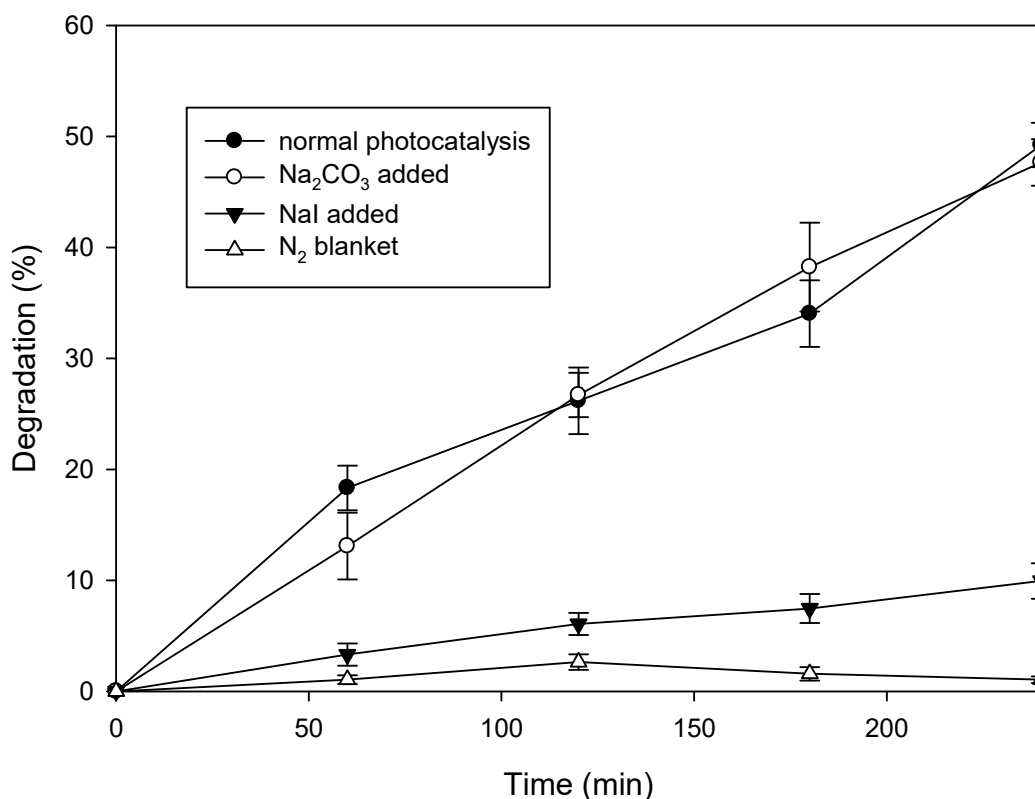


Figure 5.10 Results obtained from scavenging study employing 1.0 g/L of ZnO

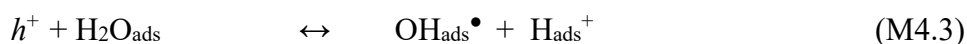
On the other hand, photoreaction (1.0 g/L of ZnO and 70 mL/min of O₂ bubbling) with Na₂CO₃ (1.0 ml, 1.35 M) added was also conducted to scavenge the OH[•]_{free}, following Equation (M4.8) in previous chapter, generating the high selectivity carbonate radical, CO₃^{•-}, as the product.



Surprisingly, no obvious deterioration in the degradation efficiency for Na₂CO₃-added photoreaction was observed, indicating that hydroxyl free radical, OH[•] species, was not the key reactive species during the *photocatalytic degradation* process. At the end of the experiment, more than 48.0 % of degradation efficiency was achieved.

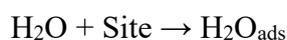
On the other hand, the photoreaction with NaI (1.0 ml, 1.35 M) as an additive showed a large deterioration in the degradation efficiency (refers to Figure 5.10). In the absence of NaI additive, photo-generated holes (h⁺) were consumed by the water molecules, eventually forming hydroxyl radicals (OH[•]) for the organics destruction in accordance with the Equation (M4.3). However, with NaI added, I⁻ ion from the salt

would occupy the generated h^+ (M4.9), subsequently inhibit the formation of OH^{\bullet} radicals and consequently causing the degradation efficiency to drop to below 10% threshold.



The findings from the scavenging study demonstrate that most likely the organics pollutants in POME has adsorbed on the surface of ZnO, followed by the destruction initiated by the UV-generated OH_{ads}^{\bullet} . Significantly, this proposition represents a total departure from our previous findings for the UV/TiO₂ system. In the previous chapter, we have found that for the UV/TiO₂ system, the organic pollutant in the POME was degraded by the bulk-phase hydroxyl radical (OH_{free}^{\bullet}) due to the poor affinity of TiO₂ towards organic adsorption. As opposed to the TiO₂ photocatalyst, organic pollutant can easily adsorb on the surface of ZnO (Abed et al., 2015; Achouri et al., 2016; Baruah et al., 2008; Di Mauro et al., 2016). Consequently, the destruction of organic caused by OH_{ads}^{\bullet} took place on the surface of photocatalyst instead of bulk solution by OH_{free}^{\bullet} . This is proven when the photoreaction with OH_{free}^{\bullet} -scavenged (Na_2CO_3 added) did not affect the degradation efficiency. On the other hand, the drastic deterioration observed during h^+ -scavenged photoreaction indicates that the OH_{ads}^{\bullet} formed from the water pathway (cf. Equation (M4.3)) was the key reactive species for organics destruction process, which contributed to about 80% of the total destruction, while the remaining was contributed by the oxygen pathway-generated OH_{ads}^{\bullet} , UV irradiation (photolysis) and the synergic effects of all the reactive species.

Hence, by combining the findings from the scavenging studies and gaseous products obtained from the photoreaction, the mechanisms of the photocatalytic degradation of POME waste are proposed herein. Firstly, the O₂, H₂O and organic molecules (denoted by C_aH_bO_c) would be adsorbed on the surface of ZnO (cf. Equations (M4.1) and (M5.1)).



In order to initiate the photoreaction, the charges, positive holes (h^+) and the negative electron (e^-) were generated under UV-irradiation through photoexcitation process according to the Equation (M5.2). Subsequently, both h^+ and e^- were consumed by water and O_2 , respectively, and eventually forming the highly reactive hydroxyl radicals (OH^\bullet) that plays a crucial role in destructing the organic pollutants. The steps in forming OH^\bullet through H_2O -pathway is represented by Equation (M4.3), while Equations (M4.4) to (M4.7) are representing the O_2 -pathway. After photoexcitation, the generated electron was scavenged by O_2 , leaving behind the super-oxide anions ($O_{2,ads}^-$) as the intermediate product as in Equation (M4.4). Subsequently, the O_2^- ion would react with H_{ads}^+ (from Equation (M4.3)) through the Equations (M4.5) and (M4.6). Hydrogen peroxide (H_2O_2) formed would further dissociate into $OH_{,ads}^\bullet$ upon exposure to the UV irradiation as in (M4.7).



Instead of desorbing as in previous chapter, these generated OH^\bullet radicals would attack the adsorbed organic molecules directly, degraded them into intermediates products, H_2O , CO_2 and CH_4 . Finally, CO_2 and CH_4 would desorb from the ZnO surface as the final products (M5.3).



Again, due to rich-oxygen environment, there is a higher tendency that the organic pollutants would be mineralized into CO_2 compared to CH_4 . This explains the lower CH_4 obtained during the photoreactions. Figure 5.11 illustrates the overall mechanisms of the current process.

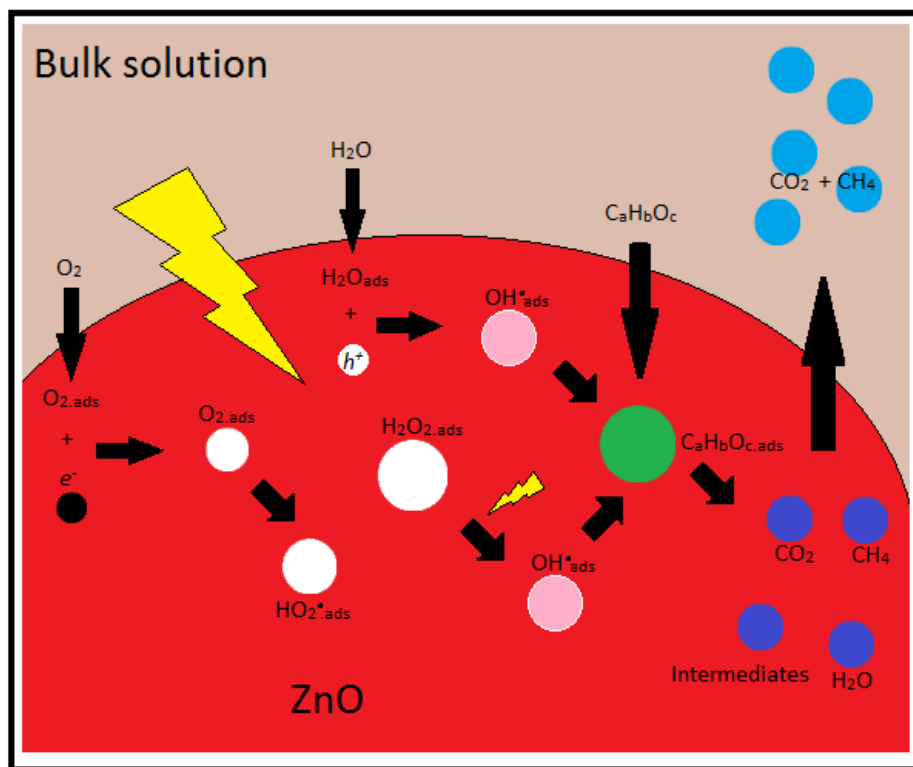


Figure 5.11 Mechanisms proposed for the photocatalytic degradation of organic pollutants in POME over ZnO photocatalyst under UV irradiation

5.3.5 Recyclability and Longevity Studies

The recyclability of ZnO photocatalyst was examined by conducting three consecutive photoreaction runs with a same batch of ZnO photocatalyst. The ZnO photocatalyst was recovered through filtering process, multiple-washing by water and ethanol, before finally being oven-dried at 323 K. Figure 5.12 shows the results obtained from photoreaction with 1.0 g/L ZnO powder and 70 ml/min of oxygen bubbling rate. Obviously, ZnO photocatalyst cannot attain its first cycle's performance, dropping from 49.4% to 35.2% and then 37.8% for second and third run, respectively. The diminishing activity albeit not drastic, could be possibly due to the deposition of carbonaceous species on the surface of photocatalyst. Consequently, this may have reduced the surface area of ZnO.

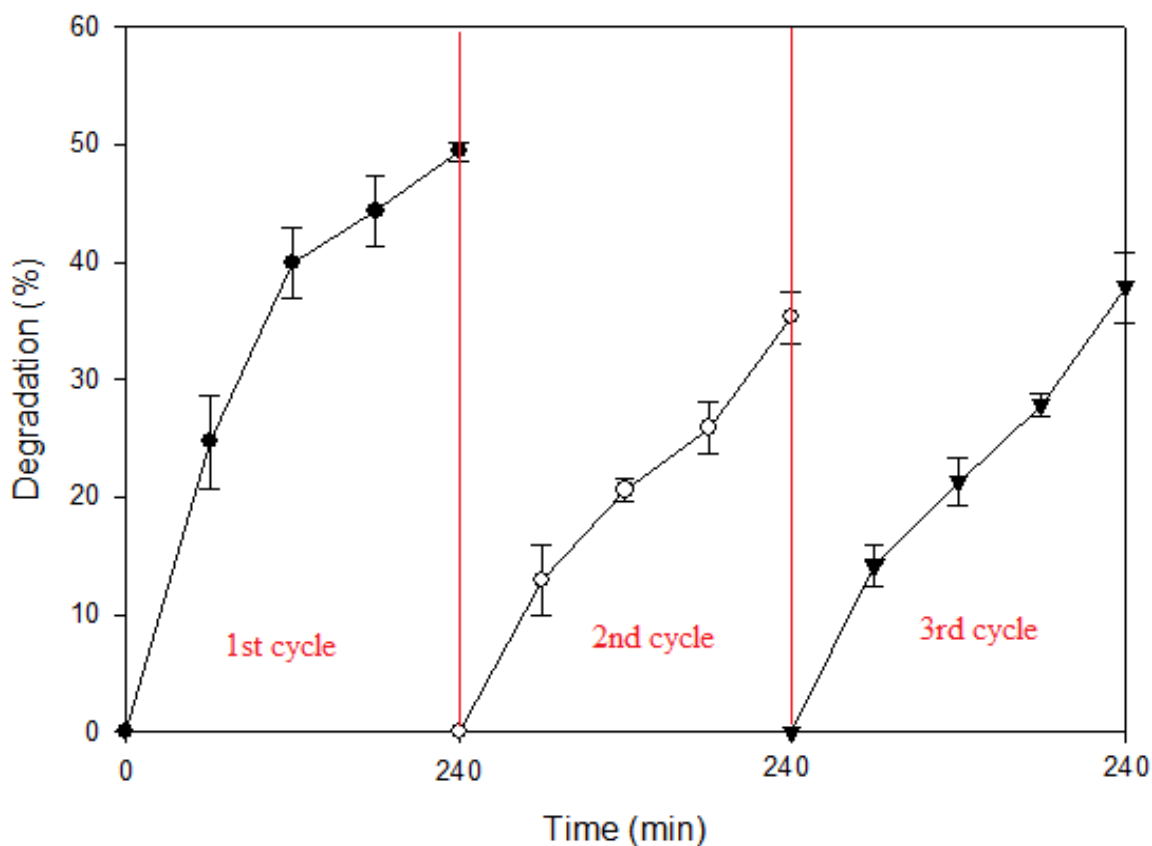


Figure 5.12 Results obtained from recyclability test with reaction conditions of 1.0 g/L ZnO and 70 ml/min of O₂-bubbling rate

Longevity run was also conducted and it is found that the COD level dropped to 44 ppm (COD standard discharge threshold is equivalent to 50 ppm) after 22 h of UV irradiation in the presence of 1.0 g/L of ZnO. The result is presented in Figure 5.13. The steep slope at the beginning of the photoreaction indicates fast degradation rate. However, after the 4th hour, the degradation rate decreases drastically, which can be attributed to the following two factors: (1) Low concentration of organic pollutants in POME waste after certain time of photoreaction and (2) loss of catalyst's reactivity due to carbon deposition. However, 74.11% of degradation efficiency was achieved after 22 h of UV irradiation.

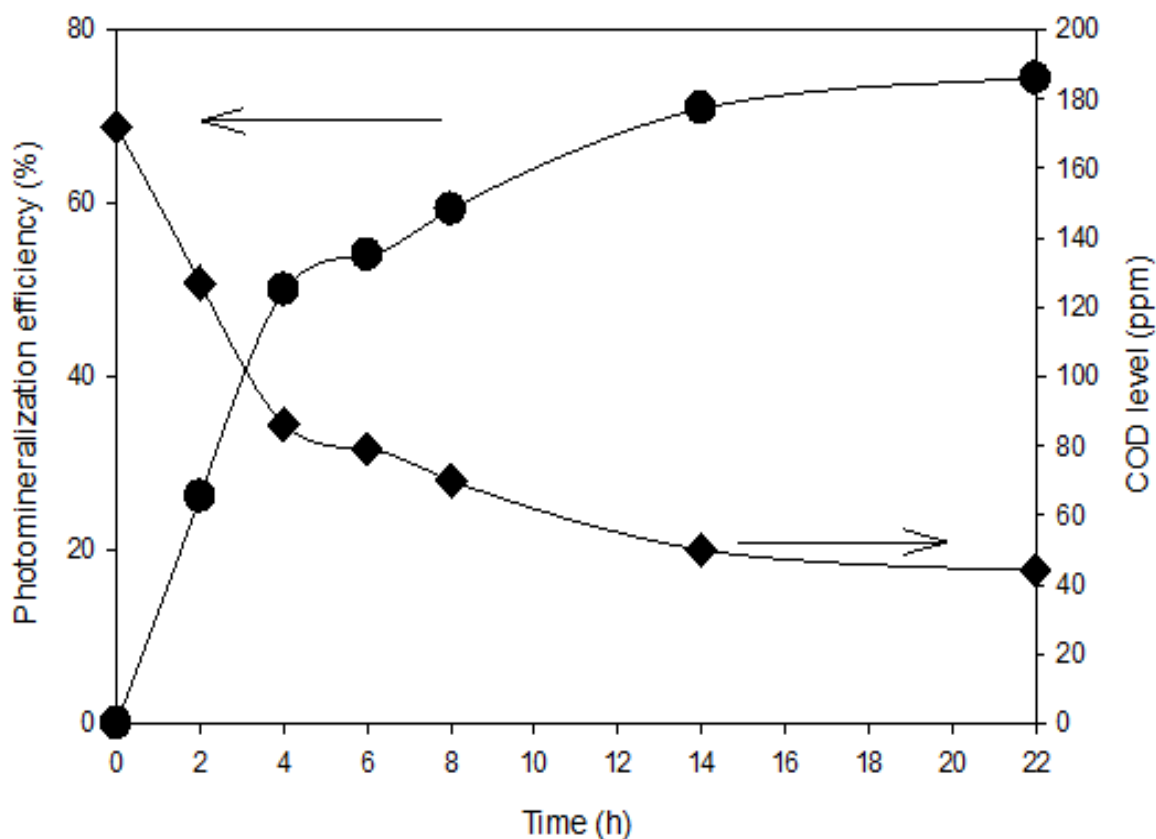


Figure 5.13 Results obtained from longevity test with reaction condition of 1.0 g/L of ZnO and 70 ml/min of O₂-bubbling

Selected POME samples (0, 2nd, 4th, and 22nd h) from the longevity test were subjected to ¹³CNMR analysis due to the same justification presented in Section 4.5.5. The spectrums obtained are illustrated in Figure 5.14. Only one peak that corresponds to the carbonyl carbon group was observed at around δ 160 ppm in all the four spectrums, suggesting that this group forming the bulk of POME solution. During photocatalytic degradation process, the entire organic degradation process occurred on the surface of ZnO, instead of occurring in bulk solution as in UV/TiO₂ system. Hence, the component in bulk solution was not altered and this explains the single signal obtained in all the ¹³CNMR spectrums. In addition, the intensity of the signal became weaker with UV irradiation time, which can be ascribed to the continuous removal of the organics during the photocatalytic degradation process.

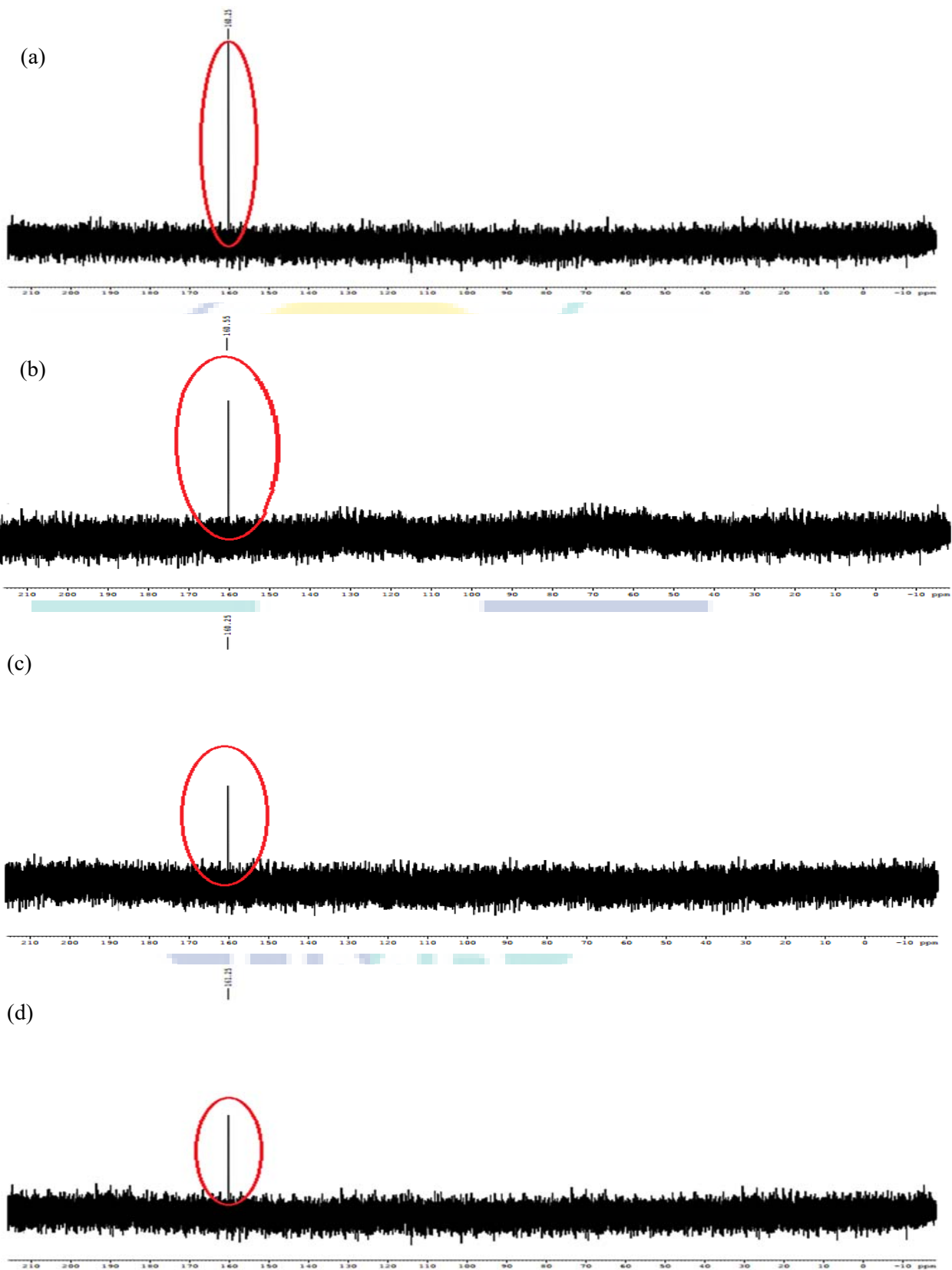


Figure 5.14 ^{13}C NMR spectrums of POME (a) 0 h (b) 2 h (c) 4 h (d) 22 h

Besides COD, the final readings of BOD and O&G (at 22nd h) for POME sample were also obtained. The results are tabulated in Table 5.3. After 22 h of UV irradiation in the presence of 10 g/L of ZnO and 70 mL/min of O₂, the final COD, BOD and O&G readings were 44 ppm, 26 ppm and 20 mg/L (recording 74.11%, 76.36% and 79.38% degradation), respectively, which have satisfied the existing regulations of DoE.

Table 5.3 Comparisons of the parameters before and after photocatalytic treatment process

Parameter	Before reaction (ppm)	After reaction (ppm)	Required level (ppm)	Degradation (%)
COD	170	44	50	74.11
BOD	110	26	20	76.36
Oil and Grease (O&G)	97	20	50	79.38

5.4 Post-reaction Analysis for ZnO Photocatalyst

After three consecutive photoreaction runs (cf. Figure 5.12), the ZnO photocatalyst was subjected to the aforementioned cleaning protocol before being subjected to post-reaction characterization due to the same justification mentioned in Section 4.6.

The FESEM images of washed ZnO are illustrated in Figure 5.15. Under 10 kx and 30 kx (Figures 5.15a and 5.15b) magnification, the irregularity of ZnO photocatalyst in shape and size were still obvious. With higher magnification (50 kx and 100 kx), the surface of ZnO seems to be rougher compared to fresh ZnO presented in Figure 5.2. Besides, ‘small nodules’ (circled in red) were observed in both high magnified images (Figure 5.15c and 5.15d), which could be due to the deposited carbonaceous species.

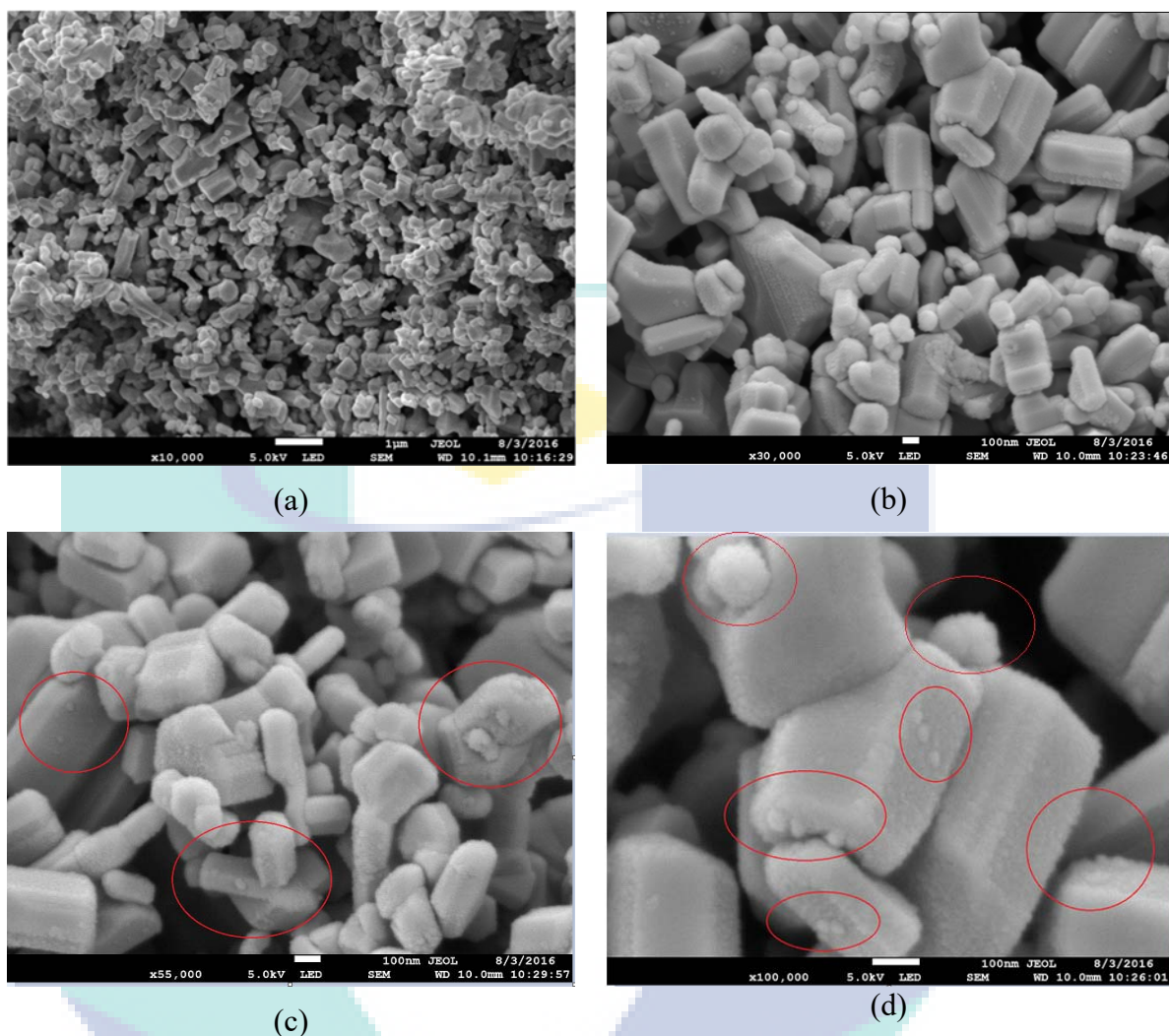


Figure 5.15 FESEM images of spent ZnO photocatalyst (a) 10kx (b) 30kx (c) 55kx (d) 100kx

Figure 5.16 shows the N₂ adsorption and desorption isotherms for the used ZnO. Similar with fresh ZnO (cf. Figure 5.3), type III isotherms was also obtained for the used ZnO. However, both BET specific surface area and pore diameter were reduced from 9.71 m²g⁻¹ and 6.47 nm to 4.05 m²g⁻¹ and 4.33 nm, respectively. This can be positively linked to the clogging of surface area by the carbonaceous compounds, whereby its presence has been observed in FESEM images discussed earlier (cf. Figure 5.15).

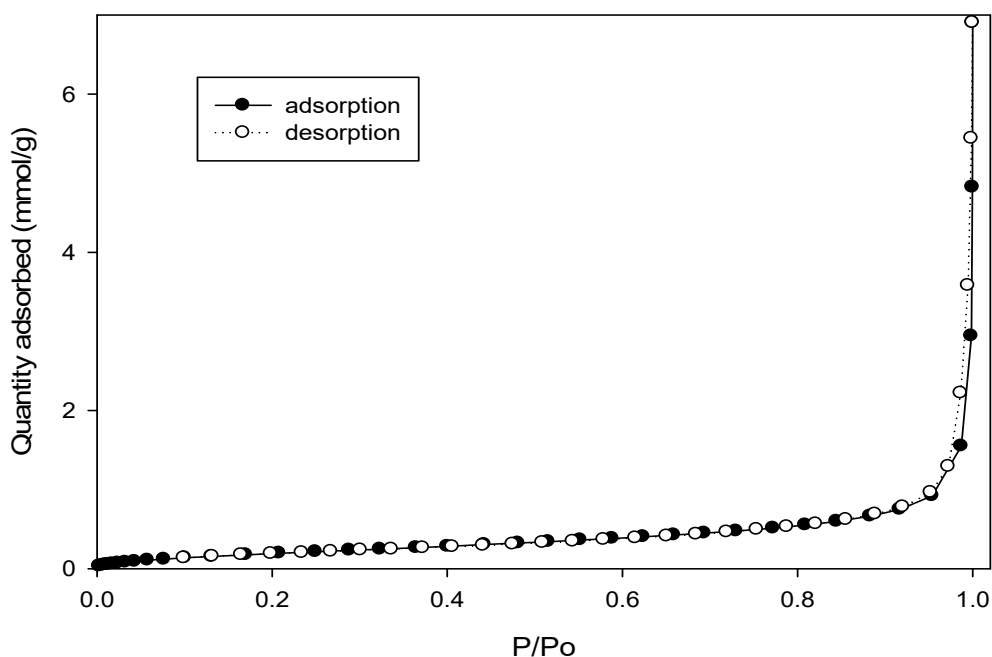


Figure 5.16 N_2 adsorption and desorption isotherms for recycled ZnO photocatalyst

In addition, same batch of spent ZnO photocatalyst was also analysed by using FTIR spectroscopy. Figure 5.17 shows the magnified FTIR spectra (inset: full figure) for both used and fresh ZnO photocatalysts. There are seven additional peaks observed for the used ZnO compared to the fresh ZnO. Interestingly, some of the peaks (labeled \square) in the used ZnO spectrum are consistent with the peaks observed in dried POME in previous chapter (refers to Figure 4.1), indicating the chemisorption of organic pollutants on the surface of ZnO. This is consistent with the FESEM images and N_2 physisorption isotherms (Figures 5.12 and 5.13). All these results also serve to confirm the results obtained from our earlier scavenging study whereby surface-adsorption of organic pollutant was postulated. In addition, two more peaks (labeled \circ) are also obtained for the used ZnO photocatalyst at wavelength of $2750\text{-}2650\text{ cm}^{-1}$ and $1283\text{-}1247\text{ cm}^{-1}$, that corresponds to the stretching of aldehyde C-H bond (Augustana University, n.d.) and stretching of aromatic C – O bond respectively (Oo et al., 2009). The emergence of these peaks could be due to the intermediate products that chemisorb on the surface of ZnO, hence confirming the formation of smaller fragments in mechanisms proposed in Section 5.3.3.

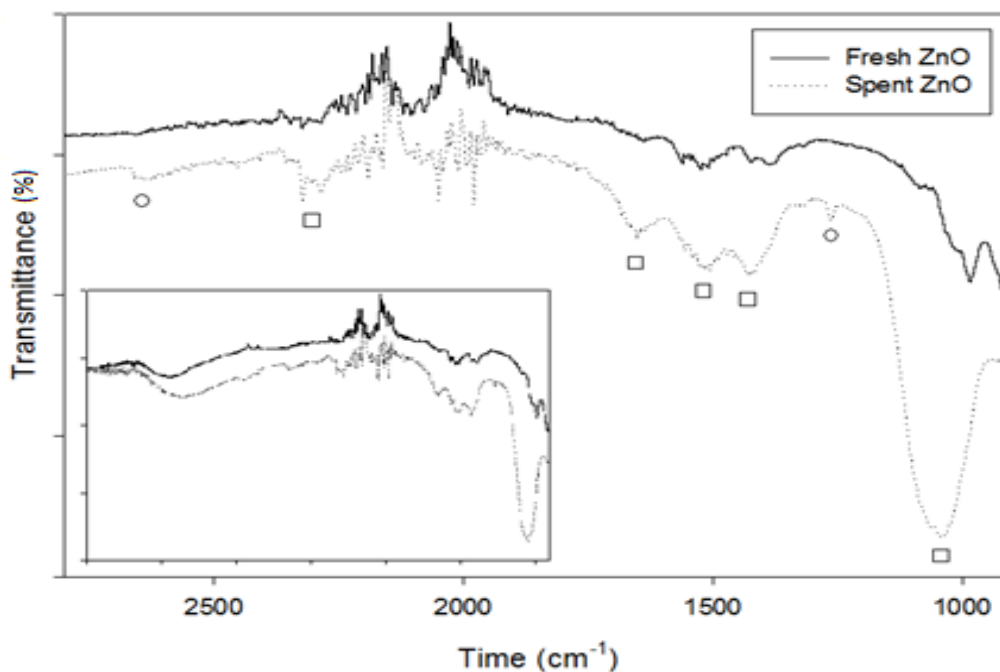


Figure 5.17 FTIR spectra of fresh and recycled ZnO

Furthermore, EDX was employed to obtain the element profile of the used ZnO. As determined by the EDX mapping in Figure 5.18, the elements in the photocatalyst are Zn (green) and O (blue), with some traces of C atom (red), consistent with the FTIR results. Based on EDX spectrum in Figure 5.19, the peaks observed in 1026 eV, 8630 eV and 536 eV correctly matched to the Zn L α , Zn K α and O K α peaks, respectively, confirming the presence of Zn and O elements in the sample. Besides, these two elements are the predominant elements in the sample (Zn, 36.86% and O, 45.38%), judging from the high molar ratio. Furthermore, the metal:oxygen ratio is approximately 1.0, suggesting high dispersion of metal element that favours the degradation process. On the other hand, the traces of C elements are believed to be the organic impurities that deposited on the surface during the photoreaction. Moreover, the EDX spectrum is also shown in Figure 5.19. Other than the Zn and O elements, EDX has also detected C element on the surface of ZnO, judging from the peak located at 227 eV (C K α peak), amounted to 17.77% of molar ratio (6.37 in wt%), sufficient to reduce the reactivity of photocatalyst as reported in the recyclability test discussed earlier.

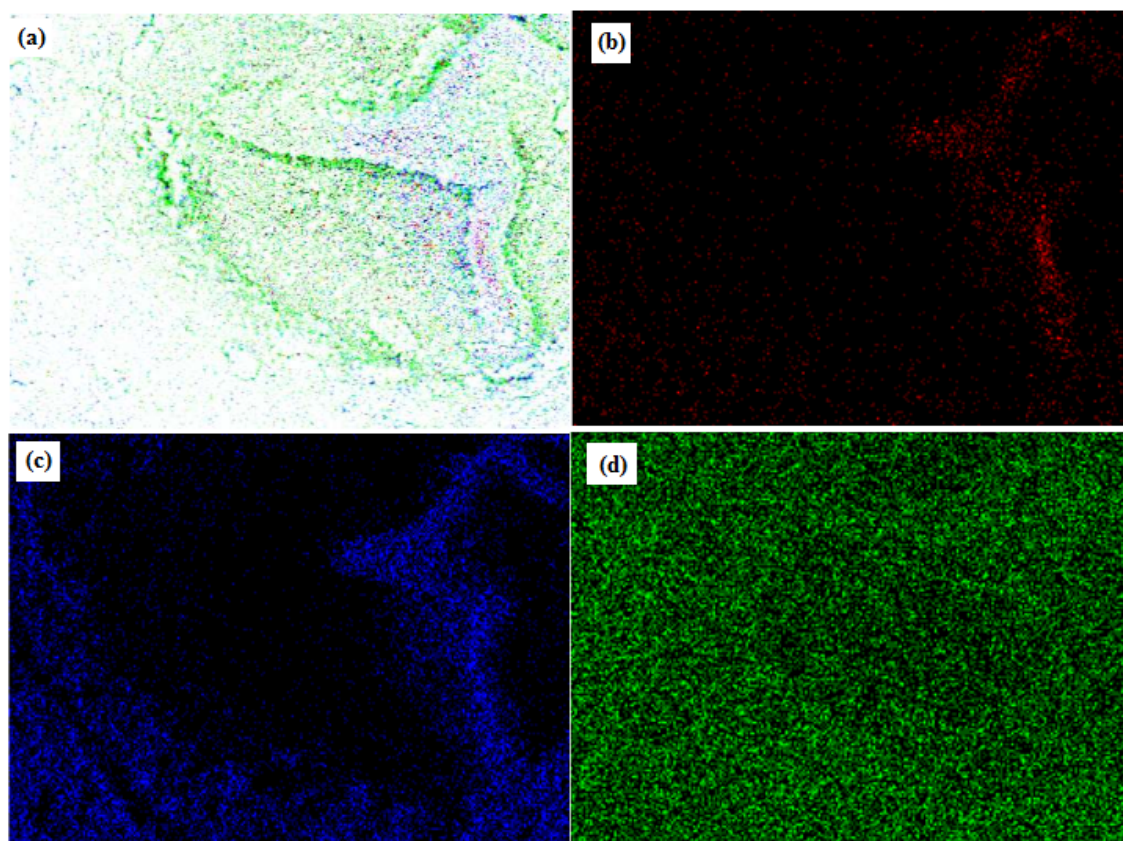


Figure 5.18 EDX mapping for (a) combined (b) Carbon (c) Zn (d) Oxygen

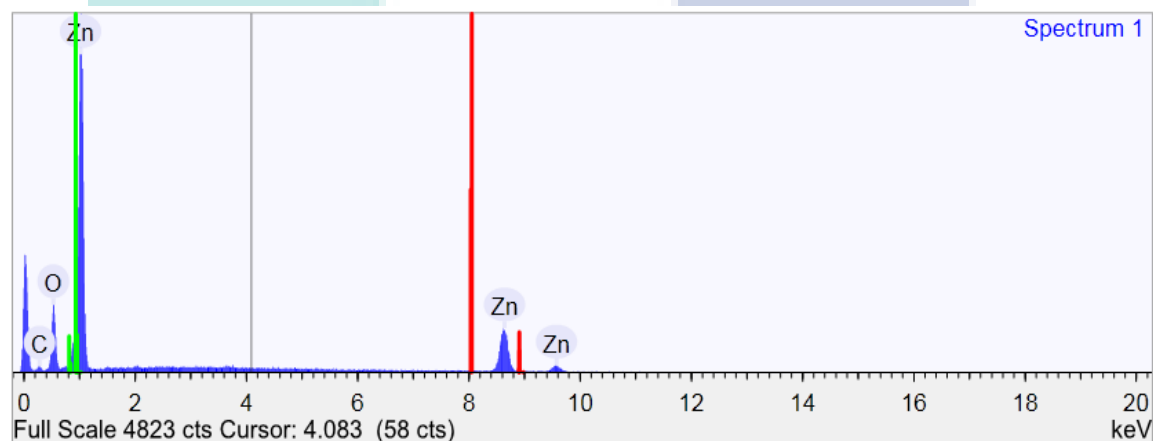


Figure 5.19 EDX spectrum of used ZnO

Summarizing from the results obtained in current section, all the post reaction analysis confirmed the deposition of the organics pollutant onto the surface of ZnO during the photocatalytic degradation process, which supports the mechanisms proposed in Section 5.3.3. At the same time, the emergence of two new peaks in FTIR spectra also confirmed the formation of intermediate products during the process. Besides, the reasoning in losing reactivity during recyclability test was also confirmed, in which the

deposition of carbonaceous species has reduced the number of active spots in ZnO photocatalyst. Hence, regeneration step was necessary to restore the activity.

5.5 Optimization of the Process

The UV/ZnO system was subjected to process optimization to further enhance the degradation that can be achieved. The factors to be optimized include oxygen flowrate, ZnO loading and initial concentration of POME. Prior to optimization, these factors were statistically screened by using 2^3 level full factorial design and subsequently being optimized by using CCD in RSM.

5.5.1 Significance Analysis of Main Factors

The significance of the main factors was statistically tested in current section using 2^3 level full factorial design, followed by the discussion.

5.5.1.1 Design of Experiment: Two-level Full Factorial Design

All three main factors were subjected to a 2^3 full factorial design for significance analysis. The investigation was conducted with wide ranges for all the main factors, viz. 0 – 150 ml/min of O₂ flowrate, 0 – 1.5 g/L of ZnO loading and 100 – 400 ppm of initial concentration of POME. All the experiments were triplicated, with total 24 sets of experiments, and were conducted in the recommended order. Table 5.4 shows the experimental conditions as well as the results obtained for each set of experiment. According to Table 5.4, the degradation efficiency (%) achieved ranged from 1.24 % (No. 2) to 30.65 % (No. 12).

Table 5.4 Significance analysis of main factors

No.	O ₂ flowrate (ml/min)	ZnO loading (g/L)	POME concentration (ppm)	Degradation (%)
1	0	1.5	100	5.22
2	0	0	100	1.24
3	0	0	400	6.28
4	150	0	100	8.53
5	0	1.5	100	4.55
6	150	1.5	100	15.6
7	150	0	400	13.66
8	0	0	100	2.35
9	150	0	100	12.33
10	150	1.5	400	28.35
11	0	1.5	400	9.22
12	150	1.5	400	30.65
13	150	1.5	100	14.49
14	0	0	100	1.88
15	0	1.5	100	4.69
16	150	0	400	15.22
17	0	1.5	400	6.98
18	0	0	400	4.35
19	150	0	100	7.66
20	150	0	400	17.36
21	0	0	400	3.66
22	150	1.5	100	18.66
23	150	1.5	400	25.66
24	0	1.5	400	8.54

5.5.1.2 Statistical Analysis

Figure 5.20 shows the half-normal plot of all the main factors as well as the interactive factors for degradation efficiency. It can be seen that all the main and interactive factors are located to the right side of the normal line, suggesting significant contributions to the degradation. Moreover, it is noteworthy that all the main factors (A , B , and C) are distributed to the far right of the normal line, indicating higher effects towards the response (degradation efficiency) compared to the interactive factors (AB , AC , BC).

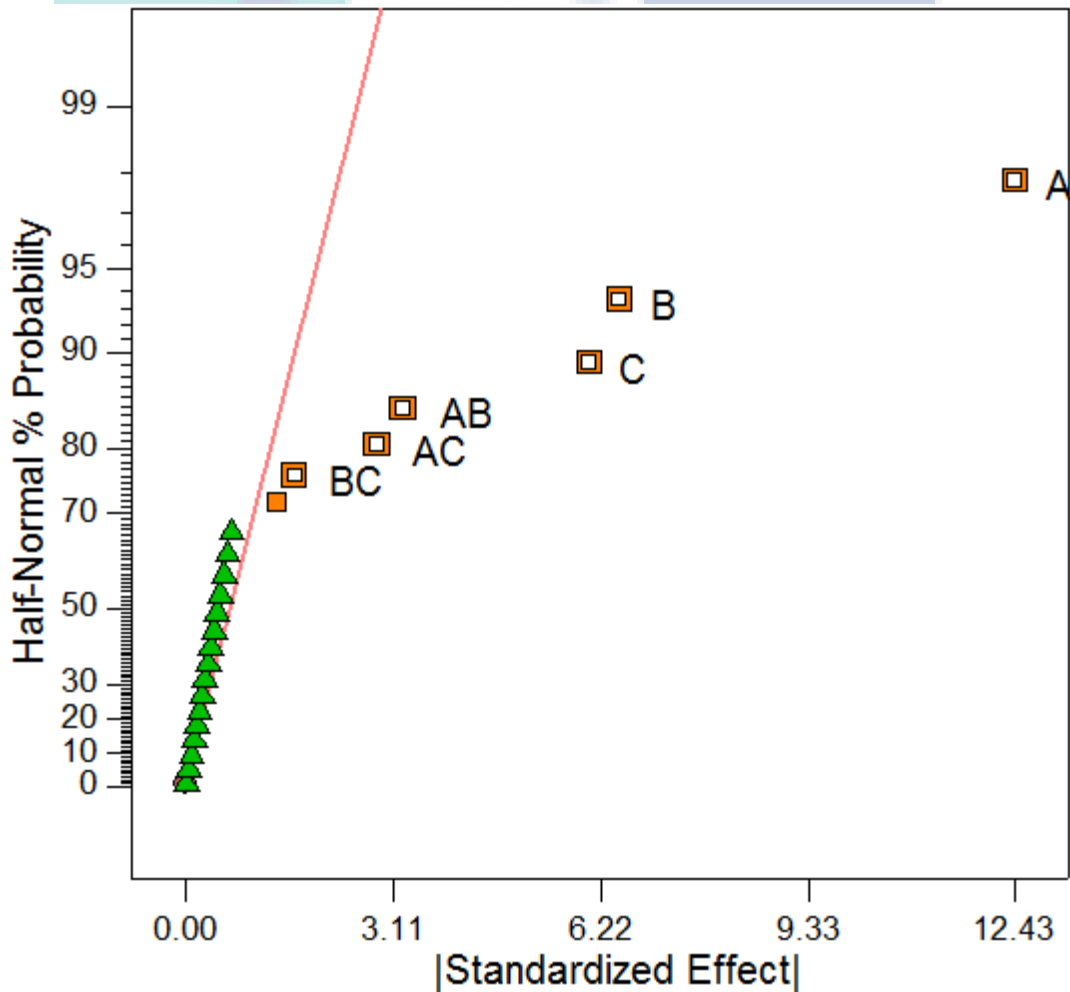


Figure 5.20 Half-normal plot of the factors for degradation efficiency (A = O_2 flowrate; B =ZnO loading; C =initial concentration of POME)

This is further confirmed by the Pareto Chart as can be seen in Figure 5.21. Based on Figure 5.21, all the factors, including the main factors (A , B , C) and interactive factors (AB , AC , BC), are contributing positive effects to the degradation efficiency.

Furthermore, all the factor bars have exceeded the t-value limit (2.1098), confirming the significance of the factors.

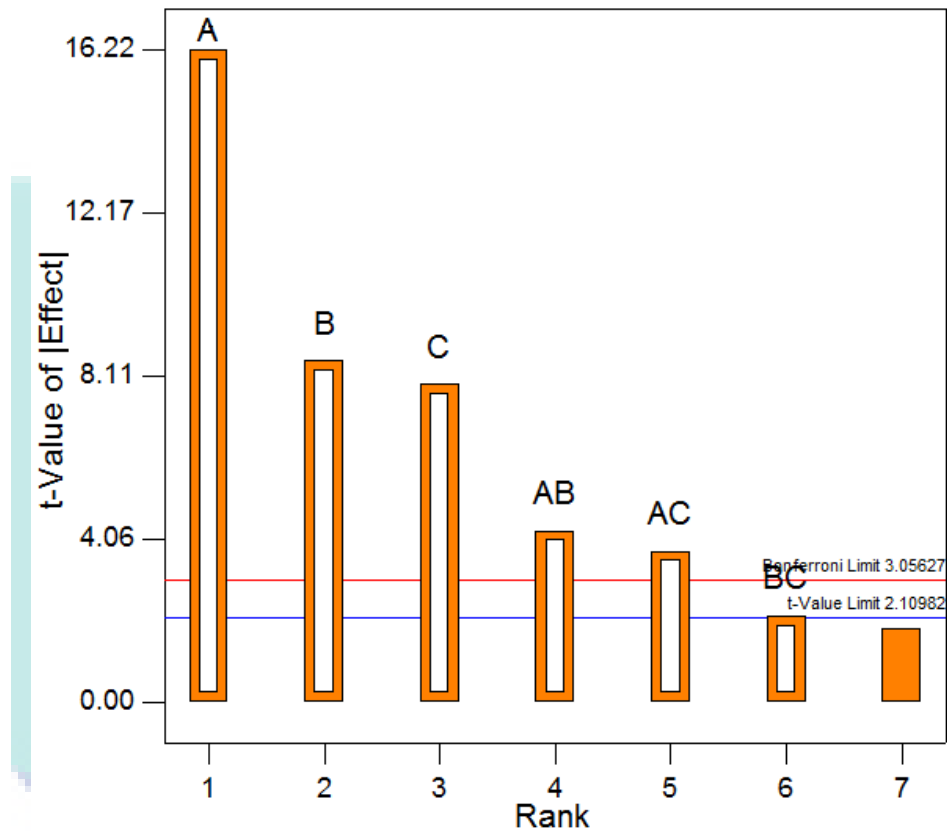


Figure 5.21 Pareto chart of the factors efficiency ($A=O_2$ flowrate; $B=ZnO$ loading; C =initial concentration of POME)

The contribution of each factors are presented in Table 5.5. Referring to Table 5.5, O_2 flowrate (A), as the biggest contributor for the degradation efficiency, has produced 58.27% of degradation, followed by ZnO loading (B , 15.96%), initial concentration of POME (C , 13.85%), AB (4.02%), AC (3.12%) and finally BC (1.01%). Apparently, the main factors (A , B , C) contributed the largest portion to the degradation efficiency (more than 87%) compared to the interactive factors. This is also consistent with the estimations in the half-normal plot (cf. Figure 5.20).

Lastly, the ANOVA analysis is presented in Table 5.6. The suggested model is confirmed significant, judging from low p-value (<0.0001), indicating a high confidence level. Besides, the high F-value (72.45) of the model also strongly implies the extremely low chances (0.01%) of noise interference. On the other hand, low p-value (<0.05) for

the factor is an indicative of the statistical significance at 95% confidence level. In addition, Table 5.6 also shows that the p-value for all the main factors and interactive factors are lesser than 0.05. This confirms that all the factors are statistically-significant.

Table 5.5 Contribution of each factor towards degradation efficiency

Factors	Contribution (%)
<i>A</i> – O ₂ flowrate (ml/min)	58.27
<i>B</i> – ZnO loading (g/L)	15.69
<i>C</i> – Initial concentration of POME (ppm)	13.85
<i>AB</i>	4.02
<i>AC</i>	3.12
<i>BC</i>	1.01

Table 5.6 ANOVA analysis obtained from the response

Source	Sum of Square	Degree of Freedom	Mean Square	F-value	p-value Prob>F
Model	1532.05	6	255.342	72.4532	< 0.0001
<i>A</i> -O ₂ flowrate	927.713	1	927.713	263.238	< 0.0001
<i>B</i> -ZnO loading	254.118	1	254.118	72.1059	< 0.0001
<i>C</i> -Initial concentration of POME	220.433	1	220.433	62.5477	< 0.0001
<i>AB</i>	64.043	1	64.043	18.1722	0.0005
<i>AC</i>	49.6657	1	49.6657	14.0926	0.0016
<i>BC</i>	16.0803	1	16.0803	4.56277	0.0475

5.5.1.3 Main Factors and Interactive Factors Effects

The main factors and interactive factors effects are illustrated in Figure 5.22. The lines in Figures 5.22a-5.22c demonstrate on the pattern of the main effects. Apparently, the line for O₂ flowrate (*A*, Figure 5.22a) has a steeper slope compared to the lines of ZnO loading (*B*) and initial concentration of POME (*C*) (Figures 5.22b and 5.22c), indicating larger effects towards the degradation efficiency (%). Coincidentally, the results in Table 5.5 also record the similar trend. The lines representing the ZnO loading (Figure 5.22b) and initial concentration of POME (Figure 5.22c) are exhibiting similar slope since both of them contributed almost equal effects towards the response.

In addition, the effects of interactive factors are also presented in Figure 5.22d – 5.22f. Two lines are observed in each of these figures and bracketed by least significant difference (LSD) bars at both ends. By observing Figures 5.22d – 5.22f, both lines in these figures are far from parallel, thus confirms the existence of the interaction effects between the main factors. From Figures 5.22d and 5.22e, the importance of O₂ flowrate to the reactive system can be easily observed. At low O₂ flowrate (*A*), neither increment of ZnO loading or POME concentration would enhance significantly the degradation efficiency, judging from the locations of LSD bars for both upper boundary (red lines) and lower boundary (black lines) at the left sides of Figures 5.22d and 5.22e. However, as the O₂ flowrate increased, the interactions between the factors occurs, inducing the synergic effects and further enhancing the degradation efficiency with higher ZnO loading or initial concentration of POME. Hence, the LSD bars are widely separated at the right sides of Figure 5.22d and 5.22e. With constant supply of O₂ (75 ml/min; Figure 5.22f), a comparatively lower interaction effect was observed, as only slight increment in the gap between the LSD bars (left vs right). Nevertheless, the combination of high ZnO loading and initial concentration of POME still induces a higher degradation efficiency compared to the lower boundary.

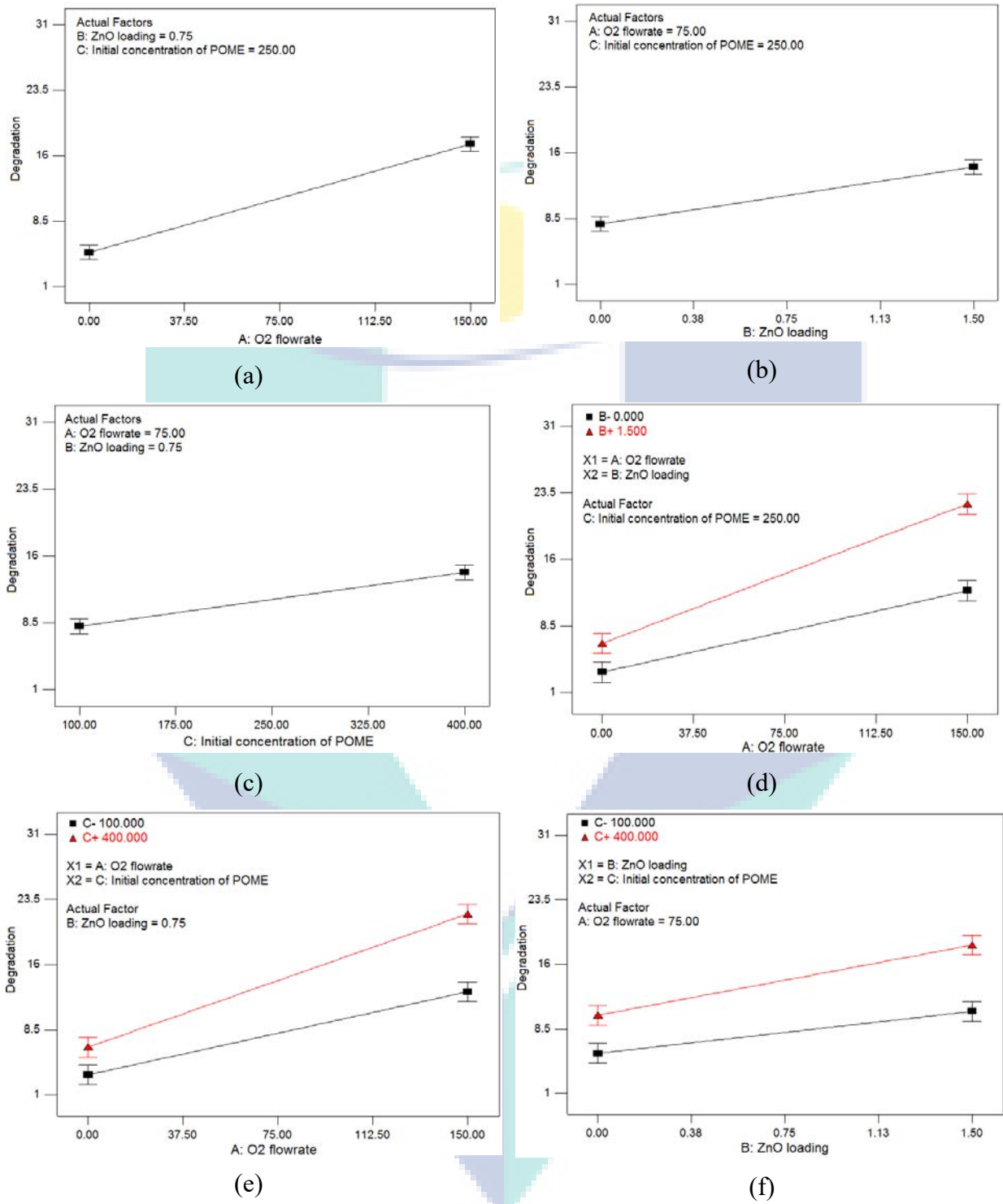


Figure 5.22 The effects of main factors and interactive factor

5.5.2 Optimization of the Factors

Based on Section 5.5.1, all three main factors seems to be statistically significant. Hence, for current section, all three factors were optimized by using CCD.

5.5.2.1 Optimization Range and Design of Experiment

Based on the discussions earlier, all three main factors are statistically significant and therefore were subjected to the optimization process. In Sections 4.4.1 and 5.3.1, the optimum oxygen flowrate and ZnO loading were in the range of 40 – 100 mL/min and 0.9 – 1.5 g/L, respectively. Hence, these ranges were employed in the investigation of optimization. In addition, the range for the initial concentration of POME was retained at 100 – 400 ppm.

As aforementioned, CCD was applied for the optimization process by developing the polynomial regression equation that portrait the relationships between the degradation efficiency of POME and the main factors. The design of experiment was generated by the Design Expert version 7.1.6. Similar with TiO₂, the center point of the design was repeated for six times, while the axial points and factorial points were duplicated to minimize the error. Consequently, a total of 34 runs of experiment were generated, and the degradation achieved for each run of experiment after 240 min of UV/ZnO process are summarized in Table 5.7.

Based on the results, the degradation achieved ranged from 11.60% to 52.50%. Highest degradation was recorded by the one of the center point experiment (Run 25), with 52.50% of COD removal, while lowest degradation (11.60 %) was achieved by Run 27. From Table 5.7, the degradation achieved tends to be higher when the operating conditions are closed to the center point. Hence, it is postulated that the optimized point is fallen in somewhere closed to the center point.

Table 5.7 The design of experiment and degradation achieved for each run

Run	O ₂ flowrate (mL/min)	ZnO loading (g/L)	Initial Concentration of POME (ppm)	Degradation (%)
1	85	1.35	325	20.12
2	55	1.05	175	42
3	40	1.2	250	35.79
4	70	1.2	250	52.03
5	55	1.35	325	30.36
6	85	1.35	175	39.77
7	70	0.9	250	29
8	70	1.2	250	51.33
9	100	1.2	250	27.55
10	55	1.05	325	29.35
11	85	1.35	175	42.33
12	55	1.35	325	32.15
13	70	1.2	250	50
14	40	1.2	250	36.71
15	70	1.5	250	39.1
16	85	1.05	325	24.31
17	85	1.05	175	35.35
18	85	1.35	325	17.39
19	70	1.2	400	11.6
20	70	1.2	250	48.6
21	70	1.2	250	49.33
22	55	1.35	175	51.33
23	70	1.5	250	37.8
24	70	1.2	100	26
25	55	1.35	175	52.5
26	70	1.2	250	48.21
27	70	0.9	250	28.54
28	55	1.05	175	43.9
29	85	1.05	325	26.55
30	100	1.2	250	29.1
31	70	1.2	400	12.32
32	55	1.05	325	28.76
33	85	1.05	175	34.66
34	70	1.2	100	27

5.5.2.2 Model Fitting ANOVA and Residual Analysis

The results obtained were fitted by using different mathematical models, such as linear, two-factor interaction (2FI) and quadratic model. The values of R^2 , adjusted R^2 , and predicted R^2 for each of the model were summarized in Table 5.8.

Table 5.8 R-values of each model

Model	R^2	Adjusted R^2	Predicted R^2
Linear	0.36	0.29	0.22
2FI	0.39	0.25	0.23
Quadratic	0.94	0.91	0.87

Results in Table 5.8 suggest that quadratic model is the best model to describe the degradation process due to highest R-values obtained. The quadratic model was the only model that has fulfilled the requirement of well fitted model ($R^2 > 0.8$), with R^2 , adjusted R^2 and Predicted R^2 of 0.94, 0.91, and 0.87, respectively. Hence, quadratic model was chosen for the description of the POME photodegradation process. Second-order polynomial equations were generated and presented as Equations 5.1 and 5.2, for coded and actual level, respectively, to describe the relationship between the response (degradation) with the O_2 flowrate (A , mL/min), ZnO loading (B , g/L) and initial concentration of POME (C , ppm).

$$\text{Degradation (\%)} = 50.15 - 3.17A + 1.87B - 5.97C - 1.47AB + 0.34AC - 2.44BC - 4.38A^2 - 4.05B^2 - 7.64C^2 \quad (5.1)$$

$$\text{Degradation (\%)} = -484.186 - 3.224A + 544.207B + 0.839C - 0.655AB + 2.983 \times 10^{-4}AC - 0.217BC - 0.0195A^2 - 179.899B^2 - 1.359 \times 10^{-3}C^2 \quad (5.2)$$

Subsequently, the selected model was subjected to ANOVA analysis. The results obtained are summarized in Table 5.9. In addition to the high R-values, a high model F-value (40.09) further confirms the adequacy of quadratic model in the optimization process. The low p-value (< 0.001) indicates that only 0.01% chance that the model F-value was interfered by noise. Besides the adequacy of the model, ANOVA also provides the useful information on the significance of the main factors and interaction effects.

Terms that possess ‘Prob>F’ of less than 0.05 are considered significant. Based on this specification, all the terms are significant, except the interaction effects of *AB* and *AC* (0.0920 and 0.6930). Hence, Equation 5.1 and 5.2 were simplified into Equations 5.3 and 5.4 by eliminating the non-significant terms. Besides that, the high adequate precision value of 23.327 (not presented) also indicates an adequate signal, proving that the quadratic model can be used to navigate the design space in the current study.

$$\text{Degradation (\%)} = 50.15 - 3.17A + 1.87B - 5.97C - 2.44BC - 4.38A^2 - 4.05B^2 - 7.64C^2 \quad (5.3)$$

$$\text{Degradation (\%)} = -484.186 - 3.224A + 544.207B + 0.839C - 0.217BC - 0.0195A^2 - 179.899B^2 - 1.359 \times 10^{-3}C^2 \quad (5.4)$$

Table 5.9 ANOVA for the quadratic model

Source	Sum of Squares	Degree of freedom	Mean Square	F Value	p-value Prob > F
Model	4074.26	9	452.696	40.095	< 0.0001
A-O ₂ flowrate	322.39	1	322.39	28.5539	< 0.0001
B-ZnO loading	111.714	1	111.714	9.89445	0.0044
C-Initial concentration of POME	1140.15	1	1140.15	100.983	< 0.0001
AB	34.7805	1	34.7805	3.08049	0.092
AC	1.80231	1	1.80231	0.15963	0.693
BC	94.9163	1	94.9163	8.4067	0.0079
A ²	742.581	1	742.581	65.77	< 0.0001
B ²	634.665	1	634.665	56.212	< 0.0001
C ²	2262.66	1	2262.66	200.403	< 0.0001

In addition, the residual analysis was also performed to enhance the adequacy of the model. The normal plot of the residual is presented in Figure 5.23a. An excellent linearity of the data was observed, demonstrating the high significance of the model. Moreover, the data in the parity plot (Figure 5.23b) are evenly distributed along the 45° line, indicating the sufficiency of the model employed. This is also supported by the high R²-value (0.93). Furthermore, the data points presented in both residuals versus predicted value plot (Figure 5.23c) and residuals vs run number plot (Figure 5.23d) are randomly

scattered and confined within the limit lines (shown as red lines), with no obvious pattern in both sides of the lines. These indicate that the experiments were free from the independence violation, at the same time confirming the adequacy of the developed model.

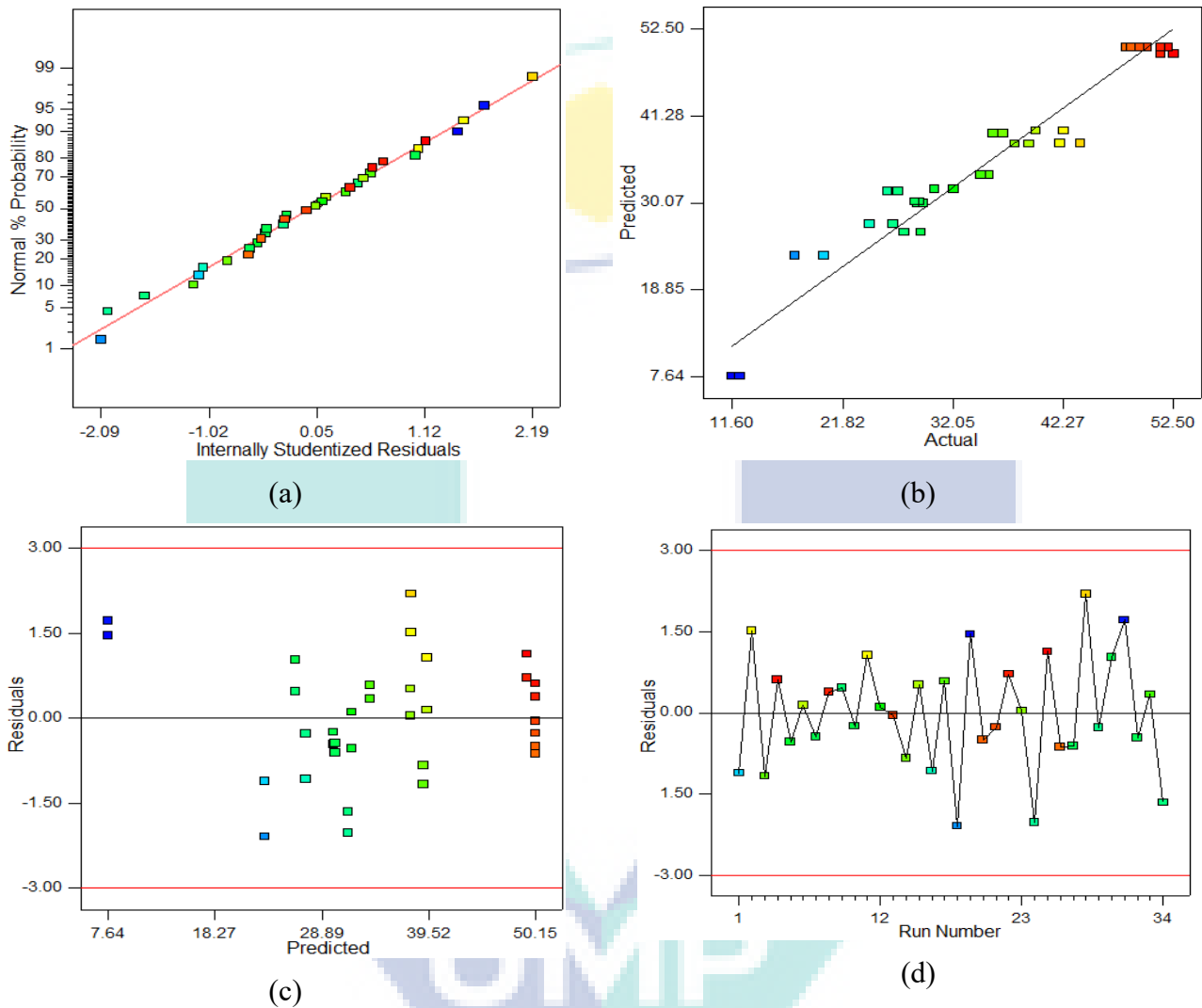


Figure 5.23 (a) Normal probability plot of residuals (b) Predicted vs actual response plot (c) Residuals vs predicted response plot (d) Residuals vs run number plot

5.5.2.3 Main Factors and Interaction Effects

The main factors effects, viz O₂ flowrate (A, mL/min), ZnO loading (B, g/L) and the initial concentration of POME (C, ppm), are presented in Figures 5.24a, 5.24b and 5.24c. Coincidentally, curvatures were observed in all three main factor effect plots indicating the existence of the optimum point for each factor. As can be observed in Figures 5.24a and 5.24b, the lines are slightly bend upward and achieved an optimum degradation

of 50 ± 2.0 %, with the range of 62.5 – 70 mL/min of O₂ flowrate (1.20 g/L of ZnO; 250 ppm of POME) and 1.20 – 1.27 g/L of ZnO (70 mL/min of O₂; 250 ppm of POME), respectively. Thereafter, the degradation decreases with both factors. Similarly, the degradation was also initially increased with the concentration of POME, with an optimum point (50 ± 2.0 %) observed in the range of 212.5 – 250 ppm of POME initial concentration (70 mL/min of O₂; 1.20 g/L of ZnO), and decreases drastically thereafter. The curve of the line is symptomizing the strength of the particular factor on the response. Compared to the two factors mentioned, the initial concentration of POME seems to have stronger negative effects on the degradation at higher concentration (> 250 ppm) as a curvier response line was obtained. However, this does not reveal the entire fact, as the interaction factors were not included in the considerations. Based on Section 5.5.1.3, the interaction of the factors was confirmed existed in the current study and was further supported by the ANOVA in Table 5.9

The interaction effects between the factors are depicted in Figure 5.25. According to Figure 5.25a, the optimum degradation can be obtained by the combination of middle-high ZnO loading (~1.27 g/L) and low O₂ flowrate (~62.5 mL/min). Indeed, increasing ZnO loading would increase the degradation efficiency due to the increment in active sites. However, as aforementioned, it would at the same time induce the light scattering effect on the system and this would reduce the degradation efficiency. It explains the deterioration in degradation performance at high ZnO loading. On the other hand, O₂ is very important, as it serves as the electron acceptor in photocatalysis process and subsequently forming hydroxyl radical (OH[•]) that is hyper active in degrading the organic compounds. Without O₂, the degradation efficiency would be highly suppressed due to the recombination of the charges. This explains the results obtained in Table 5.4 where low degradation efficiency was obtained in the absence of O₂. However, with excessive O₂ supply, the boundary layer effects induced by formation of big bubbles of O₂ gas would limit the degradation efficiency. Hence, ZnO lost part of its activity at high O₂ flowrate, judging from the flatter response trend.

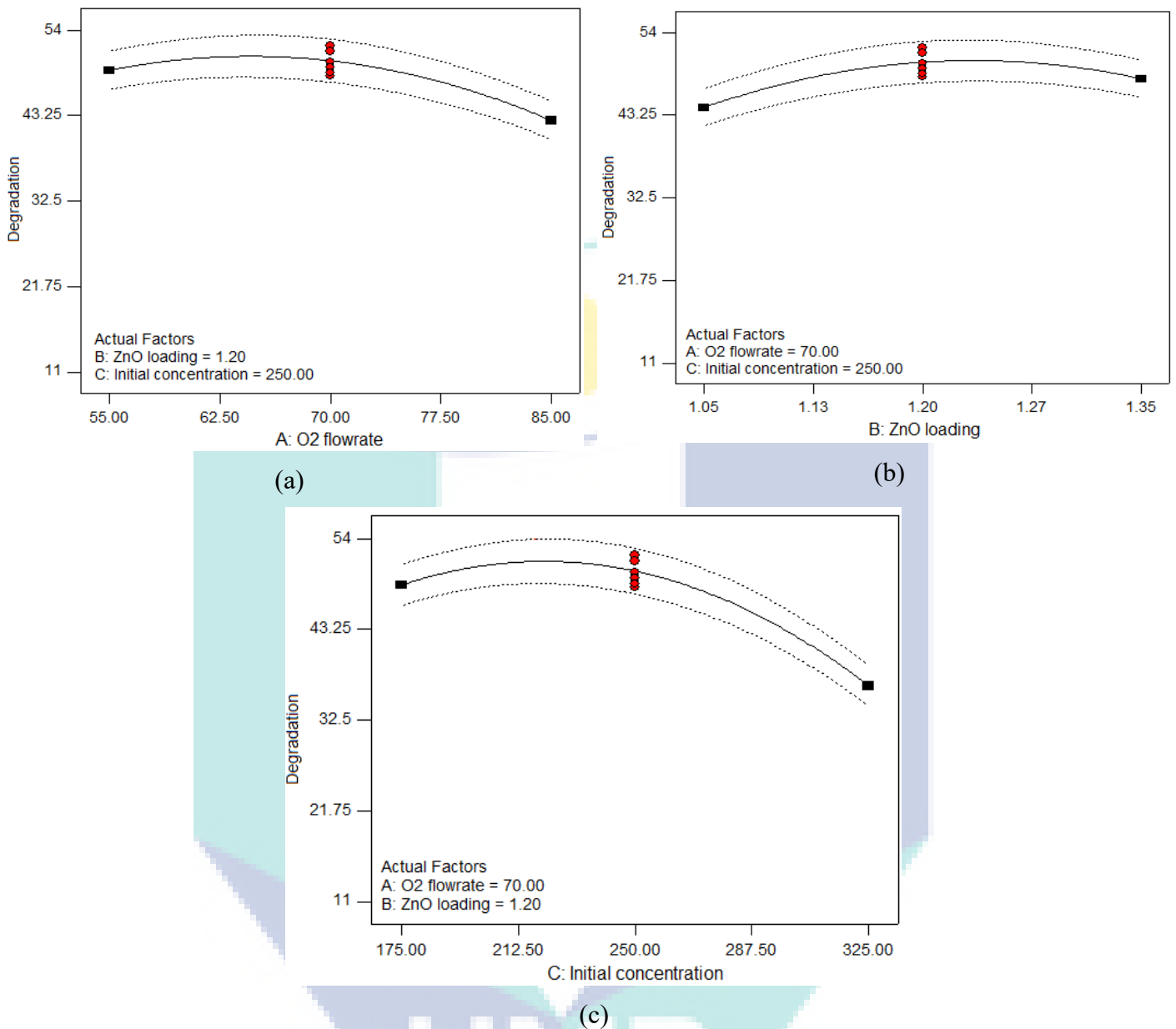


Figure 5.24 The effects of (a) O₂ flowrate (b) ZnO loading (c) initial concentration on the response

On the other hand, referring to Figures 5.24b and 5.24c, lower initial concentration of POME (~212.5 ppm) would enhance the degradation efficiency. Apparently, at low initial concentration, both O₂ flowrate (Figure 5.25b) and ZnO loading (Figure 5.25c) are playing very crucial roles in maximizing the degradation. However, with higher concentration, the colour of the POME liquid was getting darker, preventing the light from penetrating into the system, eventually inhibited the photocatalysis process. At this point, neither increasing O₂ flowrate nor ZnO loading can enhance the degradation efficiency. Instead, they would have further hindered the penetration of the light and

further diminished the degradation efficiency. These reasons answered the trend observed in Figures 5.24b and 5.24c.

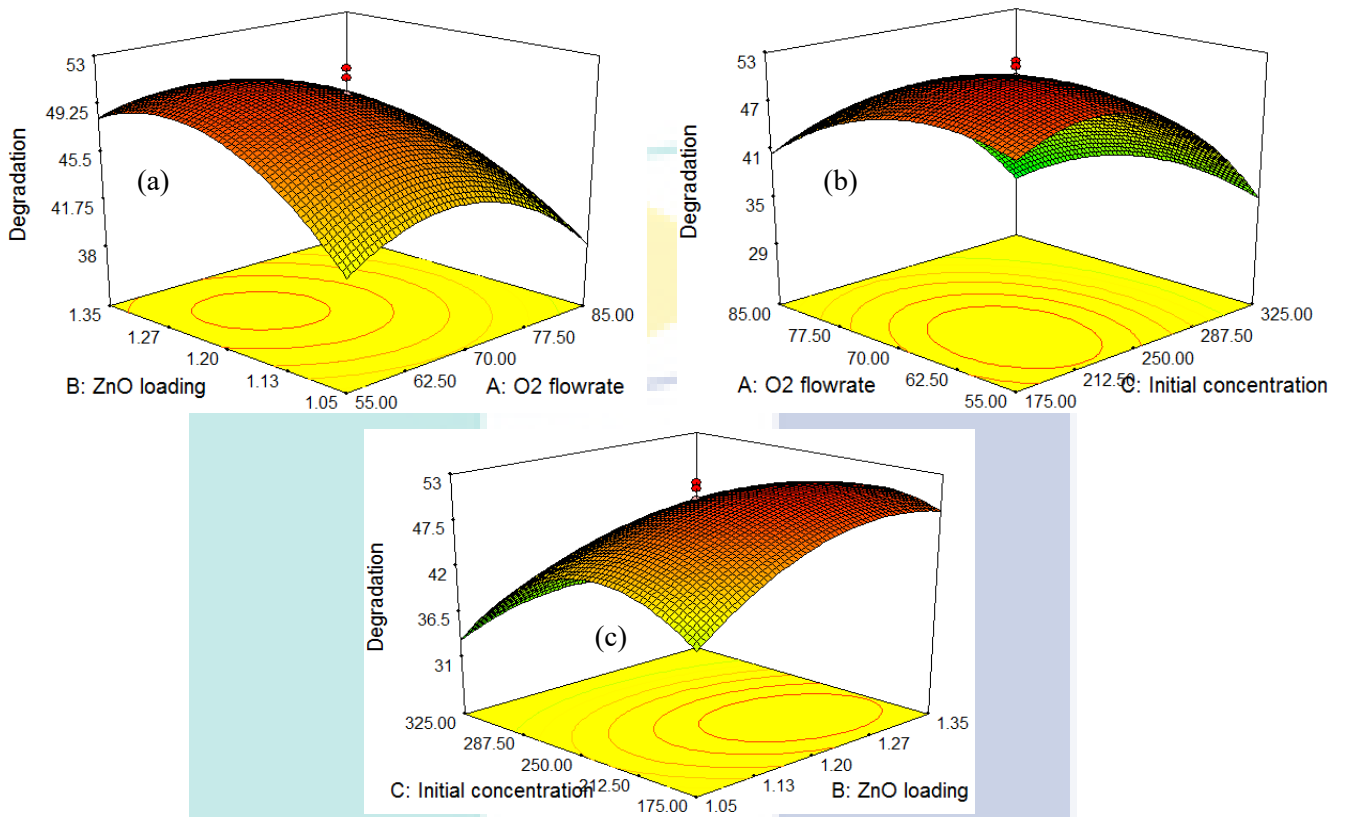


Figure 5.25 The interaction effects between (a) AB (b) AC (c) BC.

5.5.2.4 Process Optimization and Validation

A 3D response surface with an optimum point was generated by using Equation 5.3 and subsequently illustrated in Figure 5.26. With optimized condition, the degradation could be enhanced to 52.61 %. However, due to equipment limitation, for validation procedure, each of the factors was slightly round off to the whole number during experiment. The conditions of the validation experiment are presented in Table 5.10. The experiment was duplicated to avoid parallax error and the results obtained are tabulated in Table 5.10. The process was successfully optimized and the degradations achieved enhanced to 55.25% and 57.33% after 240 min of UV irradiation. Error analysis was conducted by using Equation 5.5.

$$\text{Error(\%)} = \left| \frac{(\text{R}_1 + \text{R}_2)/2 - (\text{R}_p)}{\text{R}_p} \right| \times 100\% \quad (5.5)$$

where R1 and R2 are the results obtained from the validation experiment and R_p denoted for the predicted result computed by using Equation 5.5, which is 52.61%. The margin of error between the predicted and actual data is only 5.42 %, further confirming the accuracy and the adequacy of the develop model (Equations 5.3 and 5.4).

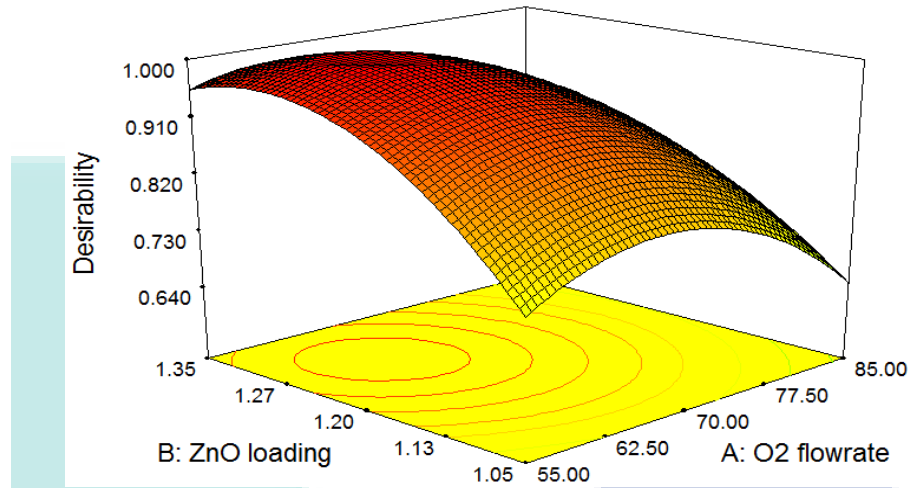


Figure 5.26 3D response surface for optimized condition

Table 5.10 Results of experimental validation

Parameters	Suggested conditions	Actual experiment
O ₂ flowrate (ml/min)	61.34	60.00
ZnO loading (g/L)	1.26	1.26
Initial concentration of POME (ppm)	216	220
Predicted Degradation (%)	52.61	52.45
Actual Degradation (%)	-	55.25 and 55.33
Averaged Degradation (%)	-	55.29
Error (%)	-	5.42

5.6 Correlation between BOD and COD of POME Treated by UV/ZnO System

Again, all the measured COD and BOD samples are plotted in Figure 5.27. As can be seen, the data points are randomly scattered in the bounded area. Similar with TiO₂ photocatalyst, ZnO photocatalyst is a versatile photocatalyst that is able to unselectively remove the organic pollutants in POME. Any adsorbed organic pollutants on the surface

of ZnO, including BOD-responsive organics or non-BOD-responsive organics, can be decomposed and eventually mineralized into CO₂ and CH₄. This explains the random behaviour of the data points observed in Figure 5.27. However, the BOD level of the sample was proven to be 40-60% of COD level, judging from the bounded area.

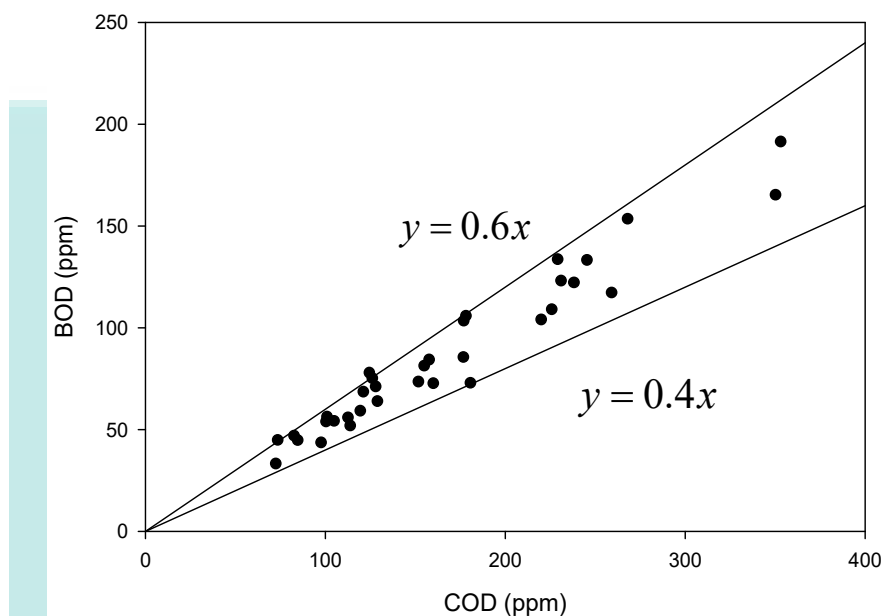


Figure 5.27 Correlation of BOD and COD after phototreatment using UV/ZnO system

5.7 Summary

In mechanistic study, the highest degradation observed is about 50%, achieved by 1.0 g/L of ZnO loading and 70 mL/min of O₂ flowrate after 240 min of UV irradiation. By assessing into the gaseous products, two species were detected, namely CO₂ and CH₄, with CO₂ as the major component. There were 36172 μmol of CO₂ and 333 μmol of CH₄ produced by photoreaction with 1.0 g/L of ZnO and 70 mL/min of O₂ flowrate, recording the highest gas production due to the most organics decomposed. Scavenging study confirmed that the main reactive species for organics decomposition in UV/ZnO system is OH[•] radical. The photocatalytic degradation mechanisms involved the adsorption of organic pollutants of POME followed by attack from surface OH[•] radical due to its organic-adsorption ability. This proposition can be confirmed by the detection of carbonaceous species on the surface of ZnO through the post-reaction analysis. Furthermore, ZnO exhibited lower stability compared to TiO₂ photocatalyst in recyclability test. The degradation achieved for 1st, 2nd, and 3rd cycle are 49.4%, 35.2%

and 37.8%, respectively, indicating a significant deactivation after the first cycle. This is attributed to the blockage of the active spots by the adsorbed carbonaceous species. In longevity test, the final COD of POME was measured as 44 ppm, recorded about 74.11% of degradation, from the initial COD of 170ppm, after 22h of UV irradiation in the presence of 1.0 g/L of ZnO and 70 mL/min of O₂ flowrate. Concurrently, the final BOD and O&G readings were 26 ppm and 20 mg/L, respectively, fulfilling the requirements of discharging. Besides, all the potential factors, viz O₂ flowrate (*A*), ZnO loading (*B*) and initial concentration of POME (*C*) are significant to the POME degradation, based on the justification of 2³ full factorial design. O₂ flowrate (*A*) holds the biggest contribution (58.27%) to the degradation, followed by ZnO loading (*B*, 15.96%) and initial concentration of POME (*C*, 13.85%). In addition, the interactions between the factors were also contributing 4.02% (*AB*), 3.12% (*AC*) and 1.01% (*BC*) of degradation, respectively. Subsequently, all three main factors were subjected to process optimization by using central composite design. A quadratic model was developed and its adequacy and sufficiency were rigorously checked. Based on the statistical analysis by ANOVA, all the main factors and interactive factors are significant, except factors *AC* and *BC*. By employing the developed quadratic model, the optimized conditions were identified and the predicted optimum degradation was 52.61% after 240 min of UV irradiation employing 61.34 mL/min of O₂ flowrate, 1.26 g/L of ZnO and 216.36 ppm of POME. In the validation process, under 60.00 mL/min of O₂ flowrate, 1.26 g/L of ZnO and 220 ppm of POME, duplicated experimental runs showed 55.25 and 55.33% of degradation, which represents circa 5.40% deviation from the predicted degradation (52.45%).

CHAPTER 6

MECHANISTICS AND PERFORMANCE COMPARISONS BETWEEN UV/TiO₂ AND UV/ZnO SYSTEMS

6.1 Introduction

In Chapter 4, photocatalytic treatment of POME in the UV/TiO₂ system was extensively discussed from the aspects of photocatalytic kinetics and optimization. Subsequently in Chapter 5, UV/ZnO system was employed to carry out the photocatalytic degradation of POME. In order to evaluate the performance of both systems, this chapter reports the comparison between the two systems. Section 6.2 compares the systems in term of the photocatalyst properties while the responses of the system towards different scavengers are presented in Section 6.3. At the same time, the differences in mechanisms of POME degradation for both systems are also presented in the same section. Subsequently, the effects of photocatalysts loading and the stability of both systems were compared in Sections 6.4 and 6.5, respectively. Finally, a short summary based on the comparisons of both systems is presented in Section 6.6.

6.2 Comparisons of Photocatalyst Properties

Sharp peaks are observed in XRD patterns of both TiO₂ and ZnO photocatalysts, presented in Figure 4.2 and Figure 5.1. This indicates excellent crystallinity in both solid samples, which favours the prevention of charges recombination during photoreaction (Kudo and Miseki, 2009). In addition, there are only anatase-TiO₂ peaks and ZnO peaks, suggesting monophasic of the photocatalysts. The crystallite sizes of both photocatalysts were estimated using Scherrer equation (cf. Equation 2.3) and the results obtained are tabulated in Table 6.1. Based on the estimation, ZnO possessed larger crystal (62.3 nm) compared to the TiO₂ (45.7 nm).

Table 6.1 Characterization of TiO₂ and ZnO

Properties	TiO ₂	ZnO
Crystal Size (nm)	45.7	62.3
Diameter (nm)	70 – 100	160 – 480
Length	70 – 100	200 – 820
Pore size (nm)	22.4	6.47
Specific Surface area (m ² /g)	11.34	9.71
Band gap energy (eV)	3.15	3.2
Density (g/cm ³)	4.10	6.16

From the FESEM images in Figure 4.3 and Figure 5.2, both photocatalysts have smooth surface. TiO₂ (cf. Figure 4.3) has spherical shape, with considerably consistent diameter, ranged 70 – 100 nm. On the other hand, ZnO (refers to Figure 5.2) exhibits variation in both shape and size. Indeed, irregular shape was observed for the ZnO photocatalyst, with the diameter ranged 160 – 480 nm and length ranged 200 – 820 nm.

Furthermore, the N₂ adsorption-desorption isotherms (cf. Figure 4.4 and Figure 5.3) revealed that both TiO₂ and ZnO photocatalysts were mesoporous materials, with very small pore size (22.4 and 6.47 nm, respectively, as in Table 6.1), computed by using *Barrett-Joyner-Halenda (BJH) model*. This is also supported by the smooth surface observed in FESEM images in Figures 4.3 and 5.2. At the same time, N₂ physisorption data showed that the specific surface area of TiO₂ is slightly higher than ZnO (11.34 and 9.71 m²/g, respectively). In addition, the optical properties of these photocatalysts were determined using UV-Vis DRS. Based on the spectrum obtained (Figure 4.5 and Figure 5.4), both photocatalysts exhibited strong absorption at UV range (< 390 nm) only, thus confirmed their functionality under UV irradiation. The band gap energy for both sets of photocatalysts were 3.15 eV for TiO₂ and 3.2 eV for ZnO, respectively, which is

consistent with the past research. The density of both TiO₂ and ZnO photocatalysts were also measured and confirmed as 4.10 and 6.16 g/cm³ after averaging from three repeated measurements. These values were required for the measurement of the textural properties such as the BET specific surface area.

6.3 Response to Scavengers and Mechanisms of Degradation

A series of controlled experiments were conducted to determine the mechanisms of the organics decomposition for both photocatalysts by using different scavenger additives. Details of the experiments were mentioned in previous chapters. The results obtained were compiled and shown in Figure 6.1. Significant suppressions were observed for both TiO₂ and ZnO systems, when the O₂-bubbling was replaced with N₂-bubbling. This could be attributed to the high recombination rate of the photo-induced charges during the photoreaction, as N₂ gas was inert towards electrons. This has led to the prevention of charge recombination by electrons-scavenging the O₂, hence the suppressions of degradation.

The OH[•] can decompose organics efficiently and unselectively, as it is one of the most common reactive species in the photocatalysis process. Hence, the role of OH[•] was also investigated, with different additives, Na₂CO₃ and NaI (1 mL; 1.35 M), which would have attack the free OH[•] and photo-generated holes, h^+ , as in Equations (M4.8) and (M4.9).

The degradation deterioration (from 51.80 % to 6.63 %) was observed in the TiO₂ system (Figure 6.1), confirming that the OH[•] was the main reactive species in this system. There are two pathway for OH[•] generation, viz. (i) the O₂-pathway through electron consumption and (ii) the H₂O-pathway through h^+ consumption. Hence, another experiment was conducted with I⁻ ions injected for the h^+ -scavenging (Equation (M4.9)) to inhibit the latter. Based on the results, the degradation achieved was halved, significantly reduced to 24.09%, indicating that both O₂ and H₂O pathway were contributing almost equally to the total degradation. Hence, it can be concluded that the main reactive species for this system was hydroxyl free radical, OH[•], and the degradation process must occur in bulk solution, based on the response towards the scavengers. This is due to the poor affinity of TiO₂ photocatalyst; the organic pollutants can hardly adsorb onto the TiO₂ surface. Consequently, the OH_{ads}[•] needs to desorb from the TiO₂ surface,

as OH^\bullet , into the bulk solution (Equation M4.10) and attacked the organic pollutant (Equation M4.11).

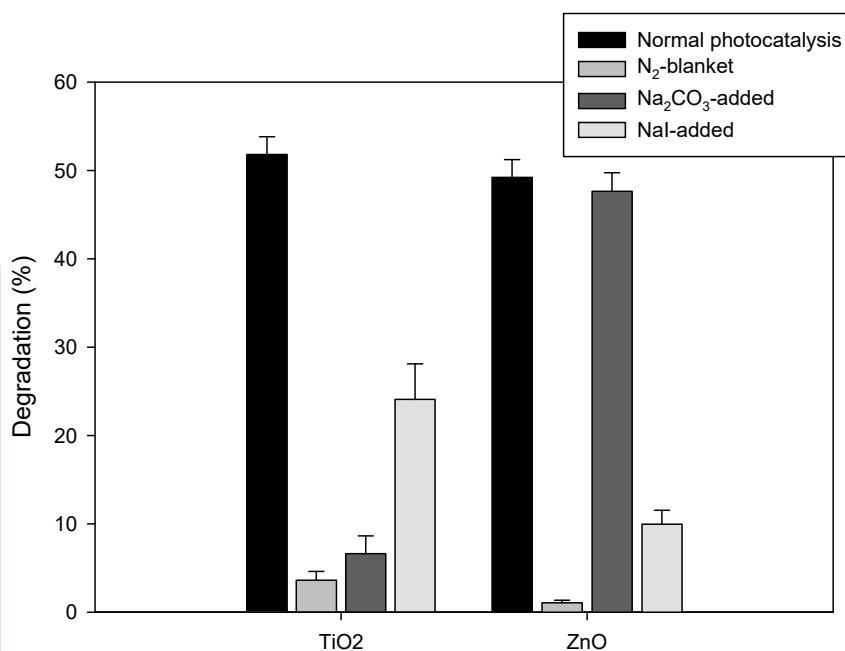


Figure 6.1 Scavenging studies for TiO₂ and ZnO (O₂-bubbling rate: 70 mL/min; photocatalyst loading: 1.0 g/L)

In contrast, ZnO system exhibited an entirely different scenario. According to Figure 6.1, there is no obvious inhibition observed when same amount of CO₃⁻ ions was introduced to the system, suggesting free hydroxyl radical, OH^\bullet , was not the major reactive component for the organics decomposition. Unlike TiO₂, ZnO photocatalysts allowed the organic pollutants to adsorb, and hence the degradation occurred on its surface during the reaction. This is in total contrast from the mechanisms proposed earlier for the TiO₂ system. Therefore, there is no significant suppression observed in degradation even though OH^\bullet was scavenged during the reaction.

On the other hand, with I⁻ ions added, the degradation achieved was reduced significantly to about 10.0% from the initial 49.2%, revealing the role of h^+ in ZnO system. This suggests that about 80.0% of total degradation was achieved by the OH^\bullet produced from the H₂O pathway (Equation (M4.3)), while the remaining was due to the OH^\bullet from O₂ pathway (Equations (M4.4)-(M4.7)), UV irradiation (photolysis) and the synergetic effects of all the reactive species. By summarizing these findings, the degradation of organics in ZnO system was confirmed to take place on the surface of ZnO photocatalyst. With the ability to adsorb organic pollutants, the $\text{OH}_{\text{ads}}^\bullet$ can directly

attack the adsorbed organic pollutants on the surface of ZnO as in Equation (M5.2), as opposed to the needs of desorbing in the case for TiO₂ photocatalyst.

The detailed mechanisms for both systems have been presented in Section 4.5.4 and 5.3.3.

6.4 Effects of Photocatalyst Loading Towards Both System

Figure 6.2 illustrates the effects of photocatalysts loading for both TiO₂ and ZnO systems. As presented in Figure 6.2, both systems exhibit a similar trend, in which the degradation achieved consistently increased with the photocatalysts loading, until an optimum point was attained at 1.0 g/L of photocatalysts. Under this condition, the TiO₂ system achieved slightly higher degradation (51.83%) compared to the ZnO system (49.36%). Beyond 1.0 g/L, with further increase in photocatalyst loading, the degradations achieved have slightly declined due to the light-scattering effects induced by the excess photocatalysts.

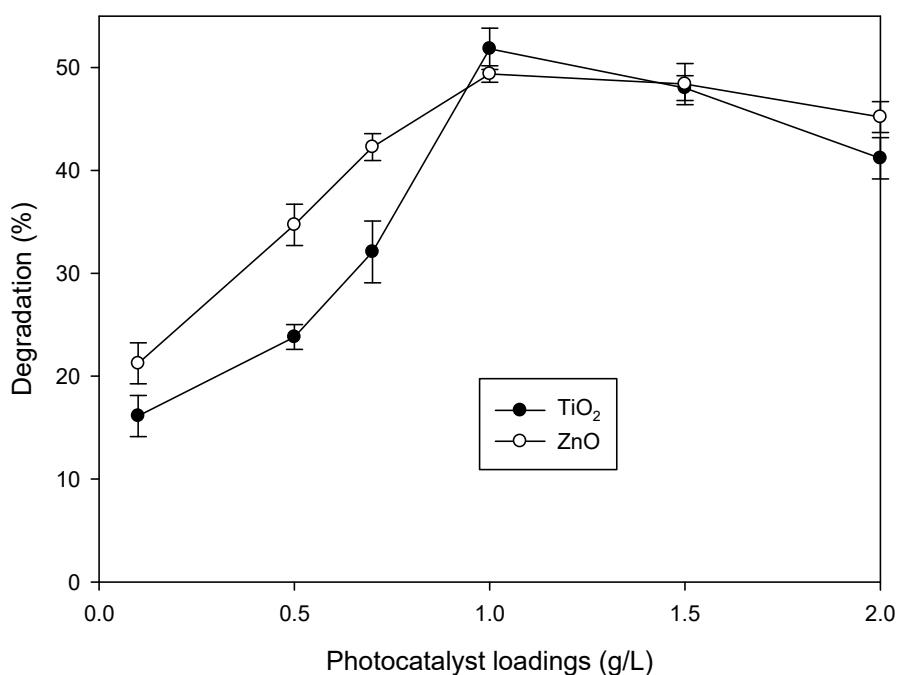


Figure 6.2 Effects of photocatalysts loading for both systems (initial concentration = 155-170 ppm; Oxygen bubbling = 70 mL/min)

However, even though both systems presented a similar trend with respect to the photocatalysts loading, there are still some noticeable differences. Firstly, at lower

photocatalyst loadings ($< \sim 0.9$ g/L), ZnO apparently performed better compared to TiO₂ photocatalyst. This can be attributed to the difference in mechanisms of both systems that was discussed earlier. For ZnO system, the degradation achieved was directly proportional to the surface area, and hence the amount of ZnO photocatalysts. This explains the perfect straight degradation line obtained at the lower photocatalysts ($< \sim 0.9$ g/L).

On the other hand, for TiO₂, the main reactive species, OH[•] radicals required to desorb from the TiO₂ surface before the degradation could happen. The schematic diagram presented in Figure 6.3 is illustrating the degradation at different TiO₂ loadings.

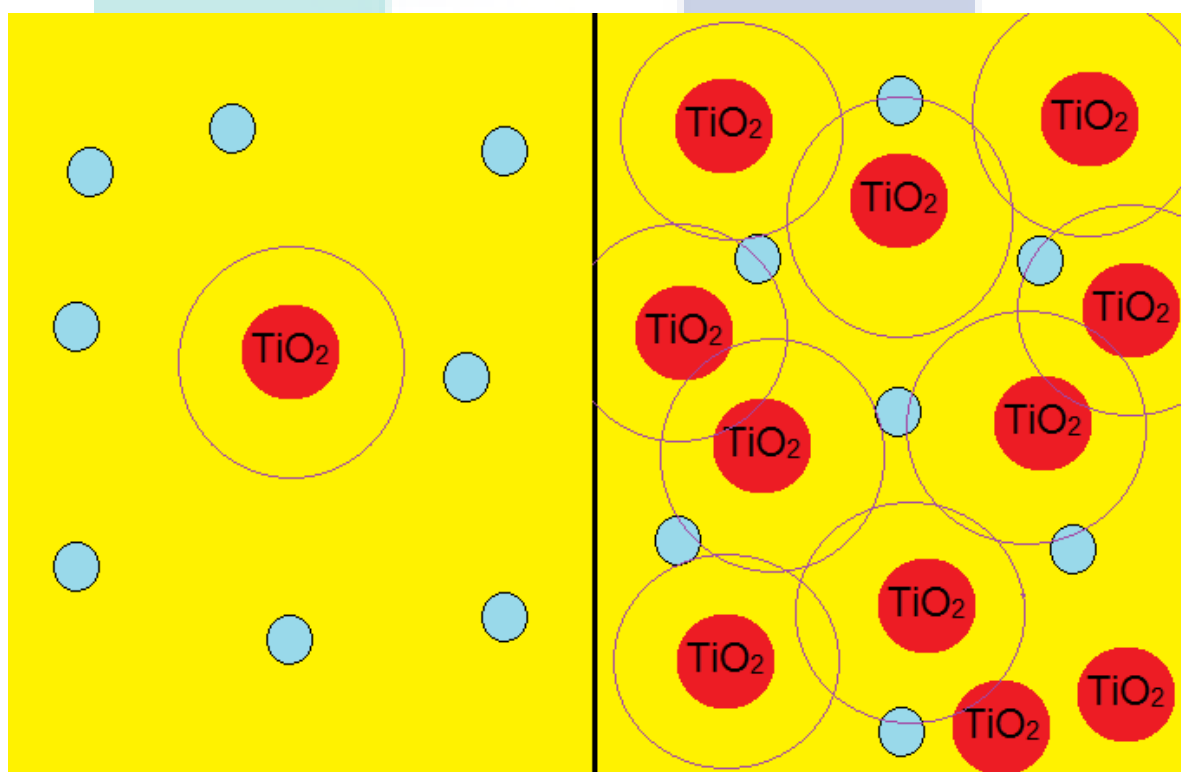


Figure 6.3 Schematic diagram of organic pollutants degradation in TiO₂ system

It is well-known that OH[•] radicals are highly reactive, but having very short half-life, *circa* 10^{-9} second (Gutowski and Kowalczyk, 2013; Pastor et al., 2000). Due to its short half-life, the OH[•] radicals normally decay in a very short time after travelling a very short distance in the bulk solution (circles around the TiO₂ particles in Figure 6.3 denoted for the travelling path). At low TiO₂ loading, the organic pollutant (blue particles) and the TiO₂ photocatalyst were widely separated, rendering most of the OH[•] radicals perished before it could start attack organic pollutant. Hence, at lower TiO₂ loading, the degradation achieved was comparatively low even though with higher BET surface area

(11.34 m²). However, beyond certain TiO₂ loading, the distance between the organic pollutants and TiO₂ photocatalysts greatly reduced (within the travel pathway of OH• radicals), allowing the OH• radicals to attack the organics before totally decayed. This explains the drastically increase of the degradation achieved after 0.5 g/L of TiO₂ loading (cf. Figure 6.2) and overtook ZnO system at 0.9 g/L of photocatalysts in terms of degradation achieved.

Within range of 0.9 – 1.4 g/L, TiO₂ system took a great leap and exceeded the degradation achieved by ZnO system (cf. Figure 6.2). At low photocatalyst loading (<0.9 g/L), the organic-adsorption ability of ZnO allowed the organic degradation occurs on its surface. This exempts the needs of desorption that causing decay of the OH• in the bulk solution like TiO₂. Hence, ZnO performed better at low photocatalyst loading. Unfortunately, at higher photocatalyst loading, its comparatively low BET specific surface area (9.71 m²/g) has now limited the degradation. Nevertheless, based on the mechanisms proposed earlier, the degradation of organic pollutant in TiO₂ took place in the entire bulk solution, which believed to have larger reaction surface. Hence, in 0.9 – 1.4 g/L photocatalyst loading, TiO₂ seems to be the better photocatalyst for POME degradation.

In photocatalysis system, it is very common that the performance of system degrades after the optimum photocatalyst loading. This phenomenon was also observed in both systems at beyond the optimum 1.0 g/L of photocatalyst loading. Referring to the results obtained from gas pycnometer, the density of ZnO (6.16 g/cm³) was almost 50% higher than the density of TiO₂ (4.10 g/cm³), which indicates that at the same weight, the volume of TiO₂ photocatalyst was about 50% higher than ZnO photocatalysts in the slurry system. This has brought negative impact to the system, especially beyond the optimum point, by inducing the light scattering effects. Hence, the degradation profile of TiO₂ system exhibited a steeper line compared to ZnO system and being overtaken by ZnO system beyond 1.4 g/L photocatalyst loading.

6.5 Recyclability and Longevity Studies

The recyclability and longevity studies were performed and the results obtained are illustrated in Figures 6.4 and 6.5. For recyclability study, photoreactions were conducted with 170 ppm of POME, 1.0 g/L of photocatalyst and 70 mL/min of O₂-

bubbling. All the photocatalysts were recovered by using filtration process after experiments, repeatedly-washed with water and ethanol, and subsequently subjected to the next cycle of photoreactions.

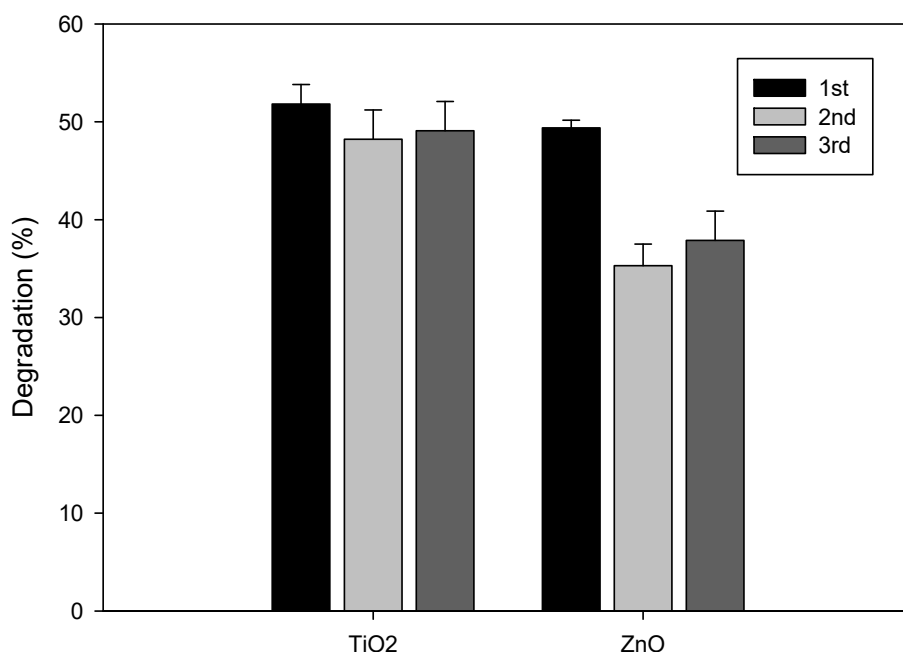


Figure 6.4 Recyclability study for both TiO₂ and ZnO system

Figure 6.4 shows that TiO₂ seems to be the more stable photocatalyst towards POME degradation, as no significant suppression in performance was observed even after three consecutive cycles. The degradations achieved were 51.80%, 48.21%, and 49.08% for 1st, 2nd, and 3rd cycle, respectively, after 240 min of UV irradiation. On the other hand, the degradations achieved by ZnO system were 49.36%, 35.29%, 37.87% for 1st, 2nd, and 3rd cycle, respectively. Obviously, ZnO photocatalyst lost almost 30% of its reactivity after the 1st cycle.

Furthermore, the results obtained (cf. Figure 6.5) from longevity study (170 ppm of POME, 1.0 g/L of photocatalysts and 70 mL/min of O₂-bubbling) also shows that TiO₂ photocatalyst performed better over extended time of photoreaction (22 h). Until the 4th h of reaction, both TiO₂ and ZnO system exhibited strong reactivity towards the organic pollutants. The degradation achieved by TiO₂ system was slightly higher (~2%) than ZnO system. However, after 4 h of UV irradiation, ZnO lost part of its reactivity and the gap between both systems in terms of degradation achieved was broaden. At the end of the

experiment (22 h), the degradations achieved were 80.35% and 74.11% for TiO₂ and ZnO systems, respectively. Based on the calculation, ZnO was 8.14% less efficient than TiO₂. This could be due the blockage of the ZnO active spots by the residue from the organic pollutants that has remained on the surface of ZnO. For TiO₂, since organic pollutants in POME can hardly adsorb onto its surface, it is always fresh and clean for the reactive OH[•] radical generation. This is proven by the results from both recyclability and longevity study. In addition, this performance was also supported by the results of post reaction analyses conducted on the used photocatalysts (presented in Sections 4.6.1 and 5.4.1). As a conclusion, TiO₂ was a better photocatalyst candidate than ZnO for photocatalytic degradation of POME due to its higher efficiency.

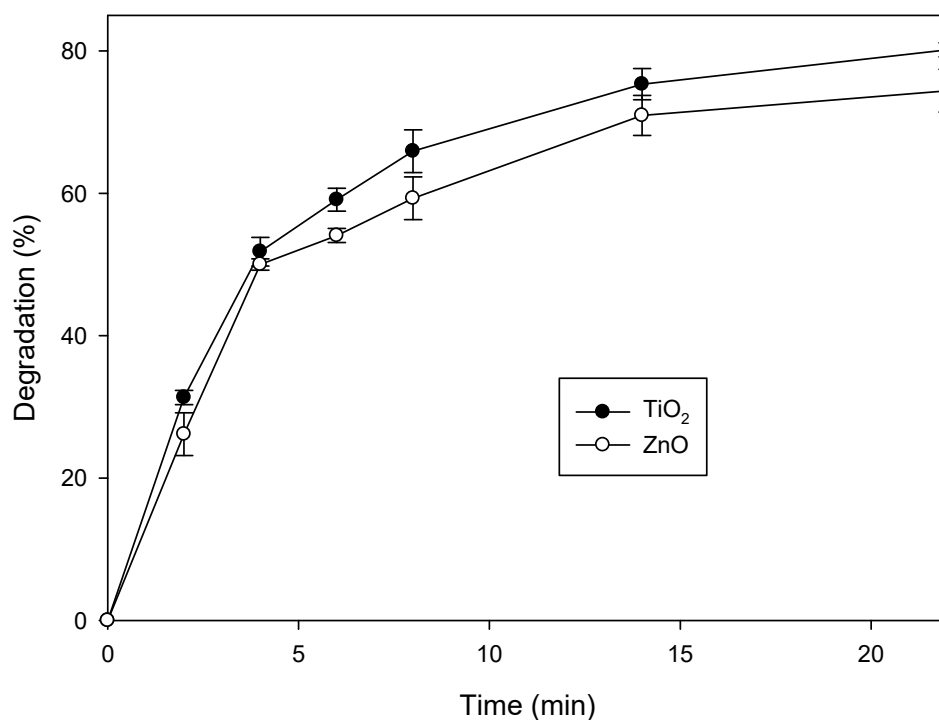
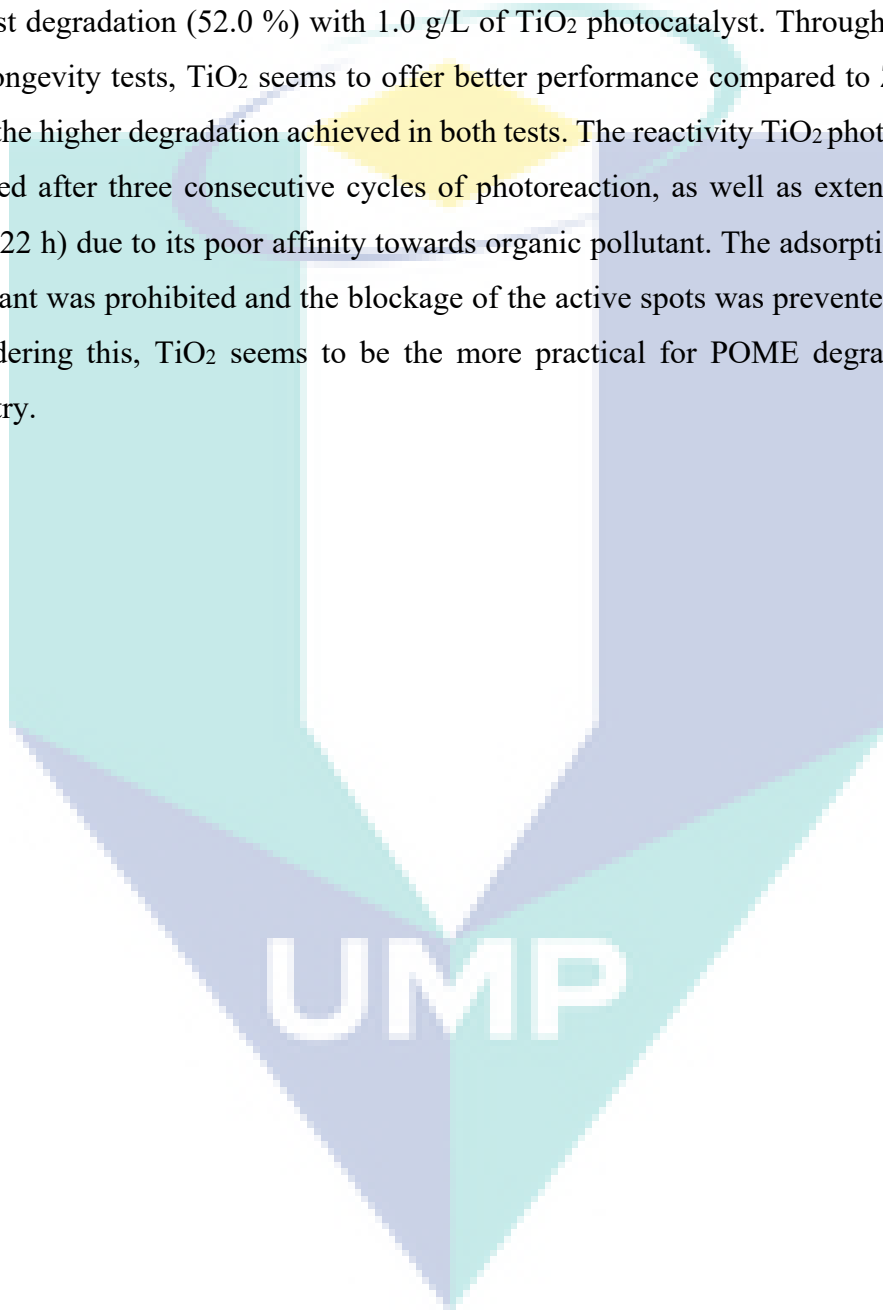


Figure 6.5 Longevity study for both TiO₂ and ZnO system

6.6 Summary

As a summary, both systems exhibit a lot of differences in POME degradation process. In scavenging study, it is found that the main reactive species for POME degradation for both systems are different. OH[•] free radical decomposed most organics in UV/TiO while UV/ZnO system generates OH_{ads}[•] for most of the organic degradation. In mechanistic study, the ability of adsorption in ZnO photocatalyst allows the

degradation process occurs on its surface. For TiO₂ photocatalyst, the organic degradation can only happen in bulk solution due to the poor affinity of TiO₂ towards organic pollutants. At low and high photocatalyst loading (<0.9 g/L and >1.4 g/L), ZnO seems to be better photocatalyst that offers higher degradation efficiency. However, at the optimum range (0.9 < X < 1.4 g/L), TiO₂ performed better than ZnO and recorded the highest degradation (52.0 %) with 1.0 g/L of TiO₂ photocatalyst. Through recyclability and longevity tests, TiO₂ seems to offer better performance compared to ZnO, judging from the higher degradation achieved in both tests. The reactivity TiO₂ photocatalyst was retained after three consecutive cycles of photoreaction, as well as extending reaction time (22 h) due to its poor affinity towards organic pollutant. The adsorption of organic pollutant was prohibited and the blockage of the active spots was prevented too. Hence, considering this, TiO₂ seems to be the more practical for POME degradation in the industry.



CHAPTER 7

CONCLUSION

7.1 Conclusion

All the objectives mentioned in Section 1.3 were successfully achieved. The kinetics of both systems were determined through the photoreactions with different photocatalyst loading, at the same time the gaseous products produced along were also eluted by gas chromatography. The followings summarize the answers for first objective:

- In the kinetics study, the highest COD degradation achieved was 52.0% with 1.0 g/L of TiO₂ and 70 mL/min of O₂ after 240 min of UV irradiation.
- The optimum ZnO loading for POME photodegradation was 1.0 g/L, with about 50% of COD degraded after 240 min of UV irradiation.
- Two species were detected in the gas phase for both systems, namely CO₂ and CH₄, with CO₂ as the major component due to O₂-rich environment.
- The degradation in both systems follow first order reaction. The highest reaction constant obtained for TiO₂ system is $2.900 \times 10^{-3} \text{ min}^{-1}$, which for the highest reaction constant was $3.118 \times 10^{-3} \text{ min}^{-1}$. Both achievements were obtained at 1.0 g/L of photocatalyst loading.

For second objective, the mechanisms of both systems were studied by using different scavenges. Based on the results, it is found that:

- For TiO₂ system, based on responses to the scavengers, the proposed mechanisms were that the degradation of the organics occurred in the bulk solution, attacked by the OH[•] radical as the main oxidizing agent. Organic

degradation did not take place on the TiO₂ surface as anticipated earlier. This proposition was also supported by the post-reaction analysis of photocatalyst that did not show carbonaceous species on the TiO₂ surface.

- For ZnO system, the photocatalytic degradation mechanisms involved the adsorption of organic pollutants of POME followed by the attack from surface OH[•] radical. This proposition can be confirmed by the detection of carbonaceous species on the surface of ZnO in all the post-reaction analysis.

For third objective, the stability of both photocatalysts were evaluated through recyclability and longevity test. As the results:

- Results in recyclability test showed that TiO₂ was a very stable photocatalyst, as demonstrated by the catalytic degradation of POME that was still at nascent level despite three consecutive cycles of photoreaction using same batch of photocatalyst. The degradation achieved for 1st, 2nd and third cycle are 52.0%, 48.0% and 49.0% respectively.
- When UV irradiation was extended to 22 h, the degradation efficiency can attain more than 80%, employing 1.0 g/L of TiO₂ and 70 mL/min of O₂ flowrate. The final COD, BOD and O&G of POME at the end of photoreaction were 33 ppm, 16 ppm and 10 ppm, which has met discharge limit set by the authority.
- Recyclability test showed the deactivation of ZnO photocatalyst, and the POME degradability dropped from 50% achieved in the first cycle to 38% in the third cycle due to the blockage of the active spots.
- Based on the longevity results, the COD of POME was successfully brought down to 44 ppm, for an overall achievement of 74.11% organics removal after 22 h of UV irradiation employing ZnO loading of 1.0 g/L and 70 ml/min of O₂-bubbling. Concurrently, the final BOD and O&G readings were 26 ppm and 20 mg/L, respectively. Significantly, these readings have met the standard discharge threshold set by DoE.

Lastly, for fourth objective, which is the statistical evaluation and optimization process, the results obtained show that:

I. For TiO₂ system

- 2³ full factorial design confirmed that O₂ flowrate, TiO₂ loading and initial concentration of POME contributed significantly to the final degradation achieved.
- O₂ flowrate contributed the highest effects to the degradation, about 63.5%, followed by initial concentration of POME (22.32%) and TiO₂ loading (5.69%).
- For process optimization, quadratic model was employed to describe the degradation due to its high R² value (0.92) and excellent residue analysis.
- According to ANOVA analysis, all the main factors and interactive factors are significant, except the interactions between O₂ flowrate and initial concentration of POME (AC), as well as TiO₂ loading and initial concentration of POME (BC).
- Validation experiments (duplicated) were conducted, with 66.0 mL/min of O₂ flowrate, 1.04 g/L of TiO₂ and 240 ppm of initial POME concentration, and the degradations achieved were 54.33 and 55.62 %, respectively, recording just 4.41% of error compared to the estimation obtained from the model equation.

II. For ZnO system

- A 2³ full factorial design confirmed that all three potential factors, viz O₂ flowrate (*A*), ZnO loading (*B*) and initial concentration of POME (*C*) are significant to the POME degradation.
- Pareto chart revealed that all three main factors are contributing positive effects to the degradation, with O₂ flowrate (*A*) contributing the biggest part (58.27%), followed by ZnO loading (*B*, 15.96%) and initial concentration of POME (*C*, 13.85%). In addition, the interactions between

the factors were also contributing 4.02% (*AB*), 3.12% (*AC*) and 1.01% (*BC*) of degradation, respectively.

- A quadratic model was developed in CCD optimization and its adequacy and sufficiency were rigorously checked. The high R^2 value of 0.94 was recorded for the developed quadratic model.
- ANOVA revealed that all the factors, including main factors and interactive factors, have significantly contributed to the degradation efficiency, except factors *AC* and *BC*.
- In the validation process, under 60.00 mL/min of O_2 flowrate, 1.26 g/L of ZnO and 220 ppm of POME, duplicated experimental runs showed 55.25 and 55.33% of degradation, which represents circa 5.40% deviation from the predicted degradation (52.45%).

As a summary, both systems exhibit a lot of differences in POME degradation process. In scavenging study, it is found that the main reactive species for UV/TiO₂ system is OH• free radical while OH_{ads}• decomposes most of the organic degradation in UV/ZnO system. In mechanistic study, ZnO photocatalyst adsorbs organic pollutants in POME and allows the degradation process occurs on its surface. For TiO₂ photocatalyst, the organic degradation can only happen in bulk solution due to the poor affinity of TiO₂ towards organic pollutants. At low and high photocatalyst loading (<0.9 g/L and >1.4 g/L), ZnO seems to be better photocatalyst that offers higher degradation efficiency. However, at the optimum range (0.9 < X < 1.4 g/L), TiO₂ performed better than ZnO and recorded the highest degradation (52.0 %) with 1.0 g/L of TiO₂ photocatalyst. In addition, TiO₂ performed better compared to ZnO in both longevity and recyclability test, judging from the higher degradation achieved. The reactivity TiO₂ photocatalyst was retained after three consecutive cycles of photoreaction, as well as extending reaction time (22 h) due to its poor affinity towards organic pollutant. This prevents the adsorption of organic pollutant and hence the blockage of the active spots was prevented too. This is further confirmed from the post-reaction analysis conducted for spent photocatalysts of both systems, in which the carbonaceous species only detected on the surface of ZnO photocatalyst and this believed to be the reason of deactivation observed in the

recyclability test. Hence, considering this, TiO₂ seems to be the more practical for POME degradation in the industry.

7.2 Recommendations

The main idea of current work is to discover a new technology, which is effective and cost-efficient for POME treatment. In the present work, the degradation of POME was conducted under UV irradiation in the presence of photocatalyst and promising results were obtained. However, the activator needed for this technology is UV irradiation, which could be costly in the term of energy cost. Solar light, on the other hand, seems to be a viable alternative to solve the problem. Unfortunately, the activator needed, UV light, only represents a fraction of solar spectrum. In lieu of this, solar light irradiation could be a good choice. Nonetheless, solar light predominantly consists of visible light that however is unable to activate the photocatalysts in the current study due to disparity in energy level. Hence for future study, it is recommended to modify the photocatalysts in current study to further extend the light absorption properties to visible light region. Introducing dopants into the photocatalysts could be an effective way for this purpose. By this, the whole photocatalytic degradation process would be different and it is recommended to study this new process in its entirety. For this new system, the mechanisms and stability of the new photocatalysts can be the subjects of investigation. In addition, optimization process for new photocatalysts is also very important in ensuring an effective implementation of photocatalysis technology.

REFERENCES

- Abed, C., Bouzidi, C., Elhouichet, H., Gelloz, B., and Ferid, M. 2015. Mg doping induced high structural quality of sol–gel ZnO nanocrystals: Application in photocatalysis. *Applied Surface Science*, 349: 855–863.
- Achouri, F., Corbel, S., Balan, L., Mozet, K., Girot, E., Medjahdi, G., ... Schneider, R. 2016. Porous Mn-doped ZnO nanoparticles for enhanced solar and visible light photocatalysis. *Materials and Design*, 101: 309–316.
- Adams, W. A., and Impellitteri, C. A. 2009. The photocatalysis of N,N-diethyl-m-toluamide (DEET) using dispersions of Degussa P-25 TiO₂ particles. *Journal of Photochemistry and Photobiology A: Chemistry*, 202(1): 28–32.
- Ahmad, A. L., Ismail, S., and Bhatia, S. 2003. Water recycling from palm oil mill effluent (POME) using membrane technology. *Desalination*, 157(1–3): 87–95.
- Ahmad, A. L., Ismail, S., and Bhatia, S. 2005. Ultrafiltration behavior in the treatment of agro-industry effluent: Pilot scale studies. *Chemical Engineering Science*, 60(19): 5385–5394.
- Ahmadi, M., Vahabzadeh, F., Bonakdarpour, B., Mofarrah, E., Mehranian, M., 2005. Application of the central composite design and response surface methodology to the advanced treatment of olive oil processing wastewater using Fenton's peroxidation. *J. Hazard. Mater.* 123, 187-195.
- Ahmad, Z., Ujang, Z., Olsson, G., and Latiff, a a A. 2009. Evaluation of Hybrid Membrane Bioreactor (MBR) For Palm Oil Mill Effluent (POME) Treatment. *International Journal of Integrated Engineering (Issue on Civil and Environmental Engineering) International Journal of Integrated Engineering (Issue on Civil and Environmental Engineering)*, 17–26.
- Ahmed, Y., Yaakob, Z., Akhtar, P., and Sopian, K. 2015. Production of biogas and performance evaluation of existing treatment processes in palm oil mill effluent (POME). *Renewable and Sustainable Energy Reviews*, 42: 1260–1278.
- Aljuboury, D. A. D. A., Palaniandy, P., Aziz, H. B. A., Feroz, S., 2015. Evaluating the TiO₂ as a solar photocatalyst process by response surface methodology to treat the petroleum waste water. *Karbala Int. J. Modern Sci.* 1, 78-85.
- Alvarez, P. M., Jaramillo, J., Lopez-Pinero, F., and Plucinski, P. K. 2010. Preparation and characterization of magnetic TiO₂ nanoparticles and their utilization for the degradation of emerging pollutants in water. *Applied Catalysis B: Environmental*, 100(1–2): 338–345.

- An, T., An, J., Yang, H., Li, G., Feng, H., and Nie, X. 2011. Photocatalytic degradation kinetics and mechanism of antiviral drug-lamivudine in TiO₂ dispersion. *Journal of Hazardous Materials*, 197: 229–36.
- An, T., Yang, H., Li, G., Song, W., Cooper, W. J., and Nie, X. 2010. Kinetics and mechanism of advanced oxidation processes (AOPs) in degradation of ciprofloxacin in water. *Applied Catalysis B: Environmental*, 94(3–4): 288–294.
- Antoniou, M. G., Shoemaker, J. A., de la Cruz, A. A., and Dionysiou, D. D. 2008. LC/MS/MS structure elucidation of reaction intermediates formed during the TiO₂ photocatalysis of microcystin-LR. *Toxicol*, 51(6): 1103–1118.
- Araujo, P. W., and Brereton, G. 1996. Experimental design. I. Screening. *TrAC - Trends in Analytical Chemistry*, 15(1): 26–31.
- Aris, A., Siew, O. B., Kee, K. S., and Ujang, Z. 2008. Tertiary treatment of palm oil mill effluent using Fenton oxidation. *Malaysian Journal of Civil Engineering*, 20(1): 12–25.
- Augustana University. n.d. IR Areas of Interest - Chem 201. <http://faculty.augie.edu/~duffy/irareaschem201.pdf> accessed on 11/10/15.
- Baruah, S., Thanachayanont, C., and Dutta, J. 2008. Growth of ZnO nanowires on nonwoven polyethylene fibers. *Science and Technology of Advanced Materials*, 9(2): 25009.
- Barr, G., 2010. Chemical and physical polishing of POME treatment. Seminar & Workshop on Palm Oil Mill Effluent Tertiary Treatment Technologies POMET³, Kota Kinabalu, Sabah, Malaysia.
- Berkani, M., Bouhelassa, M., & Bouchareb, M. K., 2015. Implementation of a venturi photocatalytic reactor: optimization of photodecolorization of an industrial Azo dye. *Arab. J. Chem.* <http://dx.doi.org/10.1016/j.arabjc.2015.07.004>
- Bennett, S. W., and Keller, A. A. 2011. Comparative photoactivity of CeO₂, Fe₂O₃, TiO₂ and ZnO in various aqueous systems. *Applied Catalysis B: Environmental*, 102(3–4): 600–607.
- Borges, M. E., Sierra, M., Cuevas, E., García, R. D., and Esparza, P. 2016. Photocatalysis with solar energy: Sunlight-responsive photocatalyst based on TiO₂ loaded on a natural material for wastewater treatment. *Solar Energy*, 135: 527–535.
- Boroski, M., Rodrigues, A. C., Garcia, J. C., Sampaio, L. C., Nozaki, J., and Hioka, N. 2009. Combined electrocoagulation and TiO₂ photoassisted treatment applied to wastewater effluents from pharmaceutical and cosmetic industries. *Journal of Hazardous Materials*, 162(1): 448–454.

- Box, G. E. P. & Wilson, K. B. 1951. On the experimental attainment of optimum conditions. *J. Roy. Statist. Soc.*, B13, 1-38.
- Cao, S., Yeung, K. L., and Yue, P. L. 2006. Preparation of freestanding and crack-free titania-silica aerogels and their performance for gas phase, photocatalytic oxidation of VOCs. *Applied Catalysis B: Environmental*, 68(3-4): 99-108.
- Central Connecticut State University. 2001. Infrared Spectroscopy- IR Absorption for Representative Functional Groups. <http://www.instruction.greenriver.edu/kmarr/chem%20162/Chem162%20Labs/Interpreting%20IR%20Spectra/IR%20Absorptions%20for%20Functional%20Groups.html> accessed on 11/10/2015.
- Chan, Y. J., Chong, M. F., and Law, C. L. 2010. Biological treatment of anaerobically digested palm oil mill effluent (POME) using a Lab-Scale Sequencing Batch Reactor (SBR). *Journal of Environmental Management*, 91(8): 1738-1746.
- Chan, Y. J., Chong, M. F., and Law, C. L. 2011. Optimization on thermophilic aerobic treatment of anaerobically digested palm oil mill effluent (POME). *Biochemical Engineering Journal*, 55(3): 193-198.
- Chan, Y. J., Chong, M. F., and Law, C. L. 2012. An integrated anaerobic-aerobic bioreactor (IAAB) for the treatment of palm oil mill effluent (POME): Start-up and steady state performance. *Process Biochemistry*, 47(3): 485-495.
- Chen, H., and Dawson, J. A. 2015. Nature of nitrogen-doped anatase TiO₂ and the origin of its visible-light activity. *Journal of Physical Chemistry C*, 119(28): 15890-15895.
- Chen, H. W., Ku, Y., and Kuo, Y. L. 2007. Effect of Pt/TiO₂ characteristics on temporal behavior of o-cresol decomposition by visible light-induced photocatalysis. *Water Research*, 41(10): 2069-2078.
- Cheng, M., Zeng, G., Huang, D., Lai, C., Xu, P., Zhang, C., and Liu, Y. 2016. Hydroxyl radicals based advanced oxidation processes (AOPs) for remediation of soils contaminated with organic compounds: A review. *Chemical Engineering Journal*, 284: 582-598.
- Cheng, X., Yu, X., Xing, Z., and Wan, J. 2012. Enhanced Photocatalytic Activity of Nitrogen Doped TiO₂ Anatase Nano-Particle under Simulated Sunlight Irradiation. *Energy Procedia*, 16: 598-605.
- Choorit, W., and Wisarnwan, P. 2007. Effect of temperature on the anaerobic digestion of palm oil mill effluent. *Electronic Journal of Biotechnology*, 10(3): 376-385.

- Chong, M. T., 2010. Bio-chem POME tertiary treatment system. Seminar & Workshop on Palm Oil Mill Effluent Tertiary Treatment Technologies POMET³, Kota Kinabalu, Sabah, Malaysia.
- Chung, Y. C., and Chen, C. Y. 2009. Degradation of azo dye reactive violet 5 by TiO₂ photocatalysis. *Environmental Chemistry Letters*, 7(4): 347–352.
- Coronado, J. M., Fresno, F., Hernández-Alonso, M. D., & Portela, R. 2013. Design of advanced photocatalytic materials for energy and environmental applications. New York: Springer-Verlag London.
- Cullity, B. D. 1957. Elements of X-Ray Diffraction. *Physics Today*, 10(3): 50–51.
- Dalrymple, O. K., Isaacs, W., Stefanakos, E., Trotz, M. A., and Goswami, D. Y. 2011. Lipid vesicles as model membranes in photocatalytic disinfection studies. *Journal of Photochemistry and Photobiology A: Chemistry*, 221(1): 64–70.
- Daneshvar, N., Aber, S., Seyed Dorraji, M. S., Khataee, A. R., and Rasoulifard, M. H. 2007. Photocatalytic degradation of the insecticide diazinon in the presence of prepared nanocrystalline ZnO powders under irradiation of UV-C light. *Separation and Purification Technology*, 58(1): 91–98.
- Dean, J. A. 1990. *Lange's Handbook of Chemistry. Materials and Manufacturing Processes* (Vol. 5).
- Di Mauro, A., Cantarella, M., Nicotra, G., Privitera, V., and Impellizzeri, G. 2016. Low temperature atomic layer deposition of ZnO: applications in photocatalysis. *Applied Catalysis B: Environmental*, 196: 68–76.
- Dias, M. G., and Azevedo, E. B. 2009. Photocatalytic decolorization of commercial acid dyes using solar irradiation. *Water, Air, and Soil Pollution*, 204(1–4): 79–87.
- Djerdj, I., and Tonejc, A. M. 2006. Structural investigations of nanocrystalline TiO₂ samples. *Journal of Alloys and Compounds*, 413(1–2): 159–174.
- Domen, K., Yoshimura, J., Sekine, T., Kondo, J., Tanaka, A., Maruya, K., and Onishi, T. 1993. A Novel Series of Photocatalysts with an Ion-Exchangeable Layered Structure of Niobate. *Studies in Surface Science and Catalysis*, 75(C): 2159–2162.
- Dong, H., Zeng, G., Tang, L., Fan, C., Zhang, C., He, X., and He, Y. 2015. An overview on limitations of TiO₂-based particles for photocatalytic degradation of organic pollutants and the corresponding countermeasures. *Water Research*, 79: 128–146.
- Echavia, G. R. M., Matzusawa, F., and Negishi, N. 2009. Photocatalytic degradation of organophosphate and phosphonoglycine pesticides using TiO₂ immobilized on silica gel. *Chemosphere*, 76(5): 595–600.

- Elmolla, E. S., and Chaudhuri, M. 2010. Photocatalytic degradation of amoxicillin, ampicillin and cloxacillin antibiotics in aqueous solution using UV/TiO₂ and UV/H₂O₂/TiO₂ photocatalysis. *Desalination*, 252(1–3): 46–52.
- Esparza, P., Borges, M. E., Diaz, L., Alvarez-Galvan, M. C., and Fierro, J. L. G. 2010. Photodegradation of dye pollutants using new nanostructured titania supported on volcanic ashes. *Applied Catalysis A: General*, 388(1–2): 7–14.
- Evgenidou, E., Fytianos, K., and Poullos, I. 2005. Semiconductor-sensitized photodegradation of dichlorvos in water using TiO₂ and ZnO as catalysts. *Applied Catalysis B: Environmental*, 59(1–2): 81–89.
- Fabbri, D., Crime, A., Davezza, M., Medana, C., Baiocchi, C., Prevot, A. B., and Pramauro, E. 2009. Surfactant-assisted removal of sweep residues from soil and photocatalytic treatment of the washing wastes. *Applied Catalysis B: Environmental*, 92(3–4): 318–325.
- Farbod, M., and Kajbafvala, M. 2013. Effect of nanoparticle surface modification on the adsorption-enhanced photocatalysis of Gd/TiO₂ nanocomposite. *Powder Technology*, 239: 434–440.
- Federal University of Minas Gerais. 2013. Characteristic Infrared Absorption bands of Functional Groups. www.biomaterial.com.br/FTIR.pdf accessed on 11/10/2015.
- Fenoll, J., Hellín, P., Martínez, C. M., Flores, P., and Navarro, S. 2012. Semiconductor-sensitized photodegradation of s-triazine and chloroacetanilide herbicides in leaching water using TiO₂ and ZnO as catalyst under natural sunlight. *Journal of Photochemistry and Photobiology A: Chemistry*, 238: 81–87.
- Fogler, H. S. 1999. Elements of chemical reaction engineering. *Chemical Engineering Science*, 42: 1000.
- Fujishima, A., Rao, T. N., and Tryk, D. A. 2000. Titanium dioxide photocatalysis. *Journal of Photochemistry and Photobiology C: Photochemistry Reviews*, 1(1): 1–21.
- Gaya, U. I., Abdullah, A. H., Zainal, Z., and Hussein, M. Z. 2009. Photocatalytic treatment of 4-chlorophenol in aqueous ZnO suspensions: Intermediates, influence of dosage and inorganic anions. *Journal of Hazardous Materials*, 168(1): 57–63.
- Gilmour, C. 2012. Water Treatment using Advanced Oxidation Processes : Application Perspectives, (September): 1–111.
- Giraldo, A. L., Pevuela, G. A., Torres-Palma, R. A., Pino, N. J., Palominos, R. A., and Mansilla, H. D. 2010. Degradation of the antibiotic oxolinic acid by photocatalysis with TiO₂ in suspension. *Water Research*, 44(18): 5158–5167.

- Gligorovski, S., Strekowski, R., Barbati, S., and Vione, D. 2015. Environmental Implications of Hydroxyl Radicals ($\bullet\text{OH}$). *Chemical Reviews*, 115(24): 13051–13092.
- Goodenough, J. B., Hammet, A., Huber, G., Hullinger, F., Leib, M., Ramasesha, S. K., & Werheit, H. 1984. Group III: Crystal and Solid State Physics, Berlin: Springer-Verlag.
- Gorska, P., Zaleska, a, Suska, a, and Hupka, J. 2009. Photocatalytic Activity and Surface Properties of Carbon-Doped Titanium Dioxide. *Physicochemical Problems of Mineral Processing*, 43(43): 21–30.
- Gratzel, M. 1989 Heterogeneous Photochemical Electron Transfer; CRC Press: Boca Raton, FL.
- Gutowski, M., and Kowalczyk, S. 2013. A study of free radical chemistry: Their role and pathophysiological significance. *Acta Biochimica Polonica*, 60(1): 1–16.
- Haibo, O., Feng, H. J., Cuiyan, L., Liyun, C., and Jie, F. 2013. Synthesis of carbon doped ZnO with a porous structure and its solar-light photocatalytic properties. *Materials Letters*, 111: 217–220.
- Han, Y. W., and Anderson, a W. 1975. Semisolid fermentation of ryegrass straw. *Applied Microbiology*, 30(6): 930–4.
- Hapeshi, E., Achilleos, A., Vasquez, M. I., Michael, C., Xekoukoulotakis, N. P., Mantzavinos, D., and Kassinos, D. 2010. Drugs degrading photocatalytically: Kinetics and mechanisms of ofloxacin and atenolol removal on titania suspensions. *Water Research*, 44(6): 1737–1746.
- Henderson, M. A. 2005. Photooxidation of acetone on $\text{TiO}_2(110)$: Conversion to acetate via methyl radical ejection. *Journal of Physical Chemistry B*, 109(24): 12062–12070.
- Henderson, M. A. 2008. Effect of coadsorbed water on the photodecomposition of acetone on $\text{TiO}_2(110)$. *Journal of Catalysis*, 256(2): 287–292.
- Hernández-Alonso, M. D., Hungría, A. B., Martínez-Arias, A., Fernández-García, M., Coronado, J. M., Conesa, J. C., and Soria, J. 2004. EPR study of the photoassisted formation of radicals on CeO_2 nanoparticles employed for toluene photooxidation. *Applied Catalysis B: Environmental*, 50(3): 167–175.
- Hoigne, J. 1988. The chemistry of ozone in water. In process technology for water treatment, S. Stucki, Ed., New York: Plenum publishing corp.

- Huang, H., He, Y., He, R., Jiang, X., Lin, Z., Zhang, Y., and Wang, S. 2014. Novel Bi-based iodate photocatalysts with high photocatalytic activity. *Inorganic Chemistry Communications*, 40: 215–219.
- Ibach, H. & Luth, H. 2010. The electronic band structure of solid. In: *Solid-State Physics – An introduction to principles of materials science*, Berlin: Springer-Verlag, 159–189.
- Idris, M. A., Jami, M. S., and Muyibi, S. A. 2010. Tertiary Treatment of Biologically Treated Palm Oil Mill Effluent (POME) Using UF Membrane System : Effect of MWCO and Transmembrane Pressure. *International Journal of Chemical and Environmental Engineering*, 1(2): 109–112.
- Ingvarsson, P. T., Yang, M., Mulvad, H., Nielsen, H. M., Rantanen, J., and Foged, C. 2013. Engineering of an inhalable dda/tdb liposomal adjuvant: A quality-by-design approach towards optimization of the spray drying process. *Pharmaceutical Research*, 30(11): 2772–2784.
- Ji, Y., Zhou, L., Ferronato, C., Salvador, A., Yang, X., Chovelon, J-M. 2013. Degradation of sunscreen agent 2-phenylbenzimidazole-5-sulfonic acid by TiO₂ photocatalysis: Kinetics, photoproducts and comparison to structurally related compounds. *Applied Catalysis B: Environmental*, 140-141, 457-467.
- Jia, T., Wang, W., Long, F., Fu, Z., Wang, H., and Zhang, Q. 2009. Fabrication, characterization and photocatalytic activity of La-doped ZnO nanowires. *Journal of Alloys and Compounds*, 484(1–2): 410–415.
- Jung, S., and Yong, K. 2011. Fabrication of CuO-ZnO nanowires on a stainless steel mesh for highly efficient photocatalytic applications. *Chemical Communications (Cambridge, England)*, 47(9): 2643–2645.
- Jurgensen, E. J. 2010. Ozone and submerged fixed film biological process of POME polishing plant. Seminar & Workshop on Palm Oil Mill Effluent Tertiary Treatment Technologies POMET3, Kota Kinabalu, Sabah, Malaysia.
- Karunakaran, C., and Senthilvelan, S. 2006. Fe₂O₃-photocatalysis with sunlight and UV light: Oxidation of aniline. *Electrochemistry Communications*, 8(1): 95–101.
- Khalid, a. R., and Mustafa, W. A. W. 1992. External benefits of environmental regulation: Resource recovery and the utilisation of effluents. *The Environmentalist*, 12(4): 277–285.
- Khataee, A.R., Fathinia, M., Aber, S., Zarei, M., 2010. Optimization of photocatalytic treatment of dye solution on supported TiO₂ nanoparticles by central composite design: intermediates identification. *J. Hazard. Mater.* 181, 886-897.

- Khodja, A. A., Sehili, T., Pilichowski, J.-F., and Boule, P. 2001. Photocatalytic degradation of 2-phenylphenol on TiO₂ and ZnO in aqueous suspensions. *Journal of Photochemistry and Photobiology A: Chemistry*, 141(2–3): 231–239.
- Klug, H. P., & Alexander, L. 1956. *X-Ray Diffraction Procedures: For Polycrystalline and Amorphous Materials*. JOHN WILEY & SONS (Vol. 4).
- Kudo, A., and Miseki, Y. 2009. Heterogeneous photocatalyst materials for water splitting. *Chemical Society Reviews*, 38(1): 253–278.
- Kuo, T. J., Lin, C. N., Kuo, C. L., and Huang, M. H. 2007. Growth of ultralong ZnO nanowires on silicon substrates by vapor transport and their use as recyclable photocatalysts. *Chemistry of Materials*, 19(21): 5143–5147.
- Lazar, M. A., and Daoud, W. A. 2013. Achieving selectivity in TiO₂-based photocatalysis. *RSC Advances*, 3(13): 4130.
- Li, G., Park, S., Kang, D.-W., Krajmalnik-Brown, R., and Rittmann, B. E. 2011. 2, 4, 5-Trichlorophenol Degradation Using a Novel TiO₂-Coated Biofilm Carrier: Roles of Adsorption, Photocatalysis, and Biodegradation. *Environmental Science & Technology*, 45(5): 8359–8367.
- Li, J., Xu, X., Liu, X., Yu, C., Yan, D., Sun, Z., and Pan, L. 2016. Sn doped TiO₂ nanotube with oxygen vacancy for highly efficient visible light photocatalysis. *Journal of Alloys and Compounds*, 679: 454–462.
- Li, Q., Wang, C., Ju, M., Chen, W., and Wang, E. 2011. Polyoxometalate-assisted electrochemical deposition of hollow ZnO nanospheres and their photocatalytic properties. *Microporous and Mesoporous Materials*, 138(1–3): 132–139.
- Li, Y., Zhao, X., & Fan, W. Structural, electronic, and optical properties of Ag-doped ZnO nanowires: first principles study. *J. Phys. Chem. C*, 115(9): 3552–3557.
- Liao, S., Donggen, H., Yu, D., Su, Y., and Yuan, G. 2004. Preparation and characterization of ZnO/TiO₂, SO₄²⁻/ZnO/TiO₂ photocatalyst and their photocatalysis. *Journal of Photochemistry and Photobiology A: Chemistry*, 168(1–2): 7–13.
- Liew, L. L., Loh, S. K., Kassim, M. A., and Muda, K. 2015. Efficiency of Nutrients Removal From Palm Oil Mill Effluent Treatment Systems. *Journal of Palm Oil Research*, 27(4): 433–443.
- Lightcap, I. V., Kosel, T. H., and Kamat, P. V. 2010. Anchoring semiconductor and metal nanoparticles on a two-dimensional catalyst mat. storing and shuttling electrons with reduced graphene oxide. *Nano Letters*, 10(2): 577–583.

- Lima, C. S., Batista, K. A., Garcia Rodriguez, A., Souza, J. R., and Fernandes, K. F. 2015. Photodecomposition and color removal of a real sample of textile wastewater using heterogeneous photocatalysis with polypyrrole. *Solar Energy*, 114: 105–113.
- Lin, Y. C., and Lee, H. S. 2010. Effects of TiO₂ coating dosage and operational parameters on a TiO₂/Ag photocatalysis system for decolorizing Procion red MX-5B. *Journal of Hazardous Materials*, 179(1–3): 462–470.
- Lin, Y., Ferronato, C., Deng, N., and Chovelon, J. M. 2011. Study of benzylparaben photocatalytic degradation by TiO₂. *Applied Catalysis B: Environmental*, 104(3–4): 353–360.
- Liu, J., Peng, K., Huang, X., Lu, L., Cheng, H., Yang, D., ... Deng, H. 2011. *Je Sc Sc*, 23(6): 1020–1026.
- Liu, W.-J., Zeng, F.-X., Jiang, H., Zhang, X.-S., and Li, W.-W. 2012. Composite Fe₂O₃ and ZrO₂/Al₂O₃ photocatalyst: Preparation, characterization, and studies on the photocatalytic activity and chemical stability. *Chemical Engineering Journal*, 180: 9–18.
- Liu, W. Z., Xu, H. Y., Ma, J. G., Liu, C. Y., Liu, Y. X., & Liu, Y. C. 2012. Effect of oxygen-related surface adsorption on the efficiency and stability of ZnO nanorod array ultraviolet light-emitting diodes. *Appl. Phys. Lett.*, 100, 203101.
- Liu, Y., He, X., Duan, X., Fu, Y., Fatta-Kassinos, D., and Dionysiou, D. D. 2016. Significant role of UV and carbonate radical on the degradation of oxytetracycline in UV-AOPs: Kinetics and mechanism. *Water Research*, 95: 195–204.
- Lomillo, M. A. A., Campo, F. J., Pascual, F. J. M. 2006. Preliminary contribution to the quantification of HMF in honey by electrochemical biosensor chips. *Electroanalysis*, 18, 2435–2440.
- Lopez, R., Goni, F., Etxandia, A., and Millan, E. 2007. Determination of organochlorine pesticides and polychlorinated biphenyls in human serum using headspace solid-phase microextraction and gas chromatography-electron capture detection. *Journal of Chromatography B: Analytical Technologies in the Biomedical and Life Sciences*, 846(1–2): 298–305.
- Lu, F., Cai, W., and Zhang, Y. 2008. ZnO hierarchical micro/nanoarchitectures: Solvothermal synthesis and structurally enhanced photocatalytic performance. *Advanced Functional Materials*, 18(7): 1047–1056.
- Ma, A. N. 1999. Treatment of palm oil mill effluent. In: Singh, G., Lim, K.H., Teo, L., David Lee, K. Eds., *Oil Palm and the Environment*. Malaysian Oil Palm Growers' Council, Malaysia.

- Makarova, O. V., Rajh, T., Thurnauer, M. C., Martin, A., Kemme, P. A., and Cropek, D. 2000. Surface modification of TiO₂ nanoparticles for photochemical reduction of nitrobenzene. *Environmental Science and Technology*, 34(22): 4797–4803.
- Mamani, M. C. V, Farfan, J. A., Reyes, F. G. R., and Rath, S. 2006. Simultaneous determination of tetracyclines in pharmaceuticals by CZE using experimental design. *Talanta*, 70(2): 236–243.
- Manassah, J. 2011. Treatment of highly polluted paper mill waste water by solar photocatalytic oxidation with synthesized nano TiO₂. *Proceedings of the International Conference on Green Technology and Environmental Conservation, GTEC-2011*, 168(1): 356–361.
- Manickam, S., Zainal Abidin, N. B., Parthasarathy, S., Alzorqi, I., Ng, E. H., Tiong, T. J., ... Ali, A. 2014. Role of H₂O₂ in the fluctuating patterns of COD (chemical oxygen demand) during the treatment of palm oil mill effluent (POME) using pilot scale triple frequency ultrasound cavitation reactor. *Ultrasonics Sonochemistry*, 21(4): 1519–1526.
- Metcalf & Eddy Inc. Tchobanoglous, G., Burton, F.L. and Stensel, H.D. ed. 2003, Wastewater engineering; treatment and reuse, McGraw-Hill, New York.
- Mijin, D., Savić, M., Snežana, P., Smiljanić, A., Glavaški, O., Jovanović, M., and Petrović, S. 2009. A study of the photocatalytic degradation of metamitron in ZnO water suspensions. *Desalination*, 249(1): 286–292.
- Minero, C., Mariella, G., Maurino, V., and Pelizzetti, E. 2000. Photocatalytic Transformation of Organic Compounds in the Presence of Inorganic Anions. 1. Hydroxyl-Mediated and Direct Electron-Transfer Reactions of Phenol on a Titanium Dioxide–Fluoride System. *Langmuir*, 16(6): 2632–2641.
- Miranda-Garcia, N., Maldonado, M. I., Coronado, J. M., and Malato, S. 2010. Degradation study of 15 emerging contaminants at low concentration by immobilized TiO₂ in a pilot plant. *Catalysis Today*, 151(1–2): 107–113.
- Miranda-Garcia, N., Suarez, S., Sanchez, B., Coronado, J. M., Malato, S., and Maldonado, M. I. 2011. Photocatalytic degradation of emerging contaminants in municipal wastewater treatment plant effluents using immobilized TiO₂ in a solar pilot plant. *Applied Catalysis B: Environmental*, 103(3–4): 294–301.
- Mohajeri, S., Aziz, H. A., Isa, M. H., Zahed, M. A., and Adlan, M. N. 2010. Statistical optimization of process parameters for landfill leachate treatment using electro-Fenton technique. *Journal of Hazardous Materials*, 176(1–3): 749–758.
- Montgomery, D. C. 2008. Design and Analysis of Experiment, Seventh ed. New York:Wiley.

- Morris, J. W. 2007. Chapter 4 : Defects in Crystals. *Materials Science*, 76–107.
- Muda, K., Liew, W. L., and Loh, S. K. 2016. Performance evaluation of pome treatment plants 1, 11(4): 2153–2159.
- Mumtaz, T., Abd-Aziz, S., Rahman, N. a, Yee, P. L., Shirai, Y., and Hassan, M. a. 2008. Pilot-scale recovery of low molecular weight organic acids from anaerobically treated palm oil mill effluent (POME) with energy integrated system. *African Journal of Biotechnology*, 7(21): 3900–3905.
- Murakami, N., Chiyoya, T., Tsubota, T., and Ohno, T. 2008. Switching redox site of photocatalytic reaction on titanium(IV) oxide particles modified with transition-metal ion controlled by irradiation wavelength. *Applied Catalysis A: General*, 348(1): 148–152.
- Murakami, N., Ono, A., Nakamura, M., Tsubota, T., and Ohno, T. 2010. Development of a visible-light-responsive rutile rod by site-selective modification of iron(III) ion on {1 1 1} exposed crystal faces. *Applied Catalysis B: Environmental*, 97(1–2): 115–119.
- Nesbitt, H. W., and Banerjee, D. 1998. Interpretation of XPS Mn(2p) spectra of Mn oxyhydroxides and constraints on the mechanism of MnO₂ precipitation. *American Mineralogist*, 83(3–4): 305–315.
- Nezamzadeh-Ejehieh, A., and Khodabakhshi-Chermahini, F. 2014. Incorporated ZnO onto nano clinoptilolite particles as the active centers in the photodegradation of phenylhydrazine. *Journal of Industrial and Engineering Chemistry*, 20(2): 695–704.
- Ng, Y. S., Lim, C. R., and Chan, D. J. C. 2016. Development of treated palm oil mill effluent (POME) culture medium for plant tissue culture of *Hemianthus callitrichoides*. *Journal of Environmental Chemical Engineering*, (2015).
- Nor, N. A. M., Jaafar, J., Ismail, A. F., Mohamed, M. A., Rahman, M. A., Othman, M. H. D., ... Yusof, N. 2015. Preparation and performance of PVDF-based nanocomposite membrane consisting of TiO₂ nanofibers for organic pollutant decomposition in wastewater under UV irradiation. *Desalination*, 391: 89–97.
- Oliveira, C., Alves, A., and Madeira, L. M. 2014. Treatment of water networks (waters and deposits) contaminated with chlorfenvinphos by oxidation with Fenton's reagent. *Chemical Engineering Journal*, 241: 190–199.
- Oo, C. W., Kassim, M. J., and Pizzi, A. P. 2009. Characterization and performance of *Rhizophora apiculata* mangrove polyflavonoid tannins in the adsorption of copper (II) and lead (II), (October).

- Palanisamy, B., Babu, C. M., Sundaravel, B., Anandan, S., and Murugesan, V. 2013. Sol-gel synthesis of mesoporous mixed Fe₂O₃/TiO₂ photocatalyst: Application for degradation of 4-chlorophenol. *Journal of Hazardous Materials*, 252–253: 233–242.
- Palominos, R. A., Mondaca, M. A., Giraldo, A., Peñuela, G., Pérez-Moya, M., and Mansilla, H. D. 2009. Photocatalytic oxidation of the antibiotic tetracycline on TiO₂ and ZnO suspensions. *Catalysis Today*, 144(1–2): 100–105.
- Pan, L., Muhammad, T., Ma, L., Huang, Z. F., Wang, S., Wang, L., ... Zhang, X. 2016. MOF-derived C-doped ZnO prepared via a two-step calcination for efficient photocatalysis. *Applied Catalysis B: Environmental*, 189: 181–191.
- Paola, A. Di, Bellardita, M., and Palmisano, L. 2013. *Brookite, the Least Known TiO₂ Photocatalyst*. *Catalysts* (Vol. 3).
- Papp, Z. 2014. Different silver-modified zinc oxides for photocatalytic degradation of imidacloprid. *Chemija*, 25(1): 1–4.
- Pastor, N., Weinstein, H., Jamison, E., and Brenowitz, M. 2000. A detailed interpretation of OH radical footprints in a TBP-DNA complex reveals the role of dynamics in the mechanism of sequence-specific binding. *Journal of Molecular Biology*, 304(1): 55–68.
- Peña-Farfal, C., Moreda-Piñeiro, A., Bermejo-Barrera, A., Bermejo-Barrera, P., Pinochet-Cancino, H., and De Gregori-Henríquez, I. 2004. Use of enzymatic hydrolysis for the multi-element determination in mussel soft tissue by inductively coupled plasma-atomic emission spectrometry. *Talanta*, 64(3): 671–681.
- Pereira, J. H. O. S., Vilar, V. J. P., Borges, M. T., González, O., Esplugas, S., and Boaventura, R. A. R. 2011. Photocatalytic degradation of oxytetracycline using TiO₂ under natural and simulated solar radiation. *Solar Energy*, 85(11): 2732–2740.
- Puzyn, T. & Mostrag-Szlichtyng, A. 2012. *Organic Pollutants Ten Years After the Stockholm Convention - Environmental and Analytical Update*. New York, NY: InTech.
- Qian, J., Chen, F., Wang, F., Zhao, X., and Chen, Z. 2012. Daylight photocatalysis performance of biomorphic CeO₂ hollow fibers prepared with lens cleaning paper as biotemplate. *Materials Research Bulletin*, 47(8): 1845–1848.
- Qourzal, S., Barka, N., Tamimi, M., Assabbane, A., Nounah, A., Ihlal, A., and Ait-Ichou, Y. 2009. Sol-gel synthesis of TiO₂-SiO₂ photocatalyst for ??-naphthol photodegradation. *Materials Science and Engineering C*, 29(5): 1616–1620.

- Rajh, T., Poluejto, O. G., & Thurnauer, M. C. 2003. Charge separation in titanium oxide nanocrystalline semiconductors revealed by magnetic resonance. In: *Chemical physics of nanostructured semiconductors*, Kokorin, A. I. & Bahnemann, D. W., Utrecht: VSP, 1-34.
- Rasmussen, S. E. 2003. Relative merits of reflection and transmission techniques in laboratory powder diffraction. *Powder Diffraction*, 4, 18, 281-284.
- Ribeiro, A. R., Nunes, O. C., Pereira, M. F. R., and Silva, A. M. T. 2015. An overview on the advanced oxidation processes applied for the treatment of water pollutants defined in the recently launched Directive 2013/39/EU. *Environment International*, 75: 33–51.
- Rizzo, L., Meric, S., Kassinos, D., Guida, M., Russo, F., and Belgiorno, V. 2009. Degradation of diclofenac by TiO₂ photocatalysis: UV absorbance kinetics and process evaluation through a set of toxicity bioassays. *Water Research*, 43(4): 979–988.
- Rosa, P. A. J., Azevedo, A. M., and Aires-Barros, M. R. 2007. Application of central composite design to the optimisation of aqueous two-phase extraction of human antibodies. *Journal of Chromatography A*, 1141(1): 50–60.
- Rupani, P., and Singh, R. 2010. Review of current palm oil mill effluent (POME) treatment methods: Vermicomposting as a sustainable practice. *World Applied Sciences* ..., 11(1): 70–81.
- Salaeh, S., Juretic, D., Biosic, M., Kusic, H., Babic, S., Lavrencic, U., ... Loncaric, A. 2016. Diclofenac removal by simulated solar assisted photocatalysis using TiO₂-based zeolite catalyst; mechanisms, pathways and environmental aspects. *Chemical Engineering Journal*, 304: 289–302.
- Sanchez, M., Rivero, M. J., and Ortiz, I. 2010. Photocatalytic oxidation of grey water over titanium dioxide suspensions. *Desalination*, 262(1–3): 141–146.
- Shahrezaei, F., Mansouri, Y., Zinatizadeh, A. A. L., and Akhbari, A. 2012. Photocatalytic degradation of aniline using TiO₂ nanoparticles in a vertical circulating photocatalytic reactor. *International Journal of Photoenergy*, 2012.
- Shen, M., and Henderson, M. A. 2011. Impact of solvent on photocatalytic mechanisms: Reactions of photodesorption products with ice overlayers on the TiO₂(110) surface. *Journal of Physical Chemistry C*, 115(13): 5886–5893.
- Smyth, M. S., and Martin, J. H. 2000. X Ray Crystallography. *Journal of Clinical Pathology: Molecular Pathology*, 53(1): 8–14.

- Stathatos, E., Pelentridou, K., Karasali, H., Dionysiou, D. D., and Lianos, P. 2008. Photocatalytic degradation of a water soluble herbicide by pure and noble metal deposited TiO₂ nanocrystalline films. *International Journal of Photoenergy*, 2008.
- Suib, S. L. 2008. Sieves and Octahedral Layered Materials. *Accounts of Chemical Research*, 41(4): 479–487.
- Sulaiman, N. M. N., and Chea, K. L. 2004. Membrane ultrafiltration of treated Palm Oil Mill Effluent (POME). 1–8.
- Sulong, M., Lim, W. K., Kandiah, S., & Top, A. G. T. 2007. Membrane Bioreactor Technology for Tertiary Treatment of Palm Oil Mill Effluent POME. MPOB Information Series. Malaysian Palm Oil Board, Malaysia.
- Sundram, K., Sambanthamurthi, R., and Tan, Y. A. 2003. Palm fruit chemistry and nutrition. *Asia Pacific Journal of Clinical Nutrition*, 12(3): 355–362.
- Tamada, I. S., Lopes, P. R. M., Montagnolli, R. N., and Bidoia, E. D. 2012. Biodegradation and toxicological evaluation of lubricant oils. *Brazilian Archives of Biology and Technology*, 55(6): 951–956.
- Tarr, M. a. 2003. *Chemical Degradation Methods for Wastes and Pollutants. Combustion*.
- Tian, L., Zhao, Y., He, S., Wei, M., and Duan, X. 2012. Immobilized Cu-Cr layered double hydroxide films with visible-light responsive photocatalysis for organic pollutants. *Chemical Engineering Journal*, 184: 261–267.
- Triantis, T. M., Fotiou, T., Kaloudis, T., Kontos, A. G., Falaras, P., Dionysiou, D. D., ... Hiskia, A. 2012. Photocatalytic degradation and mineralization of microcystin-LR under UV-A, solar and visible light using nanostructured nitrogen doped TiO₂. *Journal of Hazardous Materials*, 211–212: 196–202.
- Tripathy, N., Ahmad, R., Eun Song, J., Ah Ko, H., Hahn, Y. B., and Khang, G. 2014. Photocatalytic degradation of methyl orange dye by ZnO nanoneedle under UV irradiation. *Materials Letters*, 136: 171–174.
- Ugoji, E. O. 1997. Anaerobic digestion of palm oil mill effluent and its utilization as fertilizer for environmental protection. *Renewable Energy*, 10(2–3): 291–294.
- Valencia, S., Marin, J. M., and Restrepo, G. 2010. Study of the Bandgap of Synthesized Titanium Dioxide Nanoparticules Using the Sol-Gel Method and a Hydrothermal Treatment. *The Open Materials Science Journal*, 4(2): 9–14.

- Vaez, M., Moghaddam, A. Z., & Alijani, S. 2012. Optimization and modeling of photocatalytic degradation of azo dye using a response surface methodology (RSM) based on the central composite design with immobilized titania nanoparticles. *Ind. Eng. Chem. Res.* 51, 4199-4207.
- Vidal, L., Psillakis, E., Domini, C. E., Grané, N., Marken, F., and Canals, A. 2007. An ionic liquid as a solvent for headspace single drop microextraction of chlorobenzenes from water samples. *Analytica Chimica Acta*, 584(1): 189–195.
- Vilar, V. J. P., Pinho, L. X., Pintor, A. M. A., and Boaventura, R. A. R. 2011. Treatment of textile wastewaters by solar-driven advanced oxidation processes. *Solar Energy*, 85(9): 1927–1934.
- Wang, L. K., Tay, J., Tay, S. T. L., & Hung, Y. 2010. Handbook of Environmental Engineering, vol. 11: Environmental Bioengineering, New York, NY: Springer.
- Wang, T. C., Lu, N., Li, J., and Wu, Y. 2011. Plasma-TiO₂ catalytic method for high-efficiency remediation of p-nitrophenol contaminated soil in pulsed discharge. *Environmental Science and Technology*, 45(21): 9301–9307.
- Wang, X., He, Z., Zhong, S., and Xiao, X. 2007. Photocatalytic Synthesis of Hydrocarbon Oxygenates from C₂H₆ and CO₂ over Pd-MoO₃/SiO₂ Catalyst. *Journal of Natural Gas Chemistry*, 16(2): 173–178.
- Wang, X., Wang, W., Miao, Y., Feng, G., and Zhang, R. 2016. Facet-selective photodeposition of gold nanoparticles on faceted ZnO crystals for visible light photocatalysis. *Journal of Colloid and Interface Science*, 475: 112–118.
- Warren, B.E. 1969. X-Ray Diffraction, Addison-Wesley, New York.
- WebSpectral. 2000. Table of IR Absorption. <http://webspectra.chem.ucla.edu/irtable.html> accessed on 10/11/2015.
- White, J. M., and Henderson, M. A. 2005. Trimethyl acetate on TiO₂(110): Preparation and anaerobic photolysis. *Journal of Physical Chemistry B*, 109(25): 12417–12430.
- Williams, G., Seger, B., and Kamt, P. V. 2008. TiO₂-graphene nanocomposites. UV-assisted photocatalytic reduction of graphene oxide. *ACS Nano*, 2(7): 1487–1491.
- Wu, C., Shen, L., Zhang, Y. C., and Huang, Q. 2011. Solvothermal synthesis of Cr-doped ZnO nanowires with visible light-driven photocatalytic activity. *Materials Letters*, 65(12): 1794–1796.
- Wu, C., Zhang, Y. C., and Huang, Q. 2014. Solvothermal synthesis of N-doped ZnO microcrystals from commercial ZnO powder with visible light-driven photocatalytic activity. *Materials Letters*, 119: 104–106.

- Wu, T., Liu, G., Zhao, J., and Serpone, N. 1999. Evidence for H₂O₂ Generation during the TiO₂ -Assisted Photodegradation of Dyes in Aqueous Dispersions under Visible Light Illumination, 33(6): 4862–4867.
- Wu, T. Y., Mohammad, A. W., Md. Jahim, J., and Anuar, N. 2007. Palm oil mill effluent (POME) treatment and bioresources recovery using ultrafiltration membrane: Effect of pressure on membrane fouling. *Biochemical Engineering Journal*, 35(3): 309–317.
- Xia, H., Zhuang, H., Zhang, T., and Xiao, D. 2008. Visible-light-activated nanocomposite photocatalyst of Fe₂O₃/SnO₂. *Materials Letters*, 62(6–7): 1126–1128.
- Xu, Y., and Langford, C. H. 2001. UV- or visible-light-induced degradation of X3B on TiO₂ nanoparticles: The influence of adsorption. *Langmuir*, 17(3): 897–902.
- Y. Cho, W. Choi, C-H. Lee, T. Hyeon, H.-I. L. 2001. Visible Light-Induced Degradation of Carbon Tetrachloride on. *Environ. Sci. Technol*, 35(5): 966–970.
- Yacob, S., Ali Hassan, M., Shirai, Y., Wakisaka, M., and Subash, S. 2006. Baseline study of methane emission from anaerobic ponds of palm oil mill effluent treatment. *The Science of the Total Environment*, 366(1): 187–96.
- Yacob, S., Shirai, Y., Hassan, M. A., Wakisaka, M., and Subash, S. 2006. Start-up operation of semi-commercial closed anaerobic digester for palm oil mill effluent treatment. *Process Biochemistry*, 41(4): 962–964.
- Yu, Z., and Chuang, S. S. C. 2007. In situ IR study of adsorbed species and photogenerated electrons during photocatalytic oxidation of ethanol on TiO₂. *Journal of Catalysis*, 246(1): 118–126.
- Yusà, V., Pardo, O., Pastor, A., and De La Guardia, M. 2006. Optimization of a microwave-assisted extraction large-volume injection and gas chromatography-ion trap mass spectrometry procedure for the determination of polybrominated diphenyl ethers, polybrominated biphenyls and polychlorinated naphthalenes in sedime. *Analytica Chimica Acta*, 557(1–2): 304–313.
- Zafar, S. 2015. Properties of POME, accessed <http://www.bioenergyconsult.com/tag/properties-of-pome/> on 15 July 2015.
- Zahrim, A.Y., Rachel, F.M., Menaka, S., Su, S.Y., & Melvin, F. 2009. Decolourization of Anaerobic Palm Oil Mill Effluent via Activated Sludge-Granular Activated Carbon. *World Applied Sciences Journal*, 5(Special Issue for Environment): 126–129.
- Zhang, J., Jiang, J., and Zhao, X. S. 2011. Synthesis and Capacitive Properties of Manganese Oxide Nanosheets Dispersed on Functionalized Graphene Sheets. *The Journal of Physical Chemistry C*, 115(14): 6448–6454.

- Zhang, W., Li, Y., Su, Y., Mao, K., and Wang, Q. 2012. Effect of water composition on TiO₂ photocatalytic removal of endocrine disrupting compounds (EDCs) and estrogenic activity from secondary effluent. *Journal of Hazardous Materials*, 215–216: 252–258.
- Zhang, X., and Lei, L. 2008. Preparation of photocatalytic Fe₂O₃-TiO₂ coatings in one step by metal organic chemical vapor deposition. *Applied Surface Science*, 254(8): 2406–2412.
- Zhang, Y., Ram, M. K., Stefanakos, E. K., and Goswami, D. Y. 2012. Synthesis, characterization, and applications of ZnO nanowires. *Journal of Nanomaterials*, 2012.
- Zhou, J., Xu, N., and Wang, Z. L. 2006. Dissolving behavior and stability of ZnO wires in biofluids: A study on biodegradability and biocompatibility of ZnO nanostructures. *Advanced Materials*, 18(18): 2432–2435.
- Zhu, J., Chen, F., Zhang, J., Chen, H., and Anpo, M. 2006. Fe³⁺-TiO₂ photocatalysts prepared by combining sol-gel method with hydrothermal treatment and their characterization. *Journal of Photochemistry and Photobiology A: Chemistry*, 180(1–2): 196–204.
- Zhuang, J., Dai, W., Tian, Q., Li, Z., Xie, L., Wang, J., ... Wang, D. 2010. Photocatalytic degradation of RhB over TiO₂ bilayer films: Effect of defects and their location. *Langmuir*, 26(12): 9686–9694.
- Zinatizadeh, A. A. L., Mohamed, A. R., Abdullah, A. Z., Mashitah, M. D., Hasnain Isa, M., and Najafpour, G. D. 2006. Process modeling and analysis of palm oil mill effluent treatment in an up-flow anaerobic sludge fixed film bioreactor using response surface methodology (RSM). *Water Research*, 40(17): 3193–3208.

APPENDIX A LIST OF PUBLICATIONS

A1 Journal Publication

- **Ng, K. H.** & Cheng, C. K. (2017). Photocatalytic degradation of palm oil mill effluent over ultraviolet-responsive titania: Successive assessments of significance factors and process optimization. *Journal of Cleaner Production*, 142, 2073 - 2083.
- **Ng, K. H.** and Cheng, C. K. (2017). Optimization of Photocatalytic Degradation of Palm Oil Mill Effluent in UV/ZnO system based on Response Surface Methodology. *Journal of Environmental Management*, 184, 487-493.
- **Ng, K. H.** and Cheng, C. K. (2016). Photo-polishing of POME into CH₄-lean biogas over UV-responsive ZnO photocatalyst. *Chemical Engineering Journal*, 300, 127-138.
- **Ng, K. H.**, Lee, C. H., and Cheng, C. K. (2015). Photocatalytic degradation of recalcitrant POME waste over silver doped titania: Photokinetics and scavenging studies. *Chemical Engineering Journal*, 286, 282-290.
- Cheng, C. K., Deraman, M. R., **Ng, K. H.**, and Khan, M. R. (2015). Preparation of titania doped argentine photocatalyst and its photoactivity towards palm oil mill effluent degradation. *Journal of Cleaner Production*, 112, 1128-1135.
- **Ng, K. H.** and Cheng, C. K. (2015). A Novel Photomineralization of POME over UV-Responsive TiO₂ Photocatalyst: Kinetics of POME Degradation and Gaseous Product Formations. *RSC Advances*, 5, 53100-53110.
- **Ng, K. H.**, Deraman, M. D., Ang, C. H., Chong, S. K., Kong, Z. Y., Khan, M. R., and Cheng, C. K. (2014). Phototreatment of Palm Oil Mill Effluent (POME) over Cu/TiO₂ Photocatalyst. *Bulletin of Chemical Reaction Engineering and Catalysis*, 9(2), 121-127.

A2 Conference Proceedings

International

- **Ng, K. H.**, Kong, Z. Y., Chong, S. K., Ang, C. H., and Cheng, C. K. Photo-treatment of palm oil mill effluent (POME) over Cu/TiO₂ photocatalyst, ISCRE 23 and APCRE 7, 2014. (7th - 10th September 2014; Bangkok)
- Ang, C. H., Kong, Z. Y., **Ng, K. H.**, Chong, S. K., and Cheng, C. K. A study into the photoreaction of glycerol aqueous solution, ISCRE 23 and APCRE 7, 2014. (7th - 10th September 2014; Bangkok)

Local

- **Ng, K. H.** and Cheng, C. K. Photo-polishing of palm oil mill effluent (POME) over UV/ZnO system. ICAT2016, 2016. (20th- 21st September 2016; JB)
- **Ng, K. H.**, Khan, M. R., Cheng, C. K. Photocatalytic degradation of palm oil mills effluent (POME) over UV-responsive titania. ICENV2015, 2015. (18th - 19th August 2015; Penang)

UMP